1-1-2016

Electron Transfer Studies In Langmuir-Blodgett Films Of Metallosurfactants For Current Rectification, Corrosion Mitigation, And Water Oxidation

Sunalee Gonawala Jayasundara Mudiyanselage
Wayne State University,

ELECTRON TRANSFER STUDIES IN LANGMUIR-BLODGETT FILMS OF METALLOSURFACTANTS FOR CURRENT RECTIFICATION, CORROSION MITIGATION, AND WATER OXIDATION

by

SUNALEE GONAWALA J. M.

DISSERTATION

Submitted to the Graduate School

of Wayne State University,

Detroit, Michigan

in partial fulfillment of the requirements

for the degree of

DOCTOR OF PHILOSOPHY

2016

MAJOR: CHEMISTRY (Inorganic)

Approved By:

_____

Advisor Date

_____

_____

_____

DEDICATION

This dissertation is dedicated:

To my parents, Wijebandara Gonawala and Srimathie Gonawala for loving me unconditionally, and teaching me how to live life happily

ACKNOWLEDGEMENTS

First, I would like to express my special gratitude to my advisor, Prof. Cláudio N. Verani, for his excellence guidance, motivation, patience and for being a great mentor throughout my graduate studies. Thank you very much for believing in me and supporting me to excel as an excellent scientist and for advising me kindly in personal matters as a father to me. Dr. Verani, you are an advisor that every graduate student would like to have. You have a great understanding about each student and you know how to encourage and make them confident to face new challenges.

I would like to thank my committee members, Prof. Stanislav Groysman, Prof. Jennifer L. Stockdill, and Prof. Zhixian Zhou for their insightful feedback and valuable suggestions. A special thanks goes to all my collaborators, Prof. Zhixian Zhou and Madushanka Perera from Department of Physics and Astronomy, WSU; Prof. H. Bernhard Schlegel, Dr. Shivnath Mazumder, Bishnu Thapa, Prof. Sarah Trimpin, and Dr. Subashis Chakrabathy from Department of Chemistry, WSU; Prof. Guangzhao Mao and Lingxiao Xie from Department of Chemical Engineering & Materials Science, WSU. Thank you for making my research a success with your collaborative work.

My gratefulness extends to Lumigen Instrument center staff, Dr. Mike Mei for his help with SEM and XPS analysis; Dr. Lew Hryhorczuk and Dr. Yuri Danylyuk for performing mass spectral analysis; Dr. Bashar Ksebati for training me on the NMR instruments. I would also like to thank Nestor O'Campo for his support with software and hardware issues.

I also wish to express my sincere gratitude to Dr. Maryfrances Barber, Dr. Barbara Munk, Melissa Barton, office support staff, administrative staff and science stores staff: Dr. Barber and Dr. Munk for their valuable advices and guidance during teaching assistance ships; Melissa for

her guidance and reminders to keep in track with necessary paperwork requirements; office support, administrative, and science stores staff for their help in administrative and financial matters. I am also grateful to Wayne State University and National Science Foundation for their financial support via teaching assistance ships and research assistance ships to make this research a success.

Life in the research lab will not be enjoyable without my fellow lab mates. I would like to thank Dr. Rajendra Shakya and Dr. Fernando R. Xavier, the two post-doctoral fellows who was in the lab, for sharing their experience and guiding me through good work ethics. I would also like to extend my gratitude to Dr. Lank a Wickrmasinghe, Dr. Dakshika Wanniarachchi, Dr. Dajena Tomco for their valuable discussions, and training me on the lab instruments and techniques. A special thank goes to Dr. Lanka Wickramasinghe for being my mentor and a good friend when I first joined the Verani group. I would also like to thank Dr. Ryan Thomas, Dr. Debashis Basu for their valuable discussions, suggestions, and friendship. I also appreciate Habib Baydoun, Kenneth Kpogo, Danushka Ekanayake, Pavithra Hetti Achchi, Nour El-harake, Isuri Weeraratne, and Renata Crispim for their valuable discussions and making the lab a friendly and lively place to work at. A special thank goes to Habib and Kenneth for solving the X-ray crystal structures and further, Habib for being a good collaborator to work with. I like to extend my gratitude to Veronica Ribeiro, summer visiting scholar, for her valuable suggestions to establish the corrosion project and Krista Kulesa for proof-reading and correcting my documents with grammar. My gratitude further extends to Priscila, Dr. Verani's wife, and their daughter Clara for the hospitality and friendship provided during the group gatherings.

At last but not least, I would like to thank my parents and my sister, Dulari Gonawala for believing in me and encouraging and supporting me in every possible manner. Their guidance

and advices made me who I am today. A special thank goes to my husband, Thimanka Ranatunga for his endless encouragement and unconditional love throughout all good and bad times. I am really blessed to have you all around me in all good and bad times.

TABLE OF CONTENTS

LIST OF TABLES

LIST OF FIGURES

LIST OF SCHEMES

CHAPTER 1 INTRODUCTION

One of the main research goals in the Verani group is to translate information learnt from discrete coordination complexes into designs for solid surface coatings that foster the development of new materials. The main interest during this transition is the ability of molecules to form highly ordered assemblies with unique electronic and redox properties due to their potential uses as molecular diodes,[1] molecular displays,[2] and other high-end applications.[3] To provide context for these applications, this introduction will describe importance of Langmuir-Blodgett (LB) technique and will detail and evaluate the current progress in the fields of molecular current rectification, corrosion mitigation, and heterogeneous water oxidation catalysis. Suggestions on what areas require improvement will be provided along with a brief review on LB.

1.1. Importance of Langmuir-Blodgett Films

Due to the need for technological development, modern coordination chemistry aims toward employing information obtained from complexes in the solution phase to understand behaviors observed in the solid phase to develop new materials. A great deal of attention has been directed toward metal-containing soft materials such as metallosurfactants,[4] metallopolymers,[5] and metallomesogens.[6] These materials are considered advantageous due to the cooperativity between metal ions and the organic ligands leading to unique redox and electronic properties. There are well established techniques for film formation that rely on chemisorptive or physisorptive processes. Self-assembly, atomic vapor deposition, and chemical vapor deposition are chemisorptive processes because they form covalent bonds between the molecule and the substrate.[7] Isothermal compression and spin coating are physisorptive processes, involving adsorption of molecules onto the substrate.[8]

Although chemisorption is widely used in film formation, isothermal compression offers greater control in final film morphology, which is critical in many applications including molecular electronics, optical coatings, and energy. Besides providing superior uniform coverage, isothermal compression controls the deposition in a layer-by-layer manner, forming well-organized and highly ordered films.[9] The thickness of the film can be modulated at a molecular level or by repeated deposition.[1-3] Moreover, only minute amounts of material are needed to cover large surface areas.

1.2. Molecular Electronic Devices

With the advance of technology, silicon-based integrated circuits have gained tremendous attention in the microelectronics industry.[9,10] The ultimate goal of microelectronics is the development of smaller, less costly electronic devices that function effectively and efficiently. In the past, this miniaturization has been achieved primarily using the top-down approach on existing silicon-based chips. According to Moore's law of 1965,[11] the top-down approach will reach its physical limits due to the leakage of current once the coating of the silicon layer reaches a thickness of three atoms.[12]

To overcome the limitations in miniaturization process, an alternative bottom-up approach can be introduced, as first mentioned in Richard P. Feynman's 1959 lecture "There's Plenty of Room at the Bottom."[13] In the bottom-up approach, molecules with the desired electronic and redox properties are synthesized and combined with other components to build electronic devices. Various film formation technologies can then be used to transfer these molecules onto solid substrates.[14] Although the use of molecules in electronic devices is an advanced alternative, adequate work was not done to advance this field until 1970s.

Initial discussion on molecular-based electronics was introduced in 1974, with the theoretical proposal for single molecule rectifiers by Ari Aviram and Mark Ratner.[15] They introduced the concept of designing molecules that can function as electronic devices. Organic molecules can be beneficial to obtain different electrical components due their ability to coordinate metals and fine-tune their electronic properties. Since molecules alone cannot be used in electronic devices, metal|molecule|metal assemblies are one of the most common techniques used to assess the electrical properties of synthesized molecules.[16,17]

Incorporation of redox active metals in the molecular component can enhance the electronic and redox properties of the system. However, electronic components built using coordinated complexes are currently rather limited.[18] As such, the next section will briefly discuss the use of organic and metal complexes for molecular rectifiers from literature.

1.2.1. Molecular Rectifiers

Rectifiers are electrical devices that are able to transform alternating current into direct current which flows only in one direction. Thus, rectifiers demonstrate a unidirectional flow of current as shown in **Figure 1.1a**. Rectifiers that are built with semiconductor materials are widely used and are known as semiconductor diodes.[17] Generally, in a p-n junction diode, a group IV semiconductor material is doped with a small amount of group V elements to obtain an electron-rich n-component while an electron-deficient p-component is obtained by doping with small amount of group III elements.[19]

The organic molecule proposed by Aviram and Ratner contains an electron donor moiety (D) with relatively low ionization potential (I_D); an electron acceptor moiety (A) with relatively high electron affinity (A_A); and a σ bridge which keeps parts D and A independent from each other (**Figure 1.1b**). The highest occupied molecular orbitals (HOMO) is an approximation for

$I_{D,}$ and lowest occupied molecular orbitals (LUMO) is an approximation for A_A.[20] These HOMO and LUMO energies should be comparable to the energetic Fermi levels of the electrodes to enable electron transfer between them.[20] Theoretical studies performed using this [D-σ-A] molecule showed an asymmetric current response representing a possible current rectification behavior.[15] However, experimental studies have not been performed using this molecule.

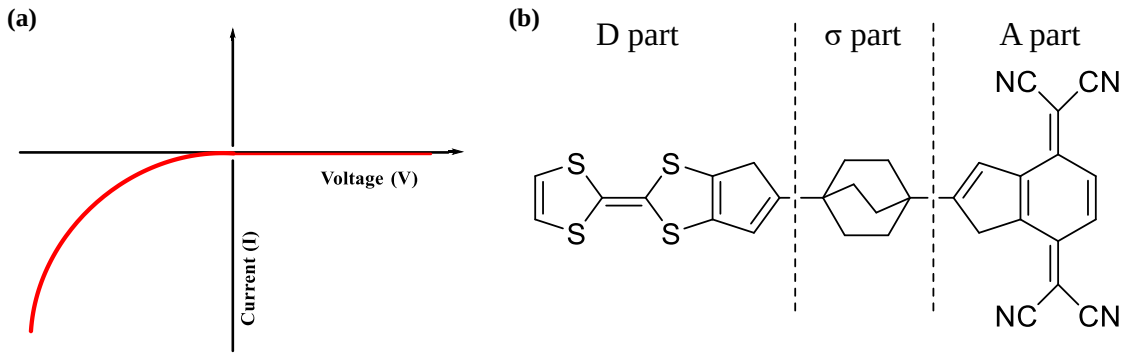

Figure 1.1. (a) Schematic representation of current-voltage curve for a rectifier (b) [D-σ-A] molecule proposed by Aviram and Ratner.

This [D-σ-A] molecule can function as a "pn" junction rectifier, where the electron rich "n" region can be correlated to the donor part D, and the electron poor "p" region can be correlated to the acceptor part A.

Metzger proposed three basic mechanisms of rectification: Schottky (S-rectifier), Asymmetric (A-rectifier), and Unimolecular (U-rectifier).[21] The rectification ability of a molecule can be identified by obtaining current/voltage measurements in a metal|molecule|metal assembly that is built by sandwiching the molecule between two electrodes. Schottky rectification is the most common mechanism that occurs due to covalent binding of the molecule to the electrode or due to use of electrodes with two different work functions.[21]

Asymmetric and unimolecular rectification mechanisms depend the HOMO and LUMO energies of a given molecule. In the asymmetric mechanism, the HOMO and LUMO energy

levels are distributed asymmetrically relative to the Fermi levels of the electrode. The LUMO of the acceptor moiety will accept one electron from the M_1 electrode and donate one electron to the M_2 electrode, as shown in **Figure 1.2**.[20] Here, the HOMO is much lower in energy making it unable to participate in electron transfer, while the LUMO is energetically comparable with the electrode Fermi levels and is involved in electron transfer. Molecules with asymmetric structures contribute more notably to the asymmetric current rectification because HOMO and LUMO energies can place asymmetrically between the electrode Fermi energy.[22]

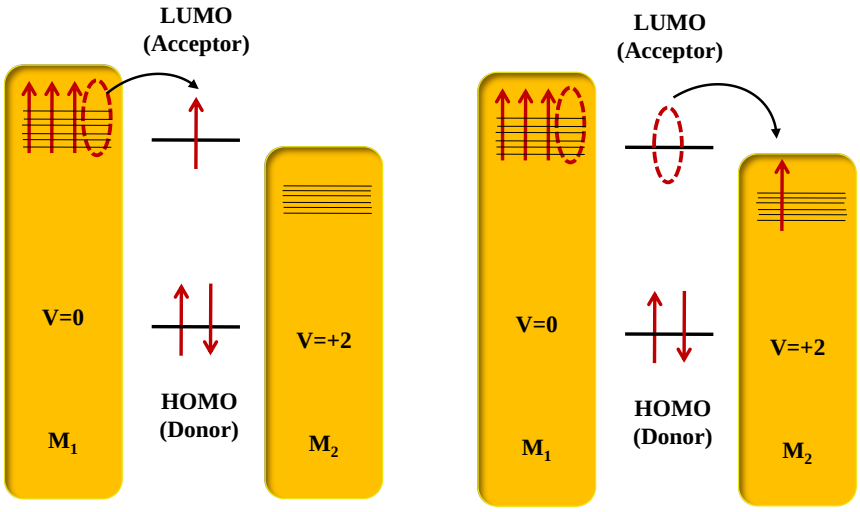

Figure 1.2. Schematic representation of an asymmetric (A) current rectification mechanism.

In the unimolecular mechanism, the LUMO of the acceptor moiety will accept one electron from the electrode M_2, and the HOMO of the donor moiety will donate one electron to the electrode M_1 (**Figure 1.3**). The small energy gap between HOMO and LUMO will allow the electron in LUMO to be transferred to HOMO to facilitate the upcoming electron transfer.[20,23,24]

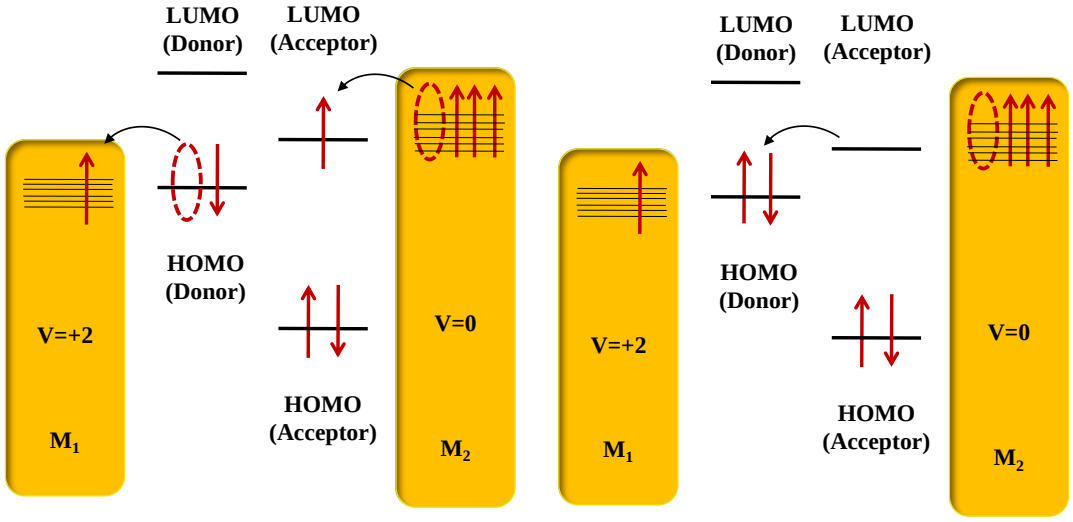

Figure 1.3. Schematic representation of a unimolecular (U) current rectification mechanism.

The rectification ratio (RR) compares the magnitude of currents at the positive (V) and corresponding negative bias (-V) (eq. 1) and can be used to evaluate the rectification ability of a particular system.[20]

$$RR\ (V) = |I\ (V)| / |I\ (-V)| \qquad (1)$$

For a system to be considered a rectifier, its RR value should be ≥2. As such, the greater the RR value, the better the rectification behavior of a given molecule. Various organic molecules with different bridging groups have been studied extensively by the Metzger and Ashwell groups as molecular current rectifiers.[20,21a,b,25] They introduced a new ground-state zwitterionic molecule with a [D^+-π-A^-] module (**Figure 1.4**) that is capable of LB film formation due to the presence of long alkyl chains, unlike the [D-σ-A] module proposed by Aviram and Ratner.[26] Both monolayers and multilayers sandwiched between platinum or gold electrodes have shown rectification behavior. Similarly, a LB monolayer sandwiched between two aluminum electrodes resulted in a higher RR of 26.4 while the device from LB multilayers showed a lower RR.[27] The results suggested that the electron flow preferentially occurs from tricyanoquinodimethanide (A^-) to (n-hexadecyl)quinolinium $(D)^+$ moiety.

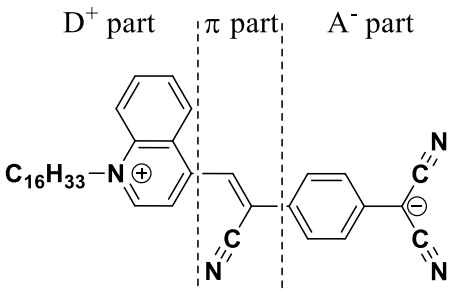

Figure 1.4. Ground-state zwitterionic molecule with a [D^{+}-π-A^{-}] module.

Other zwitterionic molecules with different alkyl chains (**Figure 1.5a**) as well as molecules containing iodide as a counter ion (**Figure 1.5b**) and fullerene containing molecules (**Figure 1.6a**) function as unimolecular current rectifiers.[20] Similarly, other organic molecule with [D-A] assemblies (**Figure 1.6b**) show rectification behavior.[20,25c,28]

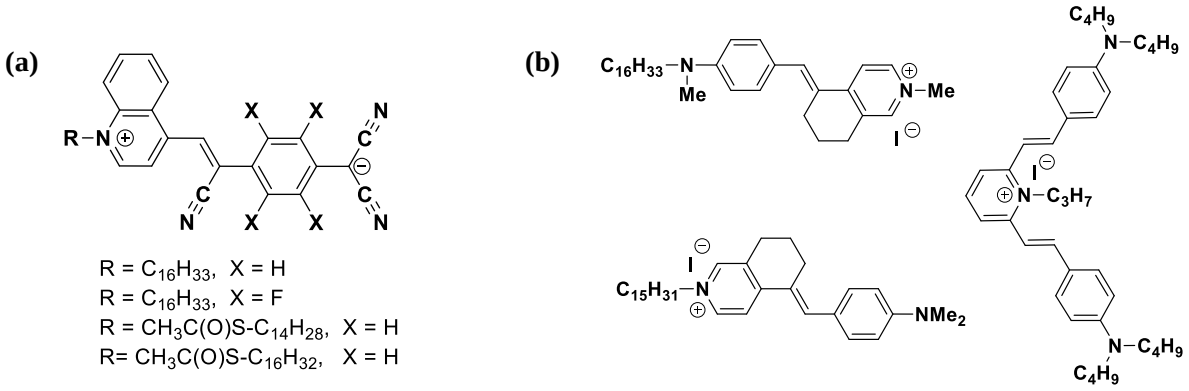

Figure 1.5. Molecules for unimolecular current rectification (a) with zwitterionic module (b) with iodide as the counterion.

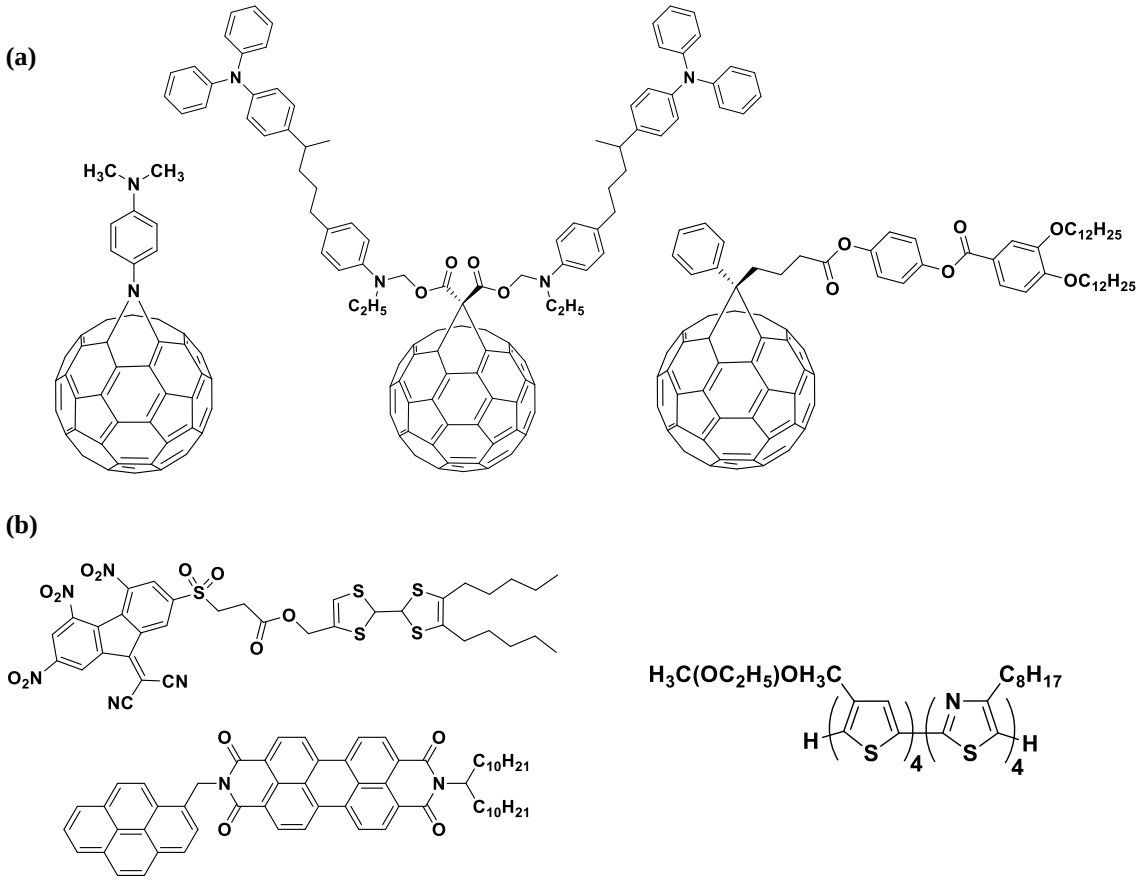

Figure 1.6. Selected organic [D-A] assemblies that show molecular current rectification.

Moving towards the use of coordination complexes for molecular current rectification, Ashwell and co-workers[29] have introduced a rectifying device fabricated using ionic coupling. They have used an anionic copper phthalocyanine donor along with a cationic bipyridinium acceptor (**Figure 1.7**) and a RR of 100 has been observed. Symmetric I/V curve has confirmed that each unit alone is not rectifying.

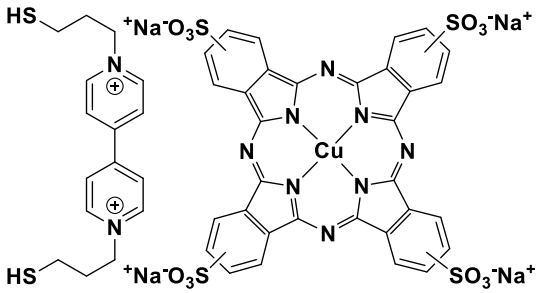

Figure 1.7. Molecular system used to observe rectification *via* ionic coupling.

Yu and coworkers[30] reported a hexa-coordinated ruthenium(II) complex (**Figure 1.8**) that functions as a unimolecular current rectifier. They observed an asymmetric current response with an RR of 3.53. The free ligand demonstrated a symmetric current response for an applied bias voltage. Despite an apparent axis of C2 symmetry, the complex has a calculated permanent dipole moment of 11.3 D perpendicular to the molecular wire ligand.[30] The report thereby affirms that the asymmetric nature of the complex is related to the observed rectification behavior. They also observed that the metallated complex can transfer an electron more efficiently than the unmetallated ligand, due to increase in the ligand planarity upon metallation, which increases conjugation.

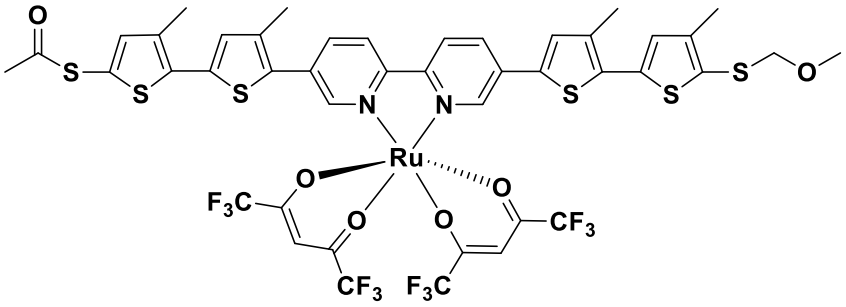

Figure 1.8. Hexa-coordinated ruthenium(II) complex from Yu group.

Our group has reported two iron(III) complexes that function as molecular rectifiers.[1] A phenolate-rich asymmetric Fe(III) complex with $[N_2O_3]$ framework (**Figure 1.9a**) has demonstrated an asymmetric current response with a RR of 4.52 to 12 when the applied bias potential is ±2 V, and a RR of 2.95 to 36.7 when the applied potential is ±4 V. We postulate that the phenolate moiety and metal center behave as the electron donor and the acceptor, respectively, during the rectification.[1a] Another Fe(III) complex with $[N_2O_2]$ framework (**Figure 1.9b**) has been studied by our group and demonstrated an asymmetric current response with a RR of 4 to 9 given a bias potential of ±2 V, and a RR of 2 to 31 given an applied potential of ±4 V.[1a] Comparison of the frontier molecular energy levels of the rectifying Fe(III) complex with a

structurally similar Cu(II) complex have shown that that metallic SOMO energies can function as electron acceptors engaging in electron transfer to follow an asymmetric current rectification mechanism. This finding demnstrates that molecules with SOMOs that are comparable to electrode Fermi levels can be involved in electron transfer to display molecular current rectification.

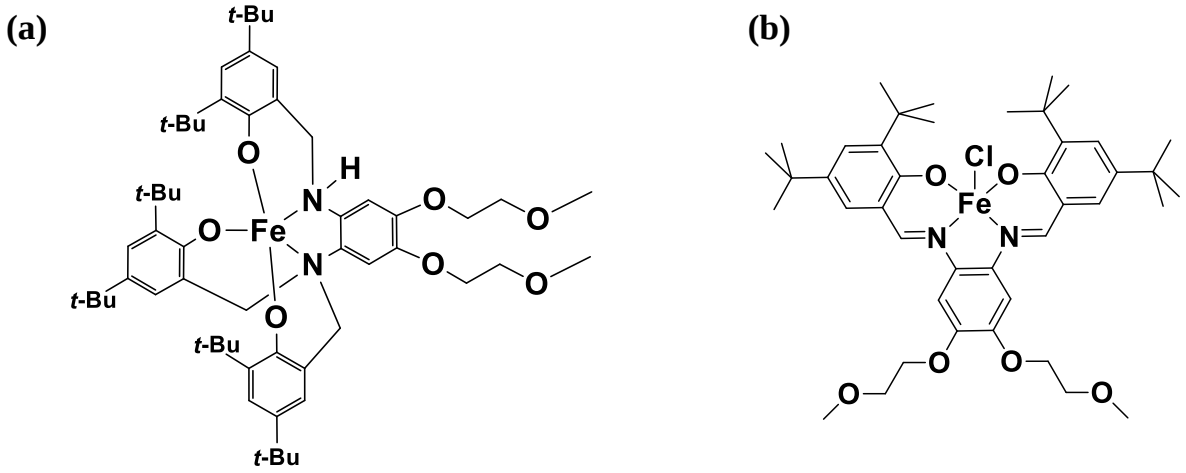

Figure 1.9. (a) Fe(III) complex with $[N_2O_3]$ coordination environment; (b) Fe(III) complex with $[N_2O_2]$ coordination environment.

A recently reported cadmium(II)-based metal organic framework demonstrates Schottky rectification when fabricated on an Al|Cd-MOF|indium tin oxide (ITO)-based device.[31] A RR of ~100 at ±10 V applied bias voltage has been observed for this device. This is the first report of using metal organic frameworks in electronic rectifiers.

Further computational studies have been performed to analyze the use of coordination complexes as molecular rectifiers. The DFT calculations performed on a molybdenum-based heterometallic complex (**Figure 1.10**) by McGrady and coworkers[32] has showed that Mo_2Co is a good candidate for rectification with a theoretical RR of 4.8 at a bias voltage of ±0.5 V. The study revealed that the localized π symmetry on Co center will induce asymmetric coupling to the electrode, resulting in a higher rectification ratio.

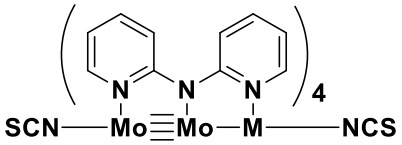

Figure 1.10. Generalized molybdenum-based heterometallic complex for current rectification.

Despite limited use in device fabrication to date, coordination complexes show great promise in electronics, with high heat tolerance being just one noteworthy advantage over their organic analogs. Therefore, considering the developments in molecular current rectification and the ramifications of the previous studies in our group, we expect to (a) pursue the use of synthetic methods to develop new metallosurfactants, (b) select appropriate candidates for current rectification based on redox, electronic, and film formation response, and (c) correlate electronic and film formation properties with I/V response to determine the mechanism for current rectification.

1.3. Corrosion Inhibition

Corrosion is an electrochemical phenomenon that leads to the degradation of metal as a consequence of reactions with its environment. With the exception of precious metals such as gold, silver, and platinum, metals tend to corrode easily since they are thermodynamically prone to form oxidized products described as M_xO_y oxides. Iron corrosion, for example, is an electrochemical process wherein a thin layer of moisture containing salts can act as an electrolyte and ultimately lead to iron oxide formation (**Figure 1.11**). Iron corrosion can be described as two half-reactions: an anodic reaction, where iron metal is oxidized into Fe^{2+} (eq. 2), and cathodic reaction, where OH^- is formed in the presence of oxygen (eq. 3).[33]

$$2Fe^0 \longrightarrow 2Fe^{2+} + 4e^- \qquad (2)$$

$$O_2 + 2H_2O + 4e^- \longrightarrow 4OH^- \qquad (3)$$

In the next step, Fe^{2+} reacts with OH^- to form $Fe^{II}(OH)_2$, which will be oxidized under aerobic conditions to $Fe^{III}(OH)_3$, the simple form of rust. Depending on oxygen supply, this simple form of rust can be further oxidized to $Fe_2O_3.H_2O$ or Fe_3O_4.[34]

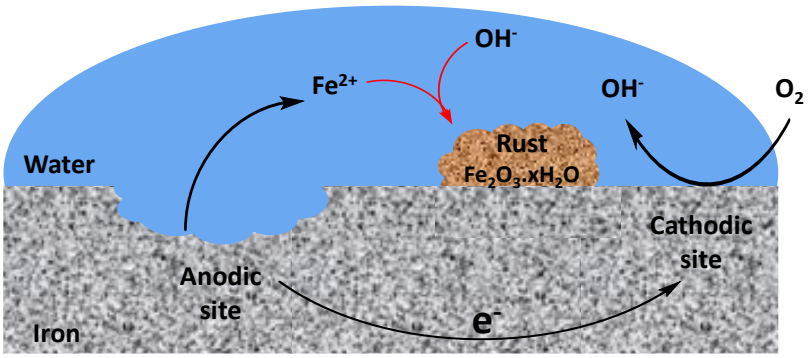

Figure 1.11. Schematic overview of the iron corrosion process.

Environmental factors such as humidity, temperature, acidity, salinity, and exposure time impact the corrosion rate of the metal.[34] It has been theoretically established that corrosion rate can double for each 10 ^oC increase in temperature.[34] High chloride concentrations and acidity can accelerate iron corrosion as well. In acidic media (< pH 4) the corrosion rate increases due to the increased solubility of the oxide layer and availability of H^+ for the reduction as shown in equations 4 and 5.[34]

$$4H^+ + 4e^- \longrightarrow 2H_2 \qquad (4)$$

$$O_2 + 4H^+ + 4e^- \longrightarrow 2H_2O \qquad (5)$$

1.3.1. Different Forms of Metal Corrosion

A metal surface can undergo several different forms of corrosion, each of which is classified by a corrosion mechanism. Common types of corrosion include:[35]

a) Uniform Corrosion

This is the simplest form of corrosion where metal loss occurs in an even rate throughout the exposed area.

b) Galvanic Corrosion

This is an electrochemical interaction between two dissimilar metals when in contact due to the presence of an electrolyte. Corrosion activity can be predicted based on the relative position of the metal in the galvanic series that determines the resistance for oxidation of the metal.

c) Pitting Corrosion

This occurs due to highly localized metal loss and appears as a deep, minute hole on the metal surface. Because pitting corrosion is more difficult to detect, it is considered to be more dangerous compared to uniform corrosion.

d) Crevice Corrosion

This is a localized corrosion due to differences in oxygen concentration within or adjacent to narrow metal-metal or metal-nonmetal gaps. Crevice corrosion shows rapid progression in the presence of chloride-containing solutions.

e) Intergranular Corrosion

Metals consist of grain structures with clearly defined boundaries. Intergranular corrosion occurs in these metallic grain boundaries, with the large granular area acting as the cathode while the boundaries act as the anode.

Apart from those aforementioned, other corrosion forms include stress corrosion cracking (due to stress), erosion corrosion (due to mechanical force), and biological corrosion (due to micro and macroorganism activity).

1.3.2. Coatings for Corrosion Protection

Protective coatings are currently the most widely used method for corrosion control.[35] Coatings vary according to environmental context and serve to control corrosion in a range of applications by functioning as a barrier between the surface and the electrolyte.

An ideal coating system for aqueous corrosion resistance should have three layers, as illustrated in **Figure 1.12**.[36] The surface pre-treatment layer is a thin layer that chiefly provides a cleaner surface for the upper primer layer, but can also act as a passive layer to protect the metal. The primer is a multi-layer coating that contains inhibitive and protective pigments. The primer layer is impermeable to moisture and provides the bulk of the corrosion protection. Lastly, the top-coat layer controls the final color and gloss of the surface. It also acts as a barrier for radiation and moisture.

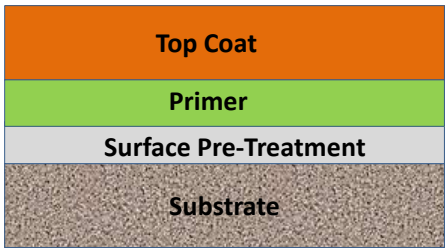

Figure 1.12. An ideal coating system for aqueous corrosion resistance.

1.3.3. Metal-Containing Anticorrosive Coatings

Organic polymers are traditionally used as corrosion prevention coatings due to their efficacy as moisture and oxygen barriers.[37] For this reason studies using metal-containing coatings are rather limited. However, metal coatings provide significant benefits in corrosion protective coatings by lowering electron density outside the steel plate, and by forming anticorrosive protective layers.[38] More than one of above features may be readily employed in a preventative system.

Schiff base complexes have received special attention in corrosion inhibition because the characteristic imine moiety can be adsorbed to the metal surface to form a protective layer.[39,40] Singh and coworkers[39] have investigated corrosion inhibition using manganese(II), copper(II), and zinc(II) complexes with the Schiff base ligand 2-aminobenzoic acid [1-(2-hydroxy-phenyl)-propylidene]-hydrazide (H_2abph) (**Figure 1.13**). Mn(II) forms a mononuclear complex whereas Cu(II) and Zn(II) form one-dimensional coordination polymers in methanolic solution. These complexes have exhibited appreciable corrosion inhibition ability for carbon steel (contains about 2 % carbon) in 1 M HCl medium in the order of H_2abph < Mn(II) complex < Cu(II) complex < Zn(II) complex.

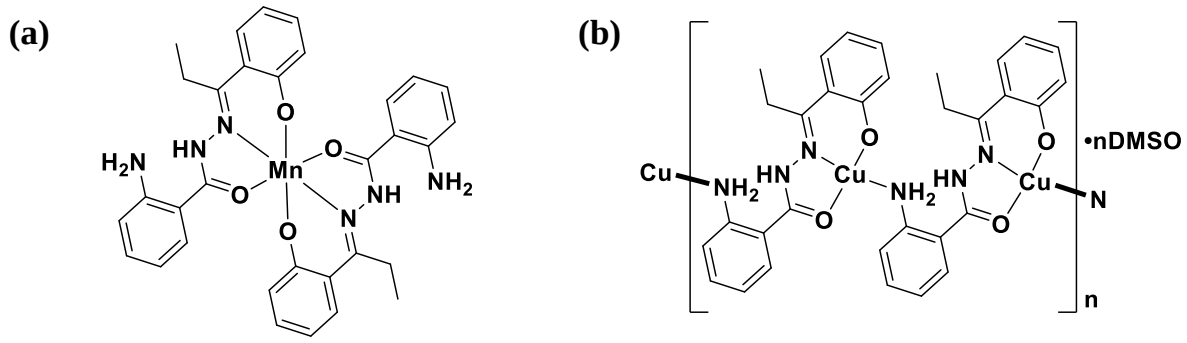

Figure 1.13. Multidentate Schiff base (a) Mn(II) and (b) Cu(II) complexes.

Cobalt(II), nickel(II), copper(II), and zinc(II) complexes with 2-acetylthiophene benzoylhydrazone (**Figure 1.14a**) have been studied for inhibition of steel corrosion as well.[40] Among these complexes, Co(II) has shown the greatest capacity for corrosion protection in 1 M HCl medium. A series of Mn(II), Co(II), Ni(II), Cu(II) and Zn(II) complexes with o-hydroxyacetophenone-2-thiophenoyl hydrazone (Hhath) (**Figure 1.14b**) have also been investigated for steel corrosion inhibition in 1 M HCl.[41] Compared to the pure ligand, the metal complexes demonstrated improved corrosion inhibition.

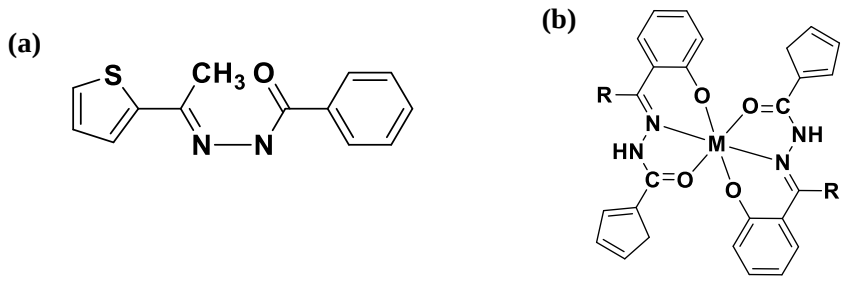

Figure 1.14. (a) 2-acetylthiophene benzoylhydrazone ligand; (b) Hhath-based metal complex.

Zinc aminophosphonates are investigated as corrosion inhibitors for carbon steel.[42] Covalent bonding between O-P-Zn-N(C) atoms of the complex and the steel surface facilitate formation of a protective layer. Zinc phosphates are commonly used as corrosion inhibitive coatings for steel protection, with best steel corrosion resistance observed at pH 2.75.[43] Hinton and coworkers[44] suggest further improvement of corrosion inhibition efficiency with the addition of rare earth metals (e.g. cerium diphenyl phosphate) to a polymer coating. Similar for steel corrosion, Schiff base metal complexes are also known as corrosion inhibitors for copper corrosion.[45]

Developing an ideal coating system for inhibition of iron corrosion certainly poses a multitude of challenges, but Schiff base metal complexes have been viably implemented in corrosion inhibitive coatings.[39-42] Therefore, based on prior studies on molecular current rectification and metallosurfactants from our group and others, we expect to (a) design and synthesize new redox-active and redox innocent salophen-based metallosurfactants to be used as protective coatings for iron corrosion, (b) investigate the electron passivation and corrosion mitigation ability of the LB films of salophen-based metallosurfactants.

1.4. Water Oxidation Catalysis

Keeping up with global energy demands while reducing greenhouse gas emission has become the priority of many scientists working to develop alternatives to fossil-based fuel

sources.[46] Intense focus has consequently shifted to hydrogen as a clean energy candidate, given its innocuous combustion. Water generated from hydrogen combustion can be used in turn as a source of hydrogen, a cycle facilitated by natural ubiquity.[47]

Splitting a water molecule into hydrogen and oxygen consists of two half reactions involving water reduction and water oxidation. Despite its apparent simplicity, water oxidation is in fact a monumentally unfavorable reaction, entailing a +237 kJ/mol Gibbs free energy change.[48] It is therefore considered the bottleneck for water splitting since it requires multielectron and multiproton transfers, as illustrated in equations 6, 7, and 8.[48,49]

$$4\ H^+ + 4\ e^- \longrightarrow 2\ H_2 \qquad E = 0\ V - 0.059\ pH\ \textit{vs}\ NHE \qquad (6)$$

$$2\ H_2O \longrightarrow O_2 + 4\ H^+ + 4e^- \qquad E = 1.23\ V - 0.059\ pH\ \textit{vs}\ NHE \qquad (7)$$

$$2\ H_2O \longrightarrow 2\ H_2 + O_2 \qquad \Delta E = -1.23\ V \qquad (8)$$

This thermodynamic and kinetic barrier can be overcome with the use of an effective catalyst. In the literature, efficient catalysts made of noble metals such as ruthenium,[50] iridium,[50b,51] and rhodium[52] abound. However, the low Earth-abundance of ruthenium and iridium severely limits widespread application of these water splitting technologies. As such, attention has been redirected toward the development of water oxidation catalysts using Earth-abundant metal ions such as manganese, iron, cobalt, nickel, and copper.[50-52]

The efficiency of a given catalyst can be determined by the turnover frequency (TOF). It refers to the number of moles of oxygen produced per mole of catalyst per hour. Turnover number (TON) represents the amount of oxygen generated per mole of catalyst. The overpotential shows the potential difference between the experimental potential and the standard thermodynamic potentials for oxygen generation. Lower the overpotential, better the catalysts is.

Finally, Faradaic efficiency (FE %) is a measure of catalyst stability during the catalytic process.[50,51]

1.4.1. Molecular Cobalt Complexes for Homogeneous Water Oxidation

In order to address the ongoing challenge to develop an efficient water oxidation catalyst (WOC) using Earth-abundant metal ions, several groups have studied homogeneous water oxidation catalysis with different Earth-abundant metals. Among them pyridine-containing cobalt complexes have been studied widely. Ye and coworkers[53] have synthesized dipyridine saloph-based Co(II) complexes soluble in aqueous media (**Figure 1.15a**). Electrochemical catalytic studies performed at pH 8.6 afforded an overpotential of 0.56 V. Bulk electrolysis performed for 5 h using an indium tin oxide (ITO) glass as the working electrode at an applied potential of 1.30 V demonstrated a Faradaic efficiency of 98.5% and a turnover frequency (TOF) of 81.54 mol(O_2) mol^{-1} s^{-1}.

Thapper and coworkers[54] have synthesized a mononuclear [Co(TPA)Cl]Cl complex as a homogenous catalyst for photoinduced water oxidation, using TPA (tris(2-pyridylmethyl)amine) ligand which contains three pyridine units (**Figure 1.15b**). The complex has exhibited catalytic activity with a TOF of 1.0 mol(O_2) mol(Co)$^{-1}$ s^{-1} at pH 8 in borate buffer using $[Ru(bpy)_3](ClO_4)_2$ as the photosensitizer and $Na_2S_2O_8$ as an electron acceptor.

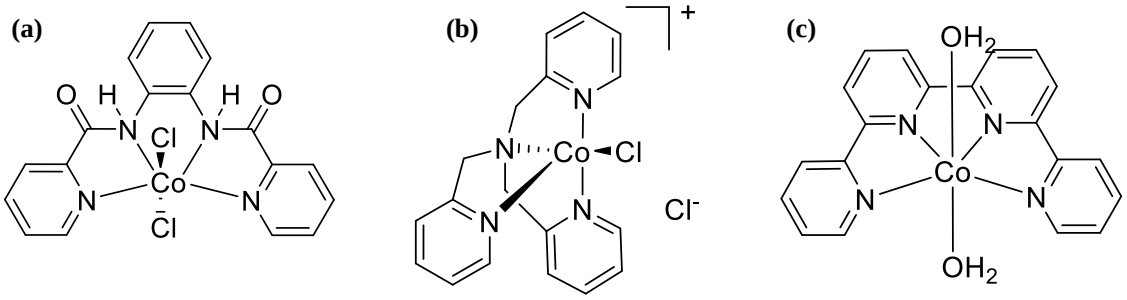

Figure 1.15. (a) Salophen-based (b) tripyridine-based and (c) tetrapyridine-based Co(II) complexes.

A tetrapyridine Co(II) complex has also been studied by the Lau group[55] as a homogeneous catalyst for photoinduced water oxidation (**Figure 1.15c**). The catalytic activity of this complex was evaluated in the presence of $[Ru(bpy)_3]Cl_2$ as the photosensitizer and $Na_2S_2O_8$ as the electron acceptor in pH 8 borate buffer. A maximum TON of 335 was observed for 1.5 h irradiation time at 457 nm. Water oxidation performed using chemical methods produced a TON of 160 ± 10 after 5 min at pH 8 in the presence of $[Ru (bpy)_3](ClO_4)_3$ as the oxidant.

Thapper and coworkers[56] have also considered polypyridyl Co(II) complexes as photoinduced water oxidation catalysts. The catalytic activity of one such pentapyridine Co(II) complex (**Figure 1.16**) has been studied at pH 8 in borate buffer using $[Ru(byp)_3]^{2+}$ as the photosensitizer and $S_2O_8^{2-}$ as the sacrificial electron acceptor.[56] A TOF of 1.3 ± 0.2 mol(O_2) mol^{-1} s^{-1} and TON of 51 ± 3 mol(O_2) mol^{-1} was observed.

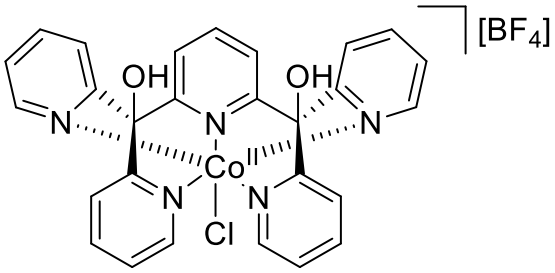

Figure 1.16. Pentapyridine Co(II) complex.

In addition, several porphyrin-based Co(II) complexes have been evaluated for photocatalytic[57] and electrocatalytic[58] water oxidation (**Figure 1.17**). Photocatalytic water oxidation studies were performed with water-soluble Co complexes at different pH values using $[Ru(bpy)_3](NO_3)_2$ and $Na_2S_2O_8$. Maximal activity was observed at pH 11, with a TOF of 0.17 s^{-1}.[57b]

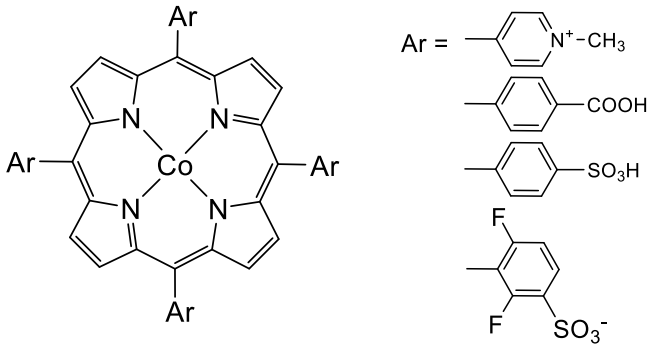

Figure 1.17. Porphyrin-based Co(II) water oxidation catalysts.

Electrocatalytic water oxidation has been explored with a series of cationic porphyrin Co complexes in neutral aqueous solutions (**Figure 1.18a**).[58a] A Faradaic efficiency near 90% was observed, with O_2 formation rate of 170 mmol cm^{-2} min^{-1}. Mechanistic studies have revealed the formation of a high-valent Co^{IV}-O porphyrin cation radical (formally Co(V) species) as the catalytically competent species. A pH 7 sodium phosphate buffer system facilitated the formation of the active species via redox-coupled proton transfer and O-O bond formation. Cobalt hangman corrole systems[58b] have also been studied as active water oxidation catalysts (**Figure 1.18b**). The rigid xanthene scaffold facilitates the placement of two water molecules above the corrole system, which is beneficial for O-O bond formation.[59] Catalytic activity has been observed at 1.25 V *vs* Ag/AgCl, with a TOF of 0.81 s^{-1}.

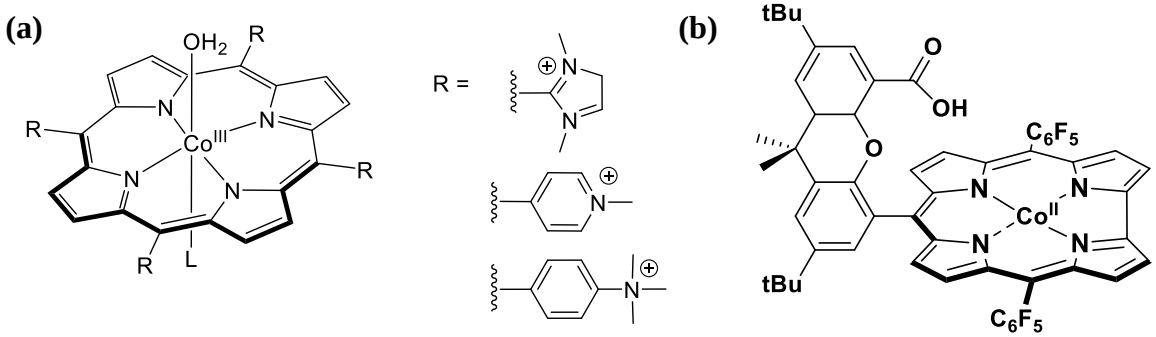

Figure 1.18. (a) Cationic porphyrin and (b) hangman corrole Co complexes.

Dinuclear Co complexes has also been investigated as homogenous water oxidation catalysts. A Co complex using TPA ligand (**Figure 1.19a**) have been reported,[60] that functions as a photoinduced water oxidation catalyst in presence of $[Ru(bpy)_3]^{2+}$ and $Na_2S_2O_8$. The complex demonstrated catalytic activity with a TOF of 1.4 ± 0.1 mol(O_2) mol^{-1} s^{-1} and maximal TON of 58 ± 5 mol(O_2) mol^{-1} in pH 8 borate buffer. Similarly, a double helical dicobalt(II) complex (**Figure 1.19b**) reported by the Lau group[61] has shown photoinduced water oxidation under comparable conditions; a maximum TON of 442 has been observed after 3 h irradiation.

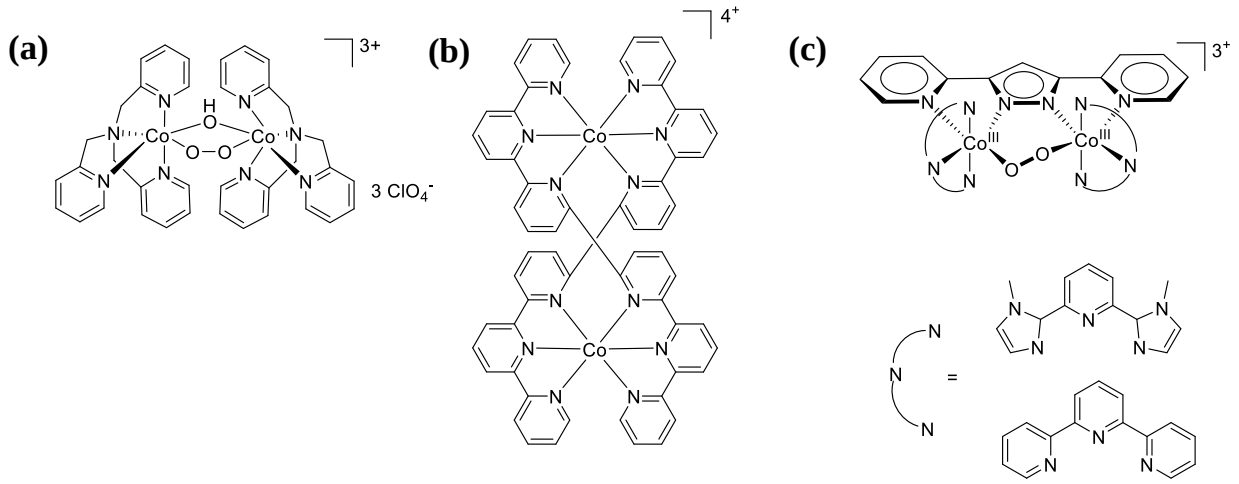

Figure 1.19. (a) TPA framework, (b) double helical, and (c) bispyridylpyrazolate dinuclear Co complexes.

The Stahl group[62] has reported electrochemical water oxidation using two bispyridylpyrazolate-ligated dicobalt(III)-peroxo complexes (**Figure 1.19c**). The complexes have shown catalytic activity at pH 2.1, 0.1 M phosphate buffer, for several hours without any signs of degradation or decomposition. Oxygen production was detected using a fluorescence quench probe, and a Faradaic efficiency of 77 % was observed after 2 h of electrolysis.

1.4.2. Molecular Cobalt Complexes for Heterogeneous Water Oxidation

Recent focus has favored the use of cobalt complexes as heterogeneous water oxidation catalysts. The report by Du and coworkers[63] showed that salophen-based Co(II) (**Figure 1.20**)

complexes can function as catalytic precursors for the formation of nanostructured amorphous films on fluorine-doped tin oxide (FTO) electrodes during electrodeposition. The complex demonstrated catalytic activity at low overpotential in pH 9.2, 0.1 M potassium borate solution, with an onset overpotential for the films observed at ~0.85 V. A Faradaic efficiency of >93 % was observed at 1.2 V. Characterization of the catalytic film via scanning electron microscopy (SEM), energy-dispersive X-ray analysis (EDX), and X-ray photoelectron spectroscopy (XPS) indicated a cobalt-based amorphous film formation.

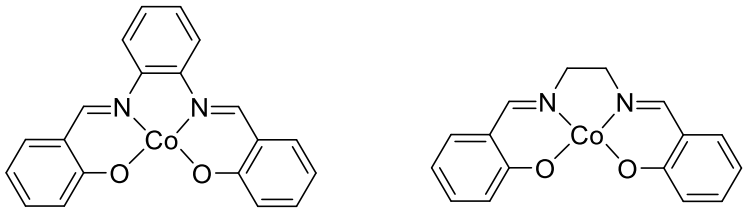

Figure 1.20. Salophen-based Co(II) catalysts.

Similarly, cobaloximes (**Figure 1.21a**) have also been probed by the Du group as heterogeneous water oxidation catalysts using catalytic films obtained by electrodeposition at 1.5 V and 1.1 V in pH 9.2, 0.1 M borate buffer.[64] Oxygen evolution was measured using a fluorescence-based oxygen sensor, and a Faradaic efficiency of >80 % was observed. Spiccia and coworkers[65] reported that electrodeposition of cobalt oxide films using cobalt aminopolycarboxylate complexes (**Figure 1.21b**) can result in a transparent film capable of catalyzing water oxidation. Electrodeposition at 1.0 V (*vs.* Ag/AgCl) in pH 9.2 borate buffer on FTO electrodes resulted in 90 % retention of transparency.

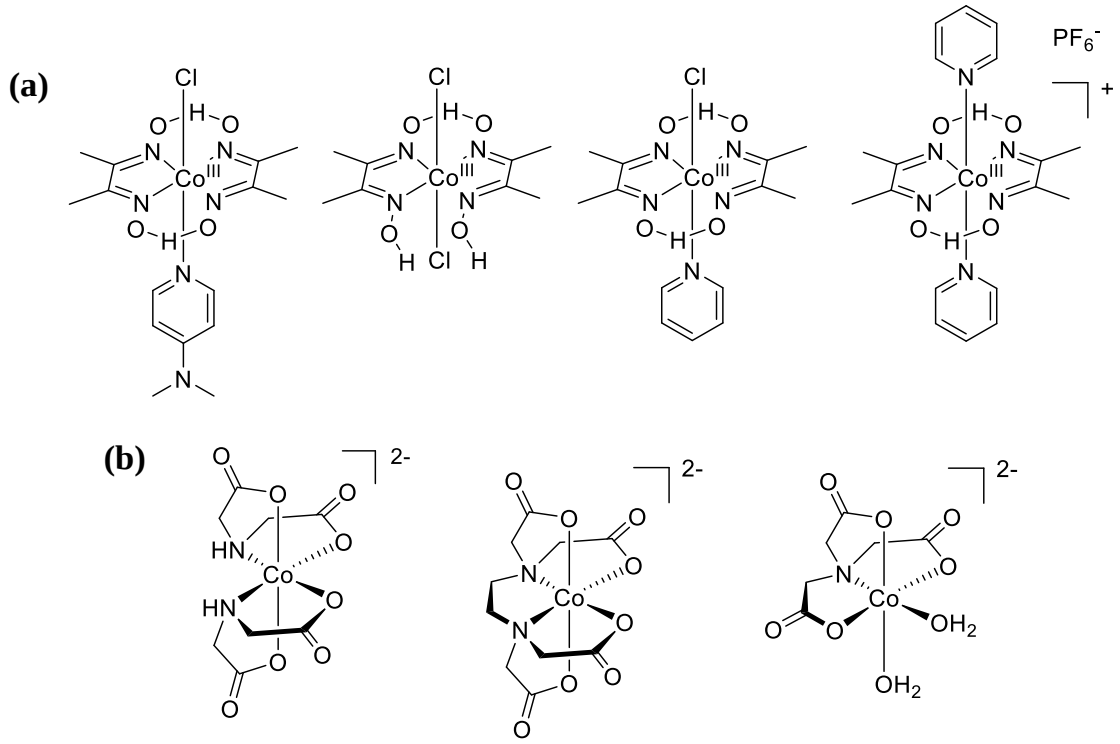

Figure 1.21. (a) Cobaloxime and (b) cobalt aminopolycarboxylate catalysts.

Thin films formed using porphyrin-based cobalt complexes have also been reported as heterogeneous catalysts for water oxidation.[66] Thin films on a FTO electrode were obtained by drop casting using a 1 mM solution in tetrahydrofuran (THF). Electrocatalytic water oxidation was observed at pH 9.2, with Faradaic efficiencies of ~100 % observed for both the aryl-substituted porphyrin-based Co complex and its brominated analog (**Figure 1.22a, b**). The TOFs of 0.50 s^{-1} and 0.40 s^{-1} were respectively observed for complexes (a) and (b) during bulk electrolysis performed at an applied potential of 1.3 V (*vs.* Ag/AgCl). According to UV-visible spectroscopy, mass spectrometry, SEM and EDX measurements, the film remained stable under catalytic conditions.

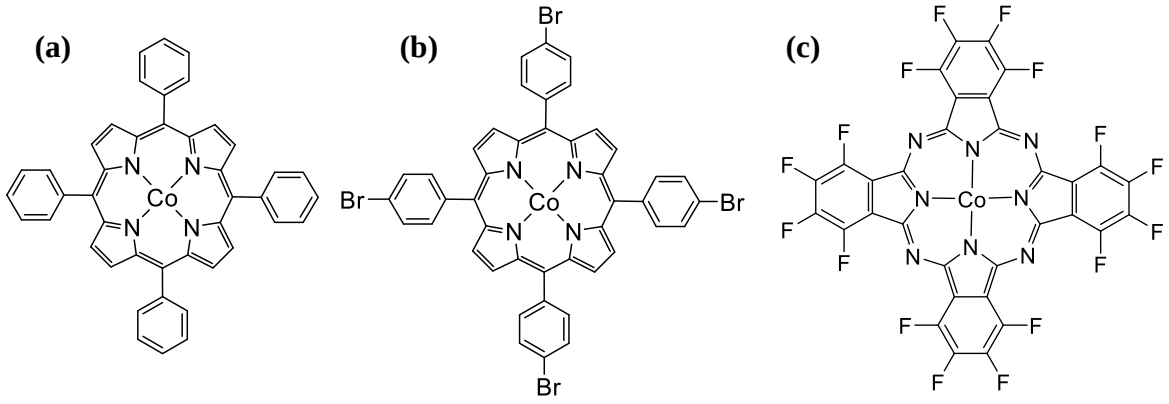

Figure 1.22. Porphyrin- and phthalocyanine-based cobalt complexes for heterogeneous water oxidation.

Takanabe and coworkers[67] have studied the catalytic water oxidation ability of Co-phthalocyanine complexes (**Figure 1.22c**) immobilized on modified FTO-coated hematite surfaces. The complex was deposited on the FTO/hematite surface via drop casting. Bulk electrolysis performed using the deposited films at 1.85 V (*vs.* RHE) at pH 13 resulted in a TOF of 4.1 s^{-1}.

In general, there is a fundamental need for effective water splitting catalysts from Earth-abundant metals for efficient fuel production from water. Therefore, based on previous knowledge from the group, we expect to (a) synthesize a cobalt containing metallosurfactant that can function as a molecular procatalyst for water oxidation, (b) introduce a novel film formation methodology to functionalize catalyst onto solid surface to drive heterogeneous catalysis, and (3) to investigate the dependence of catalytic activity based on number of deposited film layers.

1.5. Research Statement and Objectives

Research interests in the Verani group are directed toward designing and synthesizing new redox-active ligand frameworks in which different Earth-abundant metal ions can be incorporated for applications in molecular electronics, energy, and protective coatings. Furthermore, optimizing the amphiphilicity of these complexes can facilitate their use as

precursors for Langmuir-Blodgett film formation, thereby bridging the gap between solution-phase and solid-phase chemistry.

The focus of this dissertation research is to synthesize symmetric and asymmetric redox-active metallosurfactants containing cobalt(III), nickel(II), copper(II), and zinc(II) complexes, to investigate their spectroscopic, electronic, amphiphilic, and LB film formation ability, and finally to investigate the applications of these LB films in molecular electronic devices, corrosion mitigation, and heterogeneous water oxidation. The specific goals of my research are as follows:

- **Goal # 1:** ***To Evaluate Salophen-based Amphiphilic Metal Complexes Toward Film Formation and to Establish a Current Rectification Mechanism of Salophen-based Complexes.*** Based on results from previous studies by Verani and coworkers, we hypothesize that redox-active nickel(II) and copper(II) complexes can form homogeneous films due to their amphiphilic nature. Additionally, the energetic disparity between frontier molecular orbitals of a given copper complex enhances its function as an insulator. We anticipate that comparing the orbital arrangement of an insulating copper(II) complex with a rectifying iron(III) complex will lead us toward determining a rectification mechanisms of salophen-based complexes.
- **Goal # 2:** ***To Modulate the HOMO LUMO/SOMO Energy Gap by Altering the Ligand Design of Iron(III) Complexes and to Establish the Role of Axial Ligands for Current Rectification.*** Based on our preliminary results, we hypothesize that increasing complex asymmetry via incorporation of pyridine and phenolate arms will lower the HOMO-LUMO/SOMO energy gap. Furthermore, we hypothesize that the local orbital asymmetry will be modulated through incorporation of different axial ligands, which will also result in lower HOMO-LUMO/SOMO energy gaps. We

expect that these lower HOMO-LUMO/SOMO energy gaps will be energetically comparable with electrode Fermi energies to be involved in electron transfer, which in turn will facilitate current rectification.

- **Goal # 3:** ***To Evaluate the Efficiency of Amphiphilic Fe(III), Cu(II), and Zn(II) Complexes as Corrosion Mitigating Films.*** Based on our preliminary results, we hypothesize that iron plates can be functionalized with amphiphilic metal-salophen complexes using LB technique to enhance electron passivation. Thus, we expect that LB film multilayers can mitigate corrosion in these iron plates because it can behave as a barrier between the surface and corrosive media.
- **Goal # 4:** ***To Investigate the Heterogenous Catalytic Activity of Co(III) tris-Phenolate Thin Films in Water Oxidation.*** On the premise of previous results from our group, we propose that conductive substrates can be functionalized with amphiphilic molecular procatalysts *via* LB technique to drive heterogeneous water oxidation due to the superior uniform coverage obtained with minute amounts of material. We additionally hypothesize that the activity of the final catalytic film can be modified by altering the number of deposited LB layers because the LB method provides direct control over the thickness of the deposited films by varying the number of layers.

CHAPTER 2 MATERIALS, METHODS, AND INSTRUMENTATION

2.1. Materials

The chemicals needed for organic ligands and complex syntheses were purchased from Sigma-Aldrich, Alfa Aeser, Acros Organics, or Oakwood Chemicals. Solvents used were purchased from relevant commercial sources. Solid substrates (glass, mica, gold, and iron) used in the deposition of thin films were purchased from SPI Supplies, Goodfellow Supplies or Ted Pella, Inc. Fluorine doped tin oxide (FTO) glass substrates were purchased from Sigma-Aldrich.

2.1. Methods and Instrumentation

Multistep synthetic procedures were employed to synthesize the designed ligands and metal complexes. Air and moisture sensitive compounds were synthesized using standard schlenk line techniques. All the organic ligands and metal complexes were characterized using multiple techniques such as proton nuclear magnetic resonance spectroscopy (^{1}H-NMR), Fourier transform infrared spectroscopy (FTIR), electrospray ionization mass-spectrometry (ESI-MS), CHN elemental analysis, and X-ray crystallography when possible. The ^{1}H-NMR was used to identify protons in different environments, whereas FTIR spectra indicated the presence of different functional groups. ESI-MS was used to confirm the presence of the molecular ion peak, and CHN and X-ray analysis used to confirm the purity and the structural identities of the complexes respectively. Electronic and redox properties were characterized using UV-visible spectroscopy and cyclic voltammetry. The film formation ability and the surface analysis of the thin films were performed using the Langmuir-Blodgett technique (LB), Brewster angle microscopy (BAM), atomic force microscopy (AFM), and infrared reflection absorption spectroscopy (IRRAS). Finally the conductivity, corrosion, and catalytic properties of the films were analyzed using current–voltage (I-V) measurements, bulk electrolysis, optical microscopy,

and gas chromatography respectively. Detailed discussions about these methods are given in the next sections.

2.2.1. Nuclear Magnetic Resonance Spectroscopy (NMR)

^{1}H-NMR spectroscopy was used to determine the structure of compounds by identifying protons in different environments.[68] Structural characterizations of various ligands and their organic precursors were characterized based on the chemical shifts, splitting patterns, and the proton counts obtained from ^{1}H-NMR spectra. ^{1}H-NMR spectra were recorded in $CDCl_3$ using Varian 400 MHz instrument.

2.2.2. Vibrational Spectroscopy

Infrared spectroscopy (IR) is a useful technique to identify functional groups of a compound based on the vibrational frequencies. When a molecule is exposed to electromagnetic radiation in the frequency range 400-4000 cm^{-1}, it absorbs specific frequencies of radiation, depending on the functional groups and the symmetry within the molecule.[68,69] Therefore, the presence of C=C, C=N, C=O, and C≡N functional groups can be easily observed in a ligand frameworks. Furthermore, IR can be used to identify the presence of certain counterions such as perchlorate (ClO_4^-) and hexafluorophosphate (PF_6^-). The IR spectra are obtained between % transmittance and wavelength and are recorded from 4000 to 650 cm^{-1} as KBr pellets using a Bruker Tensor 27 FTIR-spectrophotometer with OPUS 5.0/6.5 software version.

2.2.3. Mass Spectrometry

Mass spectroscopy is one of the analytical techniques used to characterize the molar mass of compounds based on their mass/charge (m/z) ratios. Electrospray ionization mass spectrometry (ESI-MS) was used to obtain the molar masses of ligand precursors, ligands, and metal complexes in positive mode, since it shows m/z ratios associated with unfragmented

molecules due to the soft ionization nature of the method.[68,70] The compound is dissolved in a polar volatile solvent such as methanol or acetonitrile, and bombarded with a high energy electron beam to produce charged species with fragmented or unfragmented molecules. The mass spectrum is based on the m/z ratios and relative intensities of these charged species. Usually a cluster of peaks is obtained depending on the relative abundance of the different elements of the compound. Low-resolution spectra are obtained primarily to characterize the organic ligands, while high-resolution analyses were done for metal complexes. Low-resolution mass spectra for the research project were obtained using a Shimadzu LC-8040 Triple Quad instrument by us. High resolution mass spectra were obtained using a Water Micromass ZQ LC/MS and the analyses were performed by Dr. Lew Hryhorczuk and Dr. Yuri Danylyuk from the Lumigen Instrument Center within the department of Chemistry, Wayne State University.

2.2.4. Elemental Analysis

Elemental analysis is used to determine the percentage weights of carbon, hydrogen, and nitrogen and the purity of a given sample. The sample is combusted under extreme conditions resulting in known quantities of combustion products such as carbon dioxide (CO_2), water (H_2O), and nitrous oxide (N_2O). Then the yield of these oxides is quantitatively analyzed to determine the empirical formula of the sample. The CHN elemental analysis was performed using an Exeter analytical CHN analyzer by Midwest Microlab, Indianapolis, Indiana, an independent contractor.

2.2.5. X-ray Crystallography

The X-ray crystallography is an important technique used to identify the geometry and the coordination environment of the complex *via* bond lengths and bond distances. Different techniques, including slow evaporation, vapor diffusion, and layering were used to obtain X-ray

quality crystals. During the experiment, the crystal was mounted on a goniometer and its structure was solved according to the X-ray diffraction pattern obtained based on the atomic patterning. Diffraction data were obtained by a Bruker X8 APEX-II Kappa geometry diffractometer using Mo radiation and graphite monochromator. Different programs and software such as APEX-II,[71] SHELX,[72] and SAINT[73] were used to solve and refine the structures. Mr. Habib Baydoun and Mr. Kenneth Kpogo from the Verani Group at Wayne State University measured and solved the crystal structures.

2.2.6. Electronic Spectroscopy

The UV-visible spectroscopy is a technique widely used to analyze the electronic absorption properties of complexes. The electrons of a molecule will absorb energy from visible to UV region (200-780 nm) and will be promoted from ground state to a higher energy excited state. Electronic transitions occur based on Laporte and spin selection rules. According to the Laporte selection rule, if a molecule is centrosymmetric, transitions between a given set of p or d orbitals are forbidden while the spin selection rule forbids the transition between states of different multiplicities.[68] Sample absorbance can be calculated using the Beer-Lambert law, $A = \varepsilon C l$, where A is absorbance, ε is molar absorptivity coefficient, C is concentration of the complex, and l is path length of the cell. A metal complex generally shows three transitions originating due to ligand-centered processes, charge transfer processes and d-d transitions. Ligand centered processes are observed as high intensity bands ε from ~ 20,000 to 200,000 L mol^{-1} cm^{-1}. Charge transfer processes can occur due to ligand-to-metal charge transition (LMCT) or metal-to-ligand charge transition (MLCT) and are observed as medium intensity bands with ε ranging from ~5000 to 50,000 L mol^{-1} cm^{-1}. Both ligand-centered and charge transfer processes are allowed transitions according to Laporte and spin rules. Conversely, d-d transitions give rise

to very low intensity bands ε from ~ 10 to 100 L mol^{-1} cm^{-1} because they are forbidden by Laporte and spin selection rules.[68]

The UV-visible measurements of LB films can be used to acquire information about molecular ordering during film deposition. According to literature,[74,75] there are two types of aggregation patterns known as H- and J- aggregates. The J-aggregates show a bathochromic shift in the spectra, while H-aggregates show a hypsochromic shift in the absorption spectra. All spectra are obtained at room temperature using a Varian Cary 50 spectrophotometer or a Shimadzu UV-3600 UV-VIS-NIR spectrophotometer in a quartz cell.

2.2.7. Cyclic Voltammetry

Cyclic voltammetry is one of the main characterization techniques used to study the electrochemical properties of a complex. It allows inference on the measurement of electron transfers between a working electrode and molecules present in a test solution.[76] To investigate the redox properties of complexes cyclic voltammetry experiments were performed at room temperature in dichloromethane or acetonitrile under inert conditions. For this purpose a three-electrode system was used with glassy carbon as the working electrode, Pt wire as the auxiliary electrode, and Ag/AgCl as the reference electrode. A 0.1M tetrabutylammonium hexafluorophosphate ($TBAPF_6$) was used as the supporting electrolyte to minimize solution resistance. The ferrocene/ferroceniun couple (E° = 0.4 V *vs.* NHE)[77] was used as an internal standard by which all potentials are recorded. Reversibility of the redox processes were assigned based on the potential separation of a redox couple ($\Delta E = |E_{pc} - E_{pa}|$) and the ratio between the anodic and cathodic peak currents ($|i_{pa}/i_{pc}|$). Electrochemical experiments were performed using a BAS 50W potentiostat or CHI600E voltametric analyzer.

2.2.8. Langmuir Blodgett (LB) Isothermal Compression

Langmuir-Blodgett (LB) technique is one of the few methods used to obtain organized molecular assemblies and quantify the amphiphilicity of molecules at the air/water interface. This technique can be used to obtain mono or multilayered thin films. The thickness of these films varies based on molecular structure and packing topology.[78] The LB experiments were carried out using an automated KSV 2000 mini trough at 23 ± 0.5 °C. Barnstead NANOpure water with a resistivity of 18.2 MΩ cm^{-1} was used as the subphase solution. Different salt solutions such as sodium chloride and sodium terephthalate can also be used as subphase solutions.[79]

The LB instrument consists of a mini-trough filled with the subphase solution and two movable barriers that can skim the surface of the subphase which leads control to surface area available for the floating monolayer. In order to form Langmuir films, the compound of interest is dissolved in a volatile solvent such as chloroform (1 mg/ml), which neither reacts nor dissolves in the subphase, and placed on the subphase in a random manner. Surface pressure was monitored using a Wilhelmy plate attached to a sensitive balance. The experiment will begin after a 20-minute waiting period. During compression, the surface pressure will increase and the molecules will transfer through a gaseous 2D phase to an expanded 2D phase, and finally to a condensed 2D phase.[80] Assessment of the molecules at the air/water interface is obtained by a compression isotherm that plots the surface pressure (mN/m) *vs.* average area per molecule ($Å^2$) at 23 ± 0.5 °C as shown in **Figure 2.1**.

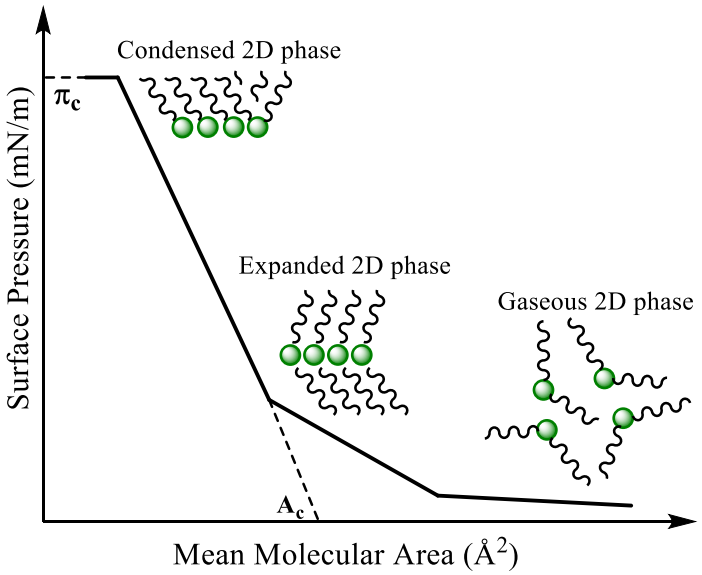

Figure 2.1. Schematic representation of isothermal compression plot.

The compression isotherm provides information regarding molecular organization, critical area per molecule (A_c), collapse pressure (π_c) and surface pressures of possible phase transitions. Film collapse can occur via two mechanisms: constant pressure collapse or constant area collapse.[81,82] The steepest region of the isotherm is obtained when the film is homogeneous.

The LB technique can be used to transfer thin films onto solid substrates like glass, mica, gold, or quartz without drastic changes in molecular orientation. Transfer of the monolayer onto the substrate is based on hydrophilic or hydrophobic interactions of the head or the tail group of the molecule and the solid substrate. A Y-type deposition that incorporates both up and down ward strokes was used to transfer LB films onto solid surfaces.[80a] The transfer ratio (TR) gives an indication about the surface coverage. A TR close to unity indicates a complete surface coverage from the LB film.[83]

2.2.9. Brewster Angle Microscopy (BAM)

Brewster angle microscopy (BAM) is a technique used for real-time evaluation of film compression at the air/water interface. The BAM technique was used to observe domain formation, Newton ring formation, collapse, and other defects of the thin film formed at the

air/water interface.[84] Collapse of the films can be observed as an array of Newton rings.[85] The BAM images were obtained using a KSV-Optrel 300 Brewster angle microscope with a He/Ne laser (10 mW, 632.8 nm) and a CCD detector.

2.2.10. Infrared Reflection Absorption Spectroscopy (IRRAS)

Infrared Reflection Absorption Spectroscopy (IRRAS) is an analytical technique used to characterize structural information and packing topologies of thin films deposited on solid substrates. The IRRAS mainly consists of four parts, namely IR light source, mid-infrared range (MIR) polarizer, photoelastic modulator, and a mercury cadmium telluride (MCT) detector as shown in **Figure 2.2**.[86]

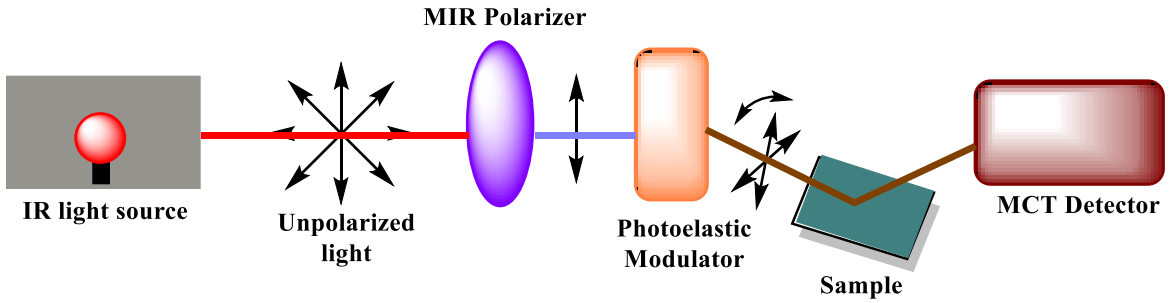

Figure 2.2. Schematic representation of IRRAS spectrophotometer.

The photoelastic modulator generates alternating linear states of polarized light. Therefore, an infrared beam can split into two components as *p*-polarized light, if the polarization plane is parallel to the incident, or *s*-polarized light, if the polarization plane is perpendicular to the plane of incident.[87] In the experimental set-up, the infrared beam was focused on the thin film at an incident angle ranging from 13 - 83˚ after being polarized by the MIR polarizer and photoelastic modulator. Then the beam reflected from the sample was collected in the MCT detector. Data were generally collected for five minutes for both the sample and blank with varying angles from 20-80˚. The final spectrum is then obtained by

dividing the film spectra at a particular angle by the blank spectra at the same angle. The IRRAS spectra for 50-layer deposited films were obtained using a Bruker Tensor 27 infrared outfitted with an A 513/Q variable angle accessory.

2.1.11. Atomic Force Microscopy

Atomic force microscopy (AFM) is a widely used technique to analyze nanoscopic surface features of film deposited solid substrates.[88] During the project, AFM images for the monolayers deposited on mica and gold were obtained using a Dimension 3100 AFM (VECCO) instrument.[89] The Nanoscope software from Digital Instruments (Version 5.12) was used to analyze the images obtained. The AFM analyses were performed in collaboration with Prof. Guangzhao Mao from Department of Chemical Engineering and Materials Science at Wayne State University.

2.1.12. Device Fabrication and Current-Voltage (I/V) Characterization

One of the goals of the research project was to incorporate amphiphilic metal complexes with desired electronic and redox properties in electrode|molecule|electrode assemblies and investigate their current rectification behavior.[90] To fabricate gold|molecule|gold assemblies, gold coated mica substrates were deposited with LB monolayers at an appropriate pressure identified by AFM analysis and dried in a desiccator for five days to get clear of any moisture. Then the top gold layer was introduced using shadow masking method.[91] In order to generate a number of isolated devices on the same substrate as shown in **Figure 2.3**, a copper TEM grid was used on top of which a gold electrode was deposited using an EffaCoater gold sputter instrument using argon as the carrier gas. The current–voltage measurements (I-V) were obtained at room temperature using a Keithley 4200 semiconductor parameter analyser and a Signatone S-1160

probe station. These measurements were obtained in collaboration with Prof. Zhixian Zhou from Department of Physics and Astronomy at Wayne State University

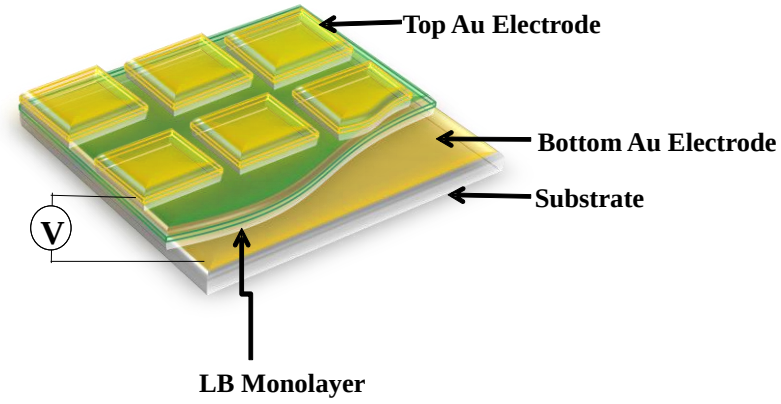

Figure 2.3. Schematic representation of Au|LB-Monolayer|Au device.

2.1.13. Electrocatalysis (Electrochemistry, Bulk Electrolysis, and Gas Chromatography)

Another goal of the research project was to study the catalytic activity of a metal complex deposited on solid substrate towards water oxidation. The catalytic activity of a complex towards water oxidation was verified in presence of pH 11, 0.1 M sodium borate buffer. The catalytic CV was obtained using a LB monolayer deposited FTO plate as the working electrode, Ag/AgCl as the reference electrode, and Pt wire as the auxiliary electrode at room temperature. The overpotential values were calculated by subtracting the thermodynamic standard potential for oxygen generation from the potential obtained from cyclic voltammogram as given in equation 1.[92]

$$\text{Over potential} = \left| E_{exp} - E^{\circ}_{H2O/O2} \right| \qquad (1)$$

In order to determine the amount of oxygen produced, bulk electrolysis experiments were carried out using CHI600E voltammetric analyzer. An ITO plate coated with one layer of the compound with 0.7 cm^2 area as the working electrode, 12 inch Pt coil as the auxiliary electrode, and Ag/AgCl as the reference electrode was used. Bulk electrolysis was performed in a custom-

made airtight H-type cell. The working electrode and reference electrode were placed in the same compartment while the auxiliary electrode was placed in the adjacent compartment separated by a frit. Both compartments were filled with pH 11, 0.1 M sodium borate buffer. The working electrode was subjected to one hour electrolysis under 1.2 V applied potential. The amount of oxygen produced was determined using a Gow-Mac 400 gas chromatograph (GC) equipped with a thermal conductivity detector, and a 8 ft x 1/8 in, 5 Å molecular sieve column operating at 60 ˚C. Helium was used as the carrier gas at a flow rate of 30 ml/min. The Faradaic efficiency and approximate turnover number were calculated according to the GC measurements. A detailed discussion on turnover number and Faradaic efficiency calculations is given in **Chapter 6**.

2.1.14. Density Functional Theory (DFT) calculations

Density Functional Theory (DFT)[93] calculations were performed to validate the electronic and redox processes of the complexes. All the calculations were performed with a development version of Gaussian,[94] using B3LYP functional[95] with SDD basis set and pseudopotentials[96] on the metal, and 6-31G(d,p) basis[97] on the other atoms. All optimized structures were confirmed as minima by analyzing the harmonic vibrational frequencies. Solvation effects (in dichloromethane) were accounted for using the implicit SMD continuum solvation model.[98] Spin density plots and molecular orbitals were visualized using Gauss View.[99] The calculations were performed in collaboration with Prof. H. Bernhard Schlegel from Department of Chemistry at Wayne State University. Dr. Shivnath Mazumdar and Mr. Bishnu Thapa are acknowledged for carrying out the calculations.

CHAPTER 3 SALOPHEN-BASED AMPHIPHILIC NICKEL(II) AND COPPER(II) COMPLEXES FOR THIN FILM FORMATION AND INVESTIGATION OF CURRENT RECTIFICATION MECHANISM

Portions of the text in this chapter were reprinted or adapted with permission from: Wickramasinghe, L. D.; Mazumder, S.; Gonawala, S.; Perera, M. M.; Baydoun, H.; Thapa, B.; Li, L.; Xie, L.; Mao, G.; Zhou, Z.; Schlegel, H. B.; Verani, C. N.; *Angew. Chem. Int. Ed.* **2014**, *53*, 14462.

3.1. Introduction

Molecular rectification was first proposed as a gedanken experiment with well-defined donor and acceptor moieties that can facilitate the directional current flow.[100] The experimental evaluation on molecular rectification was then performed using electrode|molecule|electrode assemblies.[101] The use of physisorbed Langmuir-Blodgett (LB) films during device fabrication will prevent the formation of Schottky barriers, which are common with self-assembled systems.[102] Therefore molecular rectification can follow either an asymmetric or unimolecular mechanism where frontier molecular orbitals are involved in the electron transfer. In the asymmetric mechanism, only the lowest unoccupied molecular orbital (LUMO) is involved in electron transfer, because the highest unoccupied molecular orbital (HOMO) is much lower in energy compared to the Fermi level of electrode. On the other hand in unimolecular mechanism, HOMO of donor moiety and LUMO of acceptor moiety are energetically comparable with electrode Fermi levels making both HOMO and LUMO involved in electron transfer.[101a,b] Therefore, redox active molecular systems play an important role in efficient electron transfer. The redox behavior of a complex can be modulated by incorporating a redox-active metal into redox-noninnocent ligand frameworks such as salophen chelators.[103,104]

Our group has reported that phenolate rich [$Fe^{III}L^{N2O3}$] systems can function as molecular rectifiers, with rectification ratios (RR = [I at-V_o/I at +V_o]) varying from 4.52 to 12 between-2 to +2 V and from 2.95 to 36.7 between-4 to +4 V.[105] However, the mechanism for current rectification was not well understood for this system. Therefore, in order to identify the rectification mechanism in coordination complexes, a new class of salophen-based Cu(II) and Ni(II) complexes were synthesized and corresponding electronic structure and redox behavior was evaluated with a similar rectifying Fe(III) complex which was synthesized by Dr. Wickramasinghe. Herein, we hypothesize that redox active nickel(II) and copper(II) complexes can be used in LB film formation needed for device fabrication due to the amphiphilic nature introduced by incorporating hydrophilic alkoxy groups and hydrophobic *t-butyl* groups. Furthermore, we hypothesize that the square planar geometry of Cu(II) complex will lead to a large energy difference in frontier molecular orbitals, making it an insulator which will help in the comparison with the orbital arrangement of rectifying Fe(III) complex to ultimately propose a rectification mechanism for salophen-based complexes.

In this chapter we investigate the structural, electronic, redox, and amphiphilic behavior of new salophen-based [$Ni^{II}L^{N2O2}$] (**1**) and [$Cu^{II}L^{N2O2}$] (**2**) complexes as shown in **Scheme 3.1a**. We further evaluate the frontier molecular orbital energy positioning of copper(II) complex with a similar rectifying pentacoordinated iron(III) complex [$Fe^{III}L^{N2O2}$] (**3**) (**Scheme 3.1b**) to propose a plausible rectification mechanism that salophen-based complexes would follow.

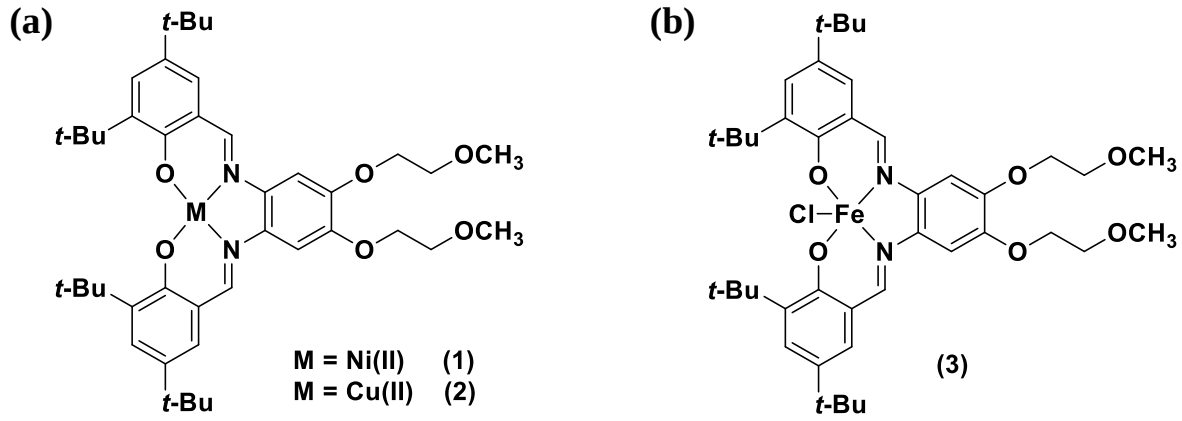

Scheme 3.1. (a) The $[Ni^{II}L^{N2O2}]$ (**1**) and $[Cu^{II}L^{N2O2}]$ (**2**) complexes, and $[Fe^{III}(L^{N2O2})Cl]$ (**3**) complex used for comparisons.

3.2. Experimental Section

3.2.1. Synthesis of the Ligand $[H_2L^{N2O2}]$

The synthetic procedure for 6,6'-(1E,1'E)-(4,5-bis(2-methoxyethoxy)-1,2-phenylene)bis(azan-1-yl-1-ylidene)bis(methan-1-yl-1-ylidene)bis(2,4-di-tert-butylphenol) which is abbreviated as $[H_2L^{N2O2}]$ has been reported elsewhere.[103]

3.2.2. Synthesis of Metal Complexes

Synthesis of Complex $[Ni^{II}L^{N2O2}]$ (1)

The complex $[Ni^{II}L^{N2O2}]$ (**1**) was synthesized by treating a 3:1 methanol:dichloromethane solution of **$[H_2L^{N2O2}]$** (0.1 g: 0.145 mmol) and $NaOCH_3$ (0.016 g: 0.3 mmol) with nickel chloride under refluxing conditions for 2 h. Complex **1** was isolated as maroon needle-like crystals from a 3:1 methanol:dichloromethane solution. Yield: 77 %. ESI (m/z^+) in CH_3OH = 745.3 (100 %) for $[C_{42}H_{58}N_2O_6Ni+H^+]$. Anal. Calc. for $[C_{42}H_{58}NiN_2O_6]$: C, 67.66; H, 7.84; N, 3.76 % Found: C, 67.83; H, 7.94; N, 3.90 % IR (KBr, cm^{-1}): 2851-2920 (ν_{C-H}), 1605 ($\nu_{C=C}$, aromatic), 1515 ($\nu_{C=C}$, aromatic) 1591 ($\nu_{C=N}$), 1278 (ν_{C-O-C}), 1132 (ν_{C-O-C}).

Synthesis of Complex [$Cu^{II}L^{N2O2}$] (2)

The [$Cu^{II}(L^{N2O2})$] complex (**2**) was synthesized by treating a 3:1 methanol:dichloromethane solution of [H_2L^{N2O2}] (0.1 g, 0.145 mmol) and $NaOCH_3$ (0.016 g, 0.3 mmol) with $CuCl_2.2H_2O$ (0.025 g, 0.147 mmol) under refluxing conditions. Brown needle-like crystals were obtained from a 3:1 methanol:dichloromethane solution. Yield: 75 %. ESI (m/z^+) in CH_3OH = 750.3661 (100 %) for [$C_{42}H_{58}N_2O_6Cu+H^+$] (calculated = 750.3669) in agreement with -1.1 ppm difference. Anal. Calc. for [$C_{42}H_{58}CuN_2O_6$]: C, 67.22; H, 7.79; N, 3.73 %. Found: C, 67.27; H, 7.71; N, 3.70 %. IR (KBr, cm^{-1}) 2870-2954 (ν_{C-H}), 1610 ($\nu_{C=C}$, aromatic), 1504 ($\nu_{C=C}$, aromatic) 1589 ($\nu_{C=N}$), 1272 (ν_{C-O-C}), 1131 (ν_{C-O-C}).

3.2.3. Molecular Structure Analysis

Single crystals of complex **4** were grown by slow evaporation of the reaction mixture. A brown needle-shaped crystal with dimensions of 0.04 × 0.04 × 0.15 mm was mounted on a mitogen loop using paratone oil. Data were collected on a Bruker APEX-II Kappa geometry diffractometer with Mo radiation and a graphite monochromator using a Bruker CCD (charge coupled device) based diffractometer equipped with an Oxford Cryostream low temperature apparatus. The data was measured at a temperature of 100 K with omega and phi scans of 0.5° per frame for 20 s. The crystal was solved to a resolution of 0.8 Å with a completeness of 100 %. The structure was solved by the direct method using the SHELXS-97 program which is a part of APEX II[106] and refined by least squares method on F2, SHELXL-97,[107] which is incorporated in OLEX2.[108] The structure was solved in the space group Pbca. Atom C42 was disordered; therefore, it was refined by assigning partial occupancies. Hydrogen atoms were placed in calculated positions. Selected crystallographic data are shown in **Table 3.1**.

	(2)
Formula	$C_{86}H_{126}N_4O_{15}Cu_2$
M	1582.99
Temperature/K	100.1
Crystal system	orthorhombic
Space group	Pbca
a/Å	30.4737(17)
b/Å	14.0120(7)
c/Å	40.726(2)
α/°	90.00
β/°	90.00
γ/°	90.00
Volume/Å^3	17389.9(16)
Z	8
D_{calc} / g cm^{-3}	1.209
μ/ mm^{-1}	0.552
R(F) (%)	5.67
Rw(F) (%)	10.55

[a]$R(F) = \sum \| F_o \| - | F_c \| / \sum | F_o |$; $Rw(F) = [\sum w(F_o^2 - F_c^2)^2 / \sum w(F_o^2)^2]^{1/2}$ for $I > 2\sigma(I)$

Table 3.1. Selected X-ray crystal data for complex **2**.

3.3. Results and Discussion

3.3.1. Synthesis and Characterization of Metal Complexes

The complexes were synthesized by reacting one equivalent of the ligand with one equivalent of appropriate metal chloride salts under refluxing conditions. The IR spectroscopic data for **1** and **2** showed symmetric and asymmetric C-H stretching vibrations in the regions of 2820–2950 cm^{-1} and a prominent peak at ~1590 cm^{-1} belonging to the C=N stretching vibrations. CHN elemental analysis showed an excellent agreement between experimental and theoretical values.

3.3.2. Molecular Structure

The structure of complex **2** was confirmed by crystal structure analysis as shown in **Figure 3.1**. It revealed that the copper(II) complex is in a square-planar geometry with an [N2O2] coordination environment where the nitrogen and oxygen atoms are *trans* to each other. The average Cu–O and Cu–N distances are 1.892 Å and 1.936 Å respectively, which are in agreement with reported values.[104a,b]

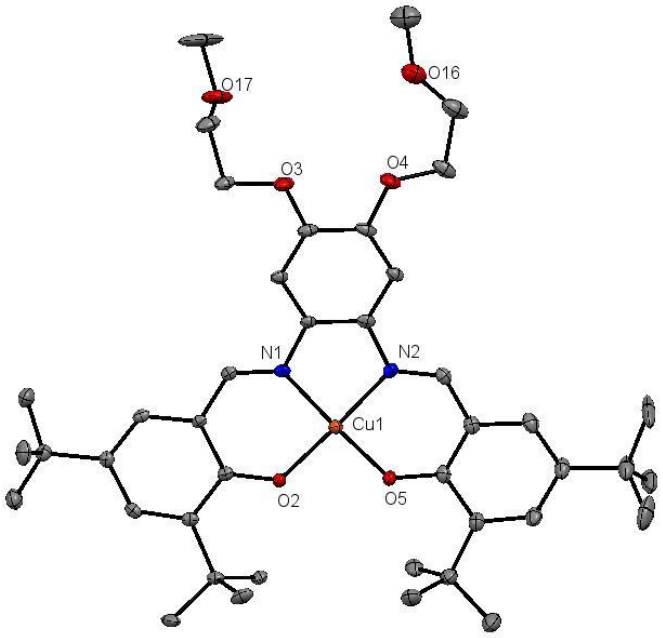

Figure 3.1. ORTEP representation at 50% probability for complex **2**. Hydrogen atoms omitted for clarity.

3.3.3. Electronic Spectral Properties

The UV-visible spectra of the ligand and the metal complexes **1** and **2** were recorded in 1.0×10^{-5} mol L^{-1} dichloromethane solutions. The observed UV-visible spectra for complexes **1** and **2** are shown in **Figure 3.2**. The uncoordinated ligand showed intense absorption bands in the range of 280-360 nm due to ligand-based $\pi \rightarrow \pi^*$ charge transitions. Complexes **1** and **2** showed high intensity bands from 250-500 nm with ε ranging from 10,200 - 39,500 L mol^{-1} cm^{-1}.

Complex **1** showed a low intensity band ~600 nm (< 500 L mol^{-1} cm^{-1}) and complex **2** shows a band at ~550 nm (< 500 L mol^{-1} cm^{-1}). According to literature,[109,110] the absorption bands in the region of 250 - 500 nm are assigned as intraligand π→π* charge transitions (ILCT). The low intensity absorption bands ~550 and 600 nm can be assigned as d-d transitions.

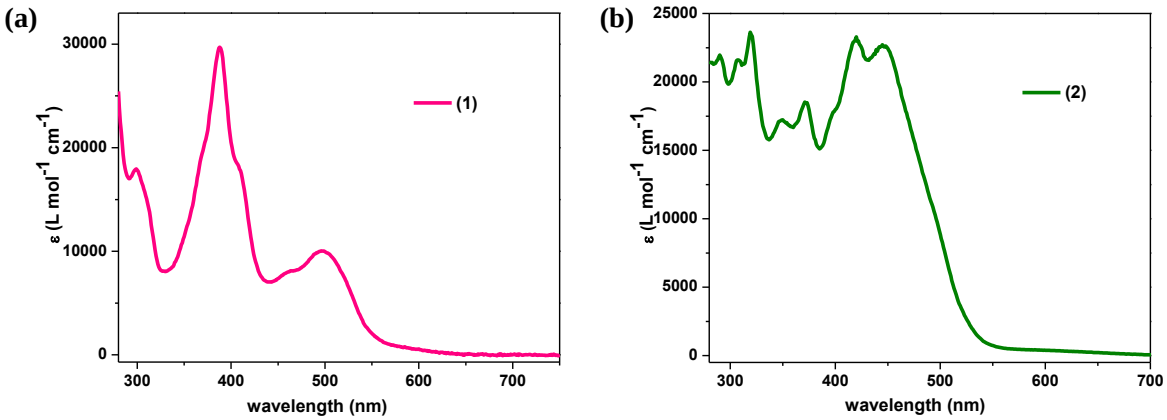

Figure 3.2. The UV-visible spectroscopic data of metal complexes **1** and **2** in 1.0 × 10^{-5} mol L^{-1}solutions.

These attributions were further confirmed by time-dependent DFT (TD-DFT)[111] calculations along with the natural transition orbital (NTO) method.[112] Four absorptions of reasonable oscillator strength were found by TD-DFT calculations in the region of 318–462 nm for ILCT as shown in **Figure 3.3**.

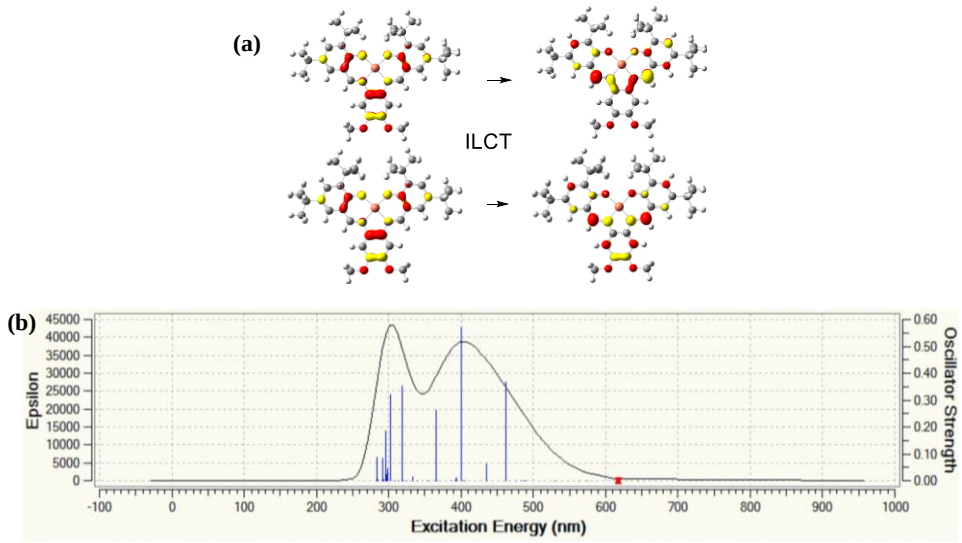

Figure 3.3. TD-DFT spectrum and NTOs (isodensity value of 0.05 a.u.) of the excitations for the complex **2**.

However, complex **3** showed both ILCT and metal-to-ligand charge transfer (MLCT) transitions between 310-400 nm originating from phenylenediamine- and phenolate-based p_{π} orbitals to $d_{\sigma*}$ and $d_{\pi*}$ iron(III)-based orbitals (**Figure 3.4**).[103] This suggests that metal-based singly occupied SOMO of complex **3** is energetically more available than of **1** and **2**.

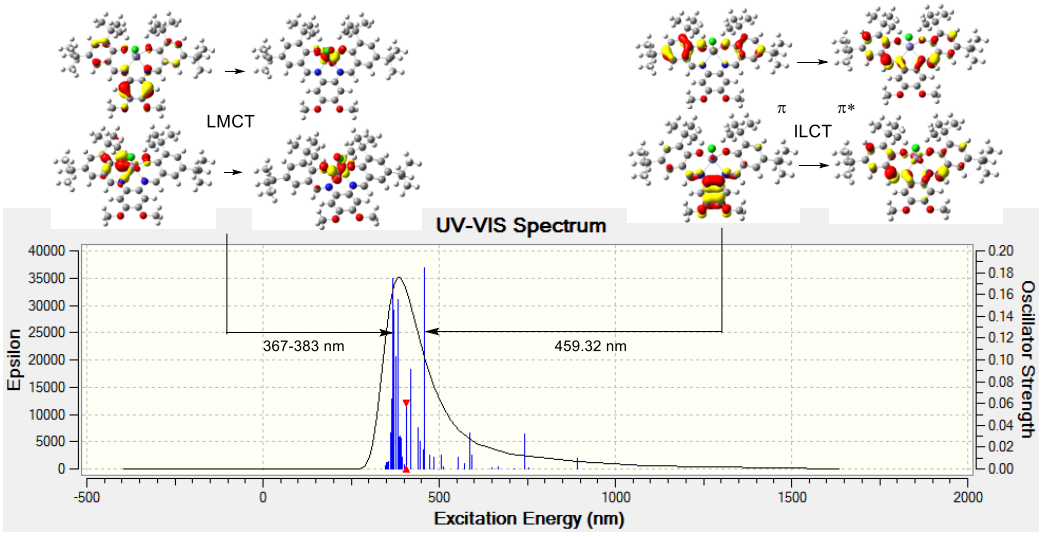

Figure 3.4. TD-DFT spectrum and NTOs (isodensity value of 0.05 a.u.) of the excitations for the complex **3**.

3.3.4. Electrochemical Properties

The cyclic voltammograms of **1** and **2** were recorded in 1.0 × 10^{-3} mol L^{-1} dichloromethane solution using $TBAPF_6$ as the supporting electrolyte. All the potential values were recorded versus the Fc/Fc^{+} couple.[113] Complex **1** showed only ligand-based processes, while complex **2** showed both ligand-based oxidation and metal-based reduction processes as shown in **Figure 3.5**.

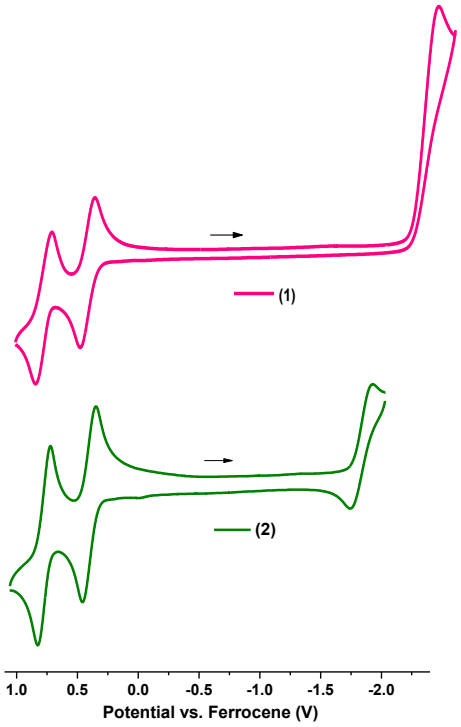

Figure 3.5. Cyclic voltammograms of complexes **1** and **2** in 1.0 × 10^{-3} mol L^{-1} dichloromethane solution.

Complexes **1** and **2** showed two reversible ligand based oxidation processes at 0.47 V (ΔE = 0.11 V, $|I_{pa}/I_{pc}|$ = 1.2), 0.80 V (ΔE = 0.12 V, $|I_{pa}/I_{pc}|$ = 1.1) for complex **1,** and 0.40 V (ΔE = 0.11 V, $|I_{pa}/I_{pc}|$ = 1.1), 0.78 V (ΔE= 0.11 V, $|I_{pa}/I_{pc}|$ = 1.0) for complex **2**. Thomas *et al.* observed similar oxidation processes for systems with methoxy substituents on phenylenediamine at ~0.41 V and 0.70 V.[110] According to literature[110,114] and DFT calculations, the first oxidation is attributed to the formation of a delocalized diiminobenzene π-radical species

whereas the second oxidation process is attributed to phenolate/ phenoxyl oxidation. Apart from the reversible oxidation processes, complex **1** showed an irreversible ligand reduction at E_{pa}= -2.18 V due to imine reduction. Complex **2** showed a quasi-reversible process at -1.85 V (ΔE = 0.19 V, $|I_{pa}/I_{pc}|$ = 1.9) attributed to the Cu^{II}/Cu^{I} reduction.[115] Similarly, complex **3** showed a quasi-reversible reduction process at-1.02 V assigned to the Fe^{III}/Fe^{II} redox couple.[103]

3.3.5. Spectroelectrochemistry and DFT Analysis

The spectroelectrochemical experiments were carried out for complex **2** because it showed both ligand oxidation and metal reduction ability, using dichloromethane solution under fixed potentials using $TBAPF_6$ as the electrolyte. The spectrum obtained for the reduction from **2** to $\mathbf{2}^-$ at $V_{Fc+/Fc}$ = -2.07 V showed a decrease in all π→π* transitions associated with the Cu^{II}/Cu^{I} couple (**Figure 3.6**) while the complex **3** showed a decrease in the bands between 300–750 nm with a new band appearing at 451 nm.[103] The first oxidation process for $\mathbf{2}^+$ at $V_{Fc+/Fc}$ = 0.49 V showed an overall increase in intensity. Dominant features were observed at 1100 nm for $\mathbf{2}^+$ and is attributed to ILCT π→π* transitions. Similar observations were obtained for complex **3**.

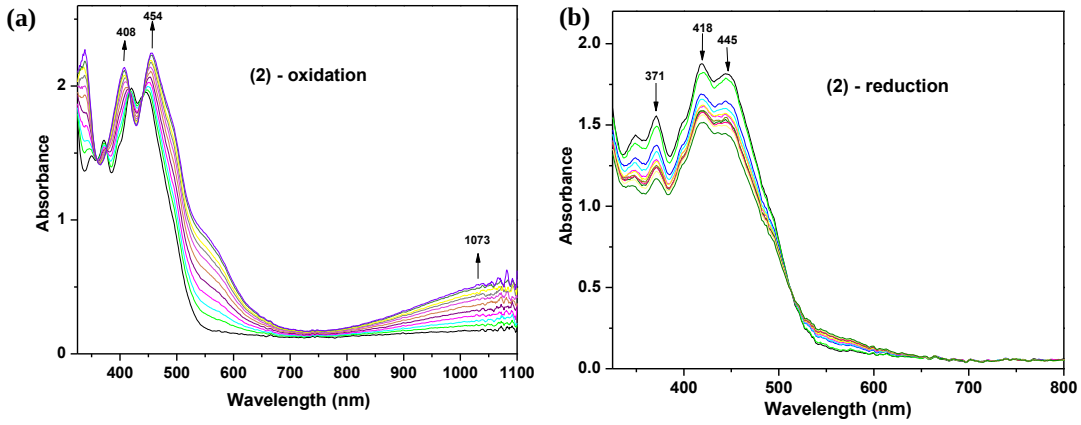

Figure 3.6. Electronic spectral changes observed for (a) oxidation and (b) reduction for complex **2** under fixed potential conditions.

The electrochemical events were further investigated using DFT methods.[116] The **Figure 3.7** shows spin densities for the relevant structures of complex **2**. The reduction of **2** was

confirmed as metal-centered, and the resulting $3d^{10}$ copper(I) complex, $\mathbf{2}^{-}$, is a closed shell singlet (S=0) and is severely distorted. The two phenoxyl rings are no longer coplanar leading to significant disruption of the π conjugation in the ligand framework which is responsible for the decrease in the ILCT processes observed in the spectroelectrochemical experiment. The first oxidation to $\mathbf{2}^{+}$ is ligand-based yielding a radical that is delocalized over the phenylenediamine moiety. The resulting phenylenediamine π radical cannot couple with the copper-based singly occupied $d_{x^2-y^2}$ orbital and the HS triplet (S=1) state is found to be lower in energy than the AF coupled state (S=0) by 1.5 kcal mol^{-1}. The second oxidation for $\mathbf{2}^{++}$ involved a phenolate/phenoxyl-based process.[117]

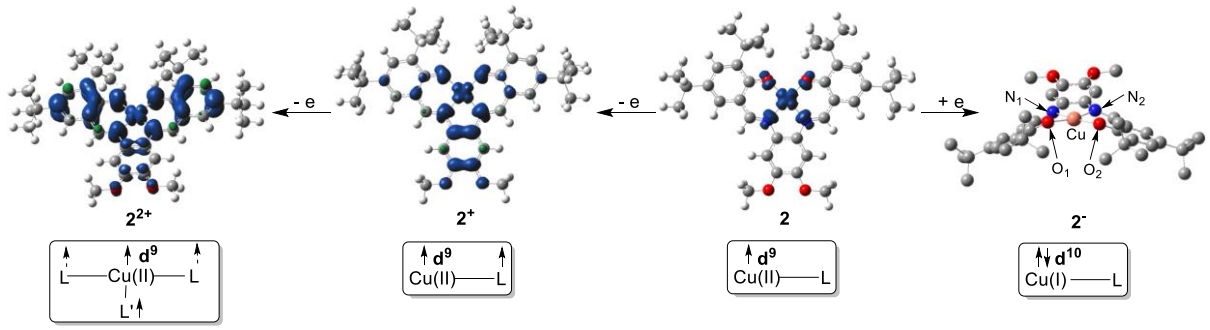

Figure 3.7. DFT-calculated spin density plots (isodensity 0.004 a.u.) showing oxidation and reduction for **2**. Hs omitted in $\mathbf{2}^{-}$.

Similarly reduction of complex **3** was confirmed as an Fe^{III}/Fe^{II} event leading to a high spin (S=4/2) iron(II) species. The first oxidation to $\mathbf{3}^{+}$ is ligand-based, yielding a radical delocalized over the phenylenediamine moiety, while second oxidation involves a phenolate/phenoxyl process[103] as illustrated in **Figure 3.8**.

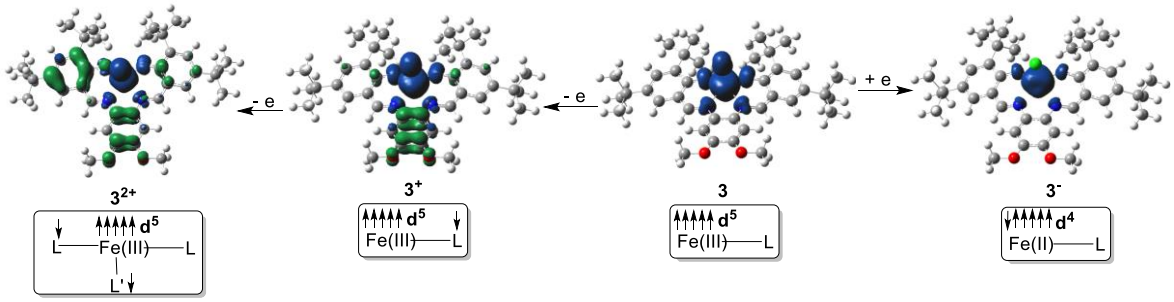

Figure 3.8. DFT-calculated spin density plots (isodensity 0.004 a.u.) showing oxidation and reduction for **3**.

3.3.6. Isothermal Compression Data

The amphiphilic properties of the complexes were assessed using isothermal compression data and Brewster angle microscopy (BAM) images at 23°C. The complexes started to interact with each other at ~50 $Å^2$ $molecule^{-1}$ and further compression resulted in a homogeneous film with a critical area of 46 $Å^2$ $molecule^{-1}$. The isotherms obtained between average molecular area *vs*. surface pressure of complexes **1** and **2** did not show any special phase transitions and showed respective collapse pressures of *ca*. 34 and 31 mN/m. Both complexes showed a constant pressure collapse,[118] following the Ries mechanism.[119] The BAM images obtained during the LB experiment showed a homogenous film formation at the air/water interface between 5-38 mN/m with no defects until arrays of Newton rings observed at the collapse of the Langmuir film.[120] The isothermal compression data obtained for the complexes **1** and **2** are shown in **Figure 3.9** along with selected BAM images.

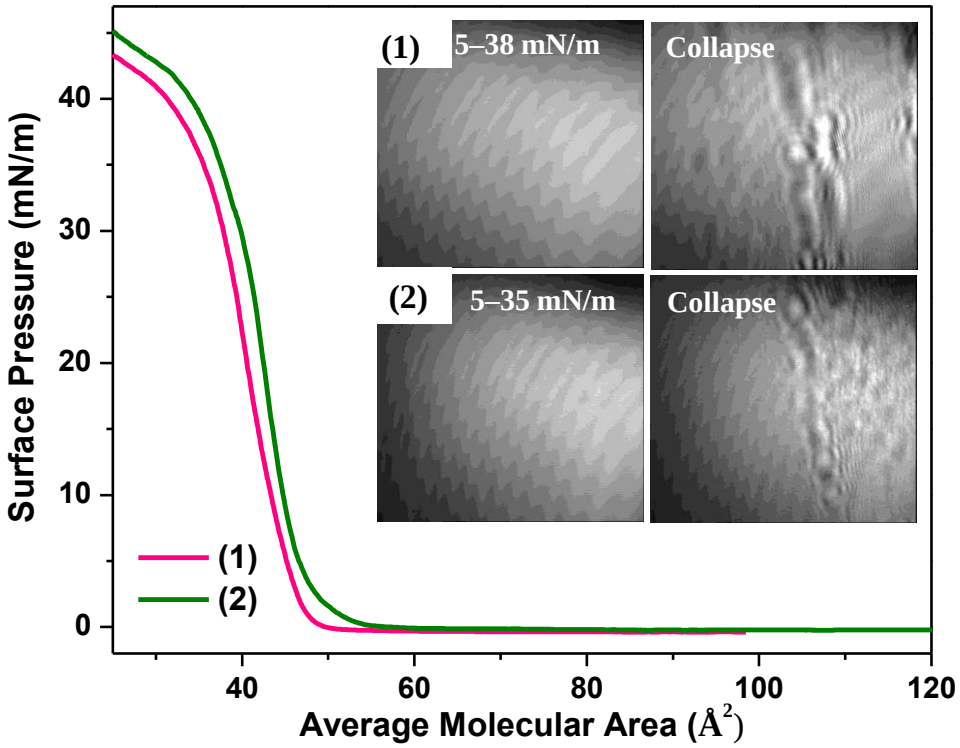

Figure 3.9. Compression isotherm data of complexes **1** and **2** with their selected BAM micrographs.

3.3.7. Surface Characterization Using Atomic Force Microscopy (AFM)

AFM analyses were performed to access the surface topology of the LB films on mica substrates, for films deposited at different surface pressures. The deposition transfer ratios were close to unity, as indicative of a near complete transfer onto the surface. The monolayers were deposited at room temperature at surface pressures of 12, 18, 20, 24, 26, and 28 mN/m for complex **1**, and at 5, 10, 20, 25, 30, and 32 and 40 mN/m for complex **2**. The AFM images obtained for complexes **1** and **2** are shown in **Figure 3.10**. According to the images, films deposited at lower surface pressures showed a random film deposition with defects as pinholes while a homogeneous film formation was observed at 20-25 mN/m with no defects. The films deposited at higher surface pressures appeared rougher with aggregates on the surface, due to multilayer formation from molecular tumbling and film folding at the film collapse.[119]

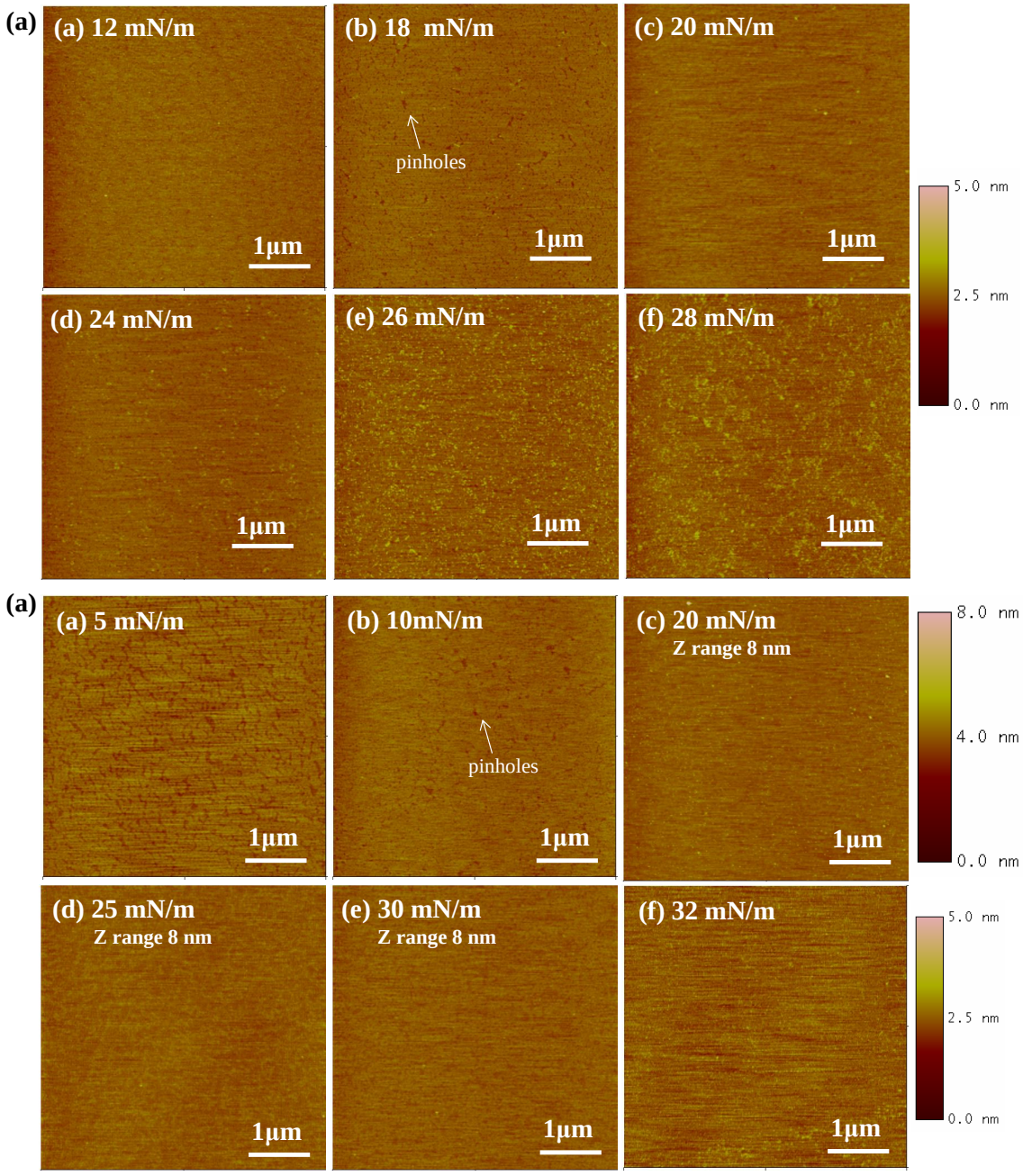

Figure 3.10. The AFM images of monolayer films deposited on mica substrates at different surface pressures (a) for complex **1,** (b) for complex **2**. Scan size 5 µm, Z range 5 nm unless otherwise noted.

3.3.8. Langmuir-Blodgett Film Characterization Using UV-visible and IRRAS Spectroscopy

The UV-visible spectra of 30-50 LB film deposited glass substrates were recorded to evaluate the retention of molecular composition after film deposition. The UV-visible spectra obtained for films of complexes **1** and **2** in comparison with that in solution is given in **Figure 3.11**. The UV-visible spectra of the LB multilayer films showed that both species conserve the main original electronic processes with minor decrease in absorptions, accompanied with a red-shift that is attributed to conformational changes associated with film packing[121] and J-type chromophore aggregation.[122] The comparable LB film UV-visible spectra with that in solution reveal that the molecular structure remains intact after film deposition process.

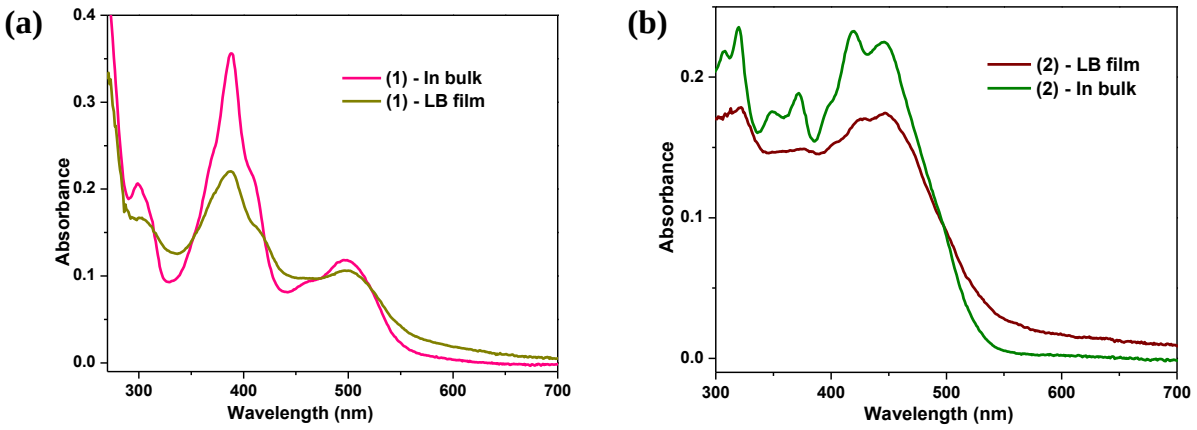

Figure 3.11. UV-visible spectra of multilayer LB films of (a) complex **1** [30 depositions], and (b) complex **2** [50 depositions] in comparison with their solution spectra.

Infrared reflection absorption spectroscopy (IRRAS) can be also used to predict the composition and ordering of the molecules after film deposition.[123] The IRRAS data were collected using 30-50 layer deposited glass substrates under *p*-polarized light at angle of incidence of 30° and 40° for complexes **1** and **2,** respectively (**Figure 3.12**). Both complexes showed bands at ~3000-2800 cm^{-1} belonging to symmetric and asymmetric C-H stretching

vibrations, as well as bands at ~1600-1300 cm^{-1} belonging to C=C aromatic stretching, CH_2/CH_3 deformation vibrations and C=N stretching vibrations. The IRRAS spectra showed both upwards and downwards bands associated with the molecular ordering during film deposition.[124] These factors suggest that the complexes have formed ordered layers during the LB film deposition and remained intact after the film deposition.

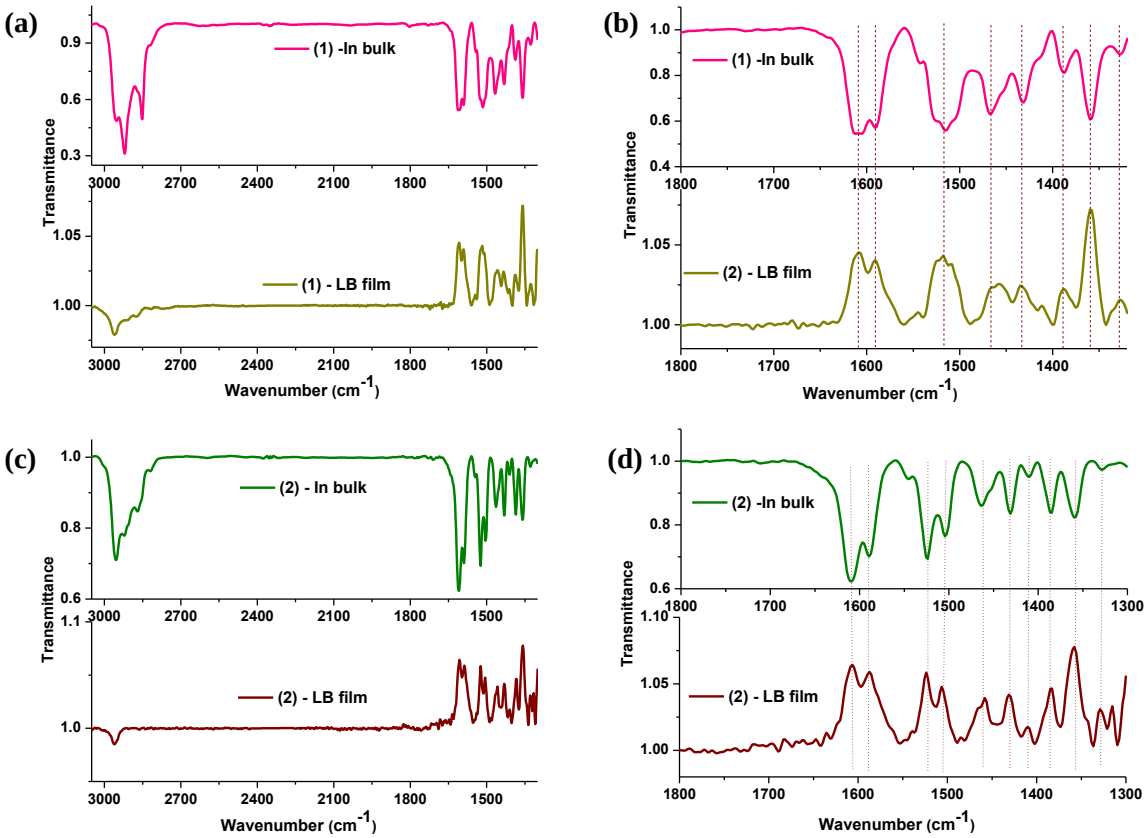

Figure 3.12. Full IRRAS spectra (a), (c) and the region between 1300-1800 cm^{-1} (b), (d) for complexes **1** and **2** in comparison with their bulk IR spectra.

3.3.9. Device Fabrication and Current-Voltage Characterization

Complex **2** was chosen from complexes **1** and **2**, for device fabrication because it showed a metal-based reduction process which can perform as an electron acceptor moiety in current rectification. The Au|LB|Au assembly was built using monolayers deposited at 25 mN/m surface pressure on gold-coated mica substrates for current-voltage measurements. The AFM images

obtained for LB monolayer deposited on gold-coated mica substrate are shown in **Figure 3.13a** and **b**. The LB films were then topped with a gold layer deposited using shadow masking method.[101a,b,125] The resulting assembly contained 16 Au|LB|Au devices and their current-voltage (I/V) curves were measured under ambient conditions. An optical micrograph image and a schematic representation of the assembly are given in **Figure 3.13c** and **d**, respectively. The reproducibility of the I-V curves were explored by measuring multiple devices of both a given assembly and different assemblies. Similar methods were followed to build the device using complex **3**.[103]

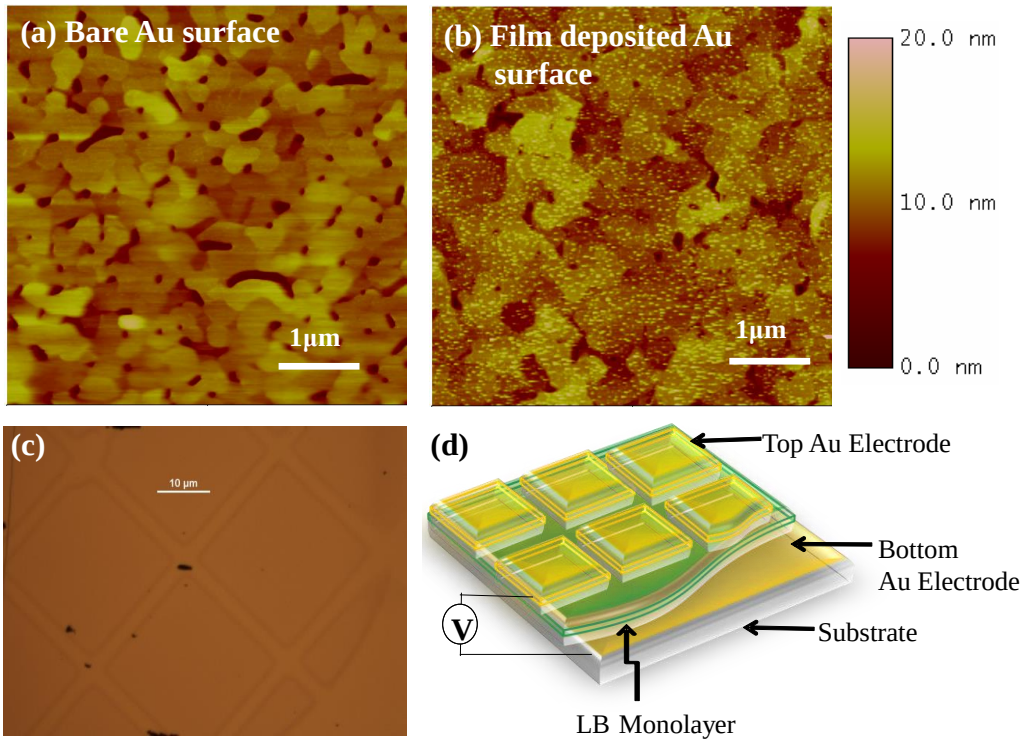

Figure 3.13. The AFM images of (a) bare gold substrate, (b) LB monolayer deposited gold substrate, (c) optical micrograph of the assembly, and (d) schematic representation of the assembly. The scan size was 5 µm and Z range was 20 nm for the AFM images.

The current-voltage measurements performed for the device assembly of complex **2** resulted in a flat I/V curve representing an insulating behavior (**Figure 3.14a**), while complex **3**

showed an asymmetric current response, representing a rectification behavior (**Figure 3.14b**). The observed rectification ratio ranged from 3.99 to 28.6 between -2 to +2 V and from 2.04 to 31 between -4 to +4 V.[103]

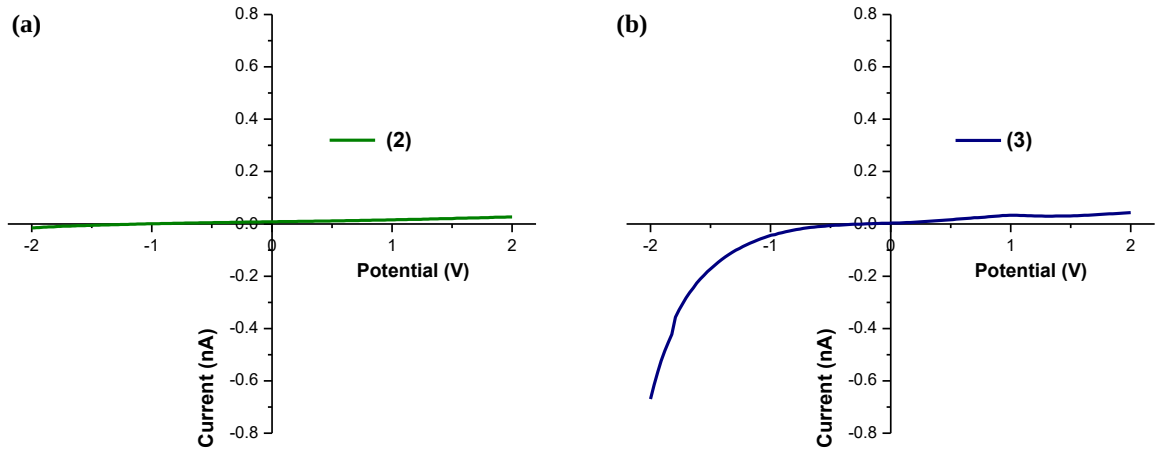

Figure 3.14. The I/V characteristics observed for Au|LB|Au device of (a) complex **2** and (b) complex **3**.

Therefore, evaluation of the possible rectification mechanisms must take into account plausible electron transfer pathways. Since the device consists of physisorbed material on two identical electrodes, a purely Schottky mechanism can be eliminated.[102] Thus, the energies of molecular frontier orbitals should be compatible with the electrode Fermi levels for electron transfer to take place. Gold electrodes Fermi level is 5.1 eV below vacuum,[126] and electron transfer will be favored by the systems with the best match between Fermi level and HOMO/LUMO or HOMO/SOMO (singly occupied) energies of the molecules. Therefore to evaluate the energy match between Fermi level and molecular frontier orbitals, the redox potentials obtained from cyclic voltammetry were converted to comparable solid state potentials using equations 1 and 2,[127] and was compared with the electrode Fermi energy (E_F) levels.

$$V_a = 4.7\ eV + E_{1/2}^{red}\,(SCE) \qquad (1)$$

$$V_i = 4.7\ eV + (1.7)\,E_{1/2}^{ox}\,(SCE) \qquad (2)$$

The values of V_a and V_i are respectively very close to the first electron affinity and first ionization energy levels of the molecule supported on the electrodes. Furthermore, the V_a values correlate with the first metal-centered lowest unoccupied molecular orbital (LUMO) or singly occupied molecular orbital (SOMO), and V_i values correspond to first ligand-centered highest occupied molecular orbital (HOMO). The $E_{1/2}^{ox}$ and $E_{1/2}^{red}$ are the half-wave first oxidation and first reduction potentials versus standard calomel electrode (SCE).

The calculated SOMO values were -3.2, and -4.1 eV while the HOMO values were -6.1, and -6.5 eV for complexes **2** and **3**, respectively. Therefore, the model depicted in **Figure 3.15**, shows that the only available SOMO for **2** is the copper-based $d_{x^2-y^2}$ orbital situated approximately 2 eV above the electrode Fermi level. This MO is likely not attainable at the applied bias, and this energetic mismatch accounts for the observed I/V insulating behavior of the copper(II) complex. For the square pyramidal iron(III) complex, SOMO is a linear combination of d_{xz} and d_{yz} orbitals that lies approximately 1.0 eV above the $E_{F,}$ making it energetically comparable for electron transfer. The calculated HOMO energies of complexes **2** and **3** are situated 1.0 and 1.4 eV below the gold Fermi energy level, respectively. Since complex **2** is not rectifying, it suggests that the ligand based HOMOs are not involved in the rectification process. This shows that only SOMO is involved in electron transfer in complex **3**, proposing an asymmetric current rectification mechanism.

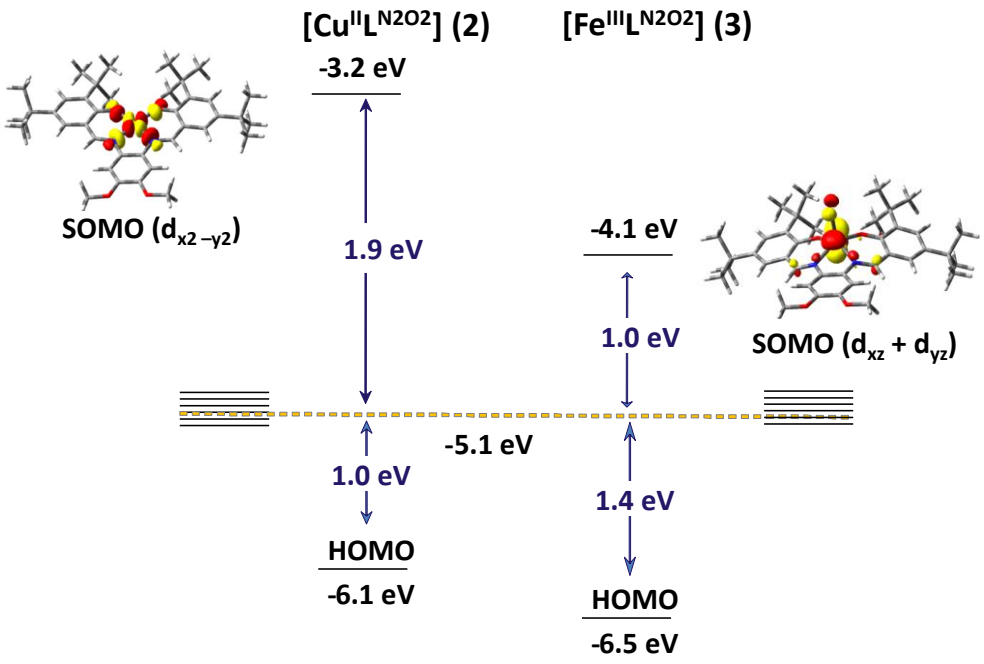

Figure 3.15. Electron transfer model involving the Fermi levels of the electrode into the metal-based SOMOs of complexes **2** and **3**.

3.4. Conclusion

In conclusion, redox-active nickel(II) and copper(II) complexes can exhibit amphiphilic properties with collapse pressures of ~35 mN/m. The LB monolayers of these complexes showed homogeneous film formation at 20-25 mN/m region. The large energy difference between Fermi level and SOMO of complex **2**, makes it unable to contribute in electron transfer resulting an insulating behavior. On the other hand, SOMO energy of complex **3** is energetically comparable with electrode Fermi level allowing electrons to transfer via SOMO. This suggests that partially filled SOMO can be involved in electron transfer instead of LUMO. However, HOMO of complex **2** is situated 1.0 eV below Fermi level and insulating behavior of the assembly suggests that HOMO energies are not engaged in electron transfer. Therefore, it suggests that only SOMO of complex **3** is involved in electron transfer proposing an asymmetric current rectification mechanism.

CHAPTER 4 NEW ASYMMETRIC IRON(III) COMPLEXES THAT CAN MODULATE FRONTIER MOLECULAR ORBITALS TO FACILITATE CURRENT RECTIFICATION

4.1. Introduction

Molecular rectification can occur due to formation of Schottky barriers or due to asymmetric or unimolecular electron transfer.[128] The Schottky mechanism can be eliminated due to the use of Langmuir-Blodgett films that are physisorbed onto surfaces.[129] Therefore, the placement of frontier molecular orbitals of the molecule with respect to the electrode Fermi energy levels plays a major role in deciding between the asymmetric and unimolecular mechanisms. In unimolecular mechanism both the highest occupied molecular orbitals (HOMO) and lowest unoccupied molecular orbitals (LUMO) are involved in electron transfer because the HOMO of the donor moiety is energetically comparable to the Fermi level of one electrode while the LUMO of acceptor moiety is comparable to the other electrode. In asymmetric mechanism, LUMO of the molecule is energetically comparable with the electrode Fermi level where as HOMO is energetically much lower and making it unable to participate in electron transfer.[130] Our group recently proposed that singly-occupied molecular orbitals (SOMO) can be involved in electron transfer instead of LUMO in asymmetric current rectification using a penta-coordinated Fe(III) complex.[131] According to the report the electron transfer occurred via the SOMO which was situated 1 eV above the Fermi level without any involvement of the HOMO which was situated 1.4 eV below the electrode Fermi level. Therefore, the energy difference between Fermi levels of the electrode and the SOMO energy of complex molecules can direct the asymmetric rectification.

Based on previous findings from our group, phenolate rich asymmetric iron(III) complexes are known as good candidates for molecular current rectification in gold|molecule|gold assemblies.[131,132] Therefore, we hypothesize that the incorporation of electron

deficient pyridine groups instead of a phenolate arms to the ligand framework will lower the SOMO energy levels (**Scheme 4.1a, b**) of Fe(III) complexes. Moreover, the replacement of an axial ligand with ligands acquiring low splitting energies will lower the SOMO energy level of the molecules (**Scheme 4.1c, d**). These lowering of SOMO energy levels with respect to electrode Fermi energy will allow lower applied potentials for current rectification.

In this chapter we investigate the structural, electronic, redox, and amphiphilic behavior of four asymmetric iron(III) complexes. We further evaluate that their HOMO-SOMO energy positioning with respect to the electrode Fermi energy levels based on calculations performed using experimental values.

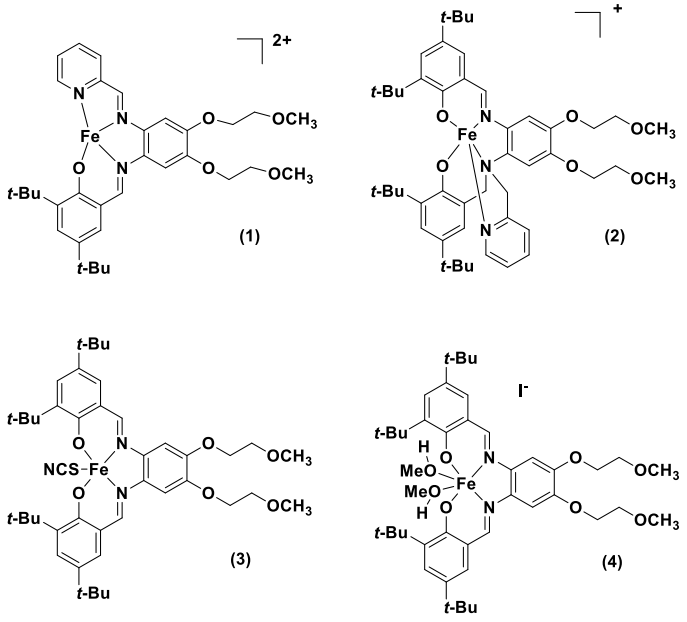

Scheme 4.1. Asymmetric iron(III) complexes with asymmetric ligand design **1**, **2** and with different axial ligands **3**, **4**.

4.2. Experimental Section

4.2.1. Synthesis of the Ligands

Synthesis of Ligand Precursors

Syntheses of 4,5-bis(2-methoxyethoxy)benzene-1,2-diamine, 2,4-di-tert-butyl-6-(hydroxymethyl)phenol, and 2,4-di-tert-butyl-6-(chloromethyl)phenol were carried out as previously described.[131,132,133] 3,5-di-tert-butyl-2-hydroxybenzaldehyde and 2-hydroxy-5-nitrobenzaldehyde were used as received from Sigma Aldrich.

Synthesis of Ligand [HL^{N3O}]

To a stirred mixture of 4,5-bis(2-methoxyethoxy)benzene-1,2-diamine in dry methanol, 1 equivalent of pyridinecarboxaldehyde dissolved in dry methanol was added drop wisely over 30 minutes at 0 °C. The solution was stirred for four hours at 0 °C and for 15 min at room temperature under inert atmosphere. Then 1 equivalent of 3,5-di-tert-butyl-2-hydroxybenzaldehyde dissolved in dry methanol was added drop wise and was refluxed for 18 h under inert atmosphere (**Scheme 4.2**).

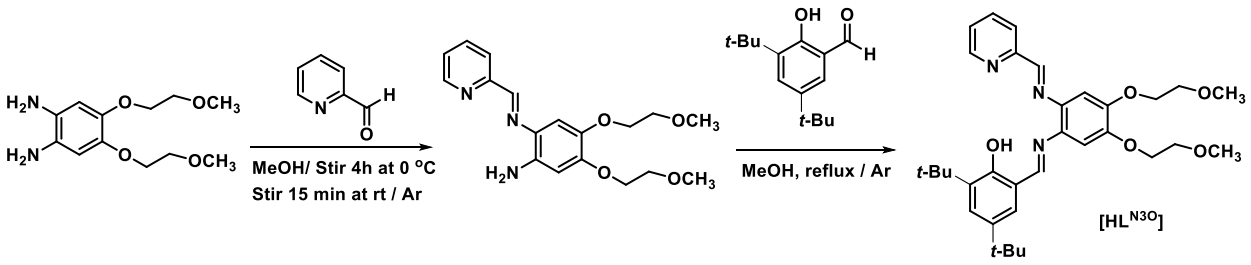

Scheme 4.2. Synthetic route of ligand [HL^{N3O}].

The solvent was removed by rotary evaporation and the resulting brown oily product was purified using column chromatography with silica as stationary phase and a hexane: ethyl acetate (1:1) solvent mixture. Yield: 38 %. ESI (m/z^+) in CH_2Cl_2 = 562.31 for [$C_{33}H_{43}N_3O_5+H^+$]. ^1H NMR, ppm ($CDCl_3$, 400 MHz): 1.06-1.48 (m, $18H^{tBu}$), 3.47 (s, $6H^{OCH3}$), 3.77-3.82 (m, $4H^{OCH2}$),

4.14-4.31 (m, 4H^{OCH2}), 6.96 (s, 1H^{ph}), 7.09 (s, 1H^{ph}), 7.28 (d, 1H^{ph}), 7.49(m, 2H^{py}), 7.89 (td, 1H^{py}), 8.26 (d, 1H^{ph}), 8.47 (s, 1H^{CH}), 8.62 (dd, 1H^{py}), 8.66 (s, 1H^{CH}). IR (KBr, cm^{-1}): 3245 (ν_{O-H}), 2871-2954 (ν_{C-H}), 1642 ($\nu_{C=C}$, aromatic), 1509 ($\nu_{C=C}$, aromatic), 1600 ($\nu_{C=N}$), 1258 (ν_{C-O-C}), 1124 (ν_{C-O-C}).

Synthesis of Ligand [H_3L^{N3O2}]

Synthesis of 6,6'-(1E,1'E)-(4,5-bis(2-methoxyethoxy)-1,2-phenylene)bis(azan-1-yl-1-ylidene)bis(methan-1-yl-1-ylidene)bis(2,4-di-tert-butylphenol) salophen precursor was carried out as previously described.[4] The salophen precursor was reduced in the presence of excess sodium borohydride in dichloromethane/methanol (1:1) mixture at 0 °C. The resulting yellow solution was concentrated and extracted with a dichloromethane and water mixture. The organic layer was collected and dried over anhydrous $NaSO_4$ and the remaining solvent was removed under vacuum. The resulting reduced salophen precursor was dissolved in dichloromethane and added to a mixture of picolyl chloride and triethyl amine dissolved in a 1:1 dicloromethane:ethanol mixture and was refluxed for 48 h (**Scheme 4.3**).

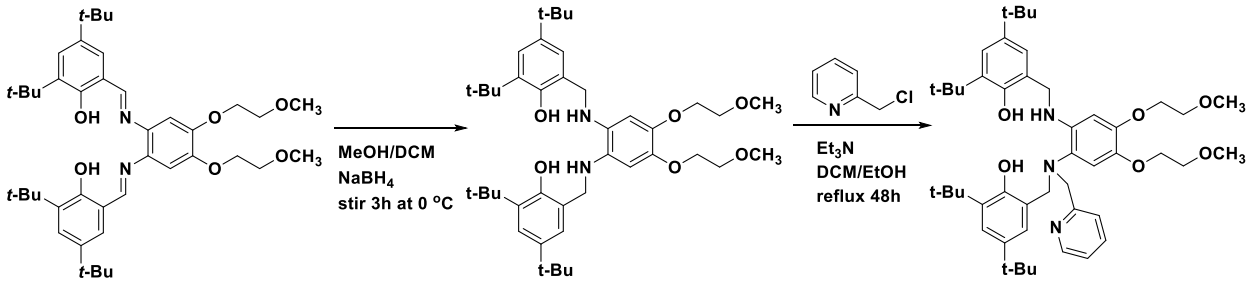

Scheme 4.3. Synthetic route of ligand [H_3L^{N3O2}].

The solvent was removed by rotary evaporation and the resulting brown oily product was purified using a silica column with hexane:ethyl acetate (1:1) solvent mixture. Yield: 25 %. ESI (m/z^+) in CH_2Cl_2 = 784.5 for [$C_{48}H_{69}N_3O_6$+H^+]. ^{1}H NMR, ppm ($CDCl_3$, 400 MHz): δ 1.08-1.48 (m, 36H^{tBu}), 3.44 (s, 3H^{OCH3}), 3.48 (s, 3H^{OCH3}), 3.74-3.83 (m, 4H^{OCH2}), 4.15-4.31 (m, 4H ^{OCH2}),

4.40 (s, 2H^{CH2}), 4.74 (s, 2H^{CH}), 6.58 (s, 1H^{ph}), 6.94 (d, 1H^{ph}), 7.11 (d, 1H^{ph}), 7.21 (d, 1H^{ph}), 7.32 (s, 1H^{ph}), 7.49 (2, 2H^{py}), 8.08 (t, 1H^{py}), 8.26 (d, 1H^{py}), 8.36 (d, 1H^{ph}), 8.48 (s, 1H^{CH}). IR (KBr, cm^{-1}): 3245 (ν_{O-H}), 2874-2956 (ν_{C-H}), 1737 ($\nu_{C=C}$, aromatic), 1516 ($\nu_{C=C}$, aromatic), 1255 (ν_{C-O-C}), 1126 (ν_{C-O-C}).

Synthesis of Ligand [H_2L^{N2O2}]

Synthesis of 6,6'-(1E,1'E)-(4,5-bis(2-methoxyethoxy)-1,2-phenylene)bis(azan-1-yl-1-ylidene)bis(methan-1-yl-1-ylidene)bis(2,4-di-tert-butylphenol) salophen ligand [H_2L^{N2O2}] was carried out as previously described.[131]

4.2.2. Syntheses of Iron(III) Complexes

Synthesis of Complex [$Fe^{III}L^{N3O}$] (1)

The complex [$Fe^{III}L^{N3O}$] was synthesized by treating a methanolic solution of [HL^{N3O}] (0.08 g : 0.14 mmol) and $NaOCH_3$ (0.008 g : 0.15 mmol) with $FeCl_3.6H_2O$ under refluxing conditions for 5 hours. A dark green precipitate was obtained from slow evaporation. Yield: 78 %. ESI (m/z+) in CH_3OH = 647.2651 (100 %) for $[C_{33}H_{42}N_3O_6Fe]^{2+}$ (calculated = 647.2658) in agreement with -1.1 ppm difference. Anal. Calc. for $[C_{34}H_{45}FeN_3O_6]$: C, 61.95; H, 7.13; N, 6.19 % Found: C, 61.57; H, 6.85; N, 5.97 %. IR (KBr, cm^{-1}) 2872-2957(ν_{C-H}), 1638 ($\nu_{C=C}$, aromatic), 1502($\nu_{C=C}$, aromatic), 1589 ($\nu_{C=N}$), 1255 (ν_{C-O-C}), 1126 (ν_{C-O-C}).

Synthesis of Complex [$Fe^{III}L^{N3O2}$] (2)

The complex [$Fe^{III}L^{N3O2}$] was synthesized by treating a 3:1 methanol:dichloromethane solution of [H_2L^{N3O2}] (0.08 g : 0.1 mmol) and $NaOCH_3$ (0.01 g : 0.2 mmol) with $FeCl_3.6H_2O$ under refluxing conditions for 5 hours. A dark green precipitate was obtained from slow evaporation. Yield: 65 %. ESI (m/z+) in CH_3OH = 835.4245 (100 %) for $[C_{48}H_{65}N_3O_6Fe]^{+}$ (calculated = 835.4223) in agreement with 2.6 ppm difference. Anal. Calc. for

$[C_{48}H_{65}ClFeN_3O_6]$: C, 66.16; H, 7.52; N, 4.82 %. Found: C, 66.39; H, 8.07; N, 3.69 %. IR (KBr, cm^{-1}) 2871-2956(ν_{C-H}), 1713 ($\nu_{C=C}$, aromatic), 1508 ($\nu_{C=C}$, aromatic), 1607 ($\nu_{C=N}$), 1271 (ν_{C-O-C}), 1127 (ν_{C-O-C}).

Synthesis of Complexes [($Fe^{III}L^{N3O2}$)SCN] (3) and [($Fe^{III}L^{N3O2}$)I] (4)

The complex [($Fe^{III}L^{N2O2}$)Cl] was synthesized as previously reported.[131] This complex (0.09 g: 0.11 mmol) was then dissolved in 20 mL of a 1:1 dichloromethane:methanol solvent mixture and treated with $AgPF_6$ (0.03 g: 0.11 mmol) while stirring for 1 h at room temperature. The mixture was then treated with excess of KSCN dissolved in methanol to obtain complex **3**, and with KI dissolved in methanol to obtain complex **4** and was refluxed for 3 h. Dark brown crystals were obtained for complex **3** from slow evaporation. Yield: 97 %. ESI (m/z+) in CH_3OH = 742.3765 for $[C_{42}H_{58}N_2O_6Fe]^+$. Anal. Calc. for $[C_{43}H_{58}FeN_3O_6S]$: C, 64.49; H, 7.30; N, 5.25 %. Found: C, 64.62; H, 7.49; N, 5.27 %. IR (KBr, cm^{-1}) 2870-2955 (ν_{C-H}), 2040 ($\nu_{C\equiv N}$), 1603($\nu_{C=N}$), 1506($\nu_{C=C}$, aromatic), 1252(ν_{C-O-C}), 1130(ν_{C-O-C}). Slow evaporation of the filtered solution resulted dark brown crystals for complex **4** as well. Yield: 78 %. ESI (m/z+) in CH_3OH = 742.37 for $[C_{42}H_{58}N_2O_6Fe]^+$. Anal. Calc. for $[C_{42}H_{58}FeN_2O_6.2CH_3OH.I]$: C, 56.60; H, 7.12; N, 3.00 %. Found: C, 57.59; H, 6.60; N, 3.18 %. IR (KBr, cm^{-1}) 2869-2953(ν_{C-H}), 1604 ($\nu_{C=N}$, aromatic), 1507 ($\nu_{C=C}$, aromatic), 1251 (ν_{C-O-C}), 1120 (ν_{C-O-C}).

4.2.3. X-Ray Crystal Structure Analysis

Single crystals of complex **4** were grown by slow evaporation of the reaction mixture. A suitable crystal was selected and mounted with a mitogen loop on a Bruker APEX-II CCD diffractometer. The crystal was kept at 100.1 K during data collection. Using Olex2,[134] the structure was solved with the ShelXT[135] structure solution program using Direct Methods and refined with the XL[136] refinement package using Least Squares minimization. A total of 13458

reflections were measured ($2.608° \leq 2\Theta \leq 59.406°$), and 13400 unique reflections (R_{int} = 0.0000, R_{sigma} = 0.0448) were used in all calculations. The final R_1 was 0.0583 ($I > 2\sigma(I)$) and wR_2 was 0.1730 (all data). A total of three constrains were used during structural refinement and hydrogen atoms were placed in calculated positions. There are two complex molecules with an -iodo anion in the asymmetric unit. Selected crystallographic data is shown in **Table 4.1**.

	(4)
Formula	$C_{90}Fe_2I_2N_6O_{16}$
M	1917.49
Temperature/K	100.1
Crystal system	Triclinic
Space group	$P\bar{1}$
a/Å	10.5201 (6)
b/Å	14.6729 (9)
c/Å	16.2372 (10)
α/°	74.617 (3)
β/°	86.136 (3)
γ/°	89.786 (3)
Volume/Å^3	2410.8 (3)
Z	1
D_{calc} / g cm^{-3}	1.321
μ/ mm^{-1}	1.004
R(F) (%)	5.83
Rw(F) (%)	16.3

[a] $R(F) = \sum \| F_o | - | F_c \| / \sum | F_o |$; $Rw(F) = [\sum w(F_o^2 - F_c^2)^2 / \sum w(F_o^2)^2]^{1/2}$ for $I > 2\sigma(I)$

Table 4.1. Selected X-ray crystal data for complex **4**.

4.2.4. Electrochemical Analysis

The cyclic voltamograms for the complexes **1**, **2**, **3**, and **4** were recorded in 1×10^{-3} M dichloromethane solutions. Tetrabutylammonium hexafluorophosphate ($TBAPF_6$) was used as the supporting electrolyte and ferrocene was added to the solution as an internal redox standard.[137] Potential values were recorded with reference to the experimental Fc/Fc^+ value.

4.3. Results and Discussion

4.3.1. Synthesis and Characterization of Iron(III) Complexes

The ligand oxidation from amine to imine during metallation to form complex **2** was observed wth the appearence of new band in IR sepcta at 1607 cm^{-1} belonging to C=N vibration. This ligand oxidation has been observed for similar Fe and Co complexes.[132,138] The presence of a band belonging to C≡N vibration at 2040 cm^{-1} in complex **3** confirms the presence of SCN^- in the complex. All the complexes showed prominent bands ~2870-2950 cm^{-1} belonging to symmetric and asymmetric C-H vibrations.

4.3.2. Molecular Structure

The structure of complex **4** was confirmed by crystal structure analysis as shown in **Figure 4.1**. The crystal structure reveals that complex **4** is six-coordinated with two methanol units as the axial ligands and one iodide as a counter anion. The N and O atoms in the ligand framework were trans to each other with Fe-O and Fe-N average bond lengths being 1.874 Å and 2.091 Å respectively. These distances are in agreement with literature reported salophen-based iron(III) complexes.[139]

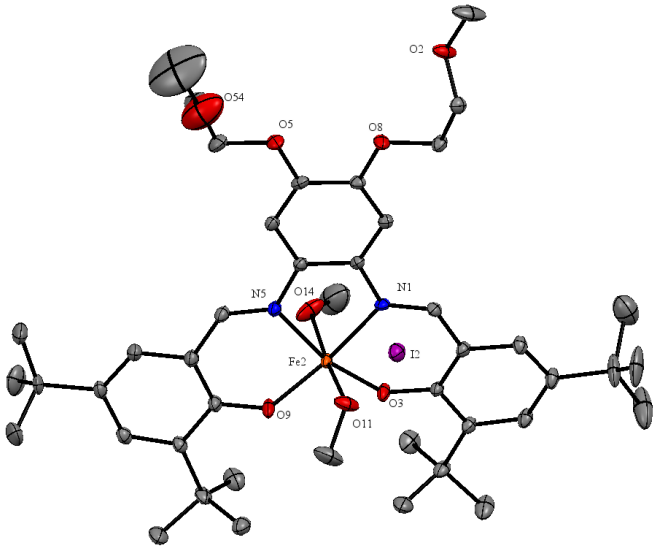

Figure 4.1. The ORTEP representation of complex 4 with two CH_3OH units as the axial ligands at 50% probability. Hydrogen atoms are omitted for clarity.

4.3.3. Electronic Spectral Properties

The UV-Visible spectra of the complexes **1**, **2**, **3**, and **4** were recorded in 1×10^{-5} M dichloromethane solutions as shown in **Figure 4.2**. The UV-visible spectrum of complex **1** showed intense absorption bands in the 250-700 nm region. The absorption band at ~ 340 nm region with ε ranging from ~9,000-24,000 L mol^{-1} cm^{-1} is due to ligand-to-metal charge transfer (LMCT) originating from the phenolate based pπ orbitals to $d_{\sigma*}$ orbital of the iron(III) center. In this spectrum the region between ~400-700 nm consisted of intraligand charge transfer (ILCT) and LMCT transitions occurring from phenolate oxygen pπ orbital to $d_{\pi*}$ of the metal center.[140]

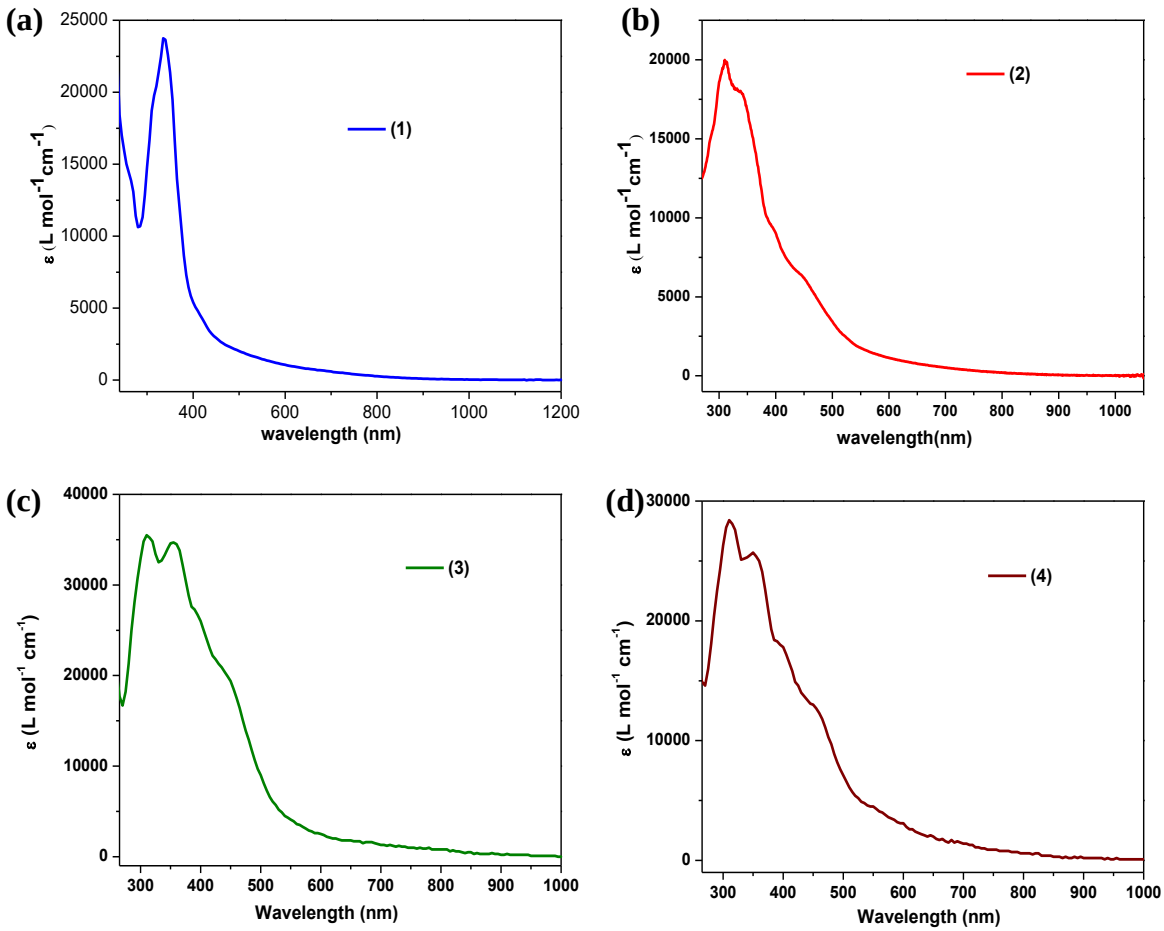

Figure 4.2. UV-visible spectra of (a) complex **1**, (b) complex **2**, (c) complex **3**, and (d) complex **4** in 1.0×10^{-5} mol L^{-1} dichloromethane solution.

The UV-visible spectra for complexes **2**, **3**, and **4** showed similar absorption peak patterns with absorption bands in the 250-700 nm regions. Complex **2** showed absorption bands at 308, 340, 400, 450 nm with ε ranging from ~63,00-20,000 L mol^{-1} cm^{-1}, complex **3** showed absorption bands at 310, 350, 400, 455 nm with ε ranging from ~19,000-35,500 L mol^{-1} cm^{-1}, and complex **4** showed absorption bands at 308, 355, 400, and 455 nm with ε ranging from ~12,550-28,600 L mol^{-1} cm^{-1}. The bands ~300-400 nm are due to LMCT transitions originating from phenolate p_π orbitals to metal d_{σ^*} and d_{π^*} orbitals. These assignments correlate well with similar Schiff-base iron(III) complexes reported in literature.[141] The other bands are due to intraligand $\pi\rightarrow\pi^*$ transitions observed for similar species.[142]

4.3.4. Electrochemical Properties

All the complexes show both metal-centered reduction processes and ligand-centered oxidation processes as shown in **Figure 4.3**.

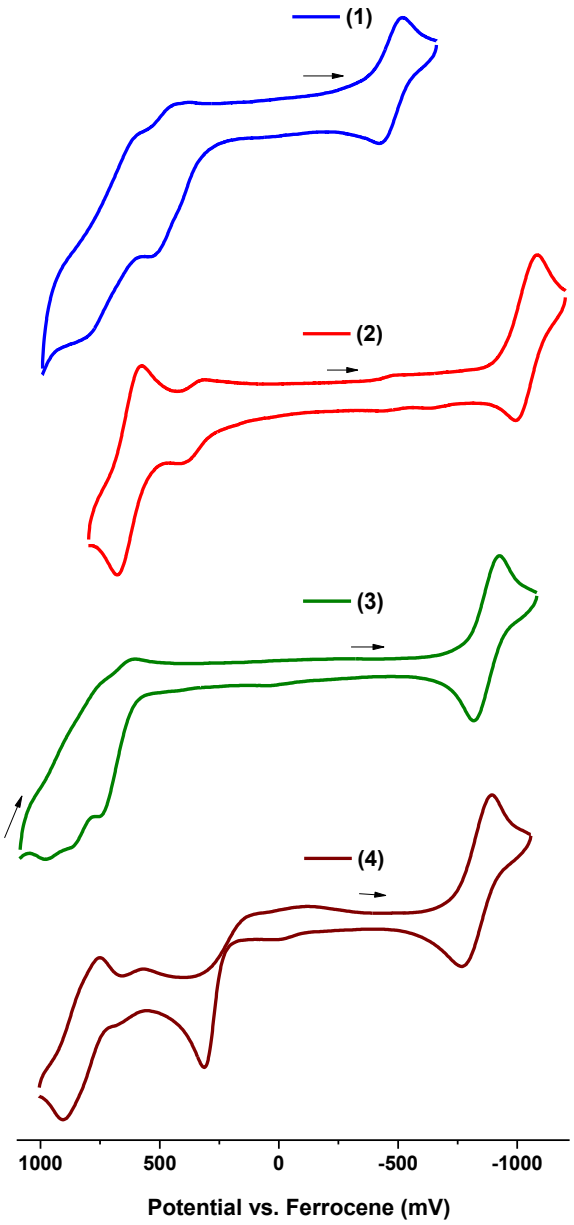

Figure 4.3. Cyclic voltammograms of complexes **1**, **2**, **3**, and **4** in 1.0×10^{-3} mol L^{-1} dichloromethane solution.

The complexes showed quasi-reversible single electron reduction process at -0.477 V (ΔEp= 0.077 V, $|I_{pa}/I_{pc}|$ = 1.5), -1.052 V (ΔEp= 0.074 V, $|I_{pa}/I_{pc}|$ = 0.40), -0.86 V (ΔE_p= 0.10 V,

$|I_{pa}/I_{pc}|$ = 1.43), and -0.83 V (ΔE_p= 0.11 V, $|I_{pa}/I_{pc}|$ = 1.56) for complexes **1**, **2**, **3**, and **4** respectively which can be assigned to the Fe^{III}/Fe^{II} reduction process. According to literature[132,143] Fe^{III}/Fe^{II} redox couples for $[N_2O_3]$ environments with electron donating *t-butyl* phenolate moiety are observed at ~-1.5 V. Nonetheless, the Fe complexes discussed here with $[N_3O]$, $[N_3O_2]$, and $[N_2O_2]$ show lower potential values because of the lower electron density around the metal by removal of one phenolate arm will make the metal easier to be reduce. Thus, complex **1** with the $[N_3O]$ environment showed the lowest reduction potential compared to other complexes. One ligand based quasi-reversible and one irreversible oxidation processes were observed at 0.485 V (ΔE_p= 0.055 V, $|I_{pa}/I_{pc}|$ = 13.8) and E_{pa} = 0.795 V for complex **1**, 0.629 V (ΔE_p= 0.084 V, $|I_{pa}/I_{pc}|$ = 2.15) and E_{pa} = 1.14 V for complex **2** respectively. Complex **3** showed three irreversible oxidation processes with E_{pa} values of 0.75, 0.88, and 0.98 V, and complex **4** showed one irreversible oxidation process with E_{pa} value of 0.35 V and one quasi-reversible process at 0.83 (ΔE_p= 0.16 V, $|I_{pa}/I_{pc}|$ = 0.77). These oxidations can be assigned to the phenelenediamine oxidation and phenolate/phenoxyl redox processes, respectively.[4,144]

4.3.5. Isothermal Compression Data

The amphiphilic properties of the complexes were assessed using isothermal compression data and Brewster angle microscopy (BAM) images at 23°C. For complexes **1**, **3**, and **4**, molecules start to interact with each other at ~ 62 $Å^2$ $molecule^{-1}$ while complex **2** showed a higher area of interaction of 75 $Å^2$ $molecule^{-1}$, because complex **2** is bulkier with respective to other complexes. Further compression resulted in a homogeneous film between 5-46 mN/m with a critical area of 55 and 68 $Å^2$ $molecule^{-1}$ for complex **1** and **2** and between 5-35 mN/m with a critical area of 60 $Å^2$ $molecule^{-1}$ for complexes **3** and **4**. The isotherms did not show any phase transitions and the films were collapsed at *ca.* 46 $Å^2$ $molecule^{-1}$ for complex **1** and **2** and at *ca.* 35

$Å^2$ molecule^{-1} for complex **3** and **4** respectively (**Figure 4.4**). These complexes showed a constant pressure collapse following the Ries mechanism[145] as observed by other metallosurfactants.[131,132,146]

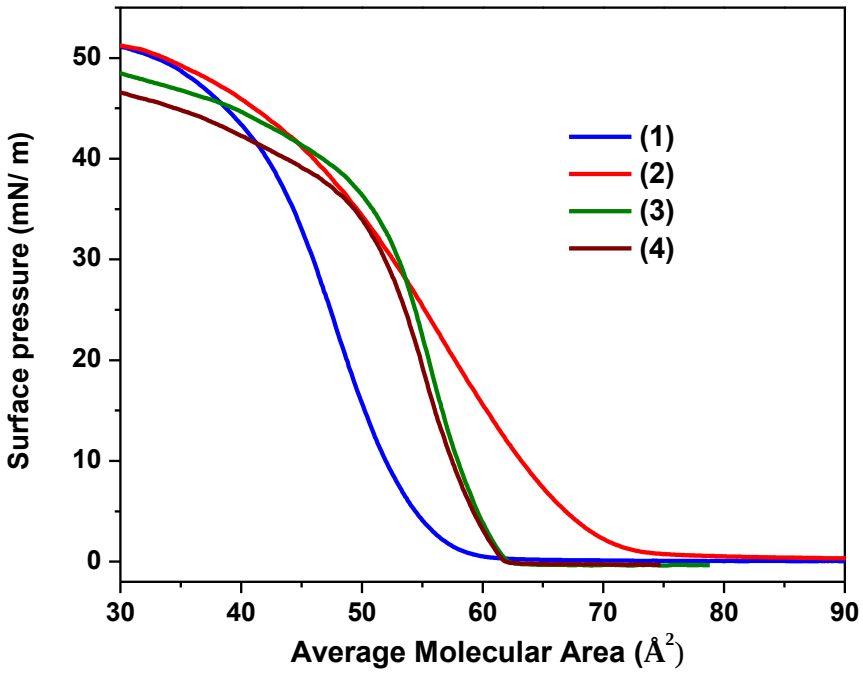

Figure 4.4. Isothermal compression data for complexes **1**, **2**, **3**, and **4**.

The BAM images showed a smooth film formation at the air/water interface and the collapse was observed as an array of Newton rings for complexes **1** and **2**. However, the lack of visible Newton rings made the collapse less perceptible from the BAM images for complexes **3** and **4** (**Figure 4.5**).

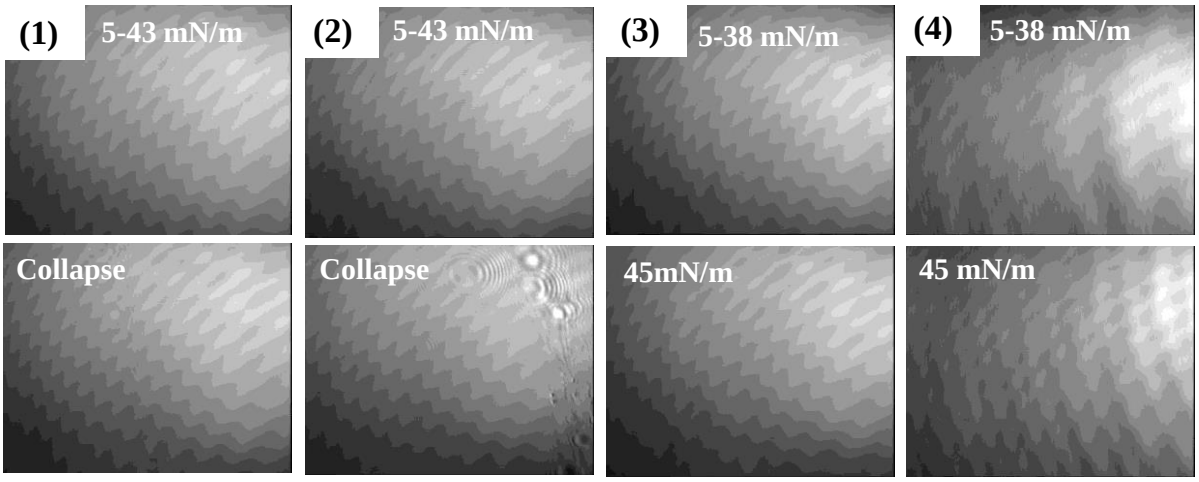

Figure 4.5. Brewster angle micrographs for complexes **1**, **2**, **3**, and **4**.

4.3.6. Surface Characterization Using Atomic Force Microscopy (AFM)

The surface topology of LB monolayer films deposited on mica substrates at different surface pressures was analyzed using AFM technique to optimize the deposition pressure that provides a homogeneous surface coverage which is critical in device fabrication. Complexes **1**, **2**, and **3** were used for further surface analysis since these complexes showed well defined redox processes. The monolayers were deposited at 18, 24, 30, 36, 42 mN/m for complex **1**, at 10, 20, 27, 33, 40 mN/m for complex **2**, and at 8, 15, 25, 30, 35 mN/m for complex **3** with a transfer ratio close to unity as indicative of near complete transfer onto the surface (**Figure 4.6**). Films deposited at lower surface pressures such as 18, 10, and 8 mN/m for complexes **1**, **2**, and **3** respectively, showed higher frequency of pinholes as shown in **Figure 4.6a**, **f**, and **k**. Monolayers deposited at moderate surface pressures of 30-36, 20-27, and 25-30 mN/m for the respective complexes **1**, **2**, and **3**, showed a homogeneous film formation with fewer defects. The films deposited at higher surface pressures resulted in rough films with aggregates due to formation of multilayers at the pressures closer to collapse.

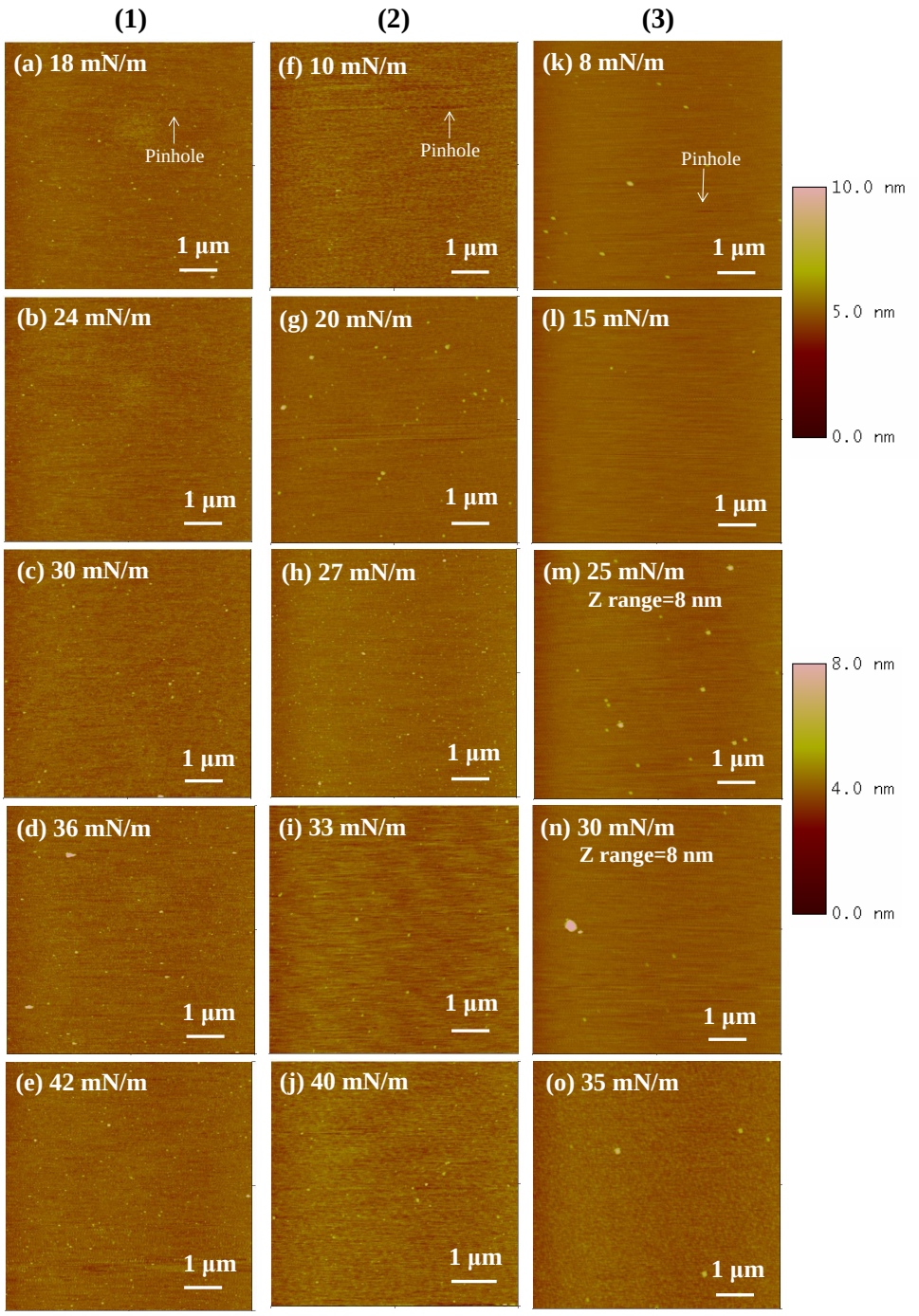

Figure 4.6. AFM images of monolayer films deposited on mica substrates at different surface pressures for complexes **1** (a)-(e), **2** (f)-(j), and complex **3** (k)-(o). The scan size was 5 µm and the Z range was 10 nm unless mentioned.

4.3.7. Langmuir-Blodgett Film Characterization using IRRAS Spectroscopy

Infrared reflection absorption spectra (IRRAS) of LB multilayer films on glass substrates were recorded to evaluate the retention of the molecular composition after their deposition onto solid substrates. During the experiment, 50 layer depositions with transfer ratio close to unity as indicative of near complete transfer onto the surface were carried out using the Y-type dipping method.[147] The IRRAS spectra were recorded using s-polarized light at an angle of incidence 30° for complex **1** and **3**, and at an angle of 40° for complex **2** as shown in **Figure 4.7**. Symmetric and asymmetric C-H stretching vibrations of CH_2 and CH_3 groups were observed ~3000-2800 cm^{-1} and prominent bands ~1600-1300 cm^{-1} were observed due to C=C aromatic stretching and CH_2/CH_3 deformation vibrations for all three complexes. Due to the molecular ordering of the LB film, the prominent bands of the IRRAS spectra showed a slight shift of band positioning compared to its bulk IR spectra along with presence of both upward and downward bands.[132,148] All these factors suggest that the complex has formed an ordered film during the LB film deposition and it remained intact after film deposition. However, for complex **3**, the characteristic band for C≡N stretching at 2040 cm^{-1} observed for bulk IR spectrum was not observed in IRRAS spectrum. Similar observations have been obtained for N_3^- and SCN^- containing complexes with long alkyl chains where the absent C≡N and N≡N vibration bands reappeared in the IR spectrum obtained by the grounded LB films.[149] This limitation is due to the orientation of the molecule during film deposition that resulting the thiocyanato group to be shielded. Further mass analysis was performed on the LB film to confirm the presence of thiocyanato group after film deposition (*vide infra*).

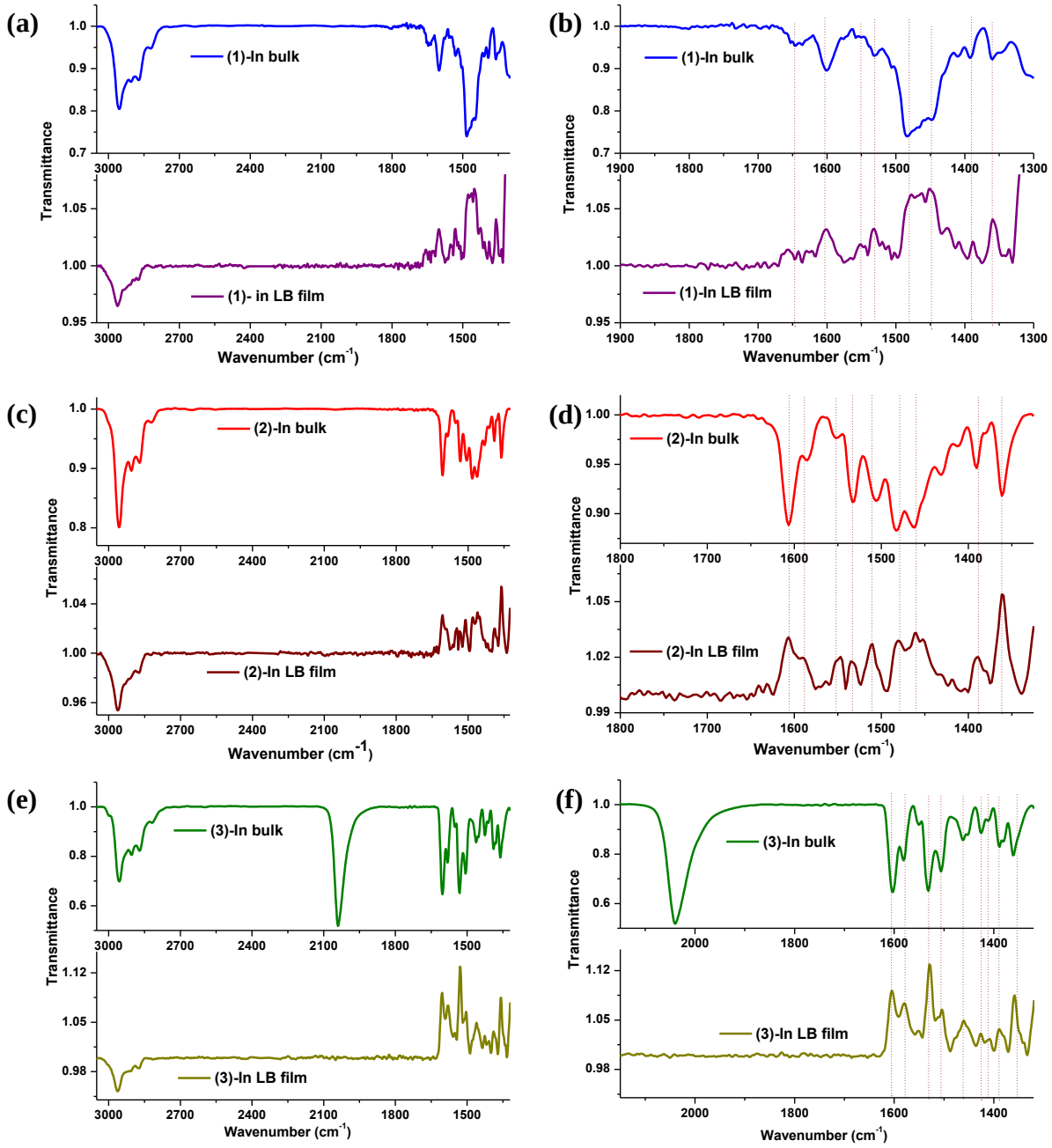

Figure 4.7. Full IRRA spectra (a), (c), (e) and the region between 1300-2200 cm^{-1} (b), (d), (f) for complexes **1**, **2**, and **3** in comparison with their bulk IR spectra.

4.3.8. Langmuir-Blodgett Film Characterization using MAIV Mass Analysis

The presence of SCN^- of complex **3** after the film deposition was analyzed by matrix assisted ionization vacuum (MAIV) mass spectrometry[150] in collaboration with Prof. Trimpin. The LB monolayer of complex **3** was directly introduced to the mass spectrometer using 50 mg of 3-nitrobenzonitrole (3-NBN) matrix in 50 µl of 3:1 acetonitrile:water mixture. The results obtained for the LB monolayer was compared with the results obtained for the bulk sample under similar conditions. The mass spectrum obtained for the monolayer clearly showed the molecular ion peak at (m/z) 800.32 belonging to $[C_{42}H_{58}N_2O_6FeSCN]^+$, which indicated the retention of axial substituent after the film deposition (**Figure 4.8**).

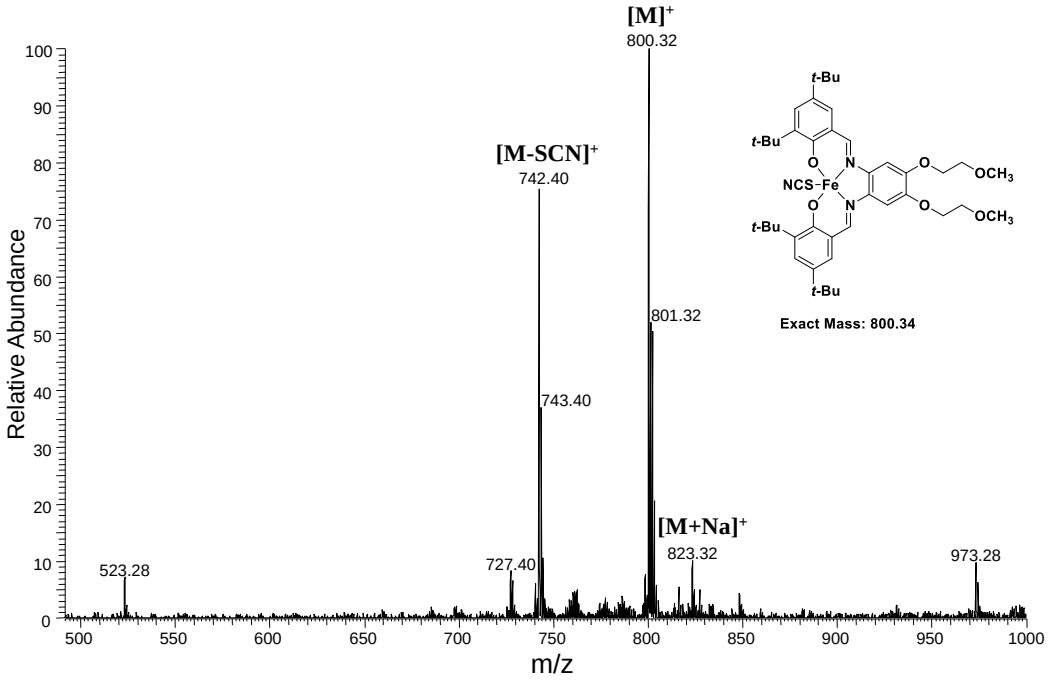

Figure 4.8. The MAIV mass analysis for LB monolayer of complex **3**.

4.3.9. Current Rectification Ability

The current rectification ability of these complexes was investigated by converting the molecular redox potentials obtained from cyclic voltammetry into comparable solid-state potentials using equations 1 and 2.[151]

$$V_a = 4.7\ eV + E_{1/2}^{red}\,(SCE) \qquad (1)$$

$$V_i = 4.7\ eV + (1.7)\ E_{1/2}^{ox}\,(SCE) \qquad (2)$$

The values V_a and V_i are very close to the respective first electron affinity and first ionization energy levels of the molecule supported on the electrodes, and they correlate to the first metal-centered singly occupied molecular orbital (SOMO) and first ligand-centered highest occupied molecular orbital (HOMO). The $E_{1/2}^{ox}$ and $E_{1/2}^{red}$ are the half-wave first oxidation and first reduction potentials versus standard calomel electrode (SCE). The calculated SOMO energies were -4.70, -4.11, -4.22, -4.26 eV for complexes **1**, **2**, **3**, and **4**, respectively, and HOMO energies were -6.33, -6.56, -6.50, -5.90 eV. According to the calculations, the SOMO energy of complex **1** lies 0.4 eV above the gold Fermi energy level where as SOMO energies of complex **2**, **3**, and **4** lie ~0.8 eV above the gold Fermi energy level. The comparison of the frontier molecular orbital energies with the Fermi levels of the gold electrode is shown in **Figure 4.9**. Previous findings have shown that energetically favorable SOMO energies with 1.0 eV difference to gold Fermi energy can transfer electrons without any involvement of HOMO energy, following an asymmetric mechanism.[131] Since the energy difference between SOMO energies and gold Fermi energies are less than 1.0 eV for complexes **1**, **2**, **3**, and **4**, SOMO can be involved in electron transfer facilitating asymmetric electron transfer.

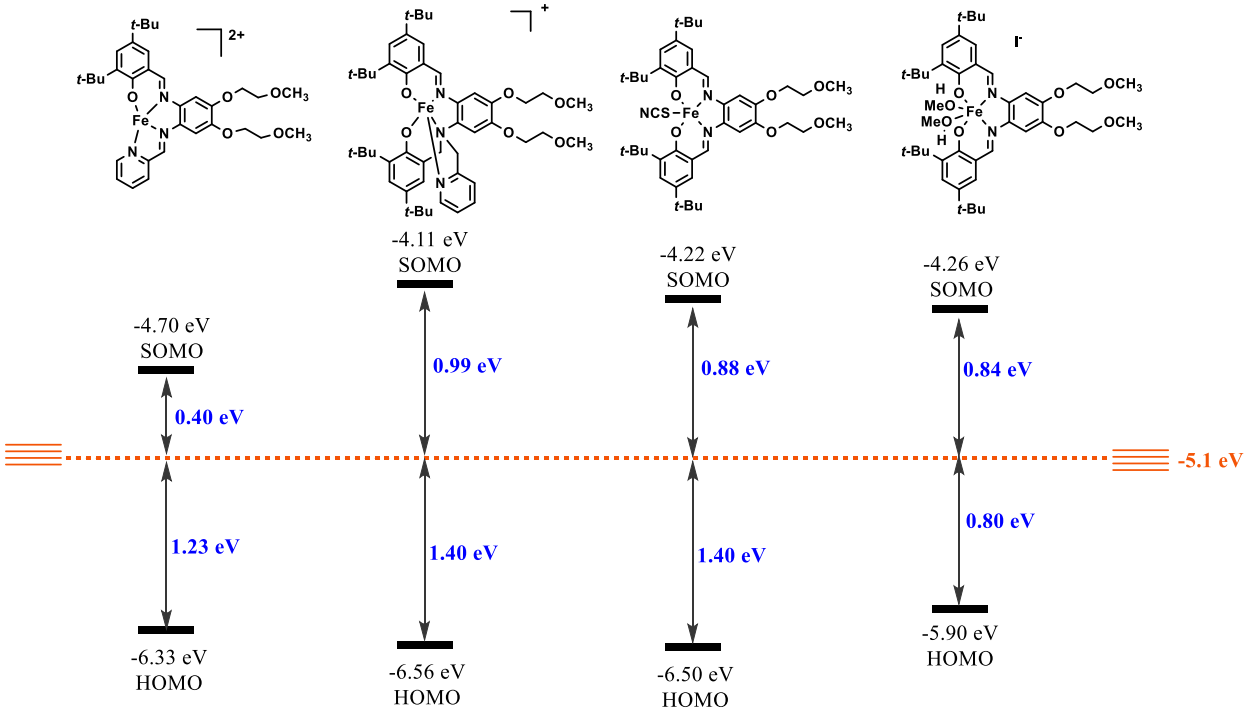

Figure 4.9. Comparison of metal frontier orbital energy levels with the gold electrode Fermi energy levels for complexes **1**, **2**, **3**, and **4**.

The calculated HOMO energies of complexes **1**, **2**, and **3** are situated ~1.4 eV below the gold Fermi energy level making it energetically unavailable for electron transfer. However, the HOMO of complex **4** lies 0.8 eV below the gold Fermi level making it more energetically accessible compared to other complexes. Therefore, the energetically accessible HOMO of complex **4** can also be involved in electron transfer following a unimolecular pathway. Therefore, these molecular designs can be used to develop Au|molecule|Au assemblies to obtain current-voltage measurements which will be done in collaboration with a new graduate student in the group.

4.4. Conclusion

In conclusion, four iron(III) complexes with [N_3O], [N_2O_2], and [N_3O_2] coordination environments were successfully synthesized as precursors for molecular rectification. All complexes showed amphiphilic and homogeneous film formation ability with collapse pressures

of ~46 mN/m for complexes **1**, **2** and ~35 mN/m for complexes **3**, **4**. Theoretical calculations performed using molecular redox potentials suggested that SOMO energies of all four complexes are energetically comparable with gold Fermi energy with energy differences of 0.4 eV for complex **1** and 0.8 eV for complexes **2**, **3**, and **4**. Therefore, all these complexes can be used as potential candidates in molecular current rectification to facilitate unidirectional electron transfer following an asymmetric rectification mechanism. Similarly, lower energy difference between HOMO and gold Fermi level of complex 4, could direct it towards a unimolecular current rectification.

CHAPTER 5 THE USE OF LANGMUIR-BLODGETT METALLOSURFACTANT FILMS AS SURFACE COATINGS FOR CORROSION MITIGATION

5.1. Introduction

Nicknamed the "billion dollar thief" since the 1930's, corrosion has long attracted considerable attention given the serious financial drain from prevention efforts.[152] Corrosion prevention often employs a protective coating, which acts as a barrier between the metal surface and corrosive media. An ideal coating system should have three layers that impede metallic contact with water and other electrolytes.[153] They are surface pretreatment, primer, and top coat. The surface pretreatment coat provides a thin oxide or phosphate layer that affords a smooth surface for the other coatings. The primer is a multilayer coating that provides the bulk of corrosion protection. The top coat allows for color selection and acts as a barrier to radiation and moisture.[154] The development of protective coatings able to mitigate corrosion remains a formidable challenge and current topic in research.

In this regard, homogeneous metallosurfactant films can be employed as barriers to water and electron transfer, involved in the corrosion mechanism. In our research towards designing and understanding new molecular diodes, we have observed that electronic configuration plays a major role in determining the rectification or insulating behavior of metallosurfactants.[155] Therefore, we expect that careful choice of metal and ligand in coating systems will lead to minimize the corrosion rate. In this chapter we describe the use of Langmuir-Blodgett (LB) films of metallosurfactants in corrosion mitigation of 99.5 % iron plates. These plates serve as modules for carbon steel corrosion, as their iron contents allow for an accelerated inspection of the corrosion process. The LB films can provide superior uniform coverage with minute amounts of material, and their thickness can be readily modulated by varying the number of layers.[155b] Herein we hypothesize that 99.5 % iron plates can be functionalized with amphiphilic metal-

salophen complexes using the LB technique to enhance electron passivation. Thus, we expect that multilayers of LB films can be used in corrosion mitigation. To address this hypothesis we have designed and synthesized a series of redox-active amphiphilic [$Fe^{III}(L^{N2O2})Cl$] (**1**), and [$Cu^{II}L^{N2O2}$] (**2**), and [$Zn^{II}(L^{N2O2})H_2O$/MeOH] (**3**) complexes as shown in **Scheme 5.1**.

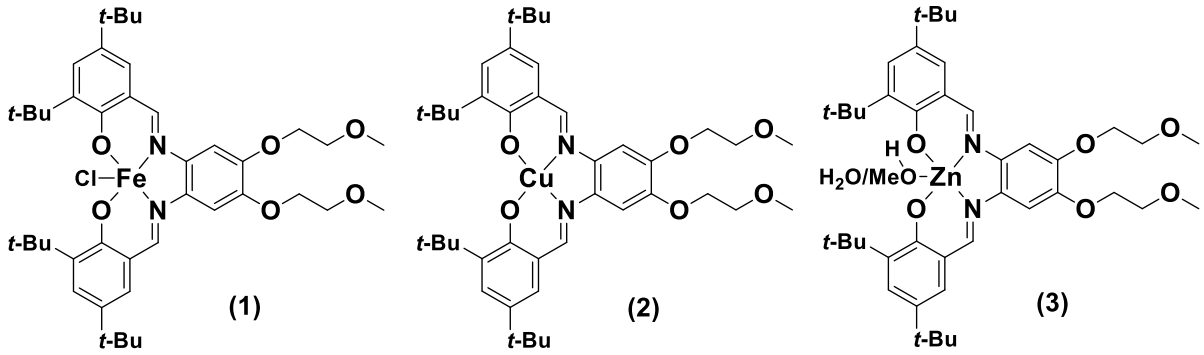

Scheme 5.1. [$Fe^{III}(L^{N2O2})Cl$] (**1**), [$Cu^{II}L^{N2O2}$] (**2**), and [$Zn^{II}(L^{N2O2})H_2O$/MeOH] (**3**) metallosurfactants.

5.2. Experimental Section

5.2.1. Synthesis of the Ligand [H_2L^{N2O2}]

The synthetic procedure of the ligand **[H_2L^{N2O2}]**, *6,6'-(1E,1'E)-(4,5-bis(2-methoxyethoxy)-1,2-phenylene)bis(azan-1-yl-1-ylidene)bis(methan-1-yl-1-ylidene)bis(2,4-di-tert-butylphenol),* has been reported elsewhere.[155a]

5.2.2. Synthesis of Metal Complexes

Synthesis of Complexes [$Fe^{III}(L^{N2O2})Cl$] (1) and [$Cu^{II}L^{N2O2}$] (2)

Synthesis of complexes **1** and **2** were carried out according to previously published procedures.[155a]

Synthesis of Complex [$Zn^{II}(L^{N2O2})H_2O$/MeOH] (3)

Complex **3** was synthesized by treating a methanolic solution of **[H_2L^{N2O2}]** (0.1 g, 0.145 mmol) and $NaOCH_3$ (0.016 g, 0.3 mmol) with zinc chloride under refluxing conditions. Orange

needle-like crystals were isolated for **[$Zn^{II}(L^{N2O2})$ H_2O/MeOH] (3)** from methanol:dichloromethane (3:1) solution. Yield: 80 %. HD-ESI (m/z^+) in CH_3OH = 751.3667 (100 %) for [$C_{42}H_{58}N_2O_6Zn+H^+$] (calculated = 751.3665) in agreement with 0.3 ppm difference. Anal. Calc. for [$C_{42}H_{58}ZnN_2O_6$•0.5H_2O•0.5CH_3OH]: C, 65.67; H, 7.91; N, 3.60 %. Found: C, 65.51; H, 7.84; N, 3.81 %. IR (KBr, cm^{-1}) 2869-2953(ν_{C-H}), 1610 ($\nu_{C=C}$, aromatic), 1503 ($\nu_{C=C}$, aromatic) 1589 ($\nu_{C=N}$), 1265 (ν_{C-O-C}), 1132 (ν_{C-O-C}).

5.2.3. Molecular Structure Analysis

Orange color X-ray quality single crystals of complex **3** were obtained by the slow evaporation of the complex dissolved in a 1:1 dichloromethane:methanol solvent mixture. A suitable crystal was selected and mounted on a mitogen loop, and diffraction data were collected on a Bruker X8 SMART APEX II CCD diffractometer using a monochromatic graphite- Mo Kα radiation source (0.7107 Å) and SMART/SAINT52 software. The crystal was kept at 100.1 K during data collection and a total of 64892 reflections were collected, with 14123 unique reflections. Using the Olex2 structure solution suite,[156] the structure was solved with the ShelXS structure solution program using Direct Methods, and refined with the XL refinement package using Least Squares minimization.[157] Hydrogen atoms were placed in calculated positions. Selected crystallographic data is shown in **Table 5.1**.

	(3)
Formula	$C_{43}H_{62}N_2O_7Zn \cdot C_{42}H_{60}N_2O_7Zn \cdot 2(CH_4O)$
M	1618.69
Temperature/K	100.1
Crystal system	Triclinic
Space group	$P\bar{1}$
a/Å	14.3039 (16)
b/Å	17.603 (2)
c/Å	20.104 (2)
α/°	64.648 (6)
β/°	74.715 (7)
γ/°	86.046 (7)
Volume/Å^3	4407.0 (9)
Z	2
D_{calc} / g cm^{-3}	1.220
μ/ mm^{-1}	0.610
R(F) (%)	8.90
Rw(F) (%)	22.8

[a]$R(F) = \sum \| F_o | - | F_c \| / \sum | F_o |$; $Rw(F) = [\sum w(F_o^2 - F_c^2)^2 / \sum w(F_o^2)^2]^{1/2}$ for $I > 2\sigma(I)$

Table 5.1. Selected X-ray crystal data for complex **3.**

5.3. Results and Discussion

5.3.1. Synthesis and Characterization of Complex 3

The FTIR spectra showed symmetric and asymmetric C-H vibrations around 2869-2953 cm^{-1} and shoulder peak ~1589 cm^{-1} belonging to C=N stretching vibrations. The high resolution ESI-mass spectrometry data showed peak clusters for [M - H_2O/MeOH + H^+] at m/z = 751.3667

(**Figure 5.1**), and CHN elemental analysis showed a good correlation with experimental and theoretical values.

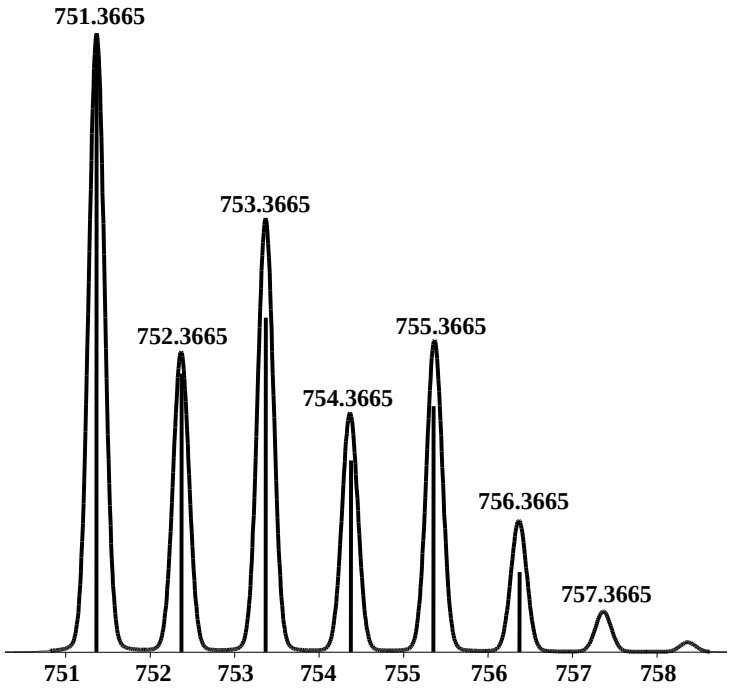

Figure 5.1. Experimental (bars) and simulated (line) isotopic distribution for the molecular ions of $[M\text{-}H_2O+H^+]^+$ for complex **3**.

5.3.2. Molecular Structure

The structure of complexes **2** and **3** were confirmed via crystal structure analysis. Complex **2** showed a square-planar geometry while complex **3** showed a square-pyramidal geometry. Complex **3** showed two independent penta-coordinated complexes with one CH_3OH and H_2O in the axial positions respectively, and two methanol solvent molecules in the asymmetric unit with a tau (τ) value of 0.13, which is consistent with a square pyramidal geometry.[158] The Cu–O, Cu–N, and Zn–O, Zn–N bond lengths are consistent with reported literature values.[159]

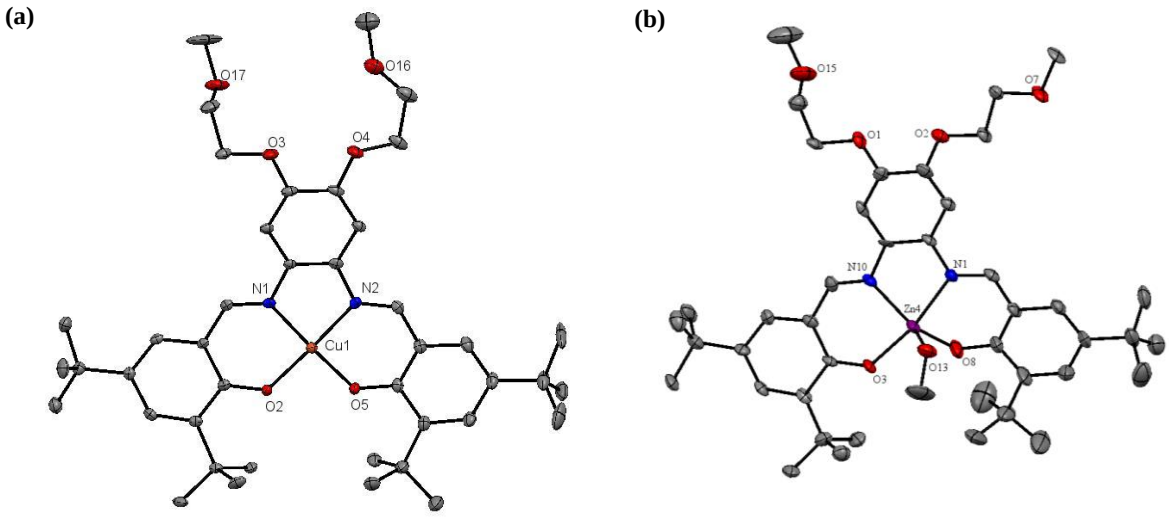

Figure 5.2. The ORTEP representation of (a) complex **2** and (b) complex **3** with CH_3OH as the axial ligand at 50% probability. Hydrogen atoms omitted for clarity.

5.3.3. Electronic Spectral Properties

The UV-visible spectra of **$[H_2L^{N2O2}]$** and the metal complexes **1** and **2** were reported previously.[155a] The spectral properties for complex **2** are discussed in Chapter 3, **Figure 3.2b**. The UV-visible spectrum of complex **2** showed high intensity absorption bands at 250-500 nm region originating due to intraligand $\pi \rightarrow \pi^*$ charge transitions (ILCT) and low intensity band at 550 nm due to d-d transitions.[155a] The UV-visible spectrum of **3** was measured in a 1.0×10^{-5} mol L^{-1} dichloromethane solution. The observed UV-visible spectrum for complexes **3** (**Figure 5.3**) showed intense absorption from 265-495 nm with ε ranging from 8,000-22,500 L mol^{-1} cm^{-1}, with a shoulder peak at 476 nm with ε of 7,500 L mol^{-1} cm^{-1} originating due to intraligand $\pi \rightarrow \pi^*$ charge transfer.[158,160]

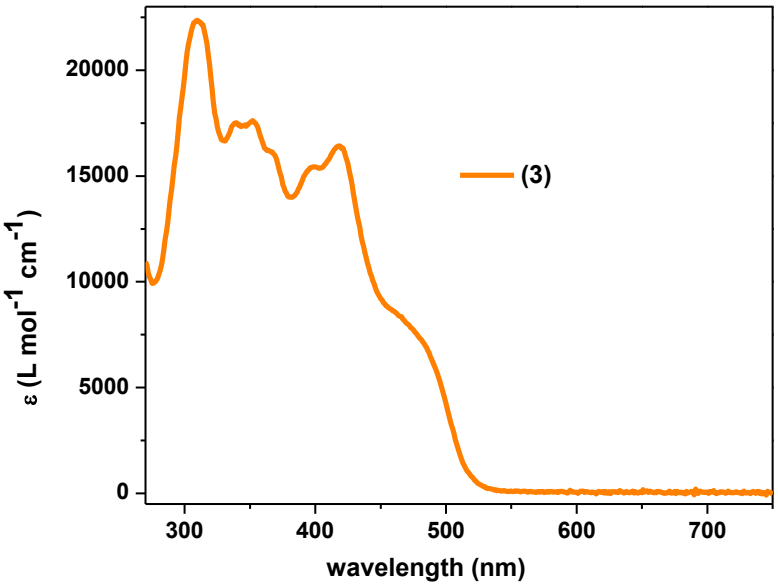

Figure 5.3. The UV-visible spectrum of complex **3** in 1.0 × 10^{-5} mol L^{-1} dichloromethane solution.

5.3.4. Electrochemical Properties

The cyclic voltammograms of complexes **1**, **2**, and **3** were recorded in 1.0 × 10^{-3} mol L^{-1} dichloromethane solution using $TBAPF_6$ as the supporting electrolyte. All potential values were recorded versus the Fc/Fc^+ couple.[161] The cyclic voltammograms for complexes **1** and **2** were reported previously.[155a] Complexes **1** and **2** showed first ligand oxidation processes at 0.64 V and 0.40 V as well as metal reduction processes at -1.02 V and -1.85 V, respectively. On the other hand, as expected for a zinc species, complex **3** showed only ligand-based oxidation processes at 0.224 V (ΔE_p= 0.78 V, $|I_{pa}/I_{pc}|$ = 0.9) and 0.557 V (ΔE_p= 0.16 V, $|I_{pa}/I_{pc}|$ = 1.2) as shown in **Figure 5.4**. The first oxidation is attributed to the formation of a delocalized diiminobenzene π-radical species,[155a,159] while the second oxidation process can be assigned as phenolate/ phenoxyl radical oxidation process.[155a,159,162]

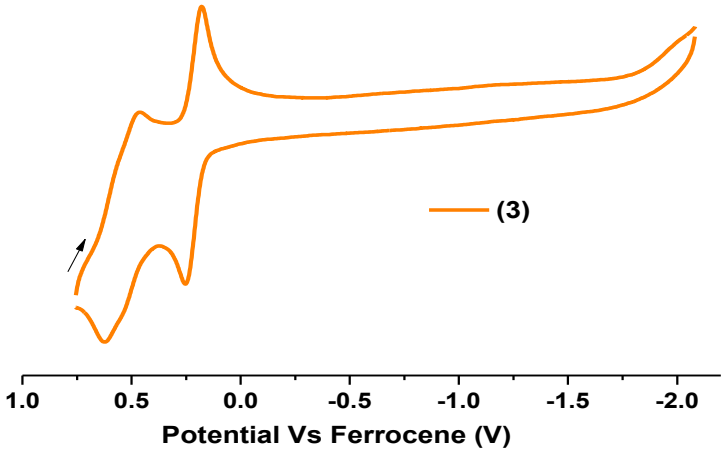

Figure 5.4. Cyclic voltammogram of 1.0×10^{-3} mol L^{-1} solutions of complex **3.**

5.3.5. Isothermal Compression Data

The amphiphilic properties of the complexes were assessed using isothermal compression data and Brewster angle microscopy (BAM) images at 23°C. All the complexes showed a high collapse pressure at ~30-45 mN/m and the isothermal compression data obtained for the complexes **1** and **2** have been previously reported.[155a] The isothermal compression graph for complex **3** is shown in **Figure 5.5** along with BAM images.

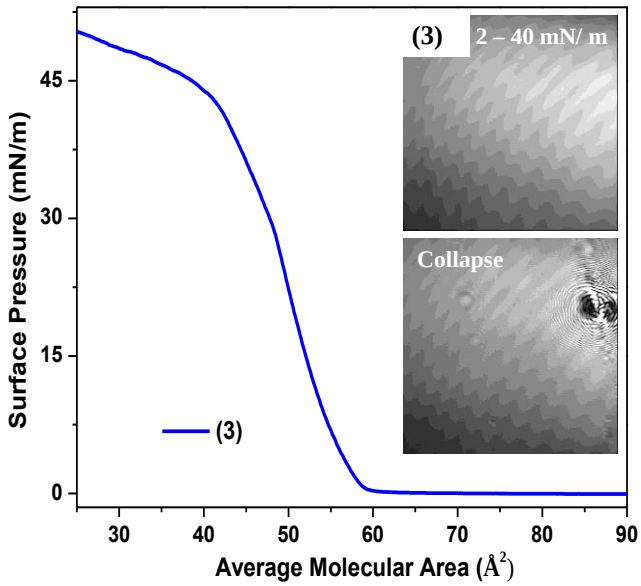

Figure 5.5. Compression isotherm data of complex **3** with selected BAM micrographs.

Complex **3** showed an interaction area of 61 $Å^2$ $molecule^{-1}$ and further compression formed a compact film at the air/water interface with a critical area of 57 $Å^2$ $molecule^{-1}$. Complex **2**, on the other hand, showed an interaction area of 50 $Å^2$ $molecule^{-1}$ and a critical area of 46 $Å^2$ $molecule^{-1}$. No phase transitions were apparent from isotherms obtained between average molecular area *vs*. surface pressure, and collapse pressures of *ca*. 34, 31 and 43 mN/m were respectively observed for complexes **1**, **2**, and **3**.[155a] All the complexes showed a constant pressure collapse,[163] abiding by the Ries mechanism.[164] The BAM images obtained during the LB experiment showed a homogenous film formation at the air/water interface with no defects until the appearance of arrays of Newton rings at the collapse of the Langmuir film.[165]

5.3.6. Surface Characterization Using Atomic Force Microscopy (AFM)

To analyze the surface topology of LB films of the complexes following deposition, AFM analysis was performed for the films deposited on mica substrates at different surface pressures. The deposition transfer ratios were close to unity as indicative of near complete transfer onto the surface and the y-type dipping method was used for all the depositions. The AFM images for complex **1** and **2** have been discussed elsewhere[155a] for complex **3**, monolayers were deposited at room temperature and surface pressures of 15, 20, 25, 30, 35, and 40 mN/m (**Figure 5.6**). According to the AFM images, complex **3** showed a random film deposition with defects at pressures lower than 15 mN/m, along with homogeneous films with fewer defects between 25–30 mN/m. Films deposited at surface pressures higher than 40 mN/m, appeared rougher with aggregate on the film surface, due to multilayer formation from molecular tumbling and film folding that takes place near collapse.

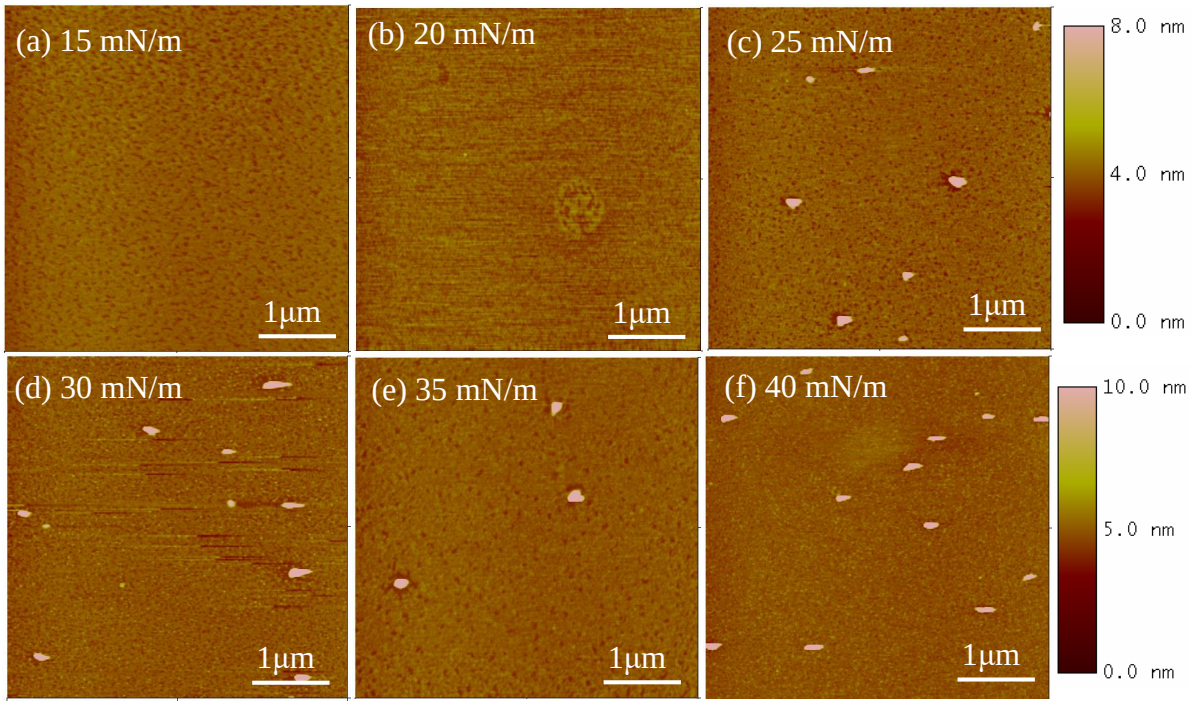

Figure 5.6. AFM images of monolayer films deposited on mica substrates at different surface pressures for complex **3** (a)-(f). Scan size of 5 μm for all images. Some dust particles observed as pink-colored dots.

5.3.7. Langmuir-Blodgett Film Characterization

Infrared reflection absorption spectra (IRRAS) were measured for 25- to 50-layer deposited glass substrates of the complexes **1**, **2**, and **3**. The IRRAS data can be used to predict the composition and ordering of molecules following film deposition.[166] The data were collected using p-polarized light at angles of incidence 30°, 40°, and 20° for complexes **1**, **2**, and **3** respectively. While the IRRAS spectra of **1** and **2** have been previously reported,[155a] the IRRAS spectrum for **3** compared to the FTIR spectrum of the bulk sample in KBr is shown in **Figure 5.7**. All the complexes showed a band ~3000-2800 cm^{-1} which belongs to the symmetric and asymmetric C-H stretching vibrations. In addition, the complexes showed prominent bands ~1600-1300 cm^{-1} due to C=C aromatic stretching and CH_2/CH_3 deformation vibrations, as well as a band ~1585 cm^{-1} belonging to C=N stretching vibrations. Due to the molecular ordering of the LB film, its IRRAS spectrum showed both upward and downward bands.[167] These results

support that the complexes have formed ordered films during the LB film deposition and remained intact after film deposition. However, determination of film orientation by analysis of CH_2 stretching position shift and intensity is limited due of the dominant contributions given by fourteen multidirectional CH_3 groups present in the complexes.

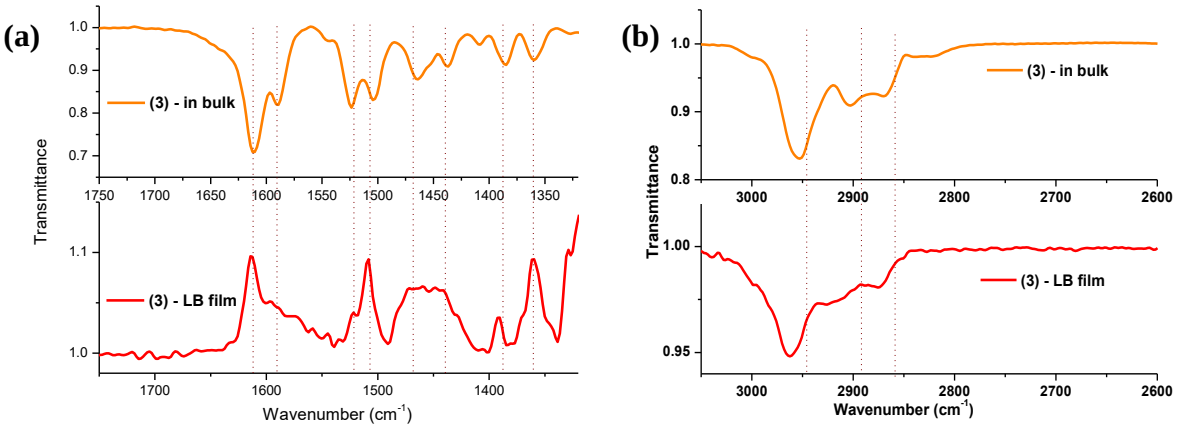

Figure 5.7. IRRAS spectra of (a) complex **3** (b) C-H stretching region in comparison with KBr in bulk infrared spectra.

An optical contact angle meter was used to evaluate the surface wettability of **1**, **2**, and **3** on carbon steel plates. Upon LB film formation, the contact angle of the bare steel increased from 81° to 100° (**1**), 95° (**2**), and 94° (**3**), confirming the LB films can enhance the hydrophobic nature of the surface and deflect water and moisture.

5.3.8. Electron Passivation by Langmuir-Blodgett Films

In order to investigate the electron passivation of the LB films of **1-3**, cyclic voltammetry was performed in 1 mM $K_3[Fe(CN)_6]$ and 0.1 M KCl aqueous solution at room temperature.[168] A three-electrode system was used: gold plates coated with LB films were used as the working electrode, Ag/AgCl and a Pt wire were used as the reference and auxiliary electrodes respectively. The $[Fe^{III}(CN)_6]^{3-}/[Fe^{II}(CN)_6]^{4-}$ process obtained for the bare gold electrode was compared with the $[Fe^{III}(CN)_6]^{3-}/[Fe^{II}(CN)_6]^{4-}$ process obtained for LB film-coated gold electrodes.

Electron passivation increased with an increasing number of layers. Optimal passivation was observed for 11-layers deposited electrodes. As illustrated in **Figure 5.8**, between the three complexes, **1** and **3** showed better passivation for 11 layers compared to **2**. Geometric differences between complexes **1** and **3** (square pyramidal) and complex **2** (square planar) can result in different packing during LB film formation, which could contribute to the passivation disparity. On the other hand, ligand showed higher current consumption for 11-layer deposited electrodes compared to complex coated electrodes, indicating the enhancement of passivation by metal (**Figure 5.8d**).

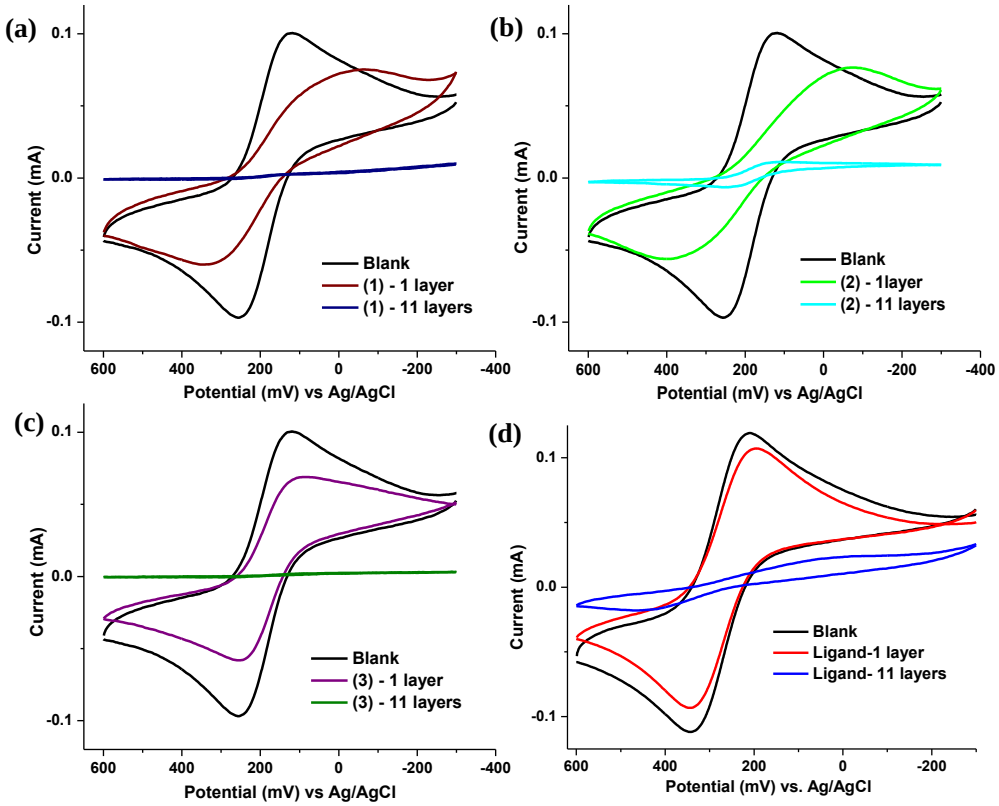

Figure 5.8. Cyclic voltammograms obtained for the passivation of gold electrode using different number of LB films of complexes **1**, **2**, and **3** and the ligand.

To assess prolonged stability in acidic medium, 11-layer deposited gold plates were immersed in 0.01 M sulfuric acid solution for five days. The cyclic voltammetry experiment was

repeated after this period. The cyclic voltammograms obtained for the immersed electrodes correlate well to the cyclic voltammograms obtained for the original electrodes (**Figure 5.9**). This indicates that there is no major degradation of the complex in acidic medium. However, the $[Fe^{III}(CN)_6]^{3-}/[Fe^{II}(CN)_6]^{4-}$ redox-process obtained for the immersed ligand-coated electrode displayed an increase in the observed current to 0.06 mA, suggesting that the ligand is likely being degraded in acidic media (**Figure 5.9d**).

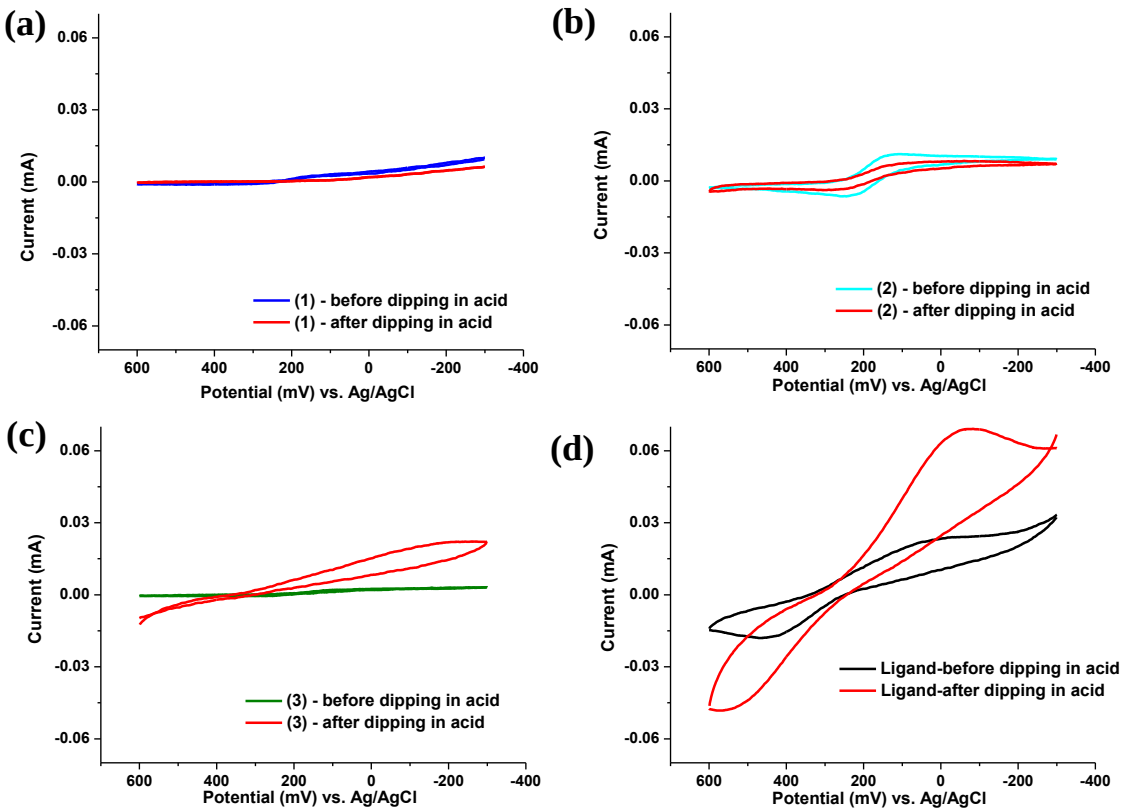

Figure 5.9. Cyclic voltammograms obtained for the passivation of 11-layer deposited gold electrodes of complexes **1**, **2**, **3**, and the ligand before and after immersing in acid solution for 5 days.

5.3.9. Agar Analysis to Study the Corrosion Rate

Marine and acidic corrosion are particularly relevant to iron surfaces. The effect of coatings on the rate of iron corrosion was investigated by covering approximately one half of three iron plates (99.5 % purity; 8 x 25 mm) with respective metal complexes **1**, **2**, and **3** to

provide qualitative information on corrosion rate. The complex-coated iron plates were immersed in agar gel containing 3% sodium chloride, 2% phenolphthalein, and 0.1 M $K_3Fe(CN)_6$ solution. In this system, the NaCl-enriched agar gel provides an electrolytically conducting medium, thus mimicking a marine environment, while $K_3Fe(CN)_6$ and phenolphthalein act as chemical indicators for anodic and cathodic reactions respectively. The $K_3Fe(CN)_6$ can form a Prussian blue complex in the presence of Fe^{2+} ions, while phenolphthalein turns pink in presence of OH^- ions. The complex-coated carbon steel plates were immersed in this agar gel and observed over the course of seven days (**Figure 5.10**). No blue coloration was observed in the complex-coated region of the iron plate after seven days. This indicates that the complexes can decrease the rate of iron corrosion in saline medium.

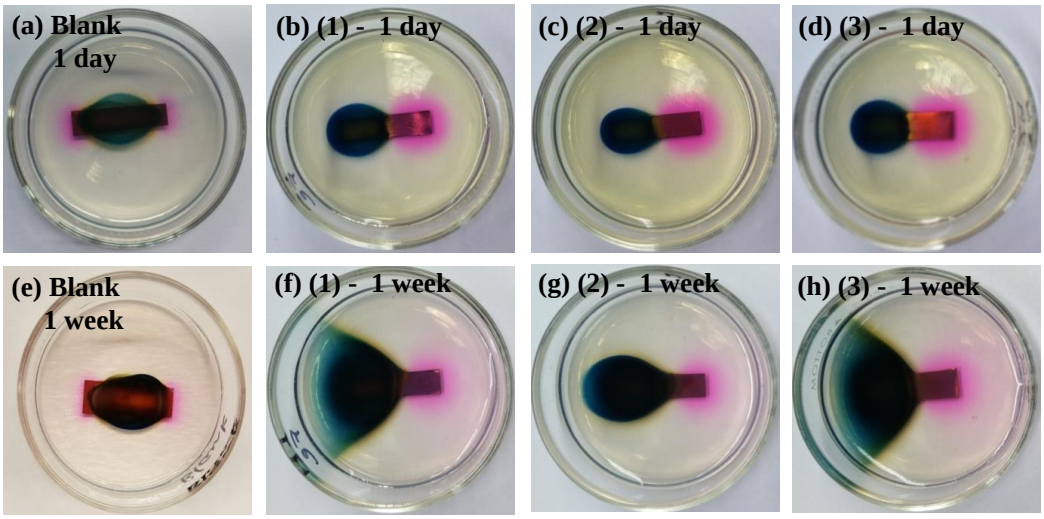

Figure 5.10. Images for saline corrosion using carbon steel plates coated with complexes **1**, **2**, and **3** (a)-(d) after one day and (e)-(h) after seven days.

Similarly, acid corrosion was simulated using an agar medium containing 0.01 M H_2SO_4, 2% phenolphthalein, and 0.1 M $K_3Fe(CN)_6$ solution. A faint pink coloration was observed in the cathodic region due to the acidic nature of the medium. However, as with saline corrosion, no blue coloration was observed in the coated region after seven days (**Figure 5.11**), thus indicating

a considerable corrosion rate reduction in acidic medium. It is expected that the corrosion rate to be increased for iron metal in presence of acidic or marine environment.[153]

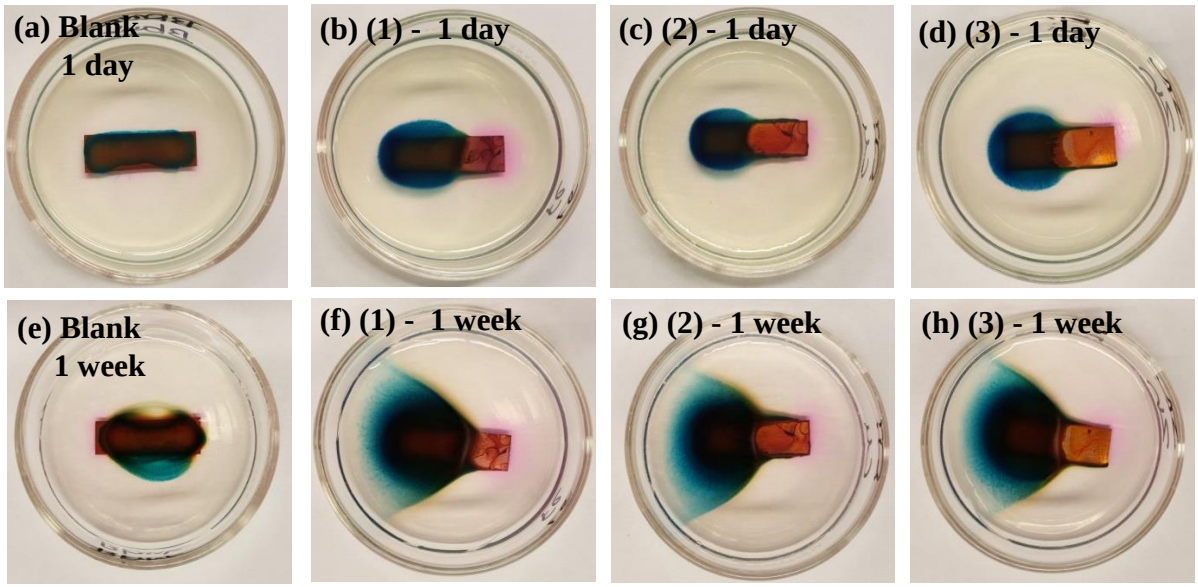

Figure 5.11. Images for acid corrosion using iron plates coated with complexes **1**, **2**, and **3** (a)-(d) after one day and (e)-(h) after seven days.

5.3.10. Surface Analysis of Corroded Samples

Optical micrographs and scanning electron micrographs (SEM) were used to evaluate rust formation on the iron plates immersed in 0.01 M H_2SO_4 and 0.1 M NaCl solution for 5 days. Visible rust formation was observed only for acidic corrosion; iron plates were dissolved in saline corrosion. Images obtained for the samples before corrosion showed the rougher surface of the iron plate. Acid corrosion resulted in extensive rust formation on the blank carbon steel plates compared to the LB film-coated carbon steel plates, as shown in **Figure 5.12**. However, no clear differences in rust formation were observed between coated plates except agglomerate formation on **2**- and **3**-coated plates.

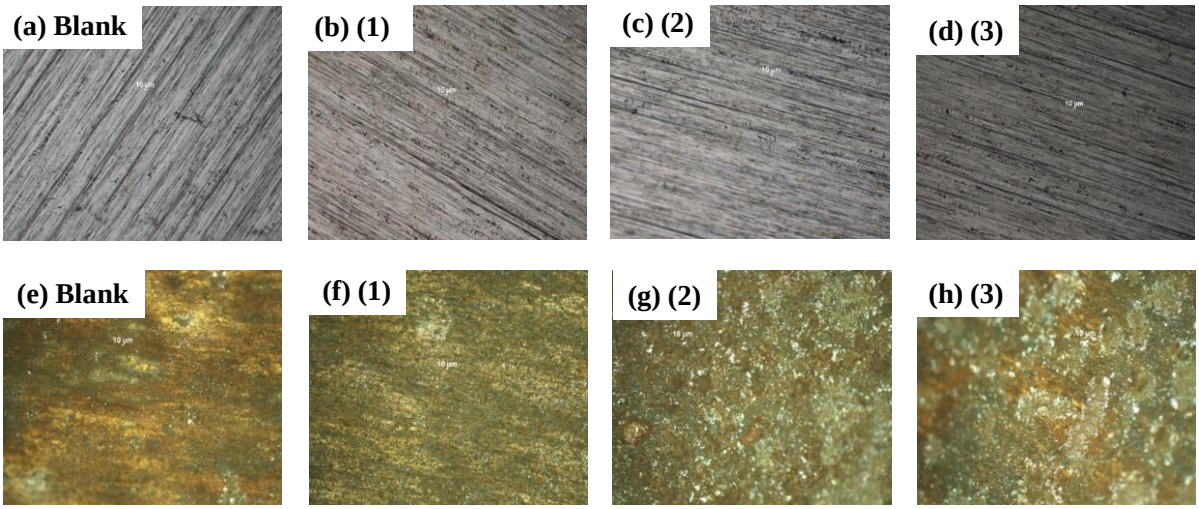

Figure 5.12. Optical micrograph images for blank and 11-layer LB film-coated carbon steel plates (a)-(d) before corrosion, and (e)-(h) after acid corrosion.

Further surface analyses were performed using SEM images. Rougher surfaces on the carbon steel plates were observed in images obtained before corrosion (**Figure 5.13a-d**). Extensive rust formation was observed for the blank carbon steel plates compared to 11-layer deposited plates after acid corrosion (**Figure 5.13e-h**). A rougher surface was observed for the blank carbon steel plate compared to 11-layer deposited plate after saline corrosion since the plates were dissolving without any rust formation (**Figure 5.13i-l**).

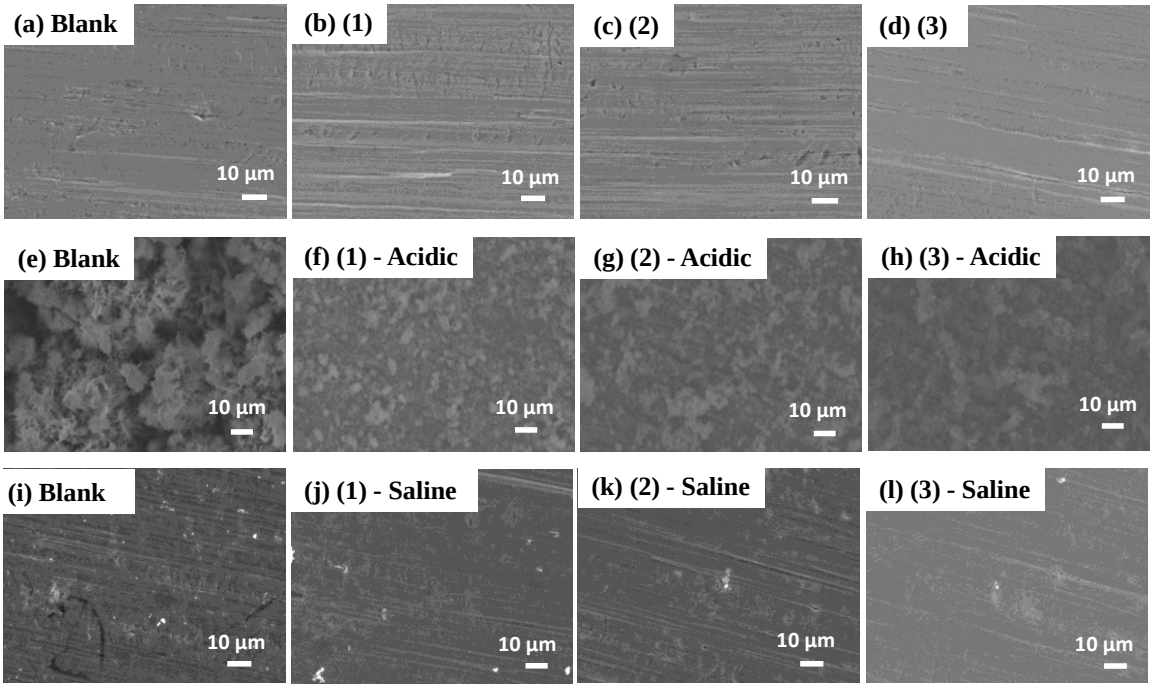

Figure 5.13. The SEM images for blank and 11-layer LB film-coated carbon steel plates (a)-(d) before corrosion, (e)-(h) after acidic corrosion, and (i)-(l) after saline corrosion.

5.3.11. Weight Loss Measurements

Weight loss measurements were calculated to compare the mean corrosion rate (*r*) and inhibition efficiency (IE %) of the 11-layer deposited iron plates of ligand and complexes **1**, **2**, and **3** with respect to the blank. The values of *r* and IE % were calculated based on equations 1 and 2.[169]

$$r = (m_1 - m_2) / S.t \qquad (1)$$

$$\text{IE\%} = (r^{\circ} - r) / r^{\circ} \times 100 \qquad (2)$$

(1) Where m_1 and m_2 are the mass of carbon steel plates before and after immersion in acid solution, respectively; *S* is the area immersed of the carbon steel plate; *t* is the immersion time.

(2) Where r° and *r* are the mean corrosion rates of the samples in the respective absence and presence of the coated inhibitor.

The blank and LB film coated plates were immersed in 0.01 M sulfuric acid for 8 days and in 0.1 M sodium chloride solution for 5 days at room temperature. Then the specimens were removed from corrosive solutions, rinsed with ultrapure water, rust was removed by gentle abrasion using steel wool, dried, and weighed. The average weight loss was used to calculate the mean corrosion rate from three trials. In acidic medium, complex **3** demonstrated the highest corrosion mitigation efficiency of 30.4 % and lowest mean corrosion rate of 0.0518 mg cm^{-2} h^{-1}. Complexes **1** and **2** showed respective acidic corrosion mitigation efficiencies of 26.6 % and 19.2 % and mean corrosion rates of 0.0556 and 0.0610 mg cm^{-2} h^{-1}. The average corrosion rate for the blank was 0.0752 mg cm^{-2} h^{-1}. The ligand showed the lowest corrosion mitigation efficiency of 6.7 %. Complex **3** also exhibited the highest corrosion mitigation efficiency of 23.4 % and lowest mean corrosion rate of 0.0355 mg cm^{-2} h^{-1} for saline corrosion. Complexes **1** and **2** showed respective saline corrosion mitigation efficiencies of 16.5 % and 6.7 % and mean corrosion rates of 0.0385 and 0.0424 mg cm^{-2} h^{-1}. These observations are in agreement with the results obtained for passivation analysis and suggest that the presence of a metal ion enhances the corrosion mitigation ability of the LB films. Furthermore, the presence of Zn(II) ion can provide the best corrosion mitigation ability since Zn is a redox-inert species. Therefore, LB films formed using complex **3** can function as a passive barrier to electron flow, which will result in the best mitigation for both acidic and saline corrosion.

5.4. Conclusion

In conclusion, iron plates can be functionalized using LB technique with salophen-based iron(III), copper(II), and nickel(II) metallosurfactants. Cyclic voltammetry experiments performed using 1- to 11-layer coated gold plates reveal that 11-layer LB films formed with these complexes can passivate electron transfer to the iron plate surface. Furthermore, the

complexes remain viable after prolonged immersion in acidic solution. Optical micrograph images, SEM images, and agar analyses confirm that coatings of all three complexes can decrease acidic and saline corrosion rates. Weight loss measurement studies show that 11-layer depositions of complex **3** demonstrate superior corrosion mitigation, with inhibition efficiencies up to 30% for acidic and 23% for saline solution.

CHAPTER 6 HETEROGENEOUS CATALYTIC ACTIVITY OF A NOVEL COBALT(III) TRIS-PHENOLATE COMPLEX TOWARDS WATER OXIDATION

Portions of the text in this chapter were reprinted from: Gonawala, S.; Baydoun, H.; Verani, C. N. *Chem. Commun.* Submitted.

6.1. Introduction

The splitting of water into hydrogen and oxygen is an accepted alternative way to harvest renewable energy.[170] The process requires multiple electron and proton transfers and is divided into water oxidation and proton reduction.[171] Efficient water oxidation has been achieved with ruthenium- and iridium-based catalysts.[172] However, the scarcity of these metals limits the transition from solution-based to heterogeneous catalysis expected to foster widespread application of water splitting technologies. In an effort to resolve this issue, recent research has focused on developing homogeneous catalysts based on Earth-abundant metals capable of driving water oxidation,[173-177] and enabling the anchoring of such molecular species onto conductive substrates to obtain heterogeneous catalytic electrodes. The main functionalization methods rely either on chemisorption or physisorption. While the former relies on direct covalent bonding between the catalyst and the substrate,[178] the latter relies exclusively on catalyst adsorption to the surface of the electrode.[179] Physisorption is advantageous because it allows for the optimization of ultrathin and highly organized catalytic surfaces by means of ligand design.

Our group has shown that phenolate-rich $[Co^{III}(L^{N2O3})H_2O]$ systems are catalytic towards proton reduction,[180] and this observation prompted us to consider water oxidation. Structurally related $[Co^{II}(N_2O_2)]$ complexes are known as molecular photocatalysts,[181] and have been used as procatalysts for electrodeposited films capable of water oxidation.[182] However, the water insolubility of our previously reported Co^{III}/N_2O_3 species led us to think about alternative approaches. In this chapter, we describe a novel application of Langmuir-Blodgett (LB) films

using molecular procatalysts to attain heterogeneous water oxidation. Besides providing superior uniform coverage with minute amounts of material, the LB method provides direct control over the thickness of the deposited films by varying the number of layers.[183] Over the years we have developed redox-active metallosurfactants aiming at molecular diodes,[183,184] molecular displays,[185] and other high-end applications.[186]

Herein we hypothesize that conductive substrates can be functionalized with amphiphilic molecular procatalysts via the LB method to drive heterogeneous water oxidation. Furthermore, we also hypothesize that we can modify the activity of the final catalytic film by altering the number of deposited LB layers. Thus, the aim of this work is to report on a novel method for the preparation of catalytic films relying on minute amounts of a procatalyst and yielding high dioxygen production. To the best of our knowledge, this is the first application of LB films as water oxidation catalysts. Development of such methodology moves the field away from solution chemistry and towards heterogeneous systems that enable the up-scaling of such systems. We have designed a new redox-active, amphiphilic **[$Co^{III}(L^{N2O3})H_2O$]** complex shown in **Scheme 6.1**.

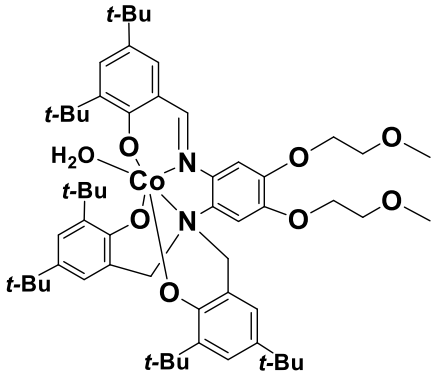

Scheme 6.1. The [$Co^{III}(L^{N2O3})H_2O$] metallosurfactant.

6.2. Experimental Section

6.2.1. Synthesis of the Ligand [H_2L^{N2O3}]

The ligand **[H_2L^{N2O3}]**, *(6,6'-(2-(3,5-di-tert-butyl-2-hydroxybenzylamino)-4,5-bis(2-methoxyethoxy)phenylazanediyl)bis(methylene)bis(2,4-di-tert-butylphenol),* was synthesized according to a previously published procedure.[183]

6.2.2. Synthesis of the Cobalt(III) Complex [$Co^{III}(L^{N2O3})H_2O$]

A methanol:dichloromethane 1:3 solution of **[H_2L^{N2O3}]** (1 equivalent) and anhydrous $NaOCH_3$ (3 equivalent) in was treated with a methanolic solution of $[Co^{II}(H_2O)_6](ClO_4)_2$ (1 equivalent). The resulting solution was kept under mild reflux for 2 h after which a reddish brown precipitate was obtained via the slow evaporation of the parent solution. Yield: 85 % ESI (m/z^+) in CH_3OH = 965.5454 (100 %) for $[C_{57}H_{81}N_2O_7Co+H^+]$ Anal. Calc. for $[C_{57}H_{83}CoN_2O_8.2H_2O]$: C, 67.17; H, 8.60; N, 2.75 % Found: C, 67.01; H, 8.48; N, 3.05 % IR (KBr, cm^{-1}): 2869-2954 (ν_{C-H}), 1613 ($\nu_{C=C}$, aromatic) 1592 ($\nu_{C=N}$), 1510 ($\nu_{C=C}$, aromatic), 1256 (ν_{C-O-C}), 1128 (ν_{C-O-C}).

6.3. Results and Discussion

6.3.1. Synthesis and Characterization of Cobalt(III) Complex

The complex **[$Co^{III}(L^{N2O3})H_2O$]** was characterized by ESI-mass spectrometry, elemental analysis, IR and UV-visible spectroscopic methods. The ESI-mass spectrometry data showed peak clusters for $[M\text{-}H2O+H^+]^+$ at m/z = 965.5468 and CHN elemental analysis showed good agreement between experimental and theoretical values. During the metallation, the ligand is oxidized from amine to imine and cobalt(II) is oxidized to cobalt(III). We have investigated this oxidation in detail for both Fe and Co complexes.[180,183,187]

6.3.2. Electronic Spectral Properties

The electronic spectra of ligand and complex were measured in 1 × 10^{-5} M dichloromethane solutions. The spectrum obtained for the **[$Co^{III}(L^{N2O3})H_2O$]** complex showed charge transfer absorptions in the region of 300–800 nm as shown in **Figure 6.1**. The absorptions observed below 400 nm are associated with intra ligand charge transfer (ILCT) processes. The two ill-solved bands observed at 405 nm and 480 nm are due phenolate to azomethine intra-ligand charge transfer and ligand to metal charge transfer originating from phenolate in-plane pπ to Co(III) dσ* respectively. Lower energy absorptions observed around 600-800 nm are associated with ligand to metal charge transfer (LMCT) transitions originating from out of-plane phenolate pπ to Co(III) dσ*.[180]

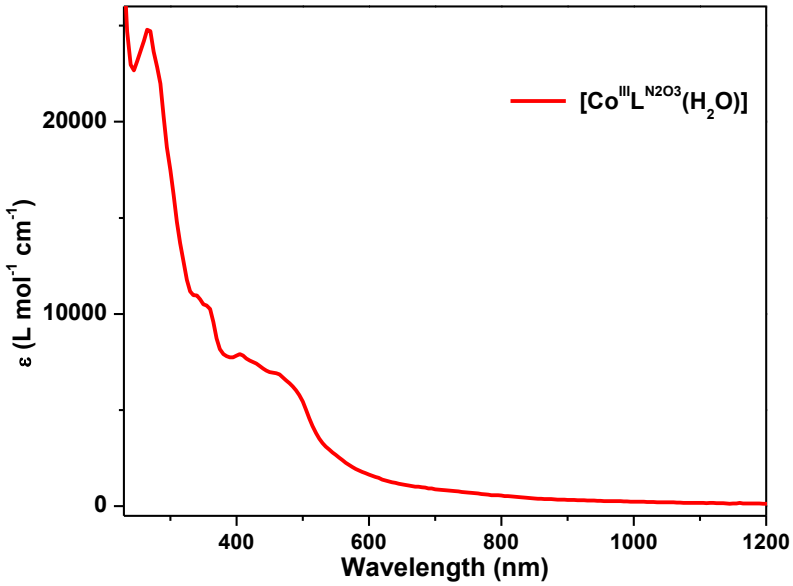

Figure 6.1. UV-visible spectrum of **[$Co^{III}(L^{N2O3})H_2O$]** in 1.0×10^{-5} mol L^{-1} dichloromethane solution.

6.3.3. Electrochemical Properties

The cyclic voltammogram of **[$Co^{III}(L^{N2O3})H_2O$]** in dichloromethane reveals both ligand- and metal-based redox processes (**Figure 6.2**). Tetrabutylammonium hexafluorophosphate

($TBAPF_6$) was used as the supporting electrolyte and ferrocene was added to the solution as an internal redox standard.[188] Potential values were recorded with reference to the experimental Fc/Fc^+ value. A cathodic process at -0.62 $V_{Fc/Fc+}$ (ΔEp = 0.09 V, $|I_{pa}/I_{pc}|$ = 1.4) is attributed to the Co^{III}/Co^{II} redox couple,[180,189] while three anodic processes at 0.18 $V_{Fc/Fc+}$ (ΔEp = 0.09 V, $|I_{pa}/I_{pc}|$ = 0.7), 0.60 $V_{Fc/Fc+}$ (ΔEp = 0.10 V, $|I_{pa}/I_{pc}|$ = 1.7), and 1.0 $V_{Fc/Fc+}$ respectively are attributed to successive phenolate/phenoxyl oxidation processes.[180,187a] The first two processes are quasi-reversible, and the third is ill-defined.

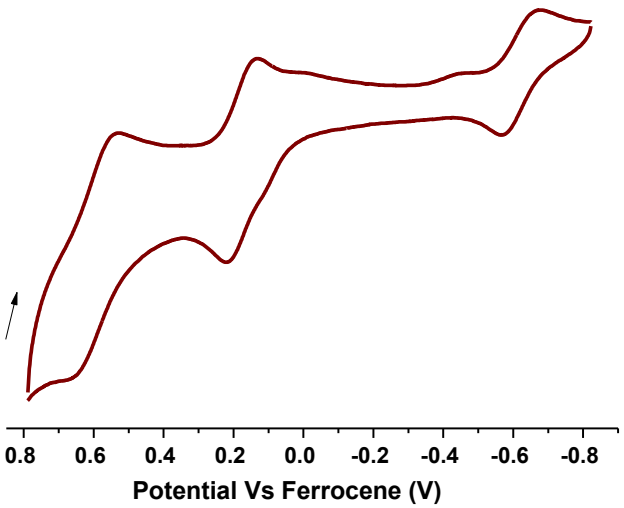

Figure 6.2. Cyclic voltammogram of complex **$[Co^{III}(L^{N2O3})H_2O]$** in dichloromethane.

6.3.4. Isothermal Compression Data

The amphiphilic behavior of **$[Co^{III}(L^{N2O3})H_2O]$** was determined by isothermal compression and by Brewster angle microscopy (BAM) at 23 ◦C (**Figure 6.3**). With increasing surface pressure, intramolecular interaction starts with an area of *ca.* 97 $Å^2$/molecule and further compression results in a homogenous film between ca. 10-40 mN/m with a critical area of 88 $Å^2$/molecule. No obvious phase transitions were recorded and a Ries-like constant pressure collapse,[190] similar to other metallosurfactants,[183,184,191] was observed at *ca.* 42 mN/m. The BAM

micrographs obtained during compression confirm a homogeneous film formation from 10-40 mN/m, when at 42 mN/m, collapse of the LB film appeared as indicated by the appearance of Newton rings.

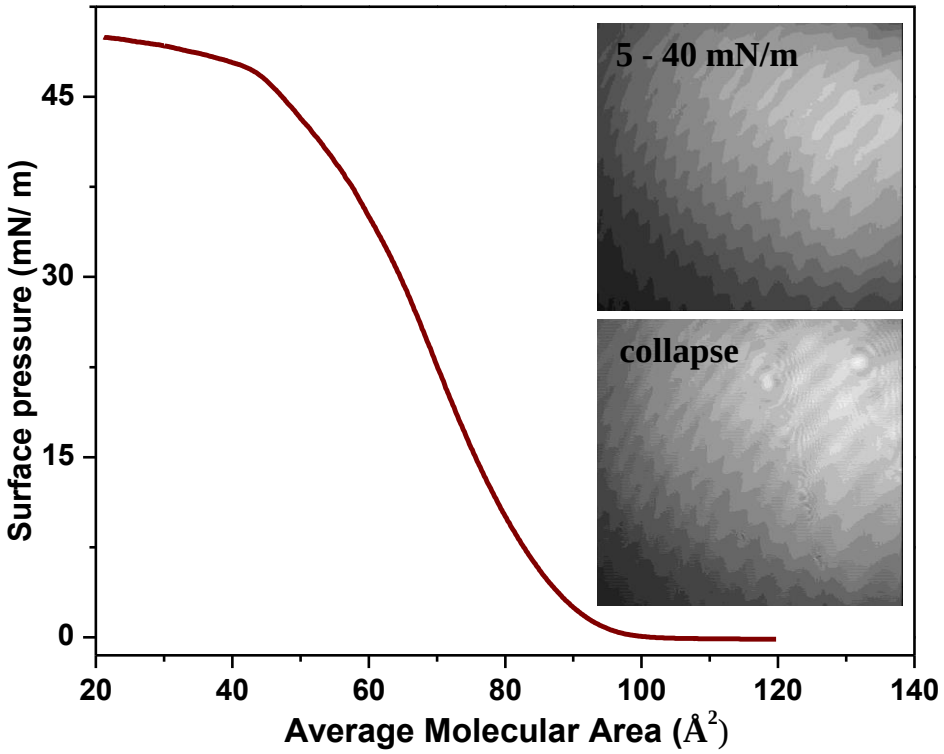

Figure 6.3. Compression isotherm for complex **[$Co^{III}(L^{N2O3})H_2O$]** and selected BAM micrographs.

6.3.5. Surface Characterization Using Atomic Force Microscopy (AFM)

The surface topology of the LB films deposited on mica substrates at different surface pressures was analyzed using AFM measurements in order to optimize deposition pressure. The monolayers were deposited at 8, 15, 22, 30, 35, 40 mN/m with a transfer ratio close to 1 (**Figure 6.4**). Films deposited at lower surface pressures showed higher frequency of pinholes while monolayers deposited at 30 and 35 mN/m show more homogeneous film formation. Films deposited at surface pressures closer to collapse showed formation of aggregates.

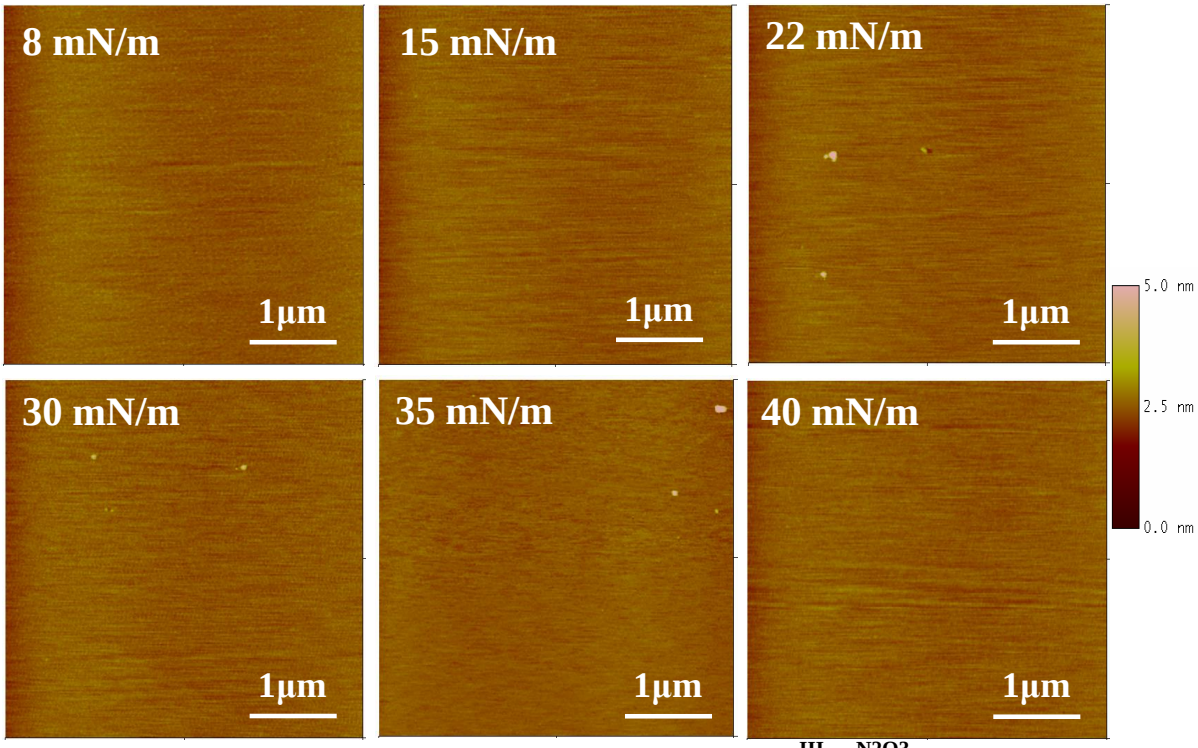

Figure 6.4. Surface morphology of monolayer films of **[$Co^{III}(L^{N2O3})H_2O$]** deposited on mica substrates at different surface pressures with 5 µm scan size.

6.3.6. Langmuir-Blodgett Film Characterization using IRRAS Spectroscopy

Maintenance of composition in the deposited film was verified via infrared reflection absorption spectroscopy (IRRAS) using a 50-layer film of **[$Co^{III}(L^{N2O3})H_2O$]** deposited on glass substrate at an angle of 40° under *s*-polarized light.[192] The IRRAS spectrum for the compound is shown in **Figure 6.5** in comparison to its bulk KBr IR spectrum. The IRRAS data is rather similar to its bulk IR spectrum with only slight band shifts typical of enhanced ordering, and confirms unchanged composition after deposition.

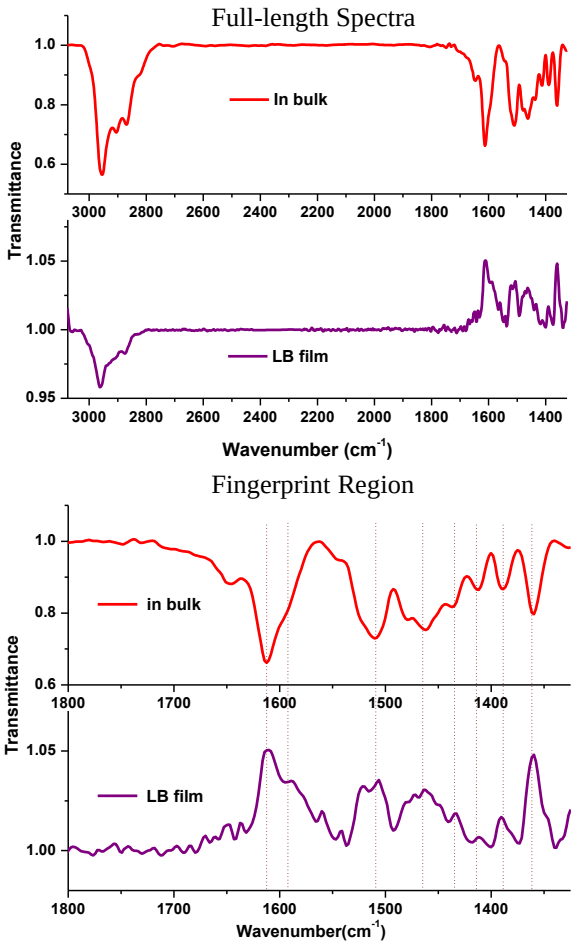

Figure 6.5. The comparison of the IR spectrum in KBr and IRRAS spectra of a 50 layer LB film.

Bands associated with symmetric and asymmetric C-H stretching vibrations were observed at 2962, 2903, and 2874 cm^{-1} (**Figure 6.6**) while bands due to aromatic C=C and C=N stretching, and CH_2/CH_3 deformations are observed in the region of ~1614-1360 cm^{-1}. Molecular ordering of the LB film is further verified by the presence of both upward and downward bands in the region of 1614-1360 cm^{-1} and 2960-2874 cm^{-1} of the IRRAS spectrum.[183,184] Nonetheless, determination of film orientation by analyzing the CH_2 vibration intensities is limited due to the presence of 18 multidirectional CH_3 groups.[183,192a,193]

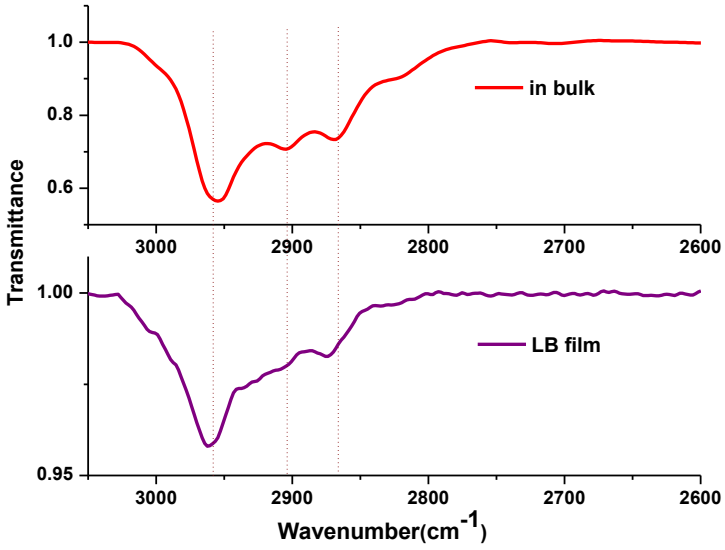

Figure 6.6. IRRAS spectrum of 50 layers deposited glass substrate of CH_n stretching region compared to its bulk infrared spectrum.

Previous contact angle measurements on the monolayer of a structurally similar [$Fe^{III}L^{N2O3}$] metallosurfactant indicate that the hydrophillic alkoxy groups attach to the glass substrate while the hydrophobic *t-butyl* groups point outwards.[183]

6.3.7. Catalytic Activity of the Langmuir-Blodgett Film

The catalytic activity of the film towards water oxidation was verified in presence of sodium borate solution (pH 11, 0.1 M). The CV of FTO plates with [$Co^{III}(L^{N2O3})H_2O$] LB monolayers showed a catalytic wave at an onset overpotential of 0.5 V (**Figure 6.7a**). In order to verify the involvement of the cobalt center with catalysis, an analogous experiment was performed using [$Ga^{III}L^{N2O3}$] (**Figure 6.7b**). The absence of a catalytic wave in the gallium-based film verifies the need of the cobalt metal for catalysis. Bulk electrolysis using electrodes with 1-13 deposited layers were performed at an applied potential of 1.2 V in pH 11, and 0.1 M sodium borate solution for 1 h.

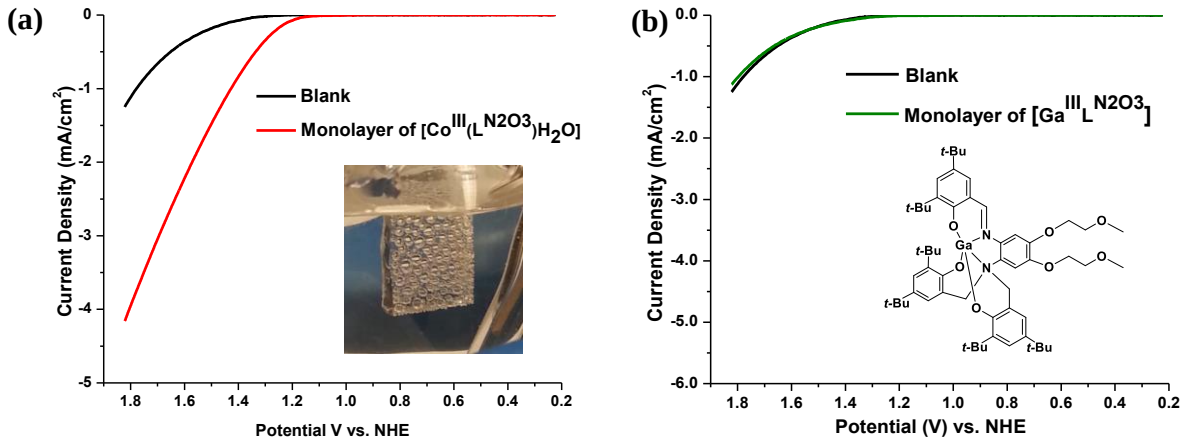

Figure 6.7. Polarization curves for catalytic activity of (a) $[Co^{III}(L^{N2O3})H_2O]$ (Inset: O_2 bubbles generated on the electrode surface) and (b) $[Ga^{III}L^{N2O3}]$ on an FTO electrode at pH 11.

The charge consumed by the catalytic films during water oxidation is shown in **Figure 6.8a**. Bubbles observed on the electrode were further confirmed to be dioxygen using gas chromatography. A direct correlation between the number of layers and charge consumption was observed incrementally up to 9 layers. Absent or marginal increase was observed for films with more layers. This implies that 9 layers is the optimal point at which catalysis takes place (**Figure 6.8b**).

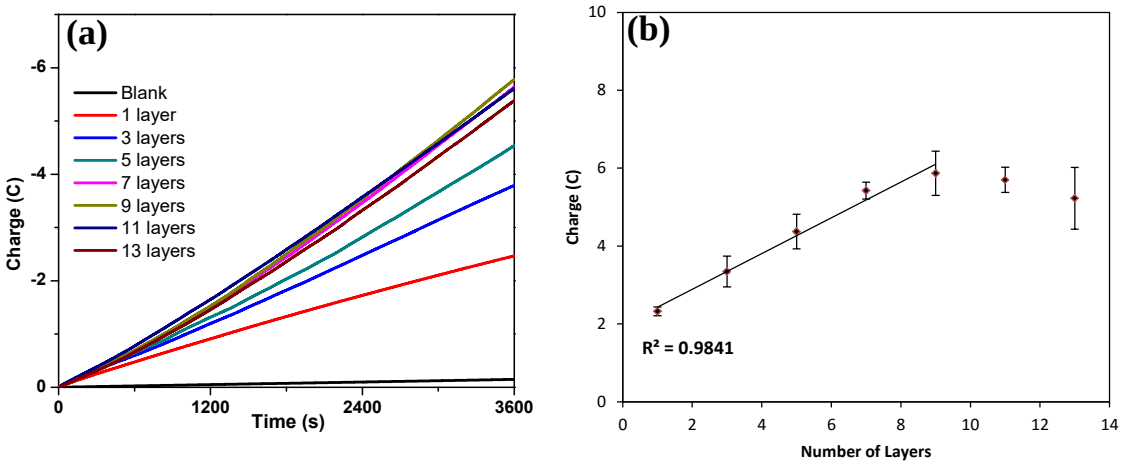

Figure 6.8. (a) Charge passed through the as-prepared catalytic films over 1 h; (b) Correlation between the number of layers and the charge consumption.

The Faradaic efficiencies of the catalytic films approach ~100%. Using the average molecular area obtained from the LB isotherm, the average surface coverage of the electrode can be roughly estimated at 1.14×10^{14} molecules/layer.cm^2 (0.189 nmol/layer.cm^2). This in turn was used to estimate the approximate turnover number (TON) for a monolayer. This apparent TON is equal to 54,000 ± 1,500 after one hour.

If catalysis is based on exclusively molecular mechanisms, it would be expected that electrodes rinsed with excess organic solvents would lead to drastically reduced catalytic activity. This is due to the fact that the molecular catalyst is highly soluble in organic solvents such as dichloromethane and acetonitrile. As such the electrolized FTO electrodes were rinsed thoroughly with these solvents, as well as with distilled water. Interestingly, bulk electrolysis with the rinsed electrodes showed activity comparable to that of the original electrodes (**Figure 6.9a**). A control experiment was performed by rinsing off with organic solvents the monolayer of a freshly prepared electrode before electrolysis, and the resulting electrode was catalytically inert at equivalent applied potentials. This suggests that the initially deposited molecular film rearranges at the surface of the electrode upon electrolysis. Evidence for this rearrangement was obtained from the plots of current density vs. time. Before rinsing, the current density of the electrodes with 1 layer was constant over time, while in electrodes with 3-13 layers the current density increases (**Figure 6.9c**). This is attributed to the ease at which monolayers can be converted into the rearranged catalyst. However, more time is required for the complete conversion of the molecular species as the number of layers increases. In contrast, the current densities were constant over time after the original electrodes were rinsed. This is tentatively attributed to the removal of residual molecules, as shown in **Figure 6.9d**. Furthermore, a linear relationship between charge consumption and number of deposited layers can be observed up to

9 layers after which no further increase is observed (**Figure 6.9b**). This suggests that although the molecular catalyst is rearranging into a more active form, the initial conditions of the molecular species dictate the final activity of the electrodeposited film. We have recently observed a similar situation where a pentadentate cobalt(III) oxime species which retains its molecular nature in acetonitrile, is converted into nanoparticles within 1 h of electrocatalysis in water.[194]

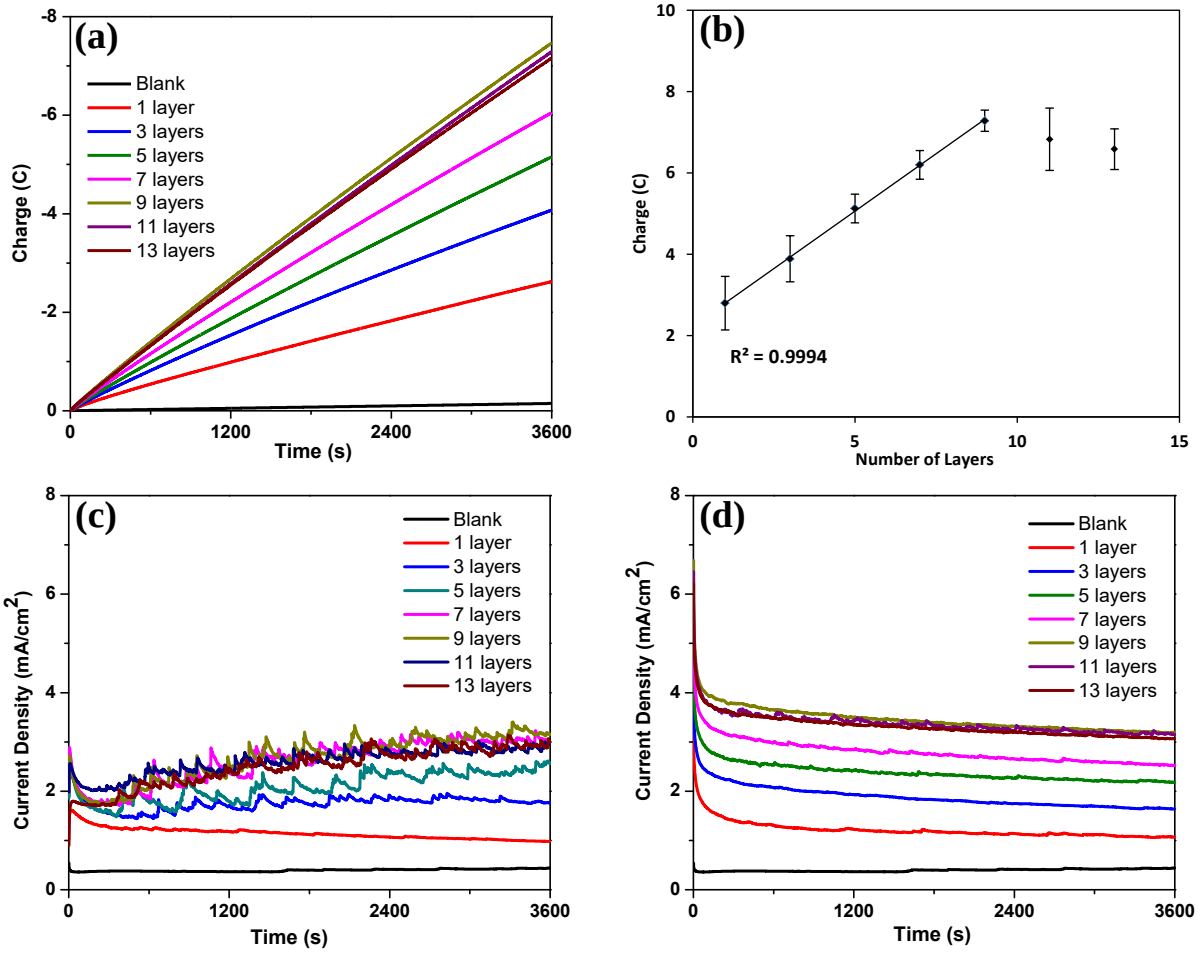

Figure 6.9. (a) Charge passed through the catalytic film over 1 hour after rinsing; (b) Correlation between the number of layers and the charge consumption after rinsing the electrode; (c) Current density vs. time plot before rinsing (d) Current density vs. time plot after rinsing the electrode.

This prompted us to study the effect of cycling two electrodes; the first is coated with a monolayer of $[Co^{III}(L^{N2O3})H_2O]$, while the second was coated with nine layers of

$[Co^{III}(L^{N2O3})H_2O]$. For the 1-layer electrode there was a slight increase in current density (~20%) after 100 cycles (**Figure 6.10a**). Interestingly, when the 9-layer electrode was cycled 100 times the current density doubled (**Figure 6.10b**). These observations confirm our previous assessment that the LB layers are rearranging and that the initial conditions of the experiment dictate the catalytic behavior.

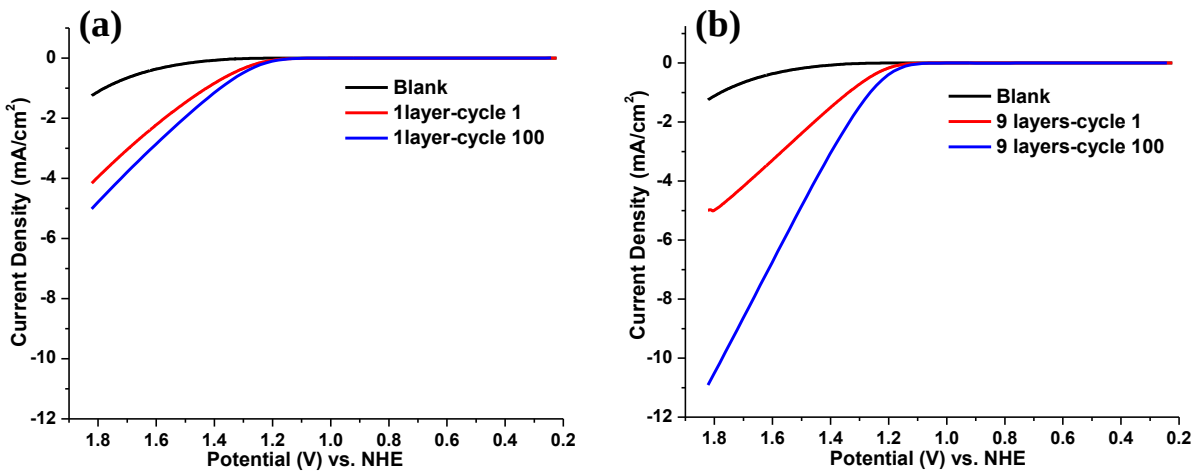

Figure 6.10. Polarization curves, initial and after 100 cycles at pH 11 for (a) one monolayer and (b) for nine layers of $[Co^{III}(L^{N2O3})H_2O]$.

6.3.8. Surface Analysis After Catalysis

Attempts to characterize the nature of the electrodeposited films were made using scanning electron microscopy (SEM) and X-ray photoelectron spectroscopy (XPS). However, the ultrathin nature of the catalytic layer proved to be taxing due to the minute amounts of sample on the electrodes. The SEM samples lacked obvious differences between the blank and the catalytic electrodes (**Figure 6.11a, b**). High resolution XPS scans of the cobalt 2P region showed a characteristic albeit weak signal, confirming the presence of the metal ion (**Figure 6.11c**). The need for cobalt is in good agreement with the lack of activity observed for the gallium-based film.

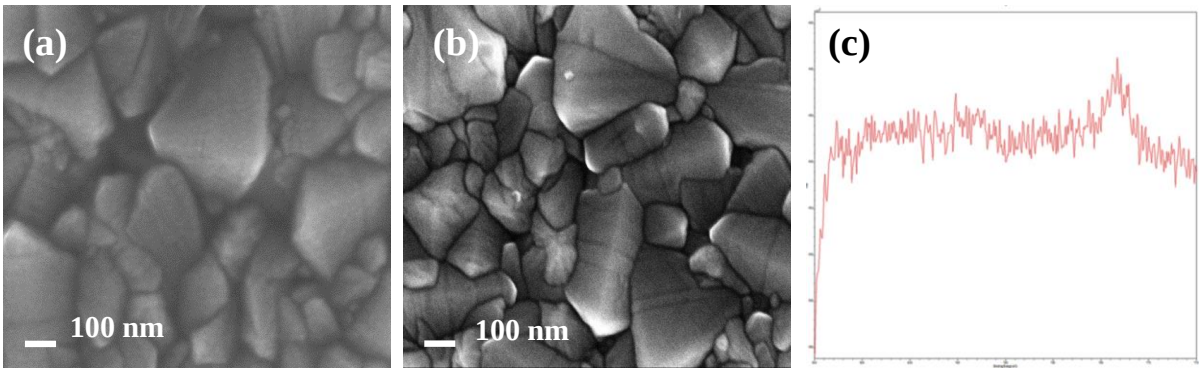

Figure 6.11. SEM images obtained for (a) bare FTO electrode (b) LB 9 layers deposited FTO electrode after 12 h catalysis; (c) XPS scan of the Co 2p region for 11 layered FTO electrode.

IRRAS spectra for 50-layer deposited FTO glass substrate were obtained before and after catalysis after rinsing with organic solvents. The appearance of symmetric and asymmetric CH_2 and CH_3 stretching vibration bands at 2952, 2914, and 2847 cm^{-1} as shown in **Figure 6.12**, indicates the presence of carbon-based residues after catalysis. These observations are in excellent agreement with the notion of a cobalt-based catalyst in which carbon-based residues act as modifiers, thus confirming that the choice of ligand is relevant to obtain efficient and robust catalytic films for water oxidation.[195]

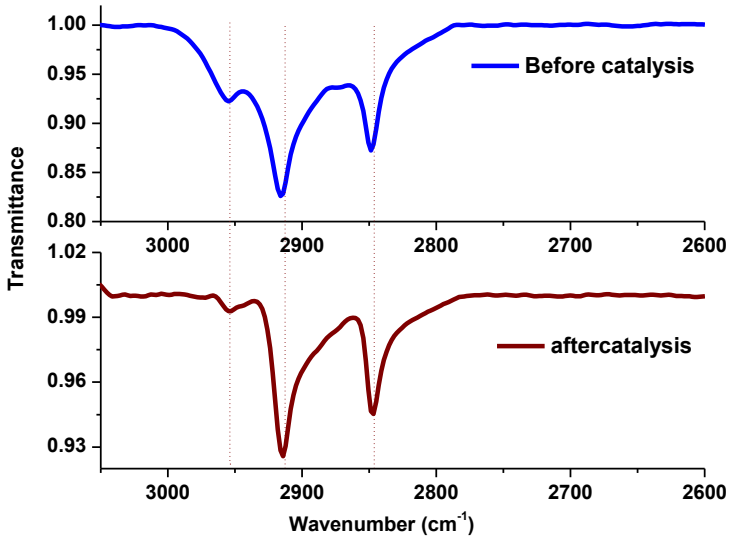

Figure 6.12. IRRAS spectra of C—H stretching of 50-layer deposited film on FTO substrate region before catalysis and after catalysis after rinsing with organic solvents.

The robustness of the catalytic films towards water oxidation was further probed on a 9-layer electrode. After 1 h of electrolysis the electrode was rinsed with organic solvents and reintroduced into a fresh catalytic cell for additional 12 h electrolysis. An increase in charge consumption was observed (**Figure 6.13**).

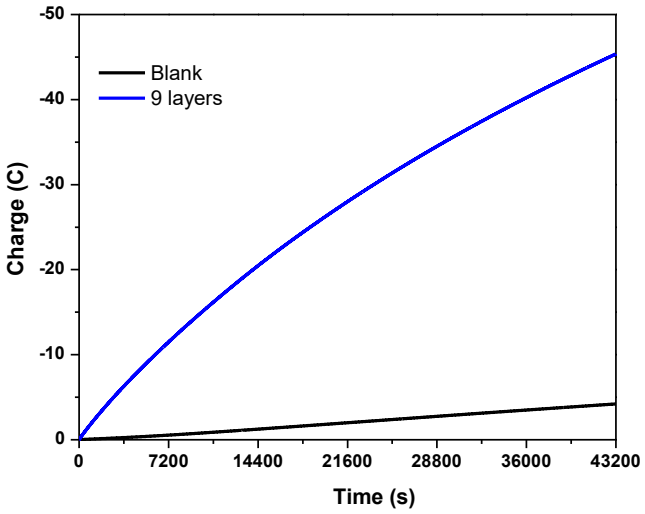

Figure 6.13. Charge passed through a 9-layer FTO electrode over 12 h electrolysis.

6.3.9. Apparent Turnover Number and Faradaic Efficiency Calculation

The turnover number and Faradaic efficiencies were calculated using a procedure adapted from the literature.[196] The GC was used to quantify the O_2 in the head space of the cell using atmospheric N_2 as internal standard. The concentration of dissolved O_2 was taken into account according to Henry's law.[197] Sample calculations are shown below.

	% O_2	% N_2	Ratio
Air	20.3	79.7	r_{air} = 0.2547
Blank	22.0	70.0	r_{blank} = 0.2821
LB	29.2	70.8	r_{LB} = 0.4124

Head space volume = 9.5 mL

Volume of solution = 36 mL

Henry's law constant = 769.23 $\frac{L.atm}{mol}$

nO$_2$ in head space before catalysis (A) = 82.5 µmol for 9.5 mL

O$_2$ produced in headspace = $\frac{r_{lb}- r_{blank}}{r_{air}} \times A = \frac{0.4124-0.2821}{0.2547} = 42.22\ \mu mol$

O$_2$ dissolved = nO$_2$ final – nO$_2$ initial

= $\frac{p_{O2\ final}}{K}$*V$_{solution}$ - $\frac{p_{O2\ initial}}{K}$*V$_{solution}$

= (0.292-0.203)($\frac{36000\ \mu L}{769.23(\frac{L.atm}{mol})}$)= 4.164 µmol

Total amount of O$_2$ produced = nO$_2$ in headspace + nO$_2$ dissolved = 4.164 + 42.22

= 46.384 μmol

nO$_2$ based on charge = $\frac{Q_{LB}- Q_{blank}}{4\times0.096485} = \frac{22.524- 4.2144}{4\times0.096485}$ = 47.44 μmol

Faradaic efficiency = $\frac{n_{O2\ experimental}}{n_{O2\ charge}} \times 100 = \frac{46.384}{47.44} \times 100 = 98\ \%$

6.4. Conclusions

In conclusion we have developed a novel amphiphilic procatalytic cobalt complex, [Co^{III}(L^{N2O3})H$_2$O], that can be orderly deposited onto an FTO electrode using the Langmuir-Blodgett method. The resulting modified electrode is an excellent water oxidation catalyst with a moderate overpotential of 0.5 V. A direct correlation between the number of deposited layers and improved catalytic activity was found for the first nine layers. Constant performance was observed when a larger number of layers were deposited. This is the first application of LB films of molecular amphiphiles for water oxidation catalysis and the results point out to the development of methodology that enables the incorporation of other potentially effective, but water insoluble, molecular catalysts.

CHAPTER 7 CONCLUSIONS AND PERSPECTIVES

Homogeneous thin film formation that occurs without any chemical alternations in structure is a critical challenge in transferring the chemistry learnt in solution phase to solid phase. The Langmuir-Blodgett (LB) technique has proven a viable method to assemble homogeneous films in an organized manner while the structure remains intact. This method allows for extrapolation of observed solution phase properties to films on the solid phase, which can be used in various applications such as molecular electronics, coatings, and energy. The film thickness can be modulated by changing the molecular structure or by repeated deposition. However, molecules should be amphiphilic in nature to be used in LB film formation. In this dissertation, I described synthesis, characterization, and LB film formation ability of symmetric and asymmetric iron(III), cobalt(III), nickel(II), copper(II), and zinc(II) complexes along with their LB film applications in molecular electronics, corrosion mitigation, and heterogeneous water oxidation.

In **Chapter 3**, amphiphilic nickel(II) and copper(II) complexes with $[N_2O_2]$ coordination environment were successfully synthesized and characterized by multiple physicochemical methods. Isothermal data confirmed the amphiphilic nature of the complexes with collapse pressures at ~35 mN/m while homogeneous film formation was observed between 20-25 mN/m surface pressure. The presence of both ligand- and metal-based redox processes made the Cu(II) complex a viable candidate in Au|molecule|Au assemblies. However, the flat curve observed for current-voltage measurements indicated an insulating behavior. Therefore, frontier molecular orbital energies of the Cu(II) complex were compared with a similar rectifying Fe(III) complex to propose a rectification mechanism. According to the energy calculations, the Cu(II) SOMO situated 1.9 eV above the Au Fermi level making it energetically inaccessible for electron

transfer, whereas the SOMO of Fe(III) situated 1.0 eV above the Au Fermi level allowing the electron transfer to display current rectification. Although the HOMO of Cu(II) situated 1.0 eV below Au Fermi level, insulating nature confirmed that HOMO is not involved in electron transfer. Therefore, it suggests that only SOMO of Fe(III) is involved in electron transfer following the asymmetric current rectification mechanism. This study also shows that SOMOs that are energetically compatible with electrode Fermi levels can accept electron instead of LUMO to facilitate asymmetric current flow.

In **Chapter 4**, a series of Fe(III) complexes were synthesized by incorporating different axial ligands or pyridine and phenolate arms into the ligand architecture to investigate their potential performance as molecular current rectifiers. According to isothermal compression data, all complexes exhibited amphiphilic character with collapse pressures of ~35-40 mN/m. Theoretical calculations performed using molecular redox potentials indicated that SOMO energies are situated 0.4 eV above Fermi level for Fe(III) complex with [N_3O] coordination environment, and 0.8 eV for Fe(III) complexes with [N_3O_2] and [N_2O_2] environment. This suggests that these SOMOs are energetically comparable with the Au Fermi level, thus allowing for electron transfer. Therefore, these complexes can be used as viable candidates for molecular current rectification.

In **Chapter 5**, a series of Fe(III), Cu(II), and Zn(II) saloph-based complexes with [N_2O_2] coordination environment were synthesized. According to isothermal compression data all the complexes showed amphiphilic character with collapse pressures of ~35-45 mN/m. Cyclic voltammetry confirmed that 11-layer deposited gold electrodes of the complexes can passivate electron flow more efficiently compared to the ligand. Agar test experiments, SEM, and optical micrograph images indicated diminished corrosion rates for LB film-coated iron plates. Weight

loss measurements confirmed that 11 layers of the Fe(III) and Zn(II) complexes demonstrate the best corrosion mitigation ability, with respective corrosion inhibition efficiencies of ~ 25 % to 30 % while ligand alone demonstrated a 6 % inhibition efficiency. This suggests that coatings of complexes can function as passive barriers to the electron flow between the electrolyte and the iron plate.

In **Chapter 6**, an amphiphilic cobalt(III) complex of phenolate-rich [N_2O_3] ligand was synthesized. A monolayer functionalized on conductive FTO substrate using LB method exhibited catalytic activity in pH 11 borate solution with an overpotential of 0.5 V. Bulk electrolysis performed at 1.2 $V_{Ag/AgCl}$ confirmed oxygen generation, with an apparent TON of 54,000 ± 1,500 and a Faradaic efficiency of ~100 % for a monolayer after 1 h. Bulk electrolysis performed for FTO electrodes coated with 1-13 layers showed a direct correlation between the number of layers and charge consumption up to 9 layers, after which no further increase was observed. This suggests that 9-layer deposits provides optimal oxygen generation after 1 h. Although the molecules are being rearranged upon electrolysis, the presence of symmetric and asymmetric vibration bands in IRRAS spectrum suggests that carbon-based residues can act as modifiers, thus confirming that the choice of ligand is relevant to obtain efficient and robust catalytic films for water oxidation.

Confirmation of the rectification ability in the complexes of **Chapter 4** necessitates I/V measurements using Gold|LB|Gold assemblies. To evaluate HOMO-LUMO/HOMO-SOMO contribution to efficient rectification behavior in coordination complexes, ligand design can be additionally varied by incorporation of different electron donating and withdrawing substituents on a phenolate arm. These modified complexes are subsequently evaluated for adherence to a unimolecular or asymmetric rectification mechanism. Likewise, systems containing metal-

centered donors (Fe^{II} and Ru^{II}) and ligand-centered acceptors (terpyridines) can be explored as viable candidates in current rectification.

Further investigations of corrosion mitigation can be performed using systems with longer alkoxy chains (e.g., $OC_{18}H_{37}$, instead of an ethoxymethoxy substituent) to enhance water repulsion through the hydrophobic nature of the alkyl chain. Further, self-assembly can be implemented in film formation, which binds chemically to the substrate. Therefore, stronger binding onto surface will minimize removal of the coatings, providing a better passivation. Investigations on heterogeneous water oxidation to obtain low overpotential can be performed by changing the substrate of the working electrode, by changing the pH of the solution, or by testing the catalytic activity of LB films of other manganese- and iron-based complexes. Additionally, electrocatalysis using LB films can be shifted toward photocatalysis to generate H_2 as a renewable energy source by investigating an assembly functionalized with LB layers of Ru^{II} and Co^{III} on top of each other.

APPENDIX -A

Crystal structure data of complex **[$Cu^{II}L^{N2O2}$]** (**2**) in **Chapter 3**

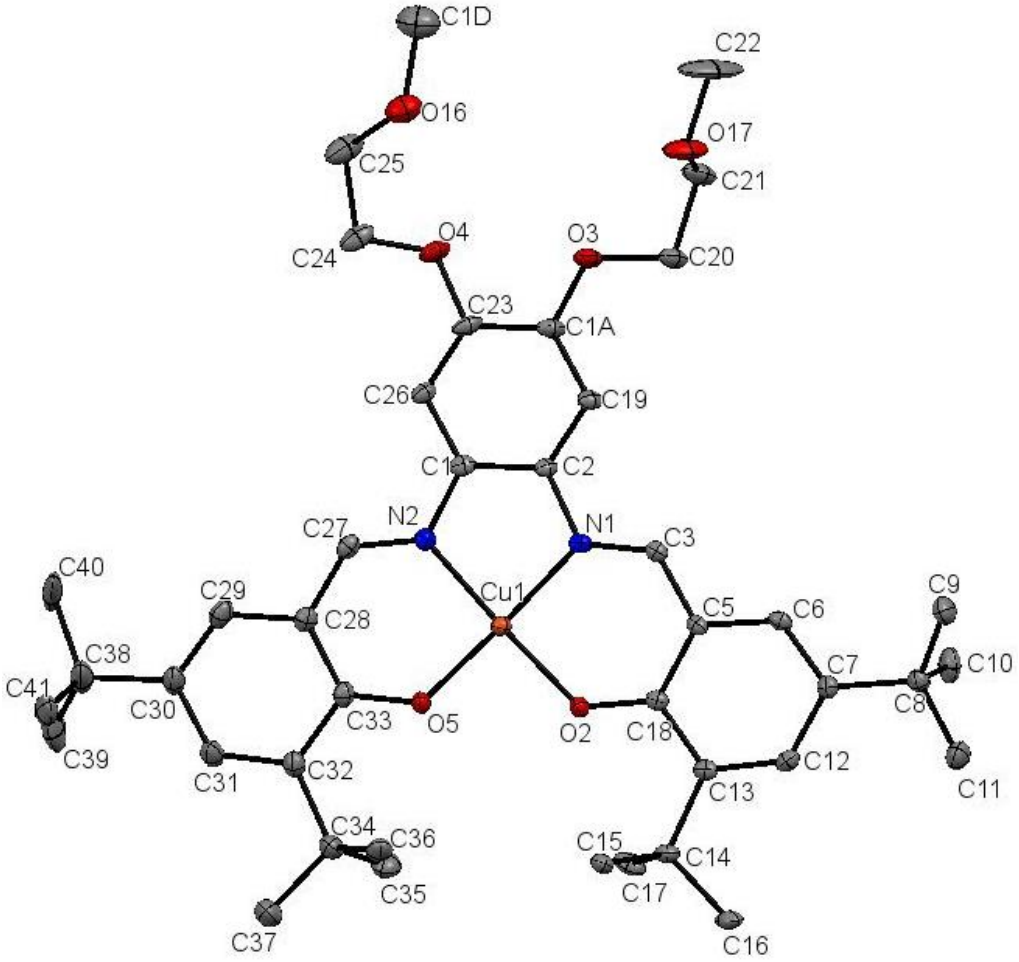

Figure A1. X-ray crystal structure of **[$Cu^{II}L^{N2O2}$]** (**2**).

Atom1	Atom2	Length		Atom1	Atom2	Length
Cu1	N1	1.934(2)		N7	C45	1.414(4)
Cu1	O2	1.896(2)		O8	C47	1.360(4)
Cu1	O5	1.891(2)		O8	C48	1.433(4)
Cu1	N2	1.938(2)		O9	C49	1.427(4)
N1	C2	1.419(4)		O9	C50	1.423(4)
N1	C3	1.298(4)		O10	C51	1.362(4)
O2	C18	1.304(4)		O10	C52	1.434(4)
O3	C1A	1.359(4)		O11	C53	1.419(4)
O3	C20	1.426(4)		O11	C54	1.416(4)
O4	C23	1.374(4)		O12	C63	1.299(4)
O4	C24	1.419(5)		C4	H4	0.95
O5	C33	1.300(4)		C4	C59	1.412(5)
N2	C1	1.417(4)		C4	C60	1.361(5)
N2	C27	1.295(4)		C42	C43	1.430(5)
O17	C21	1.425(5)		C42	C74	1.429(5)
O17	C22	1.425(7)		C43	C44	1.416(5)
O16	C25	1.462(6)		C43	C71	1.415(5)
O16	C1C	1.388(7)		C44	H44	0.952
C1	C2	1.388(5)		C45	C46	1.400(4)
C1	C26	1.398(5)		C45	C56	1.389(4)
C2	C19	1.396(5)		C46	H46	0.949
C3	H3	0.95		C46	C47	1.369(4)
C3	C5	1.426(5)		C47	C51	1.421(4)
C5	C6	1.403(4)		C48	H48A	0.992
C5	C18	1.431(4)		C48	H48B	0.989
C6	H6	0.949		C48	C49	1.502(4)
C6	C7	1.375(5)		C49	H49A	0.99
C7	C8	1.529(5)		C49	H49B	0.989
C7	C12	1.410(5)		C50	H50A	0.98
C8	C9	1.538(5)		C50	H50B	0.981
C8	C10	1.528(6)		C50	H50C	0.979
C8	C11	1.527(5)		C51	C55	1.377(5)
C9	H9A	0.98		C52	H52A	0.989
C9	H9B	0.98		C52	H52B	0.99
C9	H9C	0.981		C52	C53	1.500(5)
C10	H10A	0.981		C53	H53A	0.991
C10	H10B	0.981		C53	H53B	0.99
C10	H10C	0.98		C54	H54A	0.979
C11	H11A	0.979		C54	H54B	0.981
C11	H11B	0.981		C54	H54C	0.98

C11	H11C	0.981		C55	H55	0.949
C12	H12	0.949		C55	C56	1.406(4)
C12	C13	1.388(5)		C56	N57	1.423(4)
C13	C14	1.543(5)		N57	C58	1.300(4)
C13	C18	1.428(5)		C58	H58	0.95
C14	C15	1.529(5)		C58	C59	1.425(5)
C14	C16	1.533(5)		C59	C63	1.427(5)
C14	C17	1.546(5)		C60	C61	1.403(6)
C15	H15A	0.98		C60	C68	1.531(6)
C15	H15B	0.981		C61	H61	0.949
C15	H15C	0.979		C61	C62	1.365(5)
C16	H16A	0.981		C62	C63	1.438(5)
C16	H16B	0.981		C62	C64	1.540(5)
C16	H16C	0.979		C64	C65	1.526(6)
C17	H17A	0.981		C64	C66	1.531(5)
C17	H17B	0.978		C64	C67	1.520(6)
C17	H17C	0.98		C65	H65A	0.98
C19	H19	0.95		C65	H65B	0.981
C19	C1A	1.377(5)		C65	H65C	0.98
C1A	C23	1.407(5)		C66	H66A	0.979
C20	H20A	0.991		C66	H66B	0.979
C20	H20B	0.989		C66	H66C	0.98
C20	C21	1.487(6)		C67	H67A	0.981
C21	H21A	0.992		C67	H67B	0.981
C21	H21B	0.991		C67	H67C	0.979
C22	H22A	0.978		C68	C69	1.451(9)
C22	H22B	0.979		C68	C70	1.510(7)
C22	H22C	0.979		C68	C1B	1.61(1)
C23	C26	1.375(5)		C69	H69A	0.98
C24	H24A	0.99		C69	H69B	0.981
C24	H24B	0.99		C69	H69C	0.98
C24	C25	1.509(6)		C70	H70A	0.98
C25	H25A	0.989		C70	H70B	0.981
C25	H25B	0.989		C70	H70C	0.978
C26	H26	0.949		C71	H71	0.951
C27	H27	0.949		C71	C72	1.369(5)
C27	C28	1.430(5)		C72	C73	1.404(5)
C28	C29	1.419(5)		C72	C79	1.528(5)
C28	C33	1.417(5)		C73	H73	0.949
C29	H29	0.951		C73	C74	1.374(5)
C29	C30	1.364(5)		C74	C75	1.531(5)

C30	C31	1.402(5)		C75	C76	1.557(6)
C30	C38	1.539(6)		C75	C77	1.515(8)
C31	H31	0.951		C75	C78	1.530(9)
C31	C32	1.381(5)		C76	H76A	0.979
C32	C33	1.441(5)		C76	H76B	0.978
C32	C34	1.534(5)		C76	H76C	0.98
C34	C35	1.543(6)		C77	H77A	0.98
C34	C36	1.532(6)		C77	H77B	0.979
C34	C37	1.534(5)		C77	H77C	0.979
C35	H35A	0.979		C78	H78A	0.979
C35	H35B	0.98		C78	H78B	0.98
C35	H35C	0.979		C78	H78C	0.979
C36	H36A	0.98		C79	C80	1.499(5)
C36	H36B	0.981		C79	C81	1.539(8)
C36	H36C	0.98		C79	C82	1.509(7)
C37	H37A	0.981		C80	H80A	0.979
C37	H37B	0.982		C80	H80B	0.982
C37	H37C	0.98		C80	H80C	0.98
C38	C39	1.540(8)		C81	H81A	0.98
C38	C40	1.524(7)		C81	H81B	0.978
C38	C41	1.531(7)		C81	H81C	0.978
C39	H39A	0.979		C82	H82A	0.98
C39	H39B	0.98		C82	H82B	0.98
C39	H39C	0.978		C82	H82C	0.98
C40	H40A	0.979		C1B	H1BA	0.981
C40	H40B	0.982		C1B	H1BB	0.978
C40	H40C	0.979		C1B	H1BC	0.98
C41	H41A	0.979		O1	H1	0.838
C41	H41B	0.981		O1	C1D	1.395(5)
C41	H41C	0.98		C1D	H1DA	0.98
C1C	H1CA	0.98		C1D	H1DB	0.979
C1C	H1CB	0.981		C1D	H1DC	0.982
C1C	H1CC	0.98		O7	H7	0.84
Cu2	O6	1.886(2)		O7	C1E	1.418(6)
Cu2	N7	1.923(2)		C1E	H1EA	0.979
Cu2	O12	1.890(2)		C1E	H1EB	0.979
Cu2	N57	1.940(2)		C1E	H1EC	0.979
O6	C42	1.301(4)		O13	H13A	0.869
N7	C44	1.299(4)		O13	H13B	0.90(3)

Table A1. Bond lengths (Å) for complex **[$Cu^{II}L^{N2O2}$]** (**2**).

Atom1	Atom2	Atom3	Angle		Atom1	Atom2	Atom3	Angle
N1	Cu1	O2	92.6(1)		Cu2	N7	C45	112.6(2)
N1	Cu1	O5	175.8(1)		C44	N7	C45	122.6(3)
N1	Cu1	N2	84.4(1)		C47	O8	C48	115.4(2)
O2	Cu1	O5	89.53(9)		C49	O9	C50	112.7(2)
O2	Cu1	N2	176.4(1)		C51	O10	C52	117.8(2)
O5	Cu1	N2	93.6(1)		C53	O11	C54	112.5(2)
Cu1	N1	C2	112.3(2)		Cu2	O12	C63	128.9(2)
Cu1	N1	C3	125.2(2)		H4	C4	C59	118.9
C2	N1	C3	121.8(3)		H4	C4	C60	118.9
Cu1	O2	C18	129.1(2)		C59	C4	C60	122.1(4)
C1A	O3	C20	117.6(3)		O6	C42	C43	122.5(3)
C23	O4	C24	116.7(3)		O6	C42	C74	119.7(3)
Cu1	O5	C33	128.5(2)		C43	C42	C74	117.8(3)
Cu1	N2	C1	112.4(2)		C42	C43	C44	122.8(3)
Cu1	N2	C27	124.9(2)		C42	C43	C71	119.7(3)
C1	N2	C27	122.7(3)		C44	C43	C71	117.2(3)
C21	O17	C22	110.5(4)		N7	C44	C43	126.6(3)
C25	O16	C1C	114.7(5)		N7	C44	H44	116.7
N2	C1	C2	115.3(3)		C43	C44	H44	116.8
N2	C1	C26	125.4(3)		N7	C45	C46	124.3(3)
C2	C1	C26	119.3(3)		N7	C45	C56	115.7(3)
N1	C2	C1	115.3(3)		C46	C45	C56	119.9(3)
N1	C2	C19	123.7(3)		C45	C46	H46	119.6
C1	C2	C19	120.9(3)		C45	C46	C47	120.6(3)
N1	C3	H3	117.3		H46	C46	C47	119.8
N1	C3	C5	125.6(3)		O8	C47	C46	125.2(3)
H3	C3	C5	117.2		O8	C47	C51	115.2(3)
C3	C5	C6	116.2(3)		C46	C47	C51	119.6(3)
C3	C5	C18	122.9(3)		O8	C48	H48A	110.2
C6	C5	C18	120.8(3)		O8	C48	H48B	110.3
C5	C6	H6	118.7		O8	C48	C49	107.5(2)
C5	C6	C7	122.7(3)		H48A	C48	H48B	108.5
H6	C6	C7	118.6		H48A	C48	C49	110.2
C6	C7	C8	121.4(3)		H48B	C48	C49	110.2
C6	C7	C12	116.0(3)		O9	C49	C48	104.8(2)
C8	C7	C12	122.4(3)		O9	C49	H49A	110.8
C7	C8	C9	110.6(3)		O9	C49	H49B	110.7
C7	C8	C10	108.5(3)		C48	C49	H49A	110.8
C7	C8	C11	112.6(3)		C48	C49	H49B	110.8
C9	C8	C10	108.3(3)		H49A	C49	H49B	108.9

C9	C8	C11	107.4(3)		O9	C50	H50A	109.5
C10	C8	C11	109.4(3)		O9	C50	H50B	109.6
C8	C9	H9A	109.5		O9	C50	H50C	109.4
C8	C9	H9B	109.5		H50A	C50	H50B	109.5
C8	C9	H9C	109.5		H50A	C50	H50C	109.5
H9A	C9	H9B	109.5		H50B	C50	H50C	109.4
H9A	C9	H9C	109.4		O10	C51	C47	114.4(3)
H9B	C9	H9C	109.5		O10	C51	C55	125.6(3)
C8	C10	H10A	109.4		C47	C51	C55	120.1(3)
C8	C10	H10B	109.5		O10	C52	H52A	110.4
C8	C10	H10C	109.4		O10	C52	H52B	110.4
H10A	C10	H10B	109.3		O10	C52	C53	107.0(2)
H10A	C10	H10C	109.6		H52A	C52	H52B	108.6
H10B	C10	H10C	109.6		H52A	C52	C53	110.3
C8	C11	H11A	109.5		H52B	C52	C53	110.3
C8	C11	H11B	109.4		O11	C53	C52	109.1(2)
C8	C11	H11C	109.6		O11	C53	H53A	109.9
H11A	C11	H11B	109.5		O11	C53	H53B	109.8
H11A	C11	H11C	109.5		C52	C53	H53A	109.8
H11B	C11	H11C	109.5		C52	C53	H53B	109.9
C7	C12	H12	117.7		H53A	C53	H53B	108.3
C7	C12	C13	124.4(3)		O11	C54	H54A	109.4
H12	C12	C13	117.9		O11	C54	H54B	109.5
C12	C13	C14	121.1(3)		O11	C54	H54C	109.4
C12	C13	C18	119.0(3)		H54A	C54	H54B	109.5
C14	C13	C18	119.9(3)		H54A	C54	H54C	109.6
C13	C14	C15	111.4(3)		H54B	C54	H54C	109.4
C13	C14	C16	111.9(3)		C51	C55	H55	120
C13	C14	C17	108.4(3)		C51	C55	C56	119.9(3)
C15	C14	C16	108.3(3)		H55	C55	C56	120.1
C15	C14	C17	109.2(3)		C45	C56	C55	119.8(3)
C16	C14	C17	107.6(3)		C45	C56	N57	114.9(3)
C14	C15	H15A	109.4		C55	C56	N57	125.2(3)
C14	C15	H15B	109.4		Cu2	N57	C56	112.1(2)
C14	C15	H15C	109.5		Cu2	N57	C58	124.4(2)
H15A	C15	H15B	109.4		C56	N57	C58	122.9(3)
H15A	C15	H15C	109.6		N57	C58	H58	116.9
H15B	C15	H15C	109.5		N57	C58	C59	126.0(3)
C14	C16	H16A	109.4		H58	C58	C59	117.1
C14	C16	H16B	109.5		C4	C59	C58	116.7(3)
C14	C16	H16C	109.4		C4	C59	C63	119.8(3)

H16A	C16	H16B	109.4		C58	C59	C63	123.4(3)
H16A	C16	H16C	109.5		C4	C60	C61	116.9(4)
H16B	C16	H16C	109.5		C4	C60	C68	123.9(4)
C14	C17	H17A	109.4		C61	C60	C68	119.2(4)
C14	C17	H17B	109.4		C60	C61	H61	117.5
C14	C17	H17C	109.4		C60	C61	C62	125.1(4)
H17A	C17	H17B	109.5		H61	C61	C62	117.4
H17A	C17	H17C	109.6		C61	C62	C63	117.9(3)
H17B	C17	H17C	109.5		C61	C62	C64	122.0(3)
O2	C18	C5	122.8(3)		C63	C62	C64	120.1(3)
O2	C18	C13	120.2(3)		O12	C63	C59	122.6(3)
C5	C18	C13	117.0(3)		O12	C63	C62	119.3(3)
C2	C19	H19	120.1		C59	C63	C62	118.0(3)
C2	C19	C1A	119.8(3)		C62	C64	C65	110.4(3)
H19	C19	C1A	120.1		C62	C64	C66	111.6(3)
O3	C1A	C19	124.9(3)		C62	C64	C67	109.9(3)
O3	C1A	C23	116.0(3)		C65	C64	C66	107.7(3)
C19	C1A	C23	119.1(3)		C65	C64	C67	109.7(3)
O3	C20	H20A	110.5		C66	C64	C67	107.4(3)
O3	C20	H20B	110.4		C64	C65	H65A	109.4
O3	C20	C21	106.6(3)		C64	C65	H65B	109.5
H20A	C20	H20B	108.6		C64	C65	H65C	109.5
H20A	C20	C21	110.4		H65A	C65	H65B	109.3
H20B	C20	C21	110.4		H65A	C65	H65C	109.5
O17	C21	C20	108.1(3)		H65B	C65	H65C	109.6
O17	C21	H21A	110		C64	C66	H66A	109.4
O17	C21	H21B	110		C64	C66	H66B	109.4
C20	C21	H21A	110.1		C64	C66	H66C	109.5
C20	C21	H21B	110		H66A	C66	H66B	109.6
H21A	C21	H21B	108.6		H66A	C66	H66C	109.5
O17	C22	H22A	109.5		H66B	C66	H66C	109.4
O17	C22	H22B	109.4		C64	C67	H67A	109.4
O17	C22	H22C	109.5		C64	C67	H67B	109.4
H22A	C22	H22B	109.4		C64	C67	H67C	109.4
H22A	C22	H22C	109.5		H67A	C67	H67B	109.6
H22B	C22	H22C	109.5		H67A	C67	H67C	109.5
O4	C23	C1A	114.3(3)		H67B	C67	H67C	109.5
O4	C23	C26	124.4(3)		C60	C68	C69	112.8(5)
C1A	C23	C26	121.2(3)		C60	C68	C70	112.1(4)
O4	C24	H24A	110.5		C60	C68	C1B	107.8(4)
O4	C24	H24B	110.4		C69	C68	C70	111.8(5)

O4	C24	C25	106.2(3)		C69	C68	C1B	105.0(5)
H24A	C24	H24B	108.8		C70	C68	C1B	106.8(4)
H24A	C24	C25	110.4		C68	C69	H69A	109.4
H24B	C24	C25	110.6		C68	C69	H69B	109.5
O16	C25	C24	110.0(3)		C68	C69	H69C	109.5
O16	C25	H25A	109.7		H69A	C69	H69B	109.6
O16	C25	H25B	109.7		H69A	C69	H69C	109.3
C24	C25	H25A	109.6		H69B	C69	H69C	109.5
C24	C25	H25B	109.6		C68	C70	H70A	109.4
H25A	C25	H25B	108.3		C68	C70	H70B	109.4
C1	C26	C23	119.6(3)		C68	C70	H70C	109.4
C1	C26	H26	120.2		H70A	C70	H70B	109.4
C23	C26	H26	120.2		H70A	C70	H70C	109.7
N2	C27	H27	116.9		H70B	C70	H70C	109.5
N2	C27	C28	126.1(3)		C43	C71	H71	118.7
H27	C27	C28	117		C43	C71	C72	122.6(3)
C27	C28	C29	116.1(3)		H71	C71	C72	118.7
C27	C28	C33	123.1(3)		C71	C72	C73	116.3(3)
C29	C28	C33	120.6(3)		C71	C72	C79	124.1(3)
C28	C29	H29	119.1		C73	C72	C79	119.6(3)
C28	C29	C30	121.9(4)		C72	C73	H73	117.5
H29	C29	C30	119		C72	C73	C74	124.8(4)
C29	C30	C31	116.8(4)		H73	C73	C74	117.7
C29	C30	C38	123.5(4)		C42	C74	C73	118.7(3)
C31	C30	C38	119.7(4)		C42	C74	C75	119.4(3)
C30	C31	H31	117.5		C73	C74	C75	121.9(4)
C30	C31	C32	124.9(4)		C74	C75	C76	111.5(4)
H31	C31	C32	117.5		C74	C75	C77	109.3(4)
C31	C32	C33	118.0(3)		C74	C75	C78	110.0(4)
C31	C32	C34	121.5(3)		C76	C75	C77	106.9(4)
C33	C32	C34	120.5(3)		C76	C75	C78	107.3(4)
O5	C33	C28	123.3(3)		C77	C75	C78	111.8(4)
O5	C33	C32	119.1(3)		C75	C76	H76A	109.5
C28	C33	C32	117.7(3)		C75	C76	H76B	109.5
C32	C34	C35	109.9(3)		C75	C76	H76C	109.4
C32	C34	C36	109.5(3)		H76A	C76	H76B	109.4
C32	C34	C37	112.5(3)		H76A	C76	H76C	109.5
C35	C34	C36	109.9(3)		H76B	C76	H76C	109.6
C35	C34	C37	107.6(3)		C75	C77	H77A	109.5
C36	C34	C37	107.3(3)		C75	C77	H77B	109.5
C34	C35	H35A	109.4		C75	C77	H77C	109.4

C34	C35	H35B	109.5		H77A	C77	H77B	109.5
C34	C35	H35C	109.4		H77A	C77	H77C	109.5
H35A	C35	H35B	109.5		H77B	C77	H77C	109.5
H35A	C35	H35C	109.5		C75	C78	H78A	109.5
H35B	C35	H35C	109.6		C75	C78	H78B	109.4
C34	C36	H36A	109.4		C75	C78	H78C	109.5
C34	C36	H36B	109.5		H78A	C78	H78B	109.5
C34	C36	H36C	109.5		H78A	C78	H78C	109.5
H36A	C36	H36B	109.5		H78B	C78	H78C	109.5
H36A	C36	H36C	109.5		C72	C79	C80	112.5(3)
H36B	C36	H36C	109.5		C72	C79	C81	108.7(4)
C34	C37	H37A	109.5		C72	C79	C82	110.0(4)
C34	C37	H37B	109.5		C80	C79	C81	108.3(4)
C34	C37	H37C	109.4		C80	C79	C82	109.3(4)
H37A	C37	H37B	109.4		C81	C79	C82	108.0(4)
H37A	C37	H37C	109.3		C79	C80	H80A	109.4
H37B	C37	H37C	109.5		C79	C80	H80B	109.5
C30	C38	C39	109.1(4)		C79	C80	H80C	109.4
C30	C38	C40	111.0(4)		H80A	C80	H80B	109.5
C30	C38	C41	109.4(4)		H80A	C80	H80C	109.6
C39	C38	C40	110.1(4)		H80B	C80	H80C	109.4
C39	C38	C41	109.3(4)		C79	C81	H81A	109.5
C40	C38	C41	107.9(4)		C79	C81	H81B	109.4
C38	C39	H39A	109.5		C79	C81	H81C	109.4
C38	C39	H39B	109.5		H81A	C81	H81B	109.4
C38	C39	H39C	109.4		H81A	C81	H81C	109.6
H39A	C39	H39B	109.6		H81B	C81	H81C	109.5
H39A	C39	H39C	109.4		C79	C82	H82A	109.4
H39B	C39	H39C	109.5		C79	C82	H82B	109.5
C38	C40	H40A	109.5		C79	C82	H82C	109.4
C38	C40	H40B	109.5		H82A	C82	H82B	109.5
C38	C40	H40C	109.5		H82A	C82	H82C	109.5
H40A	C40	H40B	109.5		H82B	C82	H82C	109.5
H40A	C40	H40C	109.5		C68	C1B	H1BA	109.5
H40B	C40	H40C	109.4		C68	C1B	H1BB	109.5
C38	C41	H41A	109.5		C68	C1B	H1BC	109.5
C38	C41	H41B	109.6		H1BA	C1B	H1BB	109.5
C38	C41	H41C	109.5		H1BA	C1B	H1BC	109.4
H41A	C41	H41B	109.4		H1BB	C1B	H1BC	109.5
H41A	C41	H41C	109.4		H1	O1	C1D	109.4
H41B	C41	H41C	109.4		O1	C1D	H1DA	109.4

O16	C1C	H1CA	109.6		O1	C1D	H1DB	109.5
O16	C1C	H1CB	109.5		O1	C1D	H1DC	109.5
O16	C1C	H1CC	109.5		H1DA	C1D	H1DB	109.5
H1CA	C1C	H1CB	109.5		H1DA	C1D	H1DC	109.4
H1CA	C1C	H1CC	109.4		H1DB	C1D	H1DC	109.5
H1CB	C1C	H1CC	109.3		H7	O7	C1E	109.6
O6	Cu2	N7	93.5(1)		O7	C1E	H1EA	109.5
O6	Cu2	O12	88.8(1)		O7	C1E	H1EB	109.5
O6	Cu2	N57	175.7(1)		O7	C1E	H1EC	109.4
N7	Cu2	O12	175.3(1)		H1EA	C1E	H1EB	109.5
N7	Cu2	N57	84.7(1)		H1EA	C1E	H1EC	109.4
O12	Cu2	N57	93.3(1)		H1EB	C1E	H1EC	109.4
Cu2	O6	C42	129.2(2)		H13A	O13	H13B	106
Cu2	N7	C44	124.8(2)					

Table A2. Bond angles (°) for complex **[Cu^{II}L^{N2O2}]** (**2**).

Crystal structure data of complex **[$Fe^{III}L^{N3O2}$]** (**4**) in **Chapter 4**

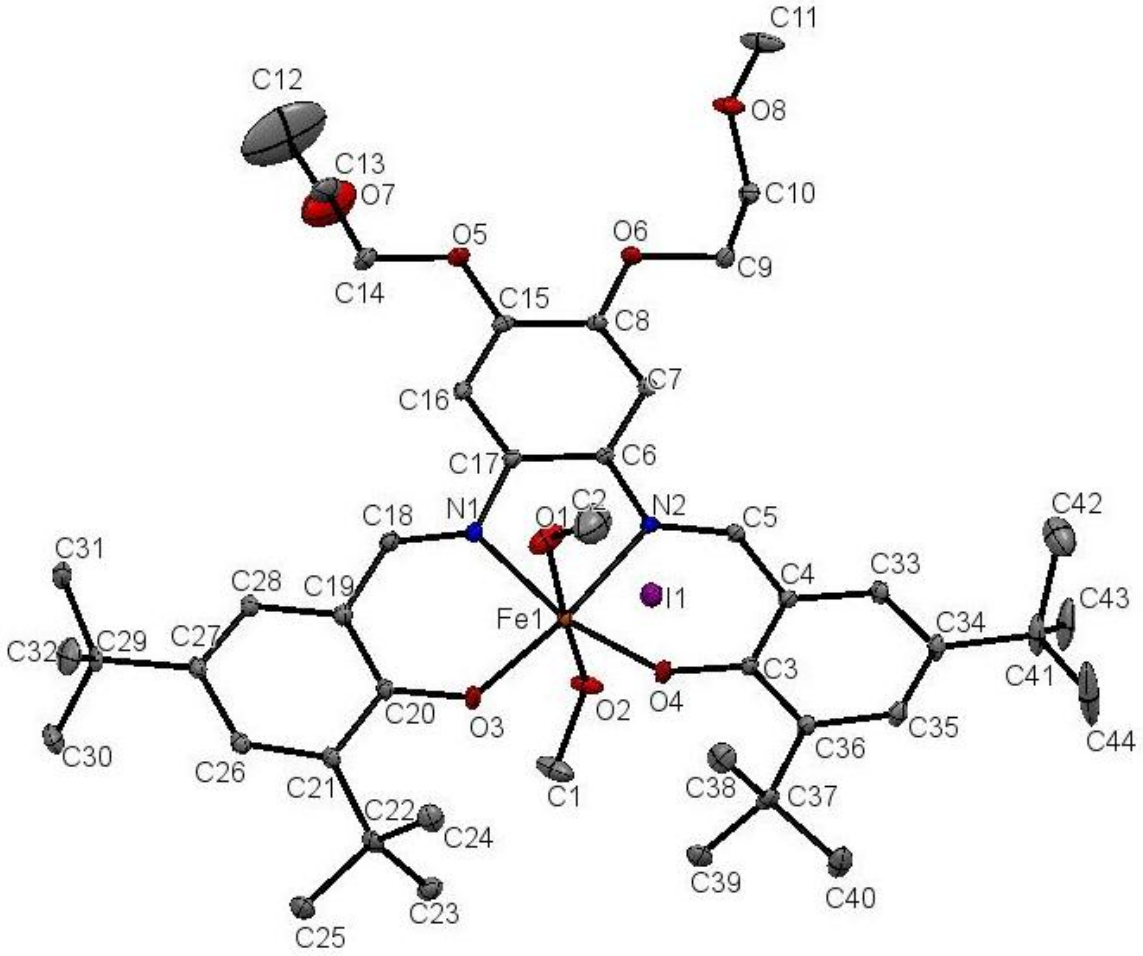

Figure A2. X-ray crystal structure of **[$Fe^{III}L^{N3O2}$]** (**4**).

Atom1	Atom2	Length		Atom1	Atom2	Length
Fe1	O1	2.097(2)		C22	C24	1.532(5)
Fe1	O2	2.127(2)		C22	C25	1.533(4)
Fe1	O3	1.883(2)		C24	H01D	0.960(4)
Fe1	O4	1.865(2)		C24	H01E	0.961(4)
Fe1	N1	2.076(3)		C24	H01F	0.960(4)
Fe1	N2	2.109(2)		C25	H01G	0.960(4)
O1	C2	1.331(8)		C25	H01H	0.959(3)
O2	H008	0.85(2)		C25	H01I	0.959(3)
O2	C1	1.424(5)		C26	H00M	0.930(3)
O3	C20	1.326(4)		C26	C27	1.411(4)
O4	C3	1.313(4)		C27	C28	1.369(4)
O5	C14	1.413(4)		C27	C29	1.536(5)
O5	C15	1.363(4)		C28	H00O	0.930(3)
O6	C8	1.364(3)		C29	C30	1.540(6)
O6	C9	1.432(4)		C29	C31	1.535(5)
O7	C12	1.46(1)		C29	C32	1.518(5)
O7	C13	1.226(7)		C30	H	0.959(4)
O8	C10	1.420(4)		C30	H01X	0.960(4)
O8	C11	1.423(4)		C30	H01Y	0.960(5)
N1	C17	1.418(3)		C31	H01U	0.960(5)
N1	C18	1.295(4)		C31	H01V	0.960(5)
N2	C5	1.301(4)		C31	H01W	0.959(4)
N2	C6	1.420(4)		C32	H0AA	0.960(4)
C1	H01	0.960(4)		C32	HE	0.959(5)
C1	HC	0.959(5)		C32	HF	0.960(5)
C1	HD	0.960(5)		C33	H00H	0.930(3)
C3	C4	1.426(4)		C33	C34	1.372(4)
C3	C36	1.417(4)		C34	C35	1.406(4)
C4	C5	1.455(4)		C34	C41	1.530(5)
C4	C33	1.401(5)		C35	H00V	0.930(3)
C5	H00K	0.930(3)		C35	C36	1.399(5)
C6	C7	1.402(4)		C36	C37	1.535(4)
C6	C17	1.401(5)		C37	C38	1.541(5)
C7	H00E	0.930(3)		C37	C39	1.541(5)
C7	C8	1.386(4)		C37	C40	1.529(5)
C8	C15	1.415(5)		C38	H01O	0.960(5)
C9	H00C	0.969(3)		C38	H01P	0.959(3)
C9	H00D	0.971(3)		C38	H01Q	0.960(4)
C9	C10	1.493(4)		C39	H01A	0.960(4)
C10	H00A	0.970(3)		C39	H01B	0.960(3)

C10	H00B	0.969(3)		C39	H01C	0.960(4)
C11	H01Z	0.960(5)		C40	H01R	0.960(4)
C11	HA	0.961(5)		C40	H01S	0.960(4)
C11	HB	0.961(4)		C40	H01T	0.960(4)
C12	H2A	0.96(1)		C41	C42	1.634(7)
C12	H2B	0.96(2)		C41	C43	1.474(6)
C12	H2C	0.96(2)		C41	C44	1.445(7)
C13	H1AA	0.930(5)		C42	H3AA	0.959(6)
C13	C14	1.475(6)		C42	HK	0.961(6)
C14	H01M	0.970(3)		C42	HL	0.960(6)
C14	H01N	0.969(3)		C43	H2AA	0.960(6)
C15	C16	1.374(4)		C43	HG	0.961(6)
C16	H00J	0.930(3)		C43	HH	0.960(5)
C16	C17	1.399(4)		C44	H0AB	0.960(7)
C18	H011	0.930(3)		C44	H0AC	0.961(8)
C18	C19	1.447(4)		C44	H0AD	0.960(8)
C19	C20	1.410(4)		O9	H00F	0.820(3)
C19	C28	1.409(5)		O9	C45	1.437(7)
C20	C21	1.440(4)		C45	H4AA	0.959(5)
C21	C22	1.536(4)		C45	HI	0.961(5)
C21	C26	1.388(5)		C45	HJ	0.960(5)
C22	C23	1.542(4)				

Table A3. Bond lengths (Å) for complex **[$Fe^{III}L^{N3O2}$] (4)**.

Atom1	Atom2	Atom3	Angle		Atom1	Atom2	Atom3	Angle
O1	Fe1	O2	173.0(1)		C24	C22	C25	107.9(3)
O1	Fe1	O3	94.3(1)		C22	C24	H01D	109.5(3)
O1	Fe1	O4	89.9(1)		C22	C24	H01E	109.4(3)
O1	Fe1	N1	83.8(1)		C22	C24	H01F	109.4(3)
O1	Fe1	N2	92.2(1)		H01D	C24	H01E	109.4(4)
O2	Fe1	O3	91.2(1)		H01D	C24	H01F	109.5(4)
O2	Fe1	O4	93.04(9)		H01E	C24	H01F	109.5(4)
O2	Fe1	N1	91.96(9)		C22	C25	H01G	109.4(3)
O2	Fe1	N2	81.50(9)		C22	C25	H01H	109.4(3)
O3	Fe1	O4	102.5(1)		C22	C25	H01I	109.5(3)
O3	Fe1	N1	90.3(1)		H01G	C25	H01H	109.5(3)
O3	Fe1	N2	166.4(1)		H01G	C25	H01I	109.5(3)
O4	Fe1	N1	166.2(1)		H01H	C25	H01I	109.5(3)
O4	Fe1	N2	89.46(9)		C21	C26	H00M	117.8(3)
N1	Fe1	N2	78.53(9)		C21	C26	C27	124.6(3)

Fe1	O1	C2	135.4(3)		H00M	C26	C27	117.6(3)
Fe1	O2	H008	119(2)		C26	C27	C28	117.0(3)
Fe1	O2	C1	128.4(2)		C26	C27	C29	120.0(3)
H008	O2	C1	109(2)		C28	C27	C29	122.9(3)
Fe1	O3	C20	132.4(2)		C19	C28	C27	121.6(3)
Fe1	O4	C3	134.4(2)		C19	C28	H00O	119.2(3)
C14	O5	C15	116.6(2)		C27	C28	H00O	119.2(3)
C8	O6	C9	116.3(2)		C27	C29	C30	108.4(3)
C12	O7	C13	111.7(7)		C27	C29	C31	112.0(3)
C10	O8	C11	110.9(3)		C27	C29	C32	109.7(3)
Fe1	N1	C17	114.9(2)		C30	C29	C31	107.4(3)
Fe1	N1	C18	123.6(2)		C30	C29	C32	110.4(3)
C17	N1	C18	121.4(3)		C31	C29	C32	108.9(3)
Fe1	N2	C5	123.0(2)		C29	C30	H	109.5(4)
Fe1	N2	C6	114.3(2)		C29	C30	H01X	109.5(4)
C5	N2	C6	122.5(2)		C29	C30	H01Y	109.5(4)
O2	C1	H01	109.5(4)		H	C30	H01X	109.5(4)
O2	C1	HC	109.4(4)		H	C30	H01Y	109.4(4)
O2	C1	HD	109.4(4)		H01X	C30	H01Y	109.4(4)
H01	C1	HC	109.6(4)		C29	C31	H01U	109.4(4)
H01	C1	HD	109.5(4)		C29	C31	H01V	109.4(4)
HC	C1	HD	109.5(4)		C29	C31	H01W	109.4(4)
O4	C3	C4	121.4(3)		H01U	C31	H01V	109.5(4)
O4	C3	C36	119.4(3)		H01U	C31	H01W	109.5(4)
C4	C3	C36	119.1(3)		H01V	C31	H01W	109.5(4)
C3	C4	C5	123.8(3)		C29	C32	H0AA	109.4(4)
C3	C4	C33	120.0(3)		C29	C32	HE	109.5(4)
C5	C4	C33	116.2(3)		C29	C32	HF	109.5(4)
N2	C5	C4	126.3(3)		H0AA	C32	HE	109.4(4)
N2	C5	H00K	116.8(3)		H0AA	C32	HF	109.4(4)
C4	C5	H00K	116.9(3)		HE	C32	HF	109.5(4)
N2	C6	C7	124.7(3)		C4	C33	H00H	119.0(3)
N2	C6	C17	115.6(3)		C4	C33	C34	122.1(3)
C7	C6	C17	119.8(3)		H00H	C33	C34	118.9(3)
C6	C7	H00E	120.0(3)		C33	C34	C35	117.1(3)
C6	C7	C8	120.0(3)		C33	C34	C41	120.5(3)
H00E	C7	C8	120.0(3)		C35	C34	C41	122.4(3)
O6	C8	C7	124.3(3)		C34	C35	H00V	118.0(3)
O6	C8	C15	115.5(3)		C34	C35	C36	124.0(3)
C7	C8	C15	120.2(3)		H00V	C35	C36	118.0(3)
O6	C9	H00C	109.9(3)		C3	C36	C35	117.6(3)

O6	C9	H00D	109.8(3)		C3	C36	C37	120.8(3)
O6	C9	C10	109.1(2)		C35	C36	C37	121.6(3)
H00C	C9	H00D	108.3(3)		C36	C37	C38	109.9(3)
H00C	C9	C10	109.8(3)		C36	C37	C39	111.3(3)
H00D	C9	C10	109.9(3)		C36	C37	C40	111.7(3)
O8	C10	C9	109.5(3)		C38	C37	C39	108.9(3)
O8	C10	H00A	109.8(3)		C38	C37	C40	108.3(3)
O8	C10	H00B	109.8(3)		C39	C37	C40	106.7(3)
C9	C10	H00A	109.7(3)		C37	C38	H01O	109.5(3)
C9	C10	H00B	109.8(3)		C37	C38	H01P	109.5(3)
H00A	C10	H00B	108.3(3)		C37	C38	H01Q	109.5(3)
O8	C11	H01Z	109.5(4)		H01O	C38	H01P	109.5(4)
O8	C11	HA	109.5(4)		H01O	C38	H01Q	109.3(4)
O8	C11	HB	109.4(4)		H01P	C38	H01Q	109.5(4)
H01Z	C11	HA	109.5(4)		C37	C39	H01A	109.4(3)
H01Z	C11	HB	109.5(4)		C37	C39	H01B	109.5(3)
HA	C11	HB	109.4(4)		C37	C39	H01C	109.5(3)
O7	C12	H2A	109(1)		H01A	C39	H01B	109.5(3)
O7	C12	H2B	110(1)		H01A	C39	H01C	109.5(3)
O7	C12	H2C	109(1)		H01B	C39	H01C	109.4(3)
H2A	C12	H2B	109(1)		C37	C40	H01R	109.4(3)
H2A	C12	H2C	109(1)		C37	C40	H01S	109.4(3)
H2B	C12	H2C	109(1)		C37	C40	H01T	109.5(3)
O7	C13	H1AA	121.6(5)		H01R	C40	H01S	109.4(4)
O7	C13	C14	116.7(5)		H01R	C40	H01T	109.5(4)
H1AA	C13	C14	121.6(4)		H01S	C40	H01T	109.6(4)
O5	C14	C13	110.2(3)		C34	C41	C42	107.1(3)
O5	C14	H01M	109.6(3)		C34	C41	C43	112.0(3)
O5	C14	H01N	109.7(3)		C34	C41	C44	115.2(4)
C13	C14	H01M	109.6(3)		C42	C41	C43	100.6(4)
C13	C14	H01N	109.6(3)		C42	C41	C44	103.6(4)
H01M	C14	H01N	108.1(3)		C43	C41	C44	116.5(4)
O5	C15	C8	116.8(3)		C41	C42	H3AA	109.5(5)
O5	C15	C16	123.7(3)		C41	C42	HK	109.4(5)
C8	C15	C16	119.6(3)		C41	C42	HL	109.4(5)
C15	C16	H00J	119.6(3)		H3AA	C42	HK	109.5(6)
C15	C16	C17	120.8(3)		H3AA	C42	HL	109.5(6)
H00J	C16	C17	119.6(3)		HK	C42	HL	109.5(6)
N1	C17	C6	116.5(3)		C41	C43	H2AA	109.5(5)
N1	C17	C16	123.8(3)		C41	C43	HG	109.4(5)
C6	C17	C16	119.6(3)		C41	C43	HH	109.5(5)

N1	C18	H011	116.7(3)		H2AA	C43	HG	109.5(5)
N1	C18	C19	126.5(3)		H2AA	C43	HH	109.5(5)
H011	C18	C19	116.7(3)		HG	C43	HH	109.4(5)
C18	C19	C20	124.1(3)		C41	C44	H0AB	109.5(6)
C18	C19	C28	115.1(3)		C41	C44	H0AC	109.5(6)
C20	C19	C28	120.8(3)		C41	C44	H0AD	109.5(6)
O3	C20	C19	122.1(3)		H0AB	C44	H0AC	109.4(7)
O3	C20	C21	119.3(3)		H0AB	C44	H0AD	109.5(7)
C19	C20	C21	118.6(3)		H0AC	C44	H0AD	109.4(7)
C20	C21	C22	121.0(3)		H00F	O9	C45	109.4(3)
C20	C21	C26	117.1(3)		O9	C45	H4AA	109.6(5)
C22	C21	C26	121.9(3)		O9	C45	HI	109.5(5)
C21	C22	C23	110.2(3)		O9	C45	HJ	109.4(5)
C21	C22	C24	109.9(3)		H4AA	C45	HI	109.5(5)
C21	C22	C25	111.4(3)		H4AA	C45	HJ	109.5(5)
C23	C22	C24	110.1(3)		HI	C45	HJ	109.4(5)
C23	C22	C25	107.3(3)					

Table A4. Bond angles (°) for complex **[$Fe^{III}L^{N3O2}$]** (**4**).

Crystal structure data of complex **[Fe^{III}L^{N3O2}]** (**4**) in **Chapter 4**

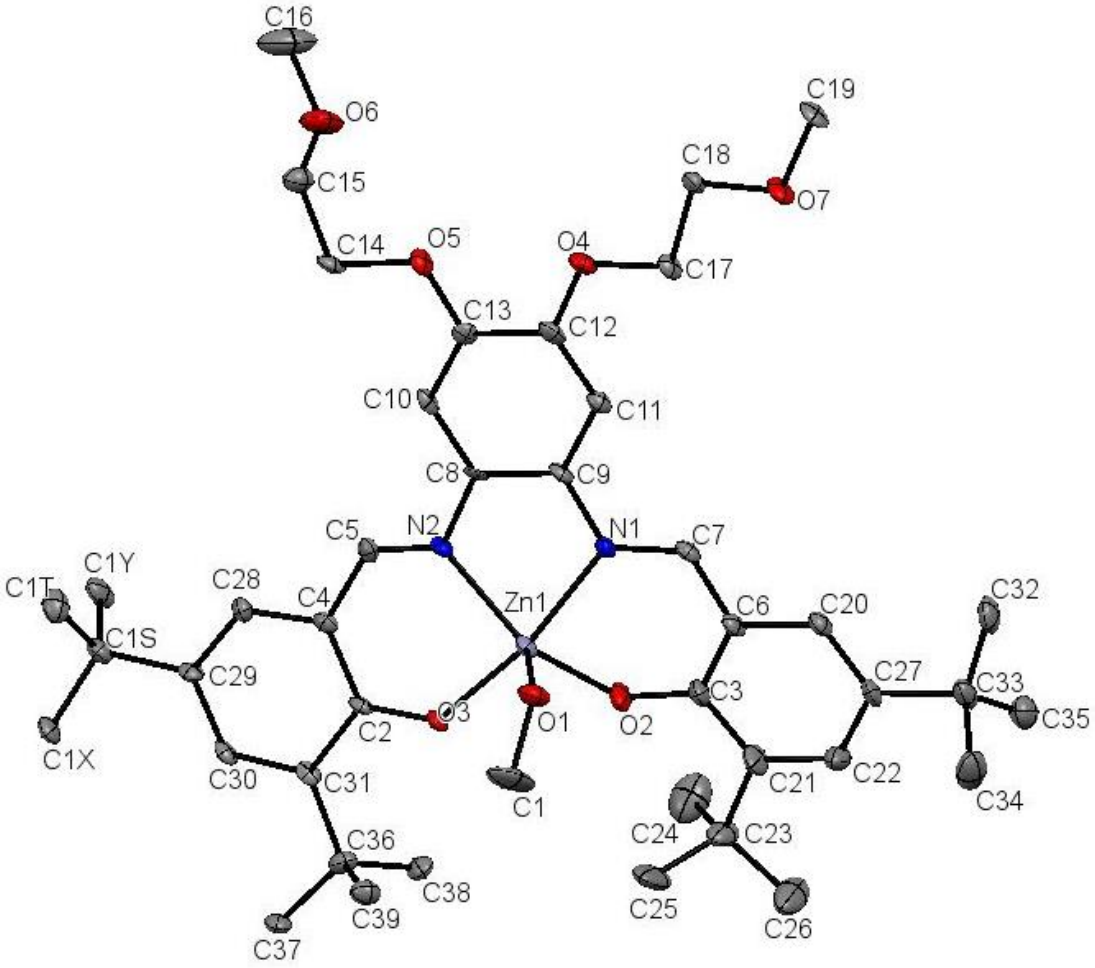

Figure A3. X-ray crystal structure of **[Zn^{II}L^{N2O2}]** (**3**).

Atom1	Atom2	Length		Atom1	Atom2	Length
C31	C30	1.407(9)		C1H	H1HA	0.98
C31	C36	1.52(1)		C1H	H1HB	0.98
C31	C2	1.446(6)		C1H	H1HC	0.981
C30	H30	0.95		C1H	O0AA	1.410(9)
C30	C29	1.39(1)		C1R	C9AA	1.40(1)
C14	H14A	0.99		C1R	C1BA	1.41(1)
C14	H14B	0.99		C1R	N24	1.399(6)
C14	C15	1.49(1)		C1W	H1WA	0.98
C14	O5	1.438(9)		C1W	H1WB	0.98
C8	C9	1.392(8)		C1W	H1WC	0.98
C8	C10	1.42(1)		C1W	C7AA	1.51(1)
C8	N2	1.391(6)		C2C	C2AA	1.379(7)
C9	C11	1.397(8)		C2C	C7AA	1.51(1)
C9	N1	1.42(1)		C2C	C43	1.41(1)
C15	H15A	0.989		C3AA	H3AA	0.98
C15	H15B	0.989		C3AA	H3AB	0.981
C15	O6	1.423(9)		C3AA	H3AC	0.981
C23	C24	1.51(1)		C3AA	O1AA	1.425(8)
C23	C26	1.49(2)		C5AA	H5AA	0.99
C23	C25	1.48(2)		C5AA	H5AB	0.989
C23	C21	1.61(1)		C5AA	O2AA	1.444(9)
C33	C34	1.59(1)		C8AA	H8AA	0.98
C33	C35	1.52(1)		C8AA	H8AB	0.98
C33	C32	1.48(1)		C8AA	H8AC	0.98
C33	C27	1.55(1)		C8AA	C4BA	1.54(1)
C34	H34A	0.98		C9AA	H9AA	0.95
C34	H34B	0.98		C9AA	C6AA	1.363(7)
C34	H34C	0.98		C2AA	H2AA	0.951
C24	H24A	0.98		C2AA	C66	1.40(1)
C24	H24B	0.98		C7AA	C46	1.540(8)
C24	H24C	0.98		C7AA	C50	1.53(1)
C35	H35A	0.98		C6AA	C0BA	1.41(1)
C35	H35B	0.98		C6AA	O2AA	1.395(8)
C35	H35C	0.979		C1BA	C4AA	1.401(7)
C26	H26A	0.98		C1BA	N5	1.425(9)
C26	H26B	0.98		C2BA	H2BA	0.949
C26	H26C	0.98		C2BA	C66	1.436(7)
C32	H32A	0.98		C2BA	N24	1.29(1)
C32	H32B	0.979		C3BA	H3BA	0.98
C32	H32C	0.979		C3BA	H3BB	0.979

C25	H25A	0.98		C3BA	H3BC	0.98
C25	H25B	0.98		C3BA	C53	1.54(1)
C25	H25C	0.98		C5BA	H5BA	0.951
C16	H16A	0.98		C5BA	C86	1.42(1)
C16	H16B	0.98		C5BA	N5	1.32(1)
C16	H16C	0.98		C0BA	C4AA	1.374(9)
C16	O6	1.41(1)		C0BA	O9	1.371(5)
C1S	C1T	1.54(1)		C4BA	C51	1.52(1)
C1S	C1X	1.520(8)		C4BA	C57	1.535(8)
C1S	C1Y	1.54(1)		C4BA	C92	1.53(1)
C1S	C29	1.54(1)		C1AA	C53	1.532(7)
C1T	H1TA	0.98		C1AA	C71	1.44(1)
C1T	H1TB	0.98		C1AA	C73	1.37(1)
C1T	H1TC	0.98		C4AA	H4AA	0.951
C39	H39A	0.98		C6BA	H6BA	0.989
C39	H39B	0.98		C6BA	H6BB	0.99
C39	H39C	0.979		C6BA	C48	1.484(8)
C39	C36	1.54(1)		C6BA	O9	1.428(9)
C38	H38A	0.979		C43	H43	0.95
C38	H38B	0.981		C43	C92	1.42(1)
C38	H38C	0.981		C46	H46A	0.979
C38	C36	1.52(1)		C46	H46B	0.98
C1X	H1XA	0.98		C46	H46C	0.98
C1X	H1XB	0.979		C48	H48A	0.989
C1X	H1XC	0.98		C48	H48B	0.99
C1Y	H1YA	0.981		C48	O1AA	1.426(9)
C1Y	H1YB	0.981		C50	H50A	0.98
C1Y	H1YC	0.98		C50	H50B	0.98
C5	H5	0.949		C50	H50C	0.98
C5	C4	1.430(8)		C51	H51A	0.98
C5	N2	1.287(8)		C51	H51B	0.981
C36	C37	1.522(8)		C51	H51C	0.98
C1	H1A	0.98		C53	C55	1.53(1)
C1	H1B	0.98		C53	C96	1.52(1)
C1	H1C	0.98		C55	H55A	0.98
C1	O1	1.445(9)		C55	H55B	0.979
C37	H37A	0.979		C55	H55C	0.98
C37	H37B	0.979		C57	H57A	0.981
C37	H37C	0.981		C57	H57B	0.98
C19	H19A	0.981		C57	H57C	0.98
C19	H19B	0.979		C60	H60	0.95

C19	H19C	0.979		C60	C72	1.38(1)
C19	O7	1.410(7)		C60	C86	1.44(1)
C12	C13	1.40(1)		C63	C66	1.43(1)
C12	C11	1.37(1)		C63	C92	1.405(8)
C12	O4	1.352(7)		C63	O43	1.342(9)
C13	C10	1.357(8)		C64	H64A	0.98
C13	O5	1.38(1)		C64	H64B	0.978
C4	C28	1.410(9)		C64	H64C	0.98
C4	C2	1.43(1)		C64	C65	1.55(1)
C28	H28	0.949		C65	C72	1.52(1)
C28	C29	1.354(7)		C65	C79	1.52(1)
C2	O3	1.294(7)		C65	C80	1.525(8)
C18	H18A	0.99		C71	C86	1.439(7)
C18	H18B	0.99		C71	O12	1.289(9)
C18	C17	1.502(9)		C72	C73	1.412(8)
C18	O7	1.423(8)		C73	H73	0.949
C17	H17A	0.989		C79	H79A	0.98
C17	H17B	0.99		C79	H79B	0.98
C17	O4	1.443(8)		C79	H79C	0.98
C10	H10	0.951		C80	H80A	0.981
C20	H20	0.951		C80	H80B	0.98
C20	C6	1.429(8)		C80	H80C	0.98
C20	C27	1.38(1)		C96	H96A	0.98
C6	C7	1.42(1)		C96	H96B	0.979
C6	C3	1.400(8)		C96	H96C	0.981
C22	H22	0.95		N5	Zn0A	2.036(4)
C22	C21	1.38(1)		N24	Zn0A	2.123(7)
C22	C27	1.41(1)		O12	Zn0A	1.945(5)
C7	H7	0.949		O22	H22A	0.907
C7	N1	1.307(9)		O22	H22B	0.907
C21	C3	1.43(1)		O22	Zn0A	2.097(6)
C3	O2	1.313(8)		O43	Zn0A	1.961(4)
C11	H11	0.95		C0AA	H0AA	0.98
N1	Zn1	2.082(4)		C0AA	H0AB	0.98
N2	Zn1	2.065(7)		C0AA	H0AC	0.98
O3	Zn1	1.952(3)		C0AA	O10	1.32(2)
O2	Zn1	1.946(6)		O10	H10A	0.84
O1	H1	0.87(2)		C40	H40A	0.98
O1	Zn1	2.116(4)		C40	H40B	0.98
C1A	H1AA	0.99		C40	H40C	0.98
C1A	H1AB	0.99		C40	O11	1.45(1)

C1A	C5AA	1.52(1)		O11	H11A	0.84
C1A	O0AA	1.404(7)				

Table A5. Bond lengths (Å) for complex **[$Zn^{II}L^{N2O2}$]** (**3**).

Atom1	Atom2	Atom3	Angle		Atom1	Atom2	Atom3	Angle
C30	C31	C36	122.5(6)		H1AB	C1A	O0AA	109.6
C30	C31	C2	117.5(5)		C5AA	C1A	O0AA	110.2(6)
C36	C31	C2	120.1(6)		H1HA	C1H	H1HB	109.6
C31	C30	H30	117.6		H1HA	C1H	H1HC	109.5
C31	C30	C29	125.0(6)		H1HA	C1H	O0AA	109.5
H30	C30	C29	117.5		H1HB	C1H	H1HC	109.5
H14A	C14	H14B	108.5		H1HB	C1H	O0AA	109.4
H14A	C14	C15	110.1		H1HC	C1H	O0AA	109.4
H14A	C14	O5	110		C9AA	C1R	C1BA	118.5(6)
H14B	C14	C15	110.1		C9AA	C1R	N24	125.7(6)
H14B	C14	O5	109.9		C1BA	C1R	N24	115.7(6)
C15	C14	O5	108.2(6)		H1WA	C1W	H1WB	109.4
C9	C8	C10	117.0(5)		H1WA	C1W	H1WC	109.5
C9	C8	N2	117.9(5)		H1WA	C1W	C7AA	109.5
C10	C8	N2	125.1(5)		H1WB	C1W	H1WC	109.5
C8	C9	C11	121.0(6)		H1WB	C1W	C7AA	109.5
C8	C9	N1	114.6(5)		H1WC	C1W	C7AA	109.5
C11	C9	N1	124.3(6)		C2AA	C2C	C7AA	121.2(6)
C14	C15	H15A	110.3		C2AA	C2C	C43	115.8(6)
C14	C15	H15B	110.3		C7AA	C2C	C43	123.0(6)
C14	C15	O6	107.2(6)		H3AA	C3AA	H3AB	109.5
H15A	C15	H15B	108.6		H3AA	C3AA	H3AC	109.4
H15A	C15	O6	110.2		H3AA	C3AA	O1AA	109.6
H15B	C15	O6	110.2		H3AB	C3AA	H3AC	109.3
C24	C23	C26	109.6(9)		H3AB	C3AA	O1AA	109.5
C24	C23	C25	108.0(9)		H3AC	C3AA	O1AA	109.5
C24	C23	C21	110.4(8)		C1A	C5AA	H5AA	110.4
C26	C23	C25	109.3(9)		C1A	C5AA	H5AB	110.4
C26	C23	C21	111.3(9)		C1A	C5AA	O2AA	106.7(6)
C25	C23	C21	108.2(8)		H5AA	C5AA	H5AB	108.7
C34	C33	C35	108.1(7)		H5AA	C5AA	O2AA	110.3
C34	C33	C32	109.1(7)		H5AB	C5AA	O2AA	110.3
C34	C33	C27	105.0(7)		H8AA	C8AA	H8AB	109.4
C35	C33	C32	111.4(7)		H8AA	C8AA	H8AC	109.5
C35	C33	C27	110.7(7)		H8AA	C8AA	C4BA	109.4

C32	C33	C27	112.1(7)		H8AB	C8AA	H8AC	109.5
C33	C34	H34A	109.4		H8AB	C8AA	C4BA	109.5
C33	C34	H34B	109.5		H8AC	C8AA	C4BA	109.5
C33	C34	H34C	109.5		C1R	C9AA	H9AA	119.2
H34A	C34	H34B	109.4		C1R	C9AA	C6AA	121.6(6)
H34A	C34	H34C	109.5		H9AA	C9AA	C6AA	119.3
H34B	C34	H34C	109.5		C2C	C2AA	H2AA	118
C23	C24	H24A	109		C2C	C2AA	C66	123.9(6)
C23	C24	H24B	110		H2AA	C2AA	C66	118.1
C23	C24	H24C	109		C1W	C7AA	C2C	110.6(6)
H24A	C24	H24B	110		C1W	C7AA	C46	108.0(6)
H24A	C24	H24C	109		C1W	C7AA	C50	108.6(7)
H24B	C24	H24C	109		C2C	C7AA	C46	111.7(6)
C33	C35	H35A	109.5		C2C	C7AA	C50	111.1(6)
C33	C35	H35B	109.4		C46	C7AA	C50	106.7(6)
C33	C35	H35C	109.5		C9AA	C6AA	C0BA	119.9(6)
H35A	C35	H35B	109.5		C9AA	C6AA	O2AA	125.7(6)
H35A	C35	H35C	109.5		C0BA	C6AA	O2AA	114.4(5)
H35B	C35	H35C	109.5		C1R	C1BA	C4AA	119.5(6)
C23	C26	H26A	109		C1R	C1BA	N5	115.8(5)
C23	C26	H26B	109		C4AA	C1BA	N5	124.6(6)
C23	C26	H26C	109		H2BA	C2BA	C66	117.8
H26A	C26	H26B	110		H2BA	C2BA	N24	117.8
H26A	C26	H26C	109		C66	C2BA	N24	124.4(6)
H26B	C26	H26C	110		H3BA	C3BA	H3BB	109.5
C33	C32	H32A	109.5		H3BA	C3BA	H3BC	109.5
C33	C32	H32B	109.4		H3BA	C3BA	C53	109.4
C33	C32	H32C	109.5		H3BB	C3BA	H3BC	109.5
H32A	C32	H32B	109.6		H3BB	C3BA	C53	109.5
H32A	C32	H32C	109.5		H3BC	C3BA	C53	109.4
H32B	C32	H32C	109.4		H5BA	C5BA	C86	117.4
C23	C25	H25A	110		H5BA	C5BA	N5	117.5
C23	C25	H25B	109		C86	C5BA	N5	125.1(6)
C23	C25	H25C	109		C6AA	C0BA	C4AA	119.5(5)
H25A	C25	H25B	109		C6AA	C0BA	O9	116.4(5)
H25A	C25	H25C	109		C4AA	C0BA	O9	124.1(5)
H25B	C25	H25C	109		C8AA	C4BA	C51	109.0(6)
H16A	C16	H16B	109		C8AA	C4BA	C57	106.7(6)
H16A	C16	H16C	109		C8AA	C4BA	C92	109.8(6)
H16A	C16	O6	109		C51	C4BA	C57	107.7(6)
H16B	C16	H16C	109		C51	C4BA	C92	111.0(6)

H16B	C16	O6	109		C57	C4BA	C92	112.5(6)
H16C	C16	O6	110		C53	C1AA	C71	119.3(6)
C1T	C1S	C1X	108.0(6)		C53	C1AA	C73	121.5(6)
C1T	C1S	C1Y	109.3(6)		C71	C1AA	C73	119.2(6)
C1T	C1S	C29	108.7(6)		C1BA	C4AA	C0BA	121.0(6)
C1X	C1S	C1Y	109.4(6)		C1BA	C4AA	H4AA	119.5
C1X	C1S	C29	111.7(6)		C0BA	C4AA	H4AA	119.5
C1Y	C1S	C29	109.7(6)		H6BA	C6BA	H6BB	108.4
C1S	C1T	H1TA	109.5		H6BA	C6BA	C48	109.8
C1S	C1T	H1TB	109.5		H6BA	C6BA	O9	109.9
C1S	C1T	H1TC	109.5		H6BB	C6BA	C48	109.8
H1TA	C1T	H1TB	109.4		H6BB	C6BA	O9	109.7
H1TA	C1T	H1TC	109.4		C48	C6BA	O9	109.3(6)
H1TB	C1T	H1TC	109.5		C2C	C43	H43	117.9
H39A	C39	H39B	109.4		C2C	C43	C92	124.1(6)
H39A	C39	H39C	109.5		H43	C43	C92	117.9
H39A	C39	C36	109.5		C7AA	C46	H46A	109.5
H39B	C39	H39C	109.5		C7AA	C46	H46B	109.5
H39B	C39	C36	109.5		C7AA	C46	H46C	109.4
H39C	C39	C36	109.5		H46A	C46	H46B	109.5
H38A	C38	H38B	109.4		H46A	C46	H46C	109.4
H38A	C38	H38C	109.5		H46B	C46	H46C	109.5
H38A	C38	C36	109.5		C6BA	C48	H48A	109.7
H38B	C38	H38C	109.4		C6BA	C48	H48B	109.8
H38B	C38	C36	109.5		C6BA	C48	O1AA	109.5(6)
H38C	C38	C36	109.5		H48A	C48	H48B	108.3
C1S	C1X	H1XA	109.5		H48A	C48	O1AA	109.8
C1S	C1X	H1XB	109.5		H48B	C48	O1AA	109.7
C1S	C1X	H1XC	109.5		C7AA	C50	H50A	109.5
H1XA	C1X	H1XB	109.4		C7AA	C50	H50B	109.6
H1XA	C1X	H1XC	109.4		C7AA	C50	H50C	109.5
H1XB	C1X	H1XC	109.5		H50A	C50	H50B	109.5
C1S	C1Y	H1YA	109.5		H50A	C50	H50C	109.4
C1S	C1Y	H1YB	109.5		H50B	C50	H50C	109.4
C1S	C1Y	H1YC	109.4		C4BA	C51	H51A	109.5
H1YA	C1Y	H1YB	109.6		C4BA	C51	H51B	109.5
H1YA	C1Y	H1YC	109.5		C4BA	C51	H51C	109.6
H1YB	C1Y	H1YC	109.4		H51A	C51	H51B	109.4
H5	C5	C4	116.4		H51A	C51	H51C	109.4
H5	C5	N2	116.3		H51B	C51	H51C	109.5
C4	C5	N2	127.3(6)		C3BA	C53	C1AA	112.7(6)

C31	C36	C39	109.0(6)		C3BA	C53	C55	106.5(6)
C31	C36	C38	111.8(6)		C3BA	C53	C96	107.1(6)
C31	C36	C37	111.6(6)		C1AA	C53	C55	110.0(6)
C39	C36	C38	110.4(6)		C1AA	C53	C96	111.4(6)
C39	C36	C37	107.3(6)		C55	C53	C96	109.0(6)
C38	C36	C37	106.5(6)		C53	C55	H55A	109.4
H1A	C1	H1B	109.5		C53	C55	H55B	109.5
H1A	C1	H1C	109.5		C53	C55	H55C	109.5
H1A	C1	O1	109.5		H55A	C55	H55B	109.5
H1B	C1	H1C	109.4		H55A	C55	H55C	109.4
H1B	C1	O1	109.5		H55B	C55	H55C	109.5
H1C	C1	O1	109.4		C4BA	C57	H57A	109.4
C36	C37	H37A	109.4		C4BA	C57	H57B	109.5
C36	C37	H37B	109.4		C4BA	C57	H57C	109.5
C36	C37	H37C	109.4		H57A	C57	H57B	109.4
H37A	C37	H37B	109.5		H57A	C57	H57C	109.5
H37A	C37	H37C	109.5		H57B	C57	H57C	109.5
H37B	C37	H37C	109.6		H60	C60	C72	119.9
H19A	C19	H19B	109.5		H60	C60	C86	119.9
H19A	C19	H19C	109.4		C72	C60	C86	120.2(6)
H19A	C19	O7	109.3		C66	C63	C92	119.6(7)
H19B	C19	H19C	109.5		C66	C63	O43	120.0(6)
H19B	C19	O7	109.6		C92	C63	O43	120.4(6)
H19C	C19	O7	109.5		H64A	C64	H64B	109.4
C13	C12	C11	118.4(7)		H64A	C64	H64C	109.4
C13	C12	O4	116.9(6)		H64A	C64	C65	109.4
C11	C12	O4	124.7(7)		H64B	C64	H64C	109.6
C12	C13	C10	121.1(6)		H64B	C64	C65	109.6
C12	C13	O5	115.2(6)		H64C	C64	C65	109.5
C10	C13	O5	123.7(6)		C64	C65	C72	109.2(6)
C5	C4	C28	116.2(6)		C64	C65	C79	108.9(6)
C5	C4	C2	124.5(6)		C64	C65	C80	108.1(6)
C28	C4	C2	119.3(6)		C72	C65	C79	110.3(6)
C4	C28	H28	117.9		C72	C65	C80	112.7(6)
C4	C28	C29	124.3(6)		C79	C65	C80	107.6(6)
H28	C28	C29	117.9		C2AA	C66	C2BA	116.5(6)
C31	C2	C4	117.8(5)		C2AA	C66	C63	119.0(6)
C31	C2	O3	120.1(5)		C2BA	C66	C63	124.5(6)
C4	C2	O3	122.1(5)		C1AA	C71	C86	116.6(6)
H18A	C18	H18B	108.9		C1AA	C71	O12	121.6(6)
H18A	C18	C17	110.8		C86	C71	O12	121.8(6)

H18A	C18	O7	110.8		C60	C72	C65	121.9(7)
H18B	C18	C17	110.8		C60	C72	C73	117.2(7)
H18B	C18	O7	110.8		C65	C72	C73	120.9(7)
C17	C18	O7	104.7(5)		C1AA	C73	C72	125.2(7)
C18	C17	H17A	110.1		C1AA	C73	H73	117.5
C18	C17	H17B	110		C72	C73	H73	117.4
C18	C17	O4	108.4(5)		C65	C79	H79A	109.5
H17A	C17	H17B	108.4		C65	C79	H79B	109.5
H17A	C17	O4	110		C65	C79	H79C	109.5
H17B	C17	O4	110		H79A	C79	H79B	109.5
C8	C10	C13	121.5(6)		H79A	C79	H79C	109.5
C8	C10	H10	119.3		H79B	C79	H79C	109.4
C13	C10	H10	119.2		C65	C80	H80A	109.5
H20	C20	C6	119.5		C65	C80	H80B	109.5
H20	C20	C27	119.5		C65	C80	H80C	109.5
C6	C20	C27	120.9(6)		H80A	C80	H80B	109.5
C20	C6	C7	114.2(6)		H80A	C80	H80C	109.4
C20	C6	C3	121.2(6)		H80B	C80	H80C	109.5
C7	C6	C3	124.6(6)		C5BA	C86	C60	113.2(6)
C30	C29	C1S	124.3(6)		C5BA	C86	C71	125.3(6)
C30	C29	C28	116.2(6)		C60	C86	C71	121.4(6)
C1S	C29	C28	119.6(6)		C4BA	C92	C43	120.9(6)
H22	C22	C21	117.9		C4BA	C92	C63	121.4(6)
H22	C22	C27	117.8		C43	C92	C63	117.7(7)
C21	C22	C27	124.3(9)		C53	C96	H96A	109.4
C6	C7	H7	118.1		C53	C96	H96B	109.5
C6	C7	N1	123.7(6)		C53	C96	H96C	109.4
H7	C7	N1	118.1		H96A	C96	H96B	109.6
C23	C21	C22	121.2(8)		H96A	C96	H96C	109.4
C23	C21	C3	120.2(8)		H96B	C96	H96C	109.6
C22	C21	C3	118.6(8)		C1BA	N5	C5BA	120.5(5)
C6	C3	C21	117.8(7)		C1BA	N5	Zn0A	115.4(4)
C6	C3	O2	123.8(7)		C5BA	N5	Zn0A	124.0(4)
C21	C3	O2	118.3(7)		C1R	N24	C2BA	123.2(6)
C33	C27	C20	121.2(7)		C1R	N24	Zn0A	113.3(4)
C33	C27	C22	121.9(7)		C2BA	N24	Zn0A	122.8(5)
C20	C27	C22	116.6(7)		C3AA	O1AA	C48	112.0(6)
C9	C11	C12	121.0(6)		C1A	O0AA	C1H	113.0(5)
C9	C11	H11	119.5		C5AA	O2AA	C6AA	114.8(5)
C12	C11	H11	119.5		C0BA	O9	C6BA	116.6(5)
C9	N1	C7	122.6(5)		C71	O12	Zn0A	129.0(4)

C9	N1	Zn1	113.2(4)		H22A	O22	H22B	107.1
C7	N1	Zn1	124.1(4)		H22A	O22	Zn0A	111.8
C8	N2	C5	122.9(6)		H22B	O22	Zn0A	111.7
C8	N2	Zn1	113.4(4)		C63	O43	Zn0A	122.6(4)
C5	N2	Zn1	123.5(5)		N5	Zn0A	N24	78.6(2)
C14	O5	C13	117.5(5)		N5	Zn0A	O12	91.1(2)
C12	O4	C17	116.4(5)		N5	Zn0A	O22	103.4(2)
C2	O3	Zn1	131.4(4)		N5	Zn0A	O43	144.6(2)
C19	O7	C18	111.8(5)		N24	Zn0A	O12	165.9(2)
C3	O2	Zn1	124.5(5)		N24	Zn0A	O22	93.2(2)
C1	O1	H1	108(3)		N24	Zn0A	O43	85.7(2)
C1	O1	Zn1	126.8(5)		O12	Zn0A	O22	98.6(2)
H1	O1	Zn1	122(3)		O12	Zn0A	O43	97.5(2)
C15	O6	C16	110.7(7)		O22	Zn0A	O43	109.0(2)
N1	Zn1	N2	79.0(2)		H0AA	C0AA	H0AB	110
N1	Zn1	O3	168.1(2)		H0AA	C0AA	H0AC	110
N1	Zn1	O2	88.5(2)		H0AA	C0AA	O10	109
N1	Zn1	O1	90.5(2)		H0AB	C0AA	H0AC	109
N2	Zn1	O3	90.2(2)		H0AB	C0AA	O10	109
N2	Zn1	O2	145.3(2)		H0AC	C0AA	O10	109
N2	Zn1	O1	107.2(2)		C0AA	O10	H10A	109
O3	Zn1	O2	97.8(2)		H40A	C40	H40B	110
O3	Zn1	O1	97.5(2)		H40A	C40	H40C	110
O2	Zn1	O1	105.1(2)		H40A	C40	O11	109.4
H1AA	C1A	H1AB	108.1		H40B	C40	H40C	109
H1AA	C1A	C5AA	109.6		H40B	C40	O11	109.4
H1AA	C1A	O0AA	109.6		H40C	C40	O11	109.4
H1AB	C1A	C5AA	109.7		C40	O11	H11A	109.5

Table A6. Bond angles (°) for complex **[$Zn^{II}L^{N2O2}$]** (**3**).

APPENDIX-B

Permission/License Agreements for copyrighted Material

Wickramasinghe, L. D.; Mazumder, S.; **Gonawala, S.**; Perera, M. M.; Baydoun, H.; Thapa, B.; Li, L.; Xie, L.; Mao, G.; Zhou, Z.; Schlegel, H. B.; Verani, C. N. "The Mechanisms of Rectification in Au|Molecule|Au Devices Based on Langmuir–Blodgett Monolayers of Iron(III) and Copper(II) Surfactants" *Angew. Chem. Int. Ed.* **2014**, *53*, 14462- Reproduced by permission of The Royal Society of Chemistry (**Chapter 3**).

JOHN WILEY AND SONS LICENSE TERMS AND CONDITIONS

Apr 18, 2016

This Agreement between Sunalee Gonawala ("You") and John Wiley and Sons ("John Wiley and Sons") consists of your license details and the terms and conditions provided by John Wiley and Sons and Copyright Clearance Center.

License Number	3851970634900
License date	Apr 18, 2016
Licensed Content Publisher	John Wiley and Sons
Licensed Content Publication	Angewandte Chemie International Edition
Licensed Content Title	The Mechanisms of Rectification in Au|Molecule|Au Devices Based on Langmuir–Blodgett Monolayers of Iron(III) and Copper(II) Surfactants
Licensed Content Author	Lanka D. Wickramasinghe,Shivnath Mazumder,Sunalee Gonawala,Meeghage Madusanka Perera,Habib Baydoun,Bishnu Thapa,Li Li,Lingxiao Xie,Guangzhao Mao,Zhixian Zhou,H. Bernhard Schlegel,Cláudio N. Verani
Licensed Content Date	Nov 3, 2014
Pages	6
Type of use	Dissertation/Thesis
Requestor type	Author of this Wiley article
Format	Print and electronic
Portion	Full article
Will you be translating?	No
Title of your thesis /	Electron Transfer Studies in Langmuir-Blodgett Films of

dissertation	Metallosurfactants for Current Rectification, Corrosion Mitigation, and Water Oxidation
Expected completion date	May 2016
Expected size (number of pages)	150
Requestor Location	Sunalee Gonawala 665 W Warren Ave Apt 112 DETROIT, MI 48201 United States Attn: Sunalee Gonawala
Billing Type	Invoice
Billing Address	Sunalee Gonawala 665 W Warren Ave Apt 112 DETROIT, MI 48201 United States Attn: Sunalee Gonawala
Total	0.00 USD

Terms and Conditions

TERMS AND CONDITIONS

This copyrighted material is owned by or exclusively licensed to John Wiley & Sons, Inc. or one of its group companies (each a"Wiley Company") or handled on behalf of a society with which a Wiley Company has exclusive publishing rights in relation to a particular work (collectively "WILEY"). By clicking "accept" in connection with completing this licensing transaction, you agree that the following terms and conditions apply to this transaction (along with the billing and payment terms and conditions established by the Copyright Clearance Center Inc., ("CCC's Billing and Payment terms and conditions"), at the time that you opened your RightsLink account (these are available at any time at http://myaccount.copyright.com).

Terms and Conditions

- The materials you have requested permission to reproduce or reuse (the "Wiley Materials") are protected by copyright.
- You are hereby granted a personal, non-exclusive, non-sub licensable (on a stand-alone basis), non-transferable, worldwide, limited license to reproduce the Wiley Materials for the purpose specified in the licensing process. This license, **and any CONTENT (PDF or image file) purchased as part of your order,** is for a one-time use only and limited to any maximum distribution number specified in the license. The first instance of republication or reuse granted by this license must be

completed within two years of the date of the grant of this license (although copies prepared before the end date may be distributed thereafter). The Wiley Materials shall not be used in any other manner or for any other purpose, beyond what is granted in the license. Permission is granted subject to an appropriate acknowledgement given to the author, title of the material/book/journal and the publisher. You shall also duplicate the copyright notice that appears in the Wiley publication in your use of the Wiley Material. Permission is also granted on the understanding that nowhere in the text is a previously published source acknowledged for all or part of this Wiley Material. Any third party content is expressly excluded from this permission.

- With respect to the Wiley Materials, all rights are reserved. Except as expressly granted by the terms of the license, no part of the Wiley Materials may be copied, modified, adapted (except for minor reformatting required by the new Publication), translated, reproduced, transferred or distributed, in any form or by any means, and no derivative works may be made based on the Wiley Materials without the prior permission of the respective copyright owner. **For STM Signatory Publishers clearing permission under the terms of the STM Permissions Guidelines only, the terms of the license are extended to include subsequent editions and for editions in other languages, provided such editions are for the work as a whole in situ and does not involve the separate exploitation of the permitted figures or extracts,**You may not alter, remove or suppress in any manner any copyright, trademark or other notices displayed by the Wiley Materials. You may not license, rent, sell, loan, lease, pledge, offer as security, transfer or assign the Wiley Materials on a stand-alone basis, or any of the rights granted to you hereunder to any other person.

- The Wiley Materials and all of the intellectual property rights therein shall at all times remain the exclusive property of John Wiley & Sons Inc, the Wiley Companies, or their respective licensors, and your interest therein is only that of having possession of and the right to reproduce the Wiley Materials pursuant to Section 2 herein during the continuance of this Agreement. You agree that you own no right, title or interest in or to the Wiley Materials or any of the intellectual property rights therein. You shall have no rights hereunder other than the license as provided for above in Section 2. No right, license or interest to any trademark, trade name, service mark or other branding ("Marks") of WILEY or its licensors is granted hereunder, and you agree that you shall not assert any such right, license or interest with respect thereto

- NEITHER WILEY NOR ITS LICENSORS MAKES ANY WARRANTY OR REPRESENTATION OF ANY KIND TO YOU OR ANY THIRD PARTY, EXPRESS, IMPLIED OR STATUTORY, WITH RESPECT TO THE MATERIALS OR THE ACCURACY OF ANY INFORMATION CONTAINED IN THE MATERIALS, INCLUDING, WITHOUT LIMITATION, ANY IMPLIED WARRANTY OF MERCHANTABILITY, ACCURACY, SATISFACTORY QUALITY, FITNESS FOR A PARTICULAR PURPOSE, USABILITY,

INTEGRATION OR NON-INFRINGEMENT AND ALL SUCH WARRANTIES ARE HEREBY EXCLUDED BY WILEY AND ITS LICENSORS AND WAIVED BY YOU.

- WILEY shall have the right to terminate this Agreement immediately upon breach of this Agreement by you.

- You shall indemnify, defend and hold harmless WILEY, its Licensors and their respective directors, officers, agents and employees, from and against any actual or threatened claims, demands, causes of action or proceedings arising from any breach of this Agreement by you.

- IN NO EVENT SHALL WILEY OR ITS LICENSORS BE LIABLE TO YOU OR ANY OTHER PARTY OR ANY OTHER PERSON OR ENTITY FOR ANY SPECIAL, CONSEQUENTIAL, INCIDENTAL, INDIRECT, EXEMPLARY OR PUNITIVE DAMAGES, HOWEVER CAUSED, ARISING OUT OF OR IN CONNECTION WITH THE DOWNLOADING, PROVISIONING, VIEWING OR USE OF THE MATERIALS REGARDLESS OF THE FORM OF ACTION, WHETHER FOR BREACH OF CONTRACT, BREACH OF WARRANTY, TORT, NEGLIGENCE, INFRINGEMENT OR OTHERWISE (INCLUDING, WITHOUT LIMITATION, DAMAGES BASED ON LOSS OF PROFITS, DATA, FILES, USE, BUSINESS OPPORTUNITY OR CLAIMS OF THIRD PARTIES), AND WHETHER OR NOT THE PARTY HAS BEEN ADVISED OF THE POSSIBILITY OF SUCH DAMAGES. THIS LIMITATION SHALL APPLY NOTWITHSTANDING ANY FAILURE OF ESSENTIAL PURPOSE OF ANY LIMITED REMEDY PROVIDED HEREIN.

- Should any provision of this Agreement be held by a court of competent jurisdiction to be illegal, invalid, or unenforceable, that provision shall be deemed amended to achieve as nearly as possible the same economic effect as the original provision, and the legality, validity and enforceability of the remaining provisions of this Agreement shall not be affected or impaired thereby.

- The failure of either party to enforce any term or condition of this Agreement shall not constitute a waiver of either party's right to enforce each and every term and condition of this Agreement. No breach under this agreement shall be deemed waived or excused by either party unless such waiver or consent is in writing signed by the party granting such waiver or consent. The waiver by or consent of a party to a breach of any provision of this Agreement shall not operate or be construed as a waiver of or consent to any other or subsequent breach by such other party.

- This Agreement may not be assigned (including by operation of law or otherwise) by you without WILEY's prior written consent.

- Any fee required for this permission shall be non-refundable after thirty (30) days from receipt by the CCC.

- These terms and conditions together with CCC's Billing and Payment terms and conditions (which are incorporated herein) form the entire agreement between you and WILEY concerning this licensing transaction and (in the absence of fraud) supersedes all prior agreements and representations of the parties, oral or written. This Agreement may not be amended except in writing signed by both parties. This Agreement shall be binding upon and inure to the benefit of the parties' successors, legal representatives, and authorized assigns.

- In the event of any conflict between your obligations established by these terms and conditions and those established by CCC's Billing and Payment terms and conditions, these terms and conditions shall prevail.

- WILEY expressly reserves all rights not specifically granted in the combination of (i) the license details provided by you and accepted in the course of this licensing transaction, (ii) these terms and conditions and (iii) CCC's Billing and Payment terms and conditions.

- This Agreement will be void if the Type of Use, Format, Circulation, or Requestor Type was misrepresented during the licensing process.

- This Agreement shall be governed by and construed in accordance with the laws of the State of New York, USA, without regards to such state's conflict of law rules. Any legal action, suit or proceeding arising out of or relating to these Terms and Conditions or the breach thereof shall be instituted in a court of competent jurisdiction in New York County in the State of New York in the United States of America and each party hereby consents and submits to the personal jurisdiction of such court, waives any objection to venue in such court and consents to service of process by registered or certified mail, return receipt requested, at the last known address of such party.

WILEY OPEN ACCESS TERMS AND CONDITIONS

Wiley Publishes Open Access Articles in fully Open Access Journals and in Subscription journals offering Online Open. Although most of the fully Open Access journals publish open access articles under the terms of the Creative Commons Attribution (CC BY) License only, the subscription journals and a few of the Open Access Journals offer a choice of Creative Commons Licenses. The license type is clearly identified on the article.

The Creative Commons Attribution License

The Creative Commons Attribution License (CC-BY) allows users to copy, distribute and transmit an article, adapt the article and make commercial use of the article. The CC-BY license permits commercial and non-

Creative Commons Attribution Non-Commercial License

The Creative Commons Attribution Non-Commercial (CC-BY-NC)License permits use, distribution and reproduction in any medium, provided the original work is properly cited and is not used for commercial purposes.(see below)

Creative Commons Attribution-Non-Commercial-NoDerivs License

The Creative Commons Attribution Non-Commercial-NoDerivs License (CC-BY-NC-ND)

REFERENCES

1. (a) Wickramasinghe, L. D.; Mazumder, S.; Gonawala, S.; Perera, M. M.; Baydoun, H.; Thapa, B.; Li, L.; Xie, L.; Mao, G., Zhou, Z.; Schlegel, H. B.; Verani, C. N. *Angew. Chem., Int. Ed.* **2014**, *53*, 14462; (b) Wickramasinghe, L. D.; Perera, M. M.; Li, L.; Mao, G.; Zhou, Z.; Verani, C. N. *Angew. Chem. Int. Ed.* **2013**, *52*, 13346.
2. (a) Verani, C. N.; Driscoll, J.; Keyes, P. H.; Heeg, M. J. *Inorg. Chem*. **2014**, *53*, 5647; (b) Shakya, R.; Keyes, P. H.; Heeg, M. J.; Moussawel, A.; Heiney, P. A.; Verani, C. N. *Inorg. Chem.* **2006**, *45*, 7587.
3. (a) Driscoll, J. A.; Allard, M. M.; Wu, L.; Heeg, M. J.; da Rocha, S. R. P.; Verani, C. N. *Chem. Eur. J.* **2008**, *14*, 9665; (b) Shakya, R.; Hindo, S. S.; Wu, L.; Ni, S.; Allard, M. M.; Heeg, M. J.; da Rocha, S. R. P.; Yee, G. T.; Hratchian, H. P.; Verani, C. N. *Chem. Eur. J.* **2007**, *13*, 9948.
4. (a) Sucheta, J.; Prabir, P.; Kumar, M. T.; Talapatra, G. B.; Goswami, S. *Chem. Eur. J.* **2012**, *18*, 1761; (b) Lesh, F. D.; Hindo, S. S.; Heeg, M. J.; Allard, M. M.; Jain, P.; Peng, B.; Hryhorczuk, L.; Verani, C. N. *Eur. J. Inorg. Chem.* **2009**, *3*, 345; (c) James, B.; Katherine, A. E.; Duncan B. W.; Richard, H. K. *Langmuir* **2005**, *21*, 5696.
5. (a) Scheid, D.; Lederle, C.; Vowinkel, S.; Schaefer, C. G.; Stuehn, B.; Gallei, M. *J. Mater. Chem. C.* **2014**, *2*, 2583; (b) Dongfang, Q.; Xiaoyu, B.; Qian, Z.; Qichao, Y.; Yuquan, F.; Hongwei, W.; Chunxia, Y.; Kecheng, L. *Inorg. Chem.* **2015**, *54*, 8264; (c) Rowan, S. J.; Beck, J. B. *J. Am. Chem. Soc.* **2003**, *125*, 13922.
6. (a) Ho-Chol, C.; Tomoki, S.; Akiko, K.; Keisuke, K.; Takeshi, O.; Daisuke, K.; Takae, Y.; Hirotaka, F.; Susumu, K. *J. Mater. Chem.* **2007**, *17*, 4136; (b) Terazzi, E.; Suarez, S.; Torelli, S.; Nozary, H.; Imbert, D.; Mamula, O.; Rivera, J. P.; Guillet, E.; Bénech, J. M.;

Bernardinelli, G.; Scopelliti, R.; Donnio, B.; Guillon, D.; Bünzli, J. C.; Piguet, C. *Adv. Funct. Mater*. **2006**, *16*, 157.

7. Khassanov, A.; Steinruck, H.; Schmaltz, T.; Magerl, A.; Halik M. *Acc. Chem. Res.* **2015**, *48*, 1901; (b) Fenwick, O.; Dyck, C. V.; Murugavel, K.; Cornil, D.; Reinders, F.; Haar, S.; Mayor, M.; Cornil, J.; Samori, P. *J. Mater. Chem. C* **2015**, *3*, 3007; (c) Yildiz, I.; Mukherjee, J.; Tomasulo, M.; Raymo, F. M. *Adv. Func. Mater.* **2007**, *17*, 814; (d) Zhang, S.; Chandra, K. L.; Gorman, C. B. *J. Am. Chem. Soc.* **2007**, *129*, 4876.
8. (a) Petty, M. C. *Langmuir–Blodgett Films: An Introduction,* Cambridge University Press, NY (USA), 1996; (b) Tredgold, R. H. *Order in Thin Organic Films,* Cambridge University Press, NY (USA), 1994.
9. (a) Nilashis, N.; Dieter, V. *Acc. Chem. Res.* **2007**, *40*, 351; (b) Wassel, R. A.; Gorman, C. B. *Angew. Chem. Int. Ed.* **2004**, *43*, 5120.
10. Carroll, R. L.; Gorman, C. B. *Angew. Chem. Int. Ed.* **2002**, *41*, 4378.
11. Moore, G. E. *Electronics* **1965**, *38*, 114.
12. (a) Rogersa, J. A.; Huangb, Y. *Proc. Natl. Acad. Sci. USA* **2009**, *106*, 10875; (b) Robertson, N. C. A. M. *Chem. Soc. Rev.* **2003**, *32*, 96.
13. http://www.zyvex.com/nanotech/feynman.html, (accessed December 15, 2014).
14. Robertson, N.; McGowan, C. A. *Chem. Soc. Rev.*, **2003**, *32*, 96.
15. Aviram, A.; Ratner, M. A. *Chem. Phys. Lett.* **1974**, *29*, 277.
16. Rigaut, S. *Dalton Trans.* **2013**, *42*, 15859.
17. (a) Dyck, V. C.; Ratner, M. A. *Nano Lett.* **2015**, *15*, 1577; (b) Guldi, D. M.; Nishihara, H.; Venkataraman, L. *Chem. Soc. Rev.* **2015**, *44*, 842; (c) Harveya, E. C.; Feringab, B. L.; Vosa,

J. G.; Browneb, W. R.; Pryce, M. T. *Coord. Chem. Rev.* **2015**, 282, 77; (d) Aviram, A. *J. Am. Chem. Soc.* **1988**, *110*, 5687.

18. Low, P. J. *DaltonTrans.* **2005**, *17*, 2821.

19.http://www.allaboutcircuits.com/textbook/semiconductors/chpt-2/the-p-n-junction, (accessed April 25, 2016).

20. (a) Metzger, R. M. *Chem. Rev.* **2015**, *115*, 5056; (b) Metzger, R. M. *J. Mater. Chem.* **2008**, *18*, 4364; (c) Metzger, R. M. *The Chemical Record* **2004**, *4*, 291.

21. (a) Somvanshi, D.; Jit, S. *IEEE Electron Device Lett.* **2014**, 35, 945; (b) Bhattacharya, B.; Layek, A.; Alam, M. M.; Maity, D. K.; Chakrabarti, S.; Ray, P. P.; Ghoshal, D. *Chem. Commun.* **2014**, *50*, 7858; (c) Naik, S. S.; Reddy, V. R. *Adv. Mat. Let.* **2012**, 3, 188; (d) Ashwell, G. J.; Urasinska, B.; Tyrrell, W. D. *Phys. Chem. Chem. Phys.* **2006**, *8*, 3314; (e) Ashwell, G. J.; Mohib, A. *J. Am. Chem. Soc.* **2005**, *127*, 16238; (f) Liu, Y.; Xu, Y.; Zhu, D. *Synth. Met.* **1997**, *90*, 143.

22. (a) Wickramasinghe, L. D.; Mazumder, S.; Gonawala, S.; Perera, M. M.; Baydoun, H.; Thapa, B.; Li, L.; Xie, L.; Mao, G.; Zhou, Z.; Schlegel, H. B.; Verani, C. N. *Angew. Chem. Int. Ed.* **2014**, *53*, 14462; (b) habinyc, C; Michael L.; Chen, X.; Erik, H. R.; Heiko, J.; Skulason, H.; Frisbie, C. D.; Mujica, V.; Ratner, M. A.; Rampi, M. A.; Whitesides, G. M. *J. Am. Chem. Soc.* **2002**, *124*, 11730; (c) Mujicaa, V.; Ratner, M. A.; Nitzan, A. *Chem. Phys.* **2002**, *281*, 147.

23. Jaiswal, A.; Rajagopal, D.; Lakshmikantham, M. V.;Cava, M. P.; Metzger, R. M. *Phys. Chem. Chem. Phys.* **2007**, *9*, 4007.

24. Krzeminski, C.; Delerue, C.; Allan, G.; Vuillaume, D.; Metzger, R. M. *Phys. Rev. B* **2001**, *64*, 085405.

25. (a) Garg, K.; Majumder, C.; Gupta, S. K.; Aswal, D. K.; Nayak, S. K.; Chattopadhyay, S. *Chem. Sci.* **2016**, *7*, 1548; (b) Van Dyck, C.; Ratner, M. A. *Nano Lett.*, **2015**, *15*, 1577; (c) Metzger, R. M. *Chem. Rev.* **2003**, *103*, 3803.

26. Metzger, R. M.; Chen, B.; Ho1pfner, U.; Lakshmikantham, M. V.; Vuillaume, D.; Kawai, T.; Wu, X.; Tachibana, H.; Hughes, T. V.; Sakurai, H.; Baldwin, J. W.; Hosch, C.; Cava, M. P.; Brehmer, L.; Ashwell, G. J. *J. Am. Chem. Soc.* **1997**, *119*, 10455.

27. (a) Metzger, R. M. *J. Mater. Chem.* **2000**, *10*, 55; (b) Martin, A. S.; Sambles, J. R.; Ashwell, G. J. *Phys. Rev. Lett.* 1993, *70*, 218.

28. (a) Baldwin, J. W.; Amaresh, R. R.; Peterson, I. R.; Shumate, W.J.; Cava, M. P.; Amiri, M. A.; Hamilton, R.; Ashwell, G. J.; Metzger, R. M. *J. Phys. Chem. B* **2002**, *106*, 12158.; (b) Metzger, R. M.; Baldwin, J. W.; Shumate, W. J.; Peterson, I. R.;Mani, P.; Mankey, G. J.; Morris, T.; Szulczewski, G.; Bosi, S.;Prato, M.; Comito, A.; Rubin, Y. *J. Phys. Chem. B* **2003**, *107*,1021; (c) Gayathri, S. S.; Patnaik, A. *Chem.Commun.* **2006**, 1977.

29. Ashwell, G. J.; Ewington, J.; Robinson, B. J. *Chem. Commun.* **2006**, 618.

30. Lee, Y.; Yuan, S.; Sanchez, A.; Yu, L. *Chem. Commun*. **2008**, *2*, 247.

31. Bhattacharya, B.; Layek, A.; Alam, M. M.; Maity, D. K.; Chakrabarti, S.; Ray, P. P.; Ghoshal, D. *Chem. Commun.* **2014**, *50*, 7858.

32. DeBrincat, D.; Keers, O.; McGrady, J. E. *Chem. Commun.* **2013**, *49*, 9116.

33. Landolt, D. *Corrosion and Surface Chemistry of Metals*, EPFL Press, Switzerland, **2007**, 1-10.

34. Saha, J. K. *Corrosion of Constructional Steels in Marine and Industrial Environment*, Springer, India, **2013**, 1-20.

35. (a) Schweitzer, P. A. *Fundamentals of Corrosion Mechanisms, Causes, and Preventative Methods*, CRC Press **2009**, 27-76; (b) Perez, N. *Electrochemistry and Corrosion Science, Kluwer Academic Publishers*, **2004**, 1-25.

36. National research council, *Research opportunities in Corrosion Science and Engineering*, The National Academic Press, 61-66.

37. (a) Xia, G.; Jiang, X.; Zhou, L.; Liao, Y.; Duan, M.; Wang, H.; Pu, Q.; Zhou, J. *Ind. Eng. Chem. Res.* **2015**, *54*, 1407.; (b) Riaz, U.; Nwaoha, C.; Ashraf, S. M. Prog. Org. Coat. **2014**, *77*, 743; (c) Xing, C.; Zhang, Z.; Yu, L.; Zhang, L.; Bowmaker, G. *RSC Adv.* **2014**, *4*, 32718; (d) Chen, F.; Liu, P. *ACS Appl. Mater. Interfaces* **2011**, *3*, 2694; (e) Andreeva, D. V.; Skorb, E. V.; Shchukin, D. G. *ACS Appl. Mater. Interfaces* **2010**, *2*, 1954; (f) Guo, D.; Xing, W.; Shan, Y.; Lu, T.; Xi, S.; *Thin Solid Films* **1994**, *243*,540.

38. Akhtar, J. *Recent Patents on Corrosion Science*, **2013**, *3*, 79.

39. Mishra, M.; Tiwari, K.; Singh, A. K.; Singh, V. P. *Inorg. Chem. Acta* **2015**, *425*, 36.

40. Singh V. P.; Singh, P.; Singh, A. K. *Inorg. Chem. Acta* **2011**, *379*, 56.

41. Singha, P.; Singh, A. K.; Singh, V. P. *Polyhedron* **2013**, *65*, 73.

42. Shabanova, I. N.; Chausov, F. F.; Naimushinab, E. A.; Somov, N. V. *Surf. Interface Anal.* **2014**, *46*, 750.

43. Abdalla, K.; Rahmat, A.; Azizan, A. *Adv. Mat. Res.* **2013**, *626*, 569.

44. Forsyth, M.; Seter, M.; Tan, M. Y.; Hinton, B. *Corros. Eng. Sci. Techn.* **2014**, *49*, 130.

45. (a) Quan, Z.; Chen, S.; Li, S. *Corros. Sci.* **2001**, *43*, 1071; (b) Li, S.; Chen, S.; Lei, S.; Ma, H.; Yu, R.; Liu, D. *Corros. Sci.* **1999**, *41*, 1273.

46. Parent, A. R.; Sakai, K. *ChemSusChem.* **2014**, *7*, 2070.

47. Nocera, D. G. *Acc. Chem. Res.* **2012**, *45*, 767; (b) Lewis, N.S.; Nocera, D. G. *Proc. Natl. Acad. Sci. USA.* **2006**, *43*, 103.

48. Kudo, A.; Kato, H.; Tsuji, I. *Chem. Lett.* **2004**, *33*, 1534.

49. Du, P.; Eisenberg, R. *Energy Environ. Sci.* **2012**, *5*, 6012.

50. (a) Blakemore, J. D.; Crabtree, R. H.; Brudvig, G. W. *Chem. Rev.* **2015**, *115*, 12974; (b) Duan, L.; Tong, L.; Xua, Y.; Sun, L. *Energy Environ. Sci.* **2011**, *4*, 3296; (c) Deng, Z.; Tseng, H.; Zong, R.; Wang, D. Thummel, R. *Inorg. Chem.* **2008**, *47*, 1835; (d) Liu, F.; Concepcion, J. J.; Jurss, J. W.; Cardolaccia, T.; Templeton, J. L.; Meyer, T. J. *Inorg. Chem.* **2008**, *47*, 1727; (e) Romero, I.; Rodriguez, M.; Sens, C.; Mola, J.; Kollipara, M. R.; Francas, L.; Mas-Marza, E.; Escriche, L.; Llobet, A. *Inorg. Chem.* **2008**, *47*, 1824.

51. Corbucci, I.; Petronilho, A.; Muller-Bunz, H.; Rocchigiani, L.; Albrecht, M.; Macchioni, A. *ACS Catal.* **2015**, *5*, 2714; (b) Woods, J. A.; Bernhard, S.; Albrecht, M. *Molecular Water Oxidation Catalysis* **2014**, 113; (c) Volpe, A.; Sartorel, A.; Tubaro, C.; Meneghini, L.; Di, V. M.; Graiff, C.; Bonchio, M. *Eur. J. Inorg. Chem.* **2014**, *4*, 568.

52. (a) Kiss, B.; Didier, C.; Johnson, T.; Manning, T. D.; Dyer, M. S.; Cowan, A. J.; Claridge, J. B.; Darwent, J. R.; Rosseinsky, M. J. *Angew. Chem. Int. Ed.* **2014**, *53*, 14480; (b) Yu, W.; He, Q.; Shi, H.; Pan, Y.; Wei, X. *Dalton Trans.* **2014**, *43*, 12221.

53. Wang, Z.; Tang, L.; Zhang, Y.; Zhan, S.; Ye, J. *J. Power Sources* **2015**, *287*, 50.

54. Wang, H.; Lu, Y.; Mijangos, E.; Thapper, A. *Chin. J. Chem.* **2014**, *32*, 467.

55. Leung, C.; Ng, S.; Ko, C.; Man, W.; Wu, J. L. C.; Lau, T. *Energy Environ. Sci.* **2012**, *5*, 7903.

56. Das, B.; Orthaber, A.; Ott, S.; Thapper, A. *Chem. Commun.* **2015**, *51*, 13074.

57. (a) Nakazono, T.; Parent, A. R.; Sakai, K. *Chem. Eur. J.* **2015**, *21*, 6723; (b) Nakazono, T.; Parenta, A. R.; Sakai, K. *Chem. Commun.* **2013**, *49*, 6325.

58. (a) Wang, D.; Groves, J. T. *Proc. Natl. Acad. Sci. USA* **2013**, 110, 15579; (b) Dogutan, D. K.; McGuire, R.; Nocera, D. G. *J. Am. Chem. Soc.* **2011**, *133*, 9178.

59. Yeh, C.; Chang, C. J.; Nocera, D. G. *J. Am. Chem. Soc.* **2001**, *123*, 1513.

60. Wang, H.; Mijangos, E.; Ott, S.; Thapper, A. *Angew. Chem. Int. Ed.* **2014**, *53*, 14499.

61. Chen, M.; Ng, S.; Yiu, S.; Lau, K.; Zeng, R. J.; Lau, T. *Chem. Commun.* **2014**, *50*, 14956.

62. Rigsby, M. L.; Mandal, S.; Nam, W.; Spencer, L. C.; Llobet, A.; Stahl, S. S. *Chem. Sci.* **2012**, *3*, 3058.

63. Chen, H.; Sun, Z.; Liu, X.; Han, A.; Du, P.; *J. Phys. Chem. C* **2015**, *119*, 8998.

64. Han, A.; Wu, H.; Sun, Z.; Jia, H.; Du, P. *Phys. Chem. Chem. Phys*. **2013**, *15*, 12534.

65. Bonke, S. A.; Wiechen, M.; Hocking, R. K.; Fang, X.; Lupton, D. W.; MacFarlane, D. R.; Spiccia, L. *ChemSusChem* **2015**, *8*, 1394.

66. Han, A.; Jia, H.; Ma, H.; Ye, S.; Wu, H.; Lei, H.; Han, Y.; Cao, R.; Du, P. *Phys. Chem. Chem. Phys.* **2014**, *16*, 11209.

67. Joya, K. S.; Morlane, N.; Maloney, E.; Rodionova, V.; Takanabe, K. *Chem. Commun.* **2015**, *51*, 13481.

68. Silverstein, R. M.; Webster, F. X.; Kiemle, D. J. *Spectrometric identification of organic compounds*, 7th ed., John Wiley & Sons: New York, USA, **2005**.

69. Smith, B. C. *Fundamentals of Fourier Transform Infrared Spectroscopy*, CRC press, Florida, USA, **1996**.

70. Field, L. D.; Sternhell, S.; Kalman, J. R. *Organic Structures from Spectra*, 5th ed., John Wiley & Sons: West Sussex, UK, 2013.

71. APEX2 V2010.11-3. Software *for the CCD Detector System*; Bruker Analytical X-ray Systems, Madison, WI (**2010**).

72. Sheldrick, G. M. *Acta Cryst.* **2008**, *A64*, 112.

73. SAINT V 7.34 Software for the Integration of CCD Detector System Bruker Analytical X-ray Systems, Madison, WI (**2008**).

74. Deng, Y.; Yuan, W.; Jia, Z.; Liu, G. *J. Phys. Chem. B* **2014**, *118*,14536.

75. Menzel, H.; Weichart, B. *Langmuir* **1994**, *10*, 1926.

76. Kissinger, P. T.; Bott, A. W. *Current Separations* **2002**, *20*, 51.

77. Gagne, R.; Koval, C.; Licenski, G. *Inorg. Chem.* **1980,** *19*, 2854.

78. Wickramasinghe, L. D.; Perera, M. M.; Li, L.; Mao, G.; Zhou, Z.; Verani, C. N. *Angew. Chem. Int. Ed.* **2013**, *52*, 13346.

79. Hindo, S. S.; Shakya, R.; Shanmugam, R.; Heeg, M. J.; Verani, C. N. *Eur. J. Inorg. Chem.* **2009**, 4686.

80. (a) Petty, M. C. *Langmuir–Blodgett Films: An Introduction*, Cambridge University Press, New York, USA, **1996**; (b) Tredgold, R. H. *Order in Thin Organic Films*, Cambridge University Press, New York, USA, **1994**.

81. Kundu, S.; Datta, A.; Hazra, S. *Langmuir* **2005**, *21*, 5894.

82. Kundu, S.; Datta, A.; Hazra, S. *Phys. Rev. E* **2006**, *73*, 051608.

83. Metzger, R. M. *J. Mater. Chem.* **2008**, *18*, 4364.

84. (a) A. Gericke, A. V. Michailov, H. Huehnerfuss, *Vib. Spectrosc*. **1993**, *4*, 335; (b) http://www.biolinscientific.com/zafepress.php.url=%2Fpdf%2FKSV%20NIMA%2FApplication%20Notes%2FKN_AN_9_ThinFilms.pdf, (accessed April 25, 2015).

85. Galvan-Miyoshi, J.; Ramos, S.; Ruiz-Garcia, J.; Castillo, R. *J. Chem. Phys.* **2001**, *115*, 8178.

86. https://www.bruker.com/fileadmin/user_upload/8-PDF-Docs/OpticalSpectrospcopy/FT-IR/VERTEX/Brochures/VERTEXseries_brochure_EN.pdf, (accessed April 25, 2016).

87. (a) Brezesinski, G.; Dobner, B.; Stefaniu, C.; Vollhardt, D. *J. Phys. Chem. C* **2011**, *115*, 8206; (b) Wang, L.; Cruz, A.; Flach, C. R.; Prez-Gil, J.; Mendelsohn, R. *Langmuir* **2007**, *23*, 4950.

88. (a) Zou, Y.; Xie, L.; Carroll, S.; Muniz, M.; Gibson, H.; Wei, W.; Liu, H.; Mao, G. *Biomacromolecules* **2014**, *15*, 3965; (b) Blacklock, J.; Mao, G.; Oupický, D.; Möhwald, H. *Langmuir*, **2010**, *26*, 8597.

89. https://www.scu.edu/media/school-of-engineering/photos/cns/Dimension3100D-Manual.pdf, (accessed April 25, 2016).

90. (a) Metzger, R. M. *Chem. Rev.* **2015**, *115*, 5056; (b) Paul, N. D.; Rana, U.; Goswami, S.; Mondal, T. K.; Goswami, S. *J. Am. Chem. Soc.* **2012**, *134*, 6520; (c) Metzger, R. M. *J. Mater. Chem.* **2008**, *18*, 4364.

91. Metzger, R. M.; Chen, B.; Hopfner, U.; Lakshmikantham, M. V.; Vuillaume, D.; Kawai, T.; Wu, X.; Tachibana, H.; Hughes, T. V.; Sakurai, H.; Baldwin, J. W.; Hosch, C.; Cava, M. P.; Brehmer, L.; Ashwell, G. J. *J. Am. Chem. Soc.* **1997**, *119*, 10455.

92. Du, P.; Eisenberg, R. *Energy Environ. Sci.* **2012**, *5*, 6012.

93. Parr, R. G.; Yang, W. *Density-functional theory of atoms and molecules*; Oxford University Press: New York, USA, **1989**.

94. Frisch, M. J.; Trucks, G. W.; Schlegel, H. B.; Scuseria, G. E.; Robb, M. A.; Cheeseman, J. R.; Scalmani, G.; Barone, V.; Mennucci, B.; Petersson, G. A.; Nakatsuji, H.; Caricato, M.; Li, X.; Hratchian, H. P.; Izmaylov, A. F.; Bloino, J.; Zheng, G.; Sonnenberg, J. L.; Hada, M.; Ehara, M.; Toyota, K.; Fukuda, R.; Hasegawa, J.; Ishida, M.; Nakajima, T.; Honda, Y.;

Kitao, O.; Nakai, H.; Vreven, T.; Montgomery, J. A.; Peralta, J. E.; Ogliaro, F.; Bearpark, M.; Heyd, J. J.; Brothers, E.; Kudin, K. N.; Staroverov, V. N.; Kobayashi, R.; Normand, J.; Raghavachari, K.; Rendell, A.; Burant, J. C.; Iyengar, S. S.; Tomasi, J.; Cossi, M.; Rega, N.; Millam, J. M.; Klene, M.; Knox, J. E.; Cross, J. B.; Bakken, V.; Adamo, C.; Jaramillo, J.; Gomperts, R.; Stratmann, R. E.; Yazyev, O.; Austin, A. J.; Cammi, R.; Pomelli, C.; Ochterski, J. W.; Salvador, P.; Dannenberg, J. J.; Dapprich, S.; Parandekar, P. V.; Mayhall, N. J.; Daniels, A. D.; Farkas, O.; Foresman, J. B.; Ortiz, J. V.; Cioslowski, J.; Fox, D. J.; *Gaussian Development Version; Revision H.31 ed.;* Gaussian, Inc.: Wallingford, CT, **2010**.

95. (a) Vosko, S. H.; Wilk, L.; Nusair, M. *Can. J. Phys.* **1980**, *58*, 1200; (b) Lee, C. T.; Yang, W. T.; Parr, R. G. *Phys. Rev. B* **1988**, *37*, 785.

96. Dolg, M.; Wedig, U.; Stoll, H.; Preuss, H. *J. Chem. Phys.* **1987**, *86*, 866.

97. (a) Francl, M. M.; Petro, W. J.; Hehre, W. J.; Binkley, J. S.; Gordon, M. S.; DeFrees, D. J.; Pople, J. A. *J. Chem. Phys.* **1982**, *77*, 3654; (b) Hariharan, P. C.; Pople, J. A. *Theor. Chim. Acta* **1973**, *28*, 213.

98. Marenich, A. V.; Cramer, C. J.; Truhlar, D. G. *J. Phys. Chem. B* **2009**, *113*, 6378.

99. Dennington, R.; Keith, T.; Millam, J. M. *GaussView, Version 5*, Semichem, Inc.: Shawnee Mission, KS, **2009**.

100. Aviram, A.; Ratner, M. *Chem. Phys. Lett.* **1974**, *29*, 277.

101. (a) Metzger, R. M. *Chem. Rev.* **2015**, *115*, 5056; (b) Metzger, R. M. *J. Mater. Chem.* **2008**, *18*, 4364; (c) Metzger, R. M. *The Chemical Record* **2004**, *4*, 291; (d) Martin, A. S.; Sambles, J. R.; Ashwell, G. J. *Phys. Rev. Lett.* **1993**, *70*, 218; (e) Ashwell, G. J.; Sambles, J. R.; Martin, A. S.; Parker, W. G.; Szablewski, M. *J. Chem. Soc. Chem. Commun.* **1990**, 1374.

102. Ariga, K.; Yamauchi, Y.; Mori, T.; Hill, J. P. *Adv. Mater.* **2013**, *25*, 6477.

103. Wickramasinghe, L. D.; Mazumder, S.; Gonawala, S.; Perera, M. M.; Baydoun, H.; Thapa, B.; Li, L.; Xie, L.; Mao, G.; Zhou, Z.; Schlegel, H. B.; Verani, C. N.; *Angew. Chem. Int. Ed.* **2014**, 53, 14462.

104. (a) Kochem, A.; Jarjayes, O.; Baptiste, B.; Philouze, C.; Vezin, H.; Tsukidate, K.; Tani, F.; Orio, M.; Shimazaki, Y.; Thomas, F. *Chem. Eur. J.* **2012**, *18*, 1068; (b) Orio, M.; Jarjayes, O.; Kanso, H.; Philouze, C.; Neese, F.; Thomas, F. Angew. Chem. Int. Ed. **2010**, *49*, 4989; Pfeiffer, P.; Breith, E.; Lübbe, E.; Tsumaki, T. *Justus Liebigs Ann. Chem*., **1933**, *503*, 84.

105. Wickramasinghe, L. D.; Perera, M. M.; Li, L.; Mao, G.; Zhou, Z.; Verani, C. N. *Angew. Chem. Int. Ed.* **2013**, *52*, 13346.

106. APEX2 V2010.11-3. Software *for the CCD Detector System*; Bruker Analytical X-ray Systems, Madison, WI (**2010**).

107. Sheldrick, G.M. *Acta Cryst. A64* **2008**, 112.

108. Dolomanov, O. V.; Bourhis, L. J.; Gildea, R. J.; Howard, J. A. K.; Puschmann, H. *J. Appl. Cryst.* **2009**, *42*, 339.

109. Rotthaus, O.; Jarjayes, O.; Philouz, C.; Valle, C. P. D.; Thomas, F.; *Dalton Trans.*, **2009**, *10*, 1792.

110. Kochem, A.; Jarjayes, O.; Baptiste, B.; Philouze, C.; Vezin, H.; Tsukidate, K.; Tani, F.; Orio, M.; Shimazaki, Y.; Thomas, F. *Chem. Eur. J.* **2012**, *18*, 1068.

111. (a) Petit, L.; Maldivi, P.; Adamo, C.; *J. Chem. Theory Comput.* **2005**, *1*, 953; (b) Stratmann, R. E.; Scuseria, G. E.; Frisch, M. J. *J. Chem. Phys.* **1998**, *109*, 8218; (c) Runge, E.; Gross, E. K. U. *Phys. Rev. Lett.* **1984**, *52*, 997.

112. Martin, R. L. *J. Chem. Phys.* **2003**, *118*, 4775.

113. Gagne, R.; Koval, C.; Licenski, G. *Inorg. Chem.* **1980,** *19,* 2854.

114. (a) Lesh, F. D.; Shanmugam, R.; Verani, C. N.; *Inorg. Chem.*, **2010**, *49*, 7226; (b) Lanznaster, M.; Hratchian, H. P.; Heeg, M. J.; Hryhorczuk, L. M.; McGarvey, B. R.; Schlegel, H. B.; Verani, C. N., *Inorg. Chem.*, **2006**, *45*, 955; (c) Pratt, R. C.; Mirica, L. M.; Stack, T. D. P.; *Inorg.Chem.*, **2004**, *43*, 8030.

115. Arora, H.; Philouze, C.; Jarjayes, O.; Thomas, F. *Dalton Trans.* **2010**, *39*, 10088.

116. Parr, R. G.; Yang, W. *Density-functional theory of atoms and molecules*, Oxford University Press, New York, **1989**.

117. (a) Lesh, F. D.; Shanmugam, R.; Allard, M. M.; Lanznaster, M.; Heeg, M. J.; Rodgers, M. T.; Shearer, J. M.; C. N. Verani, *Inorg. Chem.* **2010**, *49*, 7226; (b) Lanznaster, M.; Hratchian, H. P.; Heeg, M. J.; Hryhorczuk, L. M.; McGarvey, B. R.; Schlegel, H. B.; Verani, C. N. *Inorg. Chem.* **2006**, *45*, 955; (c) Pratt, R. C.; Mirica, L. M.; Stack, T. D. P. *Inorg. Chem.* **2004**, *43*, 8030.

118. Kundu, S.; Datta, A.; Hazra, S.; *Langmuir*, **2005**, *21*, 5894.

119. Ries, H. E. Jr. *Nature* **1979**, *281*, 287.

120. Galvan-Miyoshi, J.; Ramos, S.; Ruiz-Garcia, J.; Castillo, R. J.; *Chem. Phys.*, **2001**, *115*, 8178.

121. Dhanabalan, A.; Mello, S. V.; Oliveira, O. N Jr.; *Macromolecules* **1998**, *31*, 1827.

122. (a) Spano, F. C.; Silva, C. *Annu. Rev. Phys. Chem.* **2014**, *65*, 477; (b) Menzel, H.; McBride, J. S.; Weichart, B.; Ruther, M. *Thin Solid Films*, **1996**, *285*, 640; (c) Menzel, H.; Weichart, B.; Schmidt, A.; Paul, S.; Knoll, W.; Stumpe, J.; Fischer, T.; *Langmuir*, **1994**, *10*, 1926.

123. Brezesinski, G.; Dobner, B.; Stefaniu, C.; Vollhardt, D.; *J. Phys. Chem. C.*, **2011**, *115*, 8206; (b) Wang, L.; Cruz, A.; Flach, C. R.; Pérez-Gil, J.; Mendelsohn, R.; *Langmuir*, **2007**, *23*, 4950.

124. (a) Joy, S.; Pal, P.; Mondal, T. K.; Talapatra, G. B.; Goswami, S.; *Chem. Eur. J.*, **2012**, *18*, 1761; (b) Brezesinski, G.; Dobner, B.; Stefaniu, C.; Vollhardt, D.; *Langmuir*, **2011**, *27*, 5386; (d) Hasegawa, T.; Umemura, J.; Takenaka, T.; *J. Phys. Chem.*, **1993**, *97*, 9009.

125. Paul, N. D.; Rana, U.; Goswami, S.; Mondal, T. K.; Goswami, S. *J. Am. Chem. Soc.* **2012**, *134*, 6520.

126. (a) Seo, K.; Konchenko, A. V.; Lee, J.; Bang, G. S.; Lee, H. *J. Am. Chem. Soc.* **2008**, *130*, 2553; (b) Kitagawa, K.; Morita, T.; Kimura, S. *Langmuir* **2005**, *21*, 10624; (c) Zhang, L.; Bain, J. A.; Zhu, J. G.; Abelmann, L.; Onoue, T. *IEEE Trans. Magn.* **2004**, *40*, 2549.

127. (a) He, J.; Fu, Q.; Lindsay, S.; Ciszek, J. W.; Tour, J. M.; *J. Am. Chem. Soc.* **2006**, *128*, 14828; (b) Scudiero, L.; Barlow, D. E.; Hipps, K. W. *J. Phys. Chem. B* **2002**, *106*, 996; (c) Schmidt, A.; Armstrong, N. R.; Goeltner, C.; Muellen, K. *J. Phys. Chem.* **1994**, *98*, 11780.

128. (a) Metzger, R. M. *Chem. Rev.* **2015**, *115*, 5056; (b) Franco, I.; Solomon, G. C.; Schatz, G. C.; Ratner, M. A. *J. Am. Chem. Soc.* **2011**, *133*, 15714; (c) Ashwell, G. J.; Urasinska-Wojcik, B.; Phillips, L. *J. Angew. Chem. Int. Ed.* **2010**, *49*, 3508; (d) Troisi, A.; Ratner, M. A. *Nano Lett.* **2004**, *4*, 591; (e) Troisi, A.; Ratner, M. A. *J. Am. Chem. Soc.* **2002**, *124*, 14528; (f) Joachim, C.; Gimzewski, J. K.; Aviram, A. *Nature* **2000**, *408*, 541; (g) Metzger, R. M. Acc. Chem. Res. 1999, 32, 950.

129. Ariga, K.; Yamauchi, Y.; Mori, T.; Hill, J. P. *Adv. Mater.* **2013**, *25*, 6477.

130. (a) Jaiswal, A.; Rajagopal, D.; Lakshmikantham, M. V.;Cava, M. P.; Metzger, R. M. *Phys. Chem. Chem. Phys.* **2007**, *9*, 4007; (b) Mujica, V.; Ratner, M. A.; Nitzan, *A. Chem. Phys.* **2002**, *281*,147; (b) Krzeminski, C.; Delerue, C.; Allan, G.; Vuillaume, D.; Metzger, R. M. *Phys. Rev. B* **2001**, *64*, 085405.

131. Wickramasinghe, L. D.; Mazumder, S.; Gonawala, S.; Perera, M. M.; Baydoun, H.; Thapa, B.; Li, L.; Xie, L.; Mao, G.; Zhou, Z.; Schlegel, H. B.; Verani, C. N. *Angew. Chem. Int. Ed.* **2014**, *53*, 14462.

132. Wickramasinghe, L. D.; Perera, M. M.; Li, L.; Mao, G.; Zhou, Z.; Verani, C. N. *Angew. Chem. Int. Ed.* **2013**, *52*, 13346.

133. Lanznaster, M.; Hratchian, H. P.; Heeg, M. J.; Hryhorczuk, L. M.; McGarvey, B. R.; Schlegel, H. B.; Verani, C. N. *Inorg. Chem.* **2006**, *45*, 955.

134. Dolomanov, O.V.; Bourhis, L.J.; Gildea, R.J; Howard, J.A.K.; Puschmann, H. *J. Appl. Cryst.* **2009**, *42*, 339.

135. Sheldrick, G.M. *Acta Cryst.* **2015**, *A71*, 3.

136. Sheldrick, G.M. *Acta Cryst.* **2008**, *A64*, 112.

137. Gagne, R.; Koval, C.; Licenski, G. *Inorg. Chem.* **1980,** *19,* 2854

138. (a) Basu, D.; Allard, M. M.; Xavier, F. R.; Heeg, M. J.; Schegal, H. B.; Verani, C. N. *Dalton Trans*. **2015**, *44*, 3454; (b) Basu, D.; Mazumder, S.; Shi, X.; Baydoun, H.; Niklas, J.; Poluektov, O.; Schlegel, H. B.; Verani, C. N. *Angew. Chem. Int. Ed.* **2015**, *54*, 2105; (c) Allard, M. M.; Sonk, J. A.; Heeg, M. J.; McGarvey, B. R.; Schlegel, H. B.; Verani, C. N. *Angew. Chem. Int. Ed.* **2012**, *51*, 3178 (c) Lanznaster, M.; Heeg, M. J.; Yee, G. T.; McGarvey, B. R.; Verani, C. N. *Inorg. Chem.,* **2007**, *46*, 72.

139. (a) Mayilmurugan, R.; Stoeckli-Evans, H.; Suresh, E.; Palaniandavar, M. *Dalton Trans*. **2009**, 5101; (b) Ruan, W.; Hu, G; Wang, S;Tian, J.; Wang, Q.; Zhu, Z.; *Chin. J. Chem.* **2005**, *23*,709.

140. (a) Shongwe, M. S.; Kaschula, C. H.; Adsetts, M. S.; Ainscough, E. W.; Brodie, A. M.; Morris, M.J. *Inorg. Chem.* **2005**, *44*, 3070; (b) Gaber, B. P.; Miskowski, V.; Spiro, T. G. *J. Am. Chem. Soc.* **1974**, *96*, 6868.

141. (a) Mayilmurugan, R.; Suresh E.; Palaniandavar, M. *Inorg. Chem.* **2007**, *46*, 6038; (b) Velusamy, M.; Palaniandavar, M.; Srinivasa, R.; Gopalan; Kulkarni, G. U. *Inorg. Chem.* **2003**, *42*, 8283.

142. Rotthaus, O.; Jarjayes, O.; Philouz, C.; Valle, C. P. D.; Thomas, F. *Dalton Trans.* **2009**, *10* 1792.

143. Allard, M. M.; Sonk, J. A.; Heeg, M. J.; McGarvey, B. R.; Schlegel, H. B.; Verani, C. N. *Angew. Chem. Int. Ed.* **2012**, *51*, 3178.

144. (a) Kochem, A.; Jarjayes, O.; Baptiste, B.; Philouze, C.; Vezin, H.; Tsukidate, K.; Tani, F.; Orio, M.; Shimazaki, Y.; Thomas, F. *Chem. Eur. J.* **2012**, *18*, 1068; (b) Pratt, R. C.; Stack, T. D. P. *J. Am. Chem. Soc.* **2003**, *125*, 8716.

145. (a) Kundu, S.; Datta, A.; Hazra, S. *Langmuir* **2005**, *21*, 5894; (b) Ries Jr., H. E. *Nature* **1979**, *281*, 287.

146. Shakya, R.; Hindo, S. S.; Wu, L.; Allard, M. M.; Heeg, M. J.; Hratchian, H. P.; McGarvey, B. R.; da Rocha, S. R. P.; Verani, C. N. *Inorg. Chem.* **2007**, *46*, 9808.

147. Mitsuishi, M.; Zhao, F.; Kim, Y.; Watanabe, A.; Miyashita, T. *Chem. Mater.* **2008**, *20*, 4310.

148. (a) Joy, S.; Pal, P.; Mondal, T. K.; Talapatra, G. B.; Goswami, S. *Chem. Eur. J.* **2012**, *18*, 1761; (b) Brezesinski, G.; Dobner, B.; Stefaniu, C.; Vollhardt, D. *Langmuir*, **2011**, *27*, 5386.

149. Verani, C. N.; Shanmugam, R.; Xavier, F. R.; Allard, M. M.; Kpogo, K. K. *Dalton Trans.* **2013**, *42*, 15296.

150. (a) Trimpin, S.; Inutan, E. D. *Anal. Chem.* **2013**, *85*, 2005; (b) Trimpin, S.; Inutan, E. D. *J. Am. Soc. Mass Spectrom.* **2013**, *24*, 722; (c) Chakrabarty, S.; Pagnotti, V. S.; Inutan, E. D.; Trimpin, S.; McEwen, C. N. *J. Am. Soc. Mass Spectrom.*, **2013**, *24*, 1102.

151. (a) He, J.; Fu, Q.; Lindsay, S.; Ciszek, J. W.; Tour, J. M.; *J. Am. Chem. Soc.* **2006**, *128*, 14828; (b) Scudiero, L.; Barlow, D. E.; Hipps, K. W. *J. Phys. Chem. B* **2002**, *106*, 996; (c) Schmidt, A.; Armstrong, N. R.; Goeltner, C.; Muellen, K. *J. Phys. Chem.* **1994**, *98*, 11780.

152. (a) Rohrman, F. A. *J. Chem. Educ.* **1933**, *10*, 141; (b) Rohrman, F. A. *J. Chem. Educ.* **1933**, *10*, 215; (c) Rohrman, F. A. *J. Chem. Educ.* **1933**, *10*, 297.

153. Tiwari, A.; Rawlins, J.; Hihara, L. H. *Intelligent Coatings for Corrosion Control*, Elsevier Inc, Waltham, MA, **2015**, 1-15.

154. Committee on research opportunities in corrosion science and engineering, *Research opportunities in corrosion science and engineering*, the national academics press, Washington, DC, 61-67.

155. (a) Wickramasinghe, L. D.; Mazumder, S.; Gonawala, S.; Perera, M. M.; Baydoun, H.; Thapa, B.; Li, L.; Xie, L.; Mao, G.; Zhou, Z.; Schlegel, H. B.; Verani, C. N. *Angew. Chem. Int. Ed.* **2014**, *53*, 14462; (b) L. D. Wickramasinghe, M. M. Perera, L. Li, G. Mao, Z. Zhou, and C. N. Verani *Angew. Chem. Int. Ed.* **2013**, *52*, 13346.

156. Dolomanov, O. V.; Bourhis, L. J.; Gildea, R. J.; Howard, J. A. K.; Puschmann, H. *J. Appl. Cryst.* **2009**, *42*, 339.

157. Sheldrick, G. M. *Acta Cryst.* **2008**, *A64*, 112.

158. Addison, A. W.; Rao, T. N.; Reedijk, J.; van Rijn, J.; Verschoor, G. C. *Dalton Trans.* **1984**, *7*, 1349.

159. Rotthaus, O.; Jarjayes, O.; Thomas, F.; Philouze, C.; Saint-Aman, E.; Pierre, J. *Dalton Trans.* **2007**, 889.

160. Arora, H.; Philouze, C.; Jarjayes, O.; Thomas, F. *Dalton Trans.* **2010**, *39*, 10088.

161. Gagne, R.; Koval, C.; Licenski, G. *Inorg. Chem.* **1980,** *19*, 2854.

162. (a) Pratt, R. C.; Mirica, L. M.; Stack, T. D. P. *Inorg.Chem.* **2004**, *43*, 8030; (b) Lanznaster, M.; Hratchian, H. P.; Heeg, M. J.; Hryhorczuk, L. M.; McGarvey, B. R.; Schlegel, H. B.; Verani, C. N. *Inorg. Chem.* **2006**, *45*, 955; (c) Lesh, F. D.; Shanmugam, R.; Verani, C. N. *Inorg. Chem.* **2010**, *49*, 7226.

163. Kundu, S.; Datta, A.; Hazra, S. *Langmuir* **2005**, 21, 5894.

164. Ries, H. E. Jr. *Nature* **1979**, *281*, 287.

165. Galvan-Miyoshi, J.; Ramos, S.; Ruiz-Garcia, J.; Castillo, R. J. *Chem. Phys.* **2001**, *115*, 8178.

166. (a) Brezesinski, G.; Dobner, B.; Stefaniu, C.; Vollhardt, D. *J. Phys. Chem. C*. **2011**, *115*, 8206; (b) Wang, L.; Cruz, A.; Flach, C. R.; Pérez-Gil, J.; Mendelsohn, R. *Langmuir* **2007**, *23*, 4950.

167. (a) Joy, S.; Pal, P.; Mondal, T. K.; Talapatra, G. B.; Goswami, S. *Chem. Eur. J.* **2012**, *18*, 1761; (b) Brezesinski, G.; Dobner, B.; Stefaniu, C.; Vollhardt, D. *Langmuir* **2011**, *27*, 5386; (c) Hasegawa, T.; Umemura, J.; Takenaka, T. *J. Phys. Chem.* **1993**, *97*, 9009.

168. Cea, P.; Lopez, M. C.; Martin, S.; Villares, A.; Pera, G.; Giner, I. *J. Chem. Ed.* **2009**, *86*, 723.

169. Gao, X.; Liu, S.; Lu, H.; Gao, F.; Ma, H. *Ind. Eng. Chem. Res.* **2015**, *54*, 1941.

170. (a) Lewis, N. S.; Nocera, D. G. *PNAS*, **2006**, *103*, 15729; (b) Nocera, D. G. *Acc. Chem. Res.* **2012**, 45, 767.

171. (a) Du, P.; Eisenberg, R. *Energy Environ. Sci.* **2012**, *5*, 6012; (b) Kudo, A.; Kato, H.; Tsuji, I. *Chem. Lett.* **2004**, *33*, 1534.

172. (a) Blakemore, J. D.; Crabtree, R. H.; Brudvig, G. W.; *Chem. Rev.* **2015**, *115*, 12974; (b) Duan, L.; Tong, L.; Xua, Y.; Sun, L.; *Energy Environ. Sci.* **2011**, *4*, 3296; (c) Liu, F.; Concepcion, J. J.; Jurss, J. W.; Cardolaccia, T.; Templeton, J. L.; Meyer, T. J. *Inorg. Chem.* **2008**, *47*, 1727; (d) Deng, Z.; Tseng, H.; Zong, R.; Wang, D.; Thummel, R. *Inorg. Chem.* **2008**, *47*, 1835.

173. For Manganese see; (a) Ma, L.; Wang, Q.; Man, W.; Kwong, H.; Ko, C.; Lau, T. *Angew. Chem. Int. Ed.* **2015**, *54*, 5246; (b) Lee, W.; Muñoz III, S. B.; Dickie, D. A.; Smith, J. M. *Angew. Chem. Int. Ed.* **2014**, *53*, 9856.

174. For iron see; (a) Wickramasinghe, L. D.; Zhou, R.; Zong, R.; Vo, P.; Gagnon, K. J.; Thummel, R. P. *J. Am. Chem. Soc.* **2015**, *137*, 13260; (b) Coggins, M. K.; Zhang, M.; Vannucci, A. K.; Dares, C. J.; Meyer, T. J. *J. Am. Chem. Soc.* **2014**, *136*, 5531; (c) Hong, D.; Mandal, S.; Yamada, Y.; Lee, Y.; Nam, W.; Llobet, A.; Fukuzumi, S. *Inorg. Chem.* **2013**, *52*, 9522; (d) Fillol, J. L.; Codolà, Z.; Garcia-Bosch, I.; Gómez, L.; Pla, J. J.; Costas, M. *Nat. Chem.* **2011**, *3*, 807; (e) Ellis, W. C.; McDaniel, N. D.; Bernhard, S.; Collins, T. J. *J. Am. Chem. Soc.* **2010**, *132*, 10990.

175. For cobalt see; (a) Wang, H.; Mijangos, E.; Ott, S.; Thapper, A. *Angew. Chem. Int. Ed.* **2014**, *53*, 14499; (b) Nakazono, T. A.; Parent, R.; Sakai, K. *Chem. Commun.* **2013**, *49*, 6325; (c) Leung, C.; Ng, S.; Ko, C.; Man, W.; Wu, J.; Chen, L.; Lau, T. *Energy Environ. Sci.* **2012**, *5*, 7903.

176. For nickel see; (a) Han, Y.; Wu, Y.; Lai, W.; Cao, R. *Inorg. Chem.* **2015**, *54*, 5604; (b) Zhang, M.; Zhang, M.; Hou, C.; Ke, Z.; Lu, T. *Angew. Chem. Int. Ed.* **2014**, *53*, 13042.

177. For copper see; (a) Su, X.; Gao, M.; Jiao, L.; Liao, R.; Siegbahn, P. E. M.; Cheng, J.; Zhang, M. *Angew. Chem. Int. Ed.* **2015**, *54*, 4909; (b) Pap, J. S.; Szyrwiel, Ł.; Srankó, D.; Kerner, Z.; Setner, B.; Szewczuk, Z.; Malinka, W. *Chem. Commun.* **2015**, *51*, 6322; (c) Coggins, M. K.; Zhang, M.; Chen, Z.; Song, N.; Meyer, T. J. *Angew. Chem. Int. Ed.* **2015**, *53*, 12226; (d) Gerlach, D. L.; Bhagan, S.; Cruce, A. A.; Burks, D. B.; Nieto, I.; Truong, H. T.; Kelley, S. P.; Herbst-Gervasoni, C. J.; Jernigan, K. L.; Bowman, M. K.; Pan, S.; Zeller, M.; Papish, E. T. *Inorg. Chem.* **2014**, *53*, 12689.

178. (a) Sheehan, S. W.; Thomsen, J. M.; Hintermair, U.; Crabtree, R. H.; Brudvig, G. W.; Schmuttenmaer, C. A. *Nat. Commun.* **2015**, *6*, 6469; (b) Chen, Z.; Concepcion, J. J.; Jurss, J. W.; Meyer, T. J. *J. Am. Chem. Soc.* **2009**, *131*, 15580.

179. (a) Li, F.; Li, L.; Tong, L.; Daniel, Q.; Göthelid, M.; Sun, L. *Chem. Commun.* **2014**, *50*, 13948; (b) Li, F.; Zhang, B.; Li, X.; Jiang, Y.; Chen, L.; Li, Y.; Sun, L. *Angew. Chem. Int. Ed.* **2011**, *50*, 12276.

180. Basu, D.; Allard, M. M.; Xavier, F. R.; Heeg, M. J.; Schegal, H. B.; Verani, C. N. *Dalton Trans.* **2015**, *44*, 3454.

181. (a) Pizzolato, E.; Natali, M.; Posocco, B.; Montellano, A. L.; Bazzan, I.; Valentin, M.; Galloni, P.; Conte, V.; Bonchio, M.; Scandola, F.; Sartorel, A. *Chem. Commun.* **2013**, *49*, 9941; (b) López, A. M.; Natali, M.; Pizzolato, E.; Chiorboli, C.; Bonchio, M.; Sartorel, A.; Scandola, F. *Phys. Chem. Chem. Phys.* **2014**, *16*, 12000.

182. Chen, H.; Sun, Z.; Liu, X.; Han, A.; Du, P. *J. Phys. Chem. C* **2015**, *119*, 8998.

183. Wickramasinghe, L. D.; Perera, M. M.; Li, L.; Mao, G.; Zhou, Z.; Verani, C. N. *Angew. Chem. Int. Ed.* **2013**, *52*, 13346.

184. Wickramasinghe, L. D.; Mazumder, S.; Gonawala, S.; Perera, M. M.; Baydoun, H.; Thapa, B.; Li, L.; Xie, L.; Mao, G.; Zhou, Z.; Schlegel, H. B.; Verani, C. N. *Angew. Chem., Int. Ed.* **2014**, *53*, 14462.

185. (a) Verani, C. N.; Driscoll, J.; Keyes, P. H.; Heeg, M. J. *Inorg. Chem.* **2014**, *53*, 5647; (b) Shakya, R.; Keyes, P. H.; Heeg, M. J.; Moussawel, A.; Heiney, P. A.; Verani, C. N. *Inorg. Chem.* **2006**, 45, 7587.

186. (a) Driscoll, J. A.; Allard, M. M.; Wu, L.; Heeg, M. J.; da Rocha, S. R. P.; Verani, C. N. *Chem. Eur. J.* **2008**, *14*, 9665; (b) Shakya, R.; Hindo, S. S.; Wu, L.; Ni, S.; Allard, M. M.; Heeg, M. J.; da Rocha, S. R. P.; Yee, G. T.; Hratchian, H. P.; Verani, C. N. *Chem. Eur. J.* **2007**, *13*, 9948.

187. (a) Basu, D.; Mazumder, S.; Shi, X.; Baydoun, H.; Niklas, J.; Poluektov, O.; Schlegel, H. B.; Verani, C. N. *Angew. Chem. Int. Ed.* **2015**, *54*, 2105 (b) Allard, M. M.; Sonk, J. A.; Heeg, M. J.; McGarvey, B. R.; Schlegel, H. B.; Verani, C. N. *Angew. Chem., Int. Ed.* **2012**, *51*, 3178; (c) Lanznaster, M.; Heeg, M. J.; Yee, G. T.; McGarvey, B. R.; Verani, C. N. *Inorg. Chem.* **2007**, *46*, 72.

188. Gagne, R.; Koval, C.; Licenski, G. *Inorg. Chem.* **1980,** *19*, 2854.

189. Allard, M. M.; Xavier, F. R.; Heeg, M. J.; Schlegel, H. B.; Verani, C. N. *Eur. J. Inorg. Chem.* **2012**, *29*, 4622.

190. (a) Kundu, S.; Datta, A.; Hazra, S. *Langmuir* **2005**, *21*, 5894; (b) Ries Jr., H. E. *Nature* **1979**, *281*, 287.

191. Shakya, R.; Hindo, S. S.; Wu, L.; Allard, M. M.; Heeg, M. J.; Hratchian, H. P.; McGarvey, B. R.; da Rocha, S. R. P.; Verani, C. N. *Inorg. Chem.* **2007**, *46*, 9808.

192. (a) Brezesinski, G.; Dobner, B.; Stefaniu, C.; Vollhardt, D. *J. Phys. Chem. C.* **2011**, *115*, 8206; (b) Wang, L.; Cruz, A.; Flach, C. R.; Pérez-Gil, J.; Mendelsohn, R. *Langmuir* **2007**, *23*, 4950.

193. (a) Brezesinski, G.; Dobner, B.; Stefaniu, C.; Vollhardt, D. *Langmuir* **2011**, *27*, 5386; (b) Kattner, J.; Hoffmann, H. *External reflection spectroscopy of thin films on dielectric substrates: Hand book of vibrational spectroscopy*; John Wiley & Sons Ltd., Chichester, **2002**, pp 12-14; (c) Galvan-Miyoshi, J.; Ramos, S.; Ruiz-Garcia, J.; Castillo, R. J. *J. Chem. Phys.* **2001**, *115*, 8178; (d) Hasegawa, T.; Umemura, J.; Takenaka, T. *J. Phys. Chem.* **1993**, *97*, 9009.

194. Basu, D.; Mazumder, S.; Shi, X.; Staples, R.; Schlegel, H. B.; Verani, C. N. *Angew. Chem. Int. Ed.* **2015**, *54*, 7139.

195. Hong, D.; Jung, J.; Park, J.; Yamada, Y.; Suenobu, T.; Lee, Y.; Nam, W.; Fukuzumi, S. *Energy Environ. Sci.* **2012**, *5*, 7606.

196. Lee, W.; Mucoz, S. B.; Dickie, D. A.; Smith, J. M. *Angew. Chem. Int. Ed.* **2014**, *53*, 9856.

197. Sander, R. *Atmos. Chem. Phys.* **2015**, *15*, 4399.

ABSTRACT

ELECTRON TRANSFER STUDIES IN LANGMUIR-BLODGETT FILMS OF METALLOSURFACTANTS FOR CURRENT RECTIFICATION, CORROSION MITIGATION, AND WATER OXIDATION

by

SUNALEE GONAWALA J. M.

August 2016

Advisor: Dr. Cláudio N. Verani

Major: Chemistry (Inorganic)

Degree: Doctor of Philosophy

The work presented in this dissertation is focused on the design and synthesis of new redox-active amphiphilic architectures to optimize and understand the redox, electronic, and film formation properties for applications in current rectification, corrosion mitigation, and water oxidation. As such, new redox-active, and amphiphilic iron(III), cobalt(III), nickel(II), copper(II), and zinc(II) complexes were synthesized as precursors for Langmuir-Blodgett films used for the aforementioned applications.

For the use in molecular rectification, amphiphilic copper(II) and nickel(II) complexes with $[N_2O_2]$ ligand environment were synthesized. Homogeneous film formation ability was observed between ~20-25 mN/m pressure, with a film collapse observed at ~35 mN/m for both complexes. The presence of both ligand- and metal-based redox processes made the copper(II) complex a viable candidate for device fabrication. However, current *vs.* voltage (I/V) measurements obtained for Au|LB|Au assemblies resulted in a flat I/V curve, diagnostic of an insulating nature. Comparison of the frontier molecular orbital energy between the insulating copper(II) complex and a similar rectifying iron(III) complex provided insight as to the rectification mechanism. Considering the orbital arrangement, the singly occupied molecular

orbital (SOMO) of the Cu(II) complex is energetically high to enable electron transfer, thus making it an insulator. For comparison purposes, the SOMO of Fe(III) is situated 1.0 eV above the Fermi level of the Au electrode allowing for easy electron transfer from electrode to molecule. Furthermore, the highest occupied molecular orbital (HOMO) of Cu(II) is situated 1.0 eV below the Au Fermi level and the insulating nature of the device confirms that the HOMO is not involved in electron transfer. Therefore, only the SOMO of the Fe(III) complex should be involved in electron transfer following an asymmetric current rectification mechanism. This observation confirms that the SOMOs of such molecules can act as electron acceptors to facilitate electron transfer and assist in current rectification. In this regard, to enhance the energy compatibility between the SOMO and the Fermi level of the Au electrode, a series of new asymmetric iron(III) complexes with $[N_2O_2]$, $[N_3O]$, and $[N_3O_2]$ coordination environments were synthesized. According to isothermal compression data, new complexes exhibited amphiphilic nature with collapse pressures between ~35-40 mN/m. Calculations performed based on the redox potentials of the complexes showed that the SOMO energies of the Fe(III) complexes with $[N_2O_2]$ coordination environment were situated 0.4 eV above the electrode Fermi level, while the SOMO energies of other complexes were situated 0.8 eV above the Fermi level. The energetic compatibility of these SOMOs with electrode Fermi levels makes these complexes viable candidates for molecular current rectification. Therefore, Au|LB|Au assemblies can be used to identify the rectification behavior of theses complexes.

Based on the knowledge that Cu(II) salophen-based complexes can insulate electron transfer and therefore preclude electron transfer, a series of amphiphilic Fe(III), Cu(II), and Zn(II) complexes were synthesized to be used as protective coatings in corrosion mitigation. Cyclic voltammetry experiments revealed that 11-layer LB films of the complexes can

effectively passivate electron transfer to the surface in a better way than the ligand alone. Agar experiments revealed a low corrosion rate for LB film-coated iron plates, with no blue coloration in the complex-coated area after one week. The presence of $K_3Fe(CN)_6$ in the agar medium can form a Prussian blue complex with Fe^{2+} ions produced due to oxidation. Optical micrograph and SEM images showed considerably low rust formation on complex-coated iron plates compared to the bare iron plate. Weight loss measurement studies confirmed that 11 layers of the Fe(III) and Zn(II) complexes demonstrate the best corrosion mitigation ability, with respective corrosion inhibition efficiencies of 27 % and 30 %, while the ligand alone showed an inhibition efficiency of only 6 %. This observation suggests that metal coatings can function as passivating barriers to electron flow between the electrolyte and the iron plate.

Similarly, the use of LB films in heterogeneous water oxidation was investigated using a phenolate-rich cobalt(III) complex. This complex demonstrated homogeneous film formation ability at ~30-35 mN/m, with a collapse pressure of 42 mN/m. Monolayer-deposited FTO electrodes supported water oxidation at an overpotential of 0.50 V. Gradual enhancement of catalytic activity was observed in up to 9 deposited layers. Upon application of a potential bias, the monolayer yielded an estimated turnover number of 54,000 ± 1,500 after one hour with a Faradaic efficiency of ~100 %. Although the molecular species were rearranging into an ultrathin catalytic layer, the presence of symmetric and asymmetric C-H vibrations in IRRAS spectra suggests that carbon-based residues act as modifiers, thus confirming that the ligand choice is relevant to obtain efficient and robust catalytic films for water oxidation.

In summary, this dissertation research presented a new series of ligand designs varying from $[N_2O_2]$, $[N_3O]$, and $[N_3O_2]$ and their iron(III), cobalt(III), nickel(II), copper(II), and zinc(II) complexes, which exhibit both redox and amphiphilic character. Further, this project investigates

their LB film formation ability and use of these films on solid substrates in molecular electronics, corrosion mitigation, and heterogeneous water oxidation.

AUTOBIOGRAPHICAL STATEMENT

Sunalee Gonawala J. M.

Professional Preparation: Education

Wayne State University (MI, USA), Inorganic Chemistry, Ph.D., **2016**
University of Colombo (Sri Lanka), Chemistry, B. Sc. (Honors), **2010**

Appointments

2013-2016: Graduate Research Assistant, Department of Chemistry, Wayne State University
2011-2013: Graduate Teaching Assistant, Department of Chemistry, Wayne State University
2010-2011: Teaching Assistant, Department of Chemistry, University of Colombo

Publications

1. Wickramasinghe, L. D.*; Mazumder, S.*; **Gonawala, S.***; Perera, M. M.; Baydoun, H.; Thapa, B.; Li, L.; Xie, L.; Mao, G.; Zhou, Z.; Schlegel, H. B.; Verani, C. N. "Mechanisms of Rectification in Au|molecule|Au Devices based on Langmuir-Blodgett films of Iron(III) and Copper(II) Sufactants" (*equal contribution) *Angew. Chem. Int. Ed.* **2014**, 53, 14462-14467.
2. **Gonawala, S.**; Baydoun, H.; Wickramasinghe, L.; Verani, C. N. "Efficient Water Oxidation with Electromodified Langmuir-Blodgett Films of Procatalytic [$Co^{III}(N_2O_3)$] Metallosurfactants on Electrodes" Submitted.
3. **Gonawala, S.**; Ribeiro, V.; Verani, C. N. "Langmuir-Blodgett Films of Salophen-based Metallosurfactants as Surface Pretreatment Coatings for Corrosion Mitigation" Manuscript in preparation.

Presentations

1. Poster presentation on "Heterogeneous Water Oxidation with Langmuir-Blodgett Films of Procatalytic [$Co^{III}(N_2O_3)$] Metallosurfactant"
   The Michigan Catalysis Society, 37th Annual Spring Symposium, The Midland Country Club, Midland, Michigan, May 4, 2016
2. Oral presentation on "Salen-based Amphiphilic Copper(II) and Nickel(II) Complexes for Langmuir Blodgett Film Formation"
   246th ACS National Meeting & Exposition, Indianapolis, IN, United States, September 8-12, 2013 (2013), INOR-529

Skills

Synthesis and characterization, qualitative and quantitative analysis, FTIR, NMR, UV-visible, and IRRAS spectroscopy, electro-and spectroelectrochemistry, bulk electrolysis, gas chromatography, Langmuir-Blodgett technique, device fabrication